EFFECT OF PHYSICAL TRAFFIC & T-JUNCTION LAYOUT ON RADIO SIGNAL CHARACTERISTICS & NETWORK PERFORMANCE AT 5.9 GHZ

Thesis submitted for the degree of

Doctor of Philosophy

at the University of Leicester

by

Crishantha Jerome Clayton MEng (Leicester)

Department of Engineering

University of Leicester

July 2016

Abstract: Effect of Physical Traffic and T-Junction Layout on Radio Signal Characteristics & Network Performance by Jerome Clayton

IEEE 802.11p, which operates at 5.9 GHz, has been the widely adopted communications standard for vehicular communications and this has prompted studies at different physical locations on the network performance, pathloss, Doppler and delay spreads in the 5.9 GHz radio channel. This thesis presents novel measurements of network performance, signal strength and Doppler spread under NLOS conditions at three T-junctions with different street widths and building layouts. The study found that there was less received power and poorer network performance in intersections with single/dual lanes and fewer buildings on either side of the roads – the maximum range for reliable operation (>90%) of the network is reduced to approximately 10 m from the intersection centre. Higher signal strength in the presence of buildings is consistent with multipath propagation contributing positively towards the signal strength as shown by a site specific ray tracing model developed as part of this project. Signal strength measurements were compared with predictions from the model virtualsource11p and a median error less than 5 dB was found for measurements in urban environments and closer to the intersection centre. The median error was greater than 10 dB and increased with the distance from the intersection centre in junctions with wider roads and fewer buildings either side of the road. The relationship between a vehicle's size and the Doppler spread it causes is another unique observation of this study and has been investigated by developing a simple model. Doppler spreads become larger as the reflecting vehicle moves closer to the transmitter and receiver and when the size of this vehicle is larger. A directional antenna was used to determine the azimuth of arrival of the strongest multipath components with the observations demonstrating the importance of including transient features in maps when ray tracing.

Acknowledgements

I would like to that my parents, Sumi and Bernard Clayton, the most. Without their constant love, support and caring I would not have been able to achieve anything. I would also like to thank my siblings, Indu and Chandika, for their support, entertainment and encouragement. I would also like to thank my many uncles, especially Uncle Asoka, many aunts and numerous cousins for pushing me along the way in their own ways.

Dr. Alan Stocker has been extremely helpful over the last few years – providing very useful professional support and guidance at all times. I would also like to thank Dr. Siddle, Prof. Warrington, Dana Hassan and the rest of the research group. I would like to thank Andrew Truman, Barry Chester and Will for their technical support. Dominic Kent, Andrew Chorley, Michelle Pryce, Debbie Richardson and Julie Clayton have also been very helpful through the years. A big thank you to the rest of the Engineering Department staff for all their support and kindness. A truly special and wonderful place!

Tim Edwards, Douglas Mearns and Anthony Baxter have all been instrumental and helpful to my research and I thank them a lot for both technical guidance and equipment.

My PhD days in Leicester would not have been half as fun without the University's Cricket Club. Thank you for all the good times both on and off the field and for keeping me sane. A big thank you goes especially to Jean and Mary, Chris and Sophie, the Eds and Ishan.

Last but not least, I would like to thank the multitude of friends (flung across the world) who have helped me through this journey from day 1; Carlene, Becky, Sophie, Amelie, Julien, Martin, Alessandro and Neil to name a few and countless others who know who they are but cannot be listed due to space restrictions. Thank you all!

Table of Contents

List of Tables

List of Figures

List of Commonly used Acronyms

AP .... Access Point
ASTM .... American Society for Testing Materials
BSM .... Basic Safety Message
cm .... centimetre
COTS .... Commercial off-the-Shelf
CW .... Continuous Wave
CWS .... Continuous Wave System
d .... Distance from the centre of the intersection
DAS .... Directional Antenna System
dB .... deciBel
dBi .... decibel isotropic
dBm .... decibel-milliwatts
DSPL .... Dual-Slope Piecewise-Linear
DSRC .... Dedicated Short Range Communications
EIRP .... Effective Isotropic Radiated Power
E_m .... Median error between measured signal strength and virtualsource11p prediction
FCC .... Federal Communications Commission
FFT .... Fast Fourier Transform
GHz .... Gigehertz
Hz .... Hertz
ICI .... Inter-Channel Interference
IEEE .... Institute of Electrical and Electronic Engineers
ISI .... Inter-Symbol Interference
ITS .... Intelligent Transport Systems
ITU .... International Telecommunications Union
IVC .... Inter-Vehicular Communications
kHz .... kilohertz
km/h .... kilometres per hour
LOS .... Line-of-Sight
m .... metre
MAC .... Medium Access Control
MANET .... Mobile Ad-hoc Network

Mbps .... Megabits per second
MHz .... Megahertz
MIDR .... Median Inter-Decile Range
MIMO .... Multiple Input Multiple Output
MPC .... Multipath Components
MPP .... Median Peak Power
ms .... millisecond
NLOS .... Non Line-of-Sight
NS .... Network System
OBU .... On-Board Unit
OFDM .... Orthogonal Frequency Division Multiplexing
PC .... Personal Computer
PDR .... Packet Delivery Ratio
PHY .... Physical
RMS .... Root Mean Square
RSS .... Received Signal Strength
RSSI .... Received Signal Strength Indicator
RSU .... Road-Side Unit
s .... Second
SAE .... Society of Automotive Engineers
SIMO .... Single Input Multiple Output
$T50_{FAR}$ .... Data collected in the less urban case – receiver in the range 18 – 44.8 m and transmitter 50 m away from the centre
$T50_{NEAR}$ .... Data collected in the less urban case – receiver in the range 10 – 19 m and transmitter 50 m away from the centre
$T50_{TOT}$ .... Data collected in the less urban case - transmitter 50 m away from the centre
$T70_{FAR}$ .... Data collected in the less urban case – receiver in the range 18 – 44.8 m and transmitter 70 m away from the centre
$T70_{NEAR}$ .... Data collected in the less urban case – receiver in the range 10 – 19 m and transmitter 70 m away from the centre
$T70_{TOT}$ .... Data collected in the less urban case - transmitter 70 m away from the centre
V2I .... Vehicle-to-Infrastructure
V2X .... Vehicle-to-Vehicle/Infrastructure
VANET .... Vehicular Ah-Hoc Network

WAVE ....Wireless Access in Vehicular Environments
WLAN .... Wireless Local Area Network
Δa .... Angular resolution
Δd .... Distance resolution

1 Introduction

1.1 Ad-Hoc Networking

In its simplest form, a computer network comprises of a set of interconnected computers which are used to share information and resources. Until the late 1970s computing and communications were not closely related but then they merged. Two major components make up a current computer network: distributed applications and networking infrastructure. This project is concerned with networking and infrastructure; which is the part of the network that deals with the communications medium (Murthy & Manoj 2004).

When it comes to Wireless Local Area Networks (WLANs) the standard used most widely is the IEEE 802.11 standard. The IEEE 802.11 standard falls under the IEEE 802.x LAN standards which specify the MAC (Medium Access Control) and PHY (PHYsical) layers. This includes adaptations to specific requirements of WLANs. A *'node'* (or mobile stations, STAs) is an electronic device which can be part of a WLAN; i.e. send and receive data from within a WLAN. A WLAN can be deployed amongst wireless nodes where each node in the network broadcasts information which can be received by all nodes within its direct transmission range.

Figure 1 displays a typical WLAN where the nodes are the PC, laptop, smart phone and printer. These nodes are connected wirelessly to the access point (AP), labelled as 'Router' in the figure, shown with the two antennas. APs can be equipped with the ability to connect to both wired and wireless networks which enable them to act as a bridge between the two types of networks. This figure shows one of two main types of WLAN available; an infrastructure network, where all of a node's data is routed via an access point. The second type of WLAN is ad-hoc WLAN and they need no fixed infrastructure. These networks can be created if and when required and spontaneously. In effect, each node performs the duty of a wireless router which is a unique defining feature of an ad-hoc network. If the destination node is not within the transmitting node's radio range, the packet of data will be routed through intermediate nodes which form a connection between the source and destination. (Murthy & Manoj 2004)

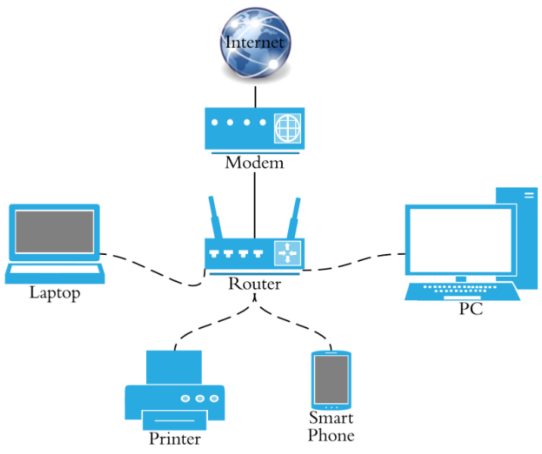

Figure 1: WLAN Example

Wireless networks also encourage mobility amongst nodes as opposed to a wired network.

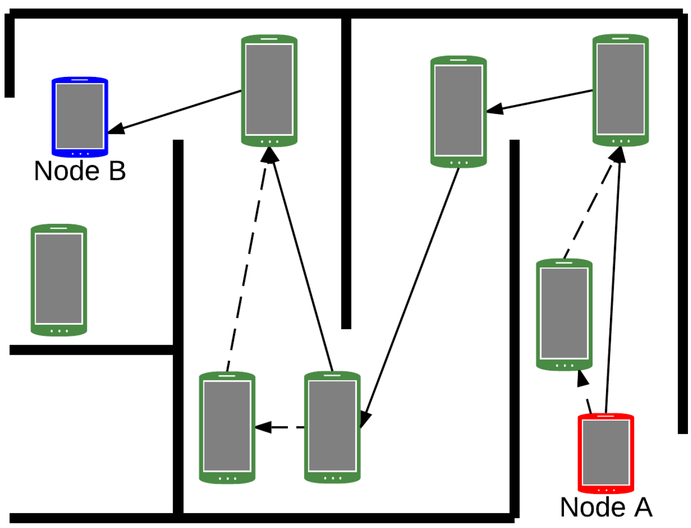

Figure 2: Example ad-hoc network

Figure 2 is an example of how an ad-hoc WLAN works. Node A wants to send data to Node B but the walls (represented by thick black lines) prevent direct connection between the two devices. The other nodes are used as intermediate nodes to relay the data packets from Node A to Node B. There is more than one path for the data to be routed using the other (green) nodes and the shortest path is shown by the solid line. The data could have been routed by three other paths using different combinations of the dashed lines.

An advantage of ad-hoc networks is that they can be created spontaneously and/or on demand. Such networks also support mobile nodes and are referred to as Mobile Ad-hoc NETworks (MANETs). This versatility of MANETs makes them ideal in locations where communications networks are required but there is no infrastructure – such as in rescue operations after a natural disaster. However, MANETs also have their disadvantages; due to their state of continuous change message routing requires continuous updates about each node's radio range and what other nodes fall into these ranges; too fewer nodes results in higher latencies and less throughput; dense node spreads can lead to packet collisions and increased energy use; the hidden node problem. More information about MANETs (including their uses) can be found in (Sarkar 2012). An example MANET is a network which will enable vehicles to communicate with other vehicles and roadside networking infrastructure.

1.2 Road Transport Issues

The world crucially depends on transport systems. As populations increase, so does the need to transport resources from locations of produce/processing to where the public live. In addition to the transportation of goods, the public also require transport. This requirement of mobility means that governments need to keep on improving and increasing the efficiency of their transport networks.

- Global automotive sales have been increasing since 2009 and 2015 will see a continuation of this trend (IHS 2015).
- The UK Department for Transport has released figures which show that in England over the last 10 years the distances travelled and the time spent travelling has been in decline (Department of Transport 2015a).
- It has also published figures which say that car travel is the most common mode for both trips and distances travelled despite the decrease in car use over the last decade (Department of Transport 2015b).
- 76% of households in England have access to at least one car with an estimated 31.8 million license holders and that the average car trip lasts for 22 minutes (Department of Transport 2015b).

This high usage of vehicles brings about its own consequences. A vast majority of vehicles are fuelled by fossil fuels which are in limited supply and whose usage leads towards climate change.

Further to this, there are road accidents which lead to injury, large economic losses and most importantly, the loss of lives which is incurable and irreparable. In 2014 the total costs of all the accidents in Great Britain was £ 16.31 billion (Department of Transport 2015c). More pressing is that in 2014 there were 194,477 adults and 16,727 children (under the age of 15) casualties whilst the number of adult and children reported as killed or seriously injured was 24,582 and 2,082 respectively. The United Kingdom however has a lot of rules and regulations in place to keep such tragic events low whilst in countries with medium and low incomes, 84% of the human population reside and 92% of road accident deaths takes place despite only containing 53% of all the registered vehicles (World Health Organisation 2013).

Globally the eighth highest cause of death is due to road accidents and when it comes to people aged 15-29, the global leading cause for death is also due to road accidents (World Health Organisation 2008), (Lozano et al. 2012). According to Lozano et al. unless urgent action is taken, by 2030 the fifth leading cause of death globally will be due to road traffic accidents.

1.3 Intelligent Transport Systems; Using Wireless Ad-Hoc Networking to Increase Road Safety – WAVE IEEE 802.11p and ETSI G5

In order to improve the human transport experience, Intelligent Transport Systems (ITS) have been implemented. ITS are expected to improve economic growth, increase national productivity, increase fuel efficiency and reduce climatic effects. These systems have are being used by the public already; some examples are variable speed highways, adaptive traffic control and road trains (Robinson et al. 2010), automated toll collection systems (Karagiannis et al. 2011), driver assist systems, and collision avoidance systems (VSC-A 2011; C2C-CC 2007).

One particular branch of ITS is wireless inter-vehicular communications (IVC) in order to create a vehicular ad-hoc network (VANET); this is the design and implementation of wireless networks which will enable vehicles to exchange information between themselves (V2V) and other roadside infrastructure (V2I). A standard released by the Institute of Electrical and Electronic Engineers (IEEE) has protocols for inter-vehicular communication and this is named Wireless Access in Vehicular Environments (WAVE) (IEEE Vehicular Technology Society 2013). The main objective of such communications are envisaged as to connect stationary and mobile devices which will contain applications to increase a driver or vehicle's situational awareness of their surroundings – such as potential threats and hazards beyond a driver's field of view. A requirement for such communications is to be able to communicate between vehicles up to 1000 m apart and with speeds up to 200 km/h. Examples of applications are in Section 1.3.2

It is expected that WAVE communications will help promote eco-friendly driving, increase the efficiency of road transport systems and last but not least, prevent accidents and save lives. In the keynote address of VANET 2012 (Kenney et al. 2012) Gruteser (2012) mentions that designing reliable vehicle-to-vehicle (V2V) communication systems in a highly mobile area with rapidly varying vehicle density has been the main function of the vehicular networks community. He also mentioned how advances in the mobile/smart phone industry could be adopted into vehicular networking such as *app stores* for cars.

A Transceiver placed in a vehicle is defined as an on-board unit (OBU) whilst one placed on the side of the road (and are stationary) is defined as a road-side unit (RSU).

1.3.1 IEEE 802.11p Spectrum Allocation, Radio Channel Properties and Comparison with IEEE 802.11a

The Federal Communications Commission (FCC) has allocated 75 MHz of bandwidth for Dedicated Short Range Communications (DSRC) for ITS purposes and this is from 5.850 to 5.925 GHz – this 75 MHz band can be split into 5 or 7 channels (Figure 3 – (ASTM International 2010)).

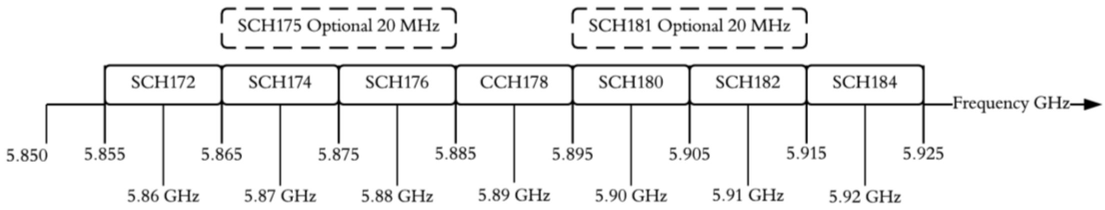

Figure 3: DSRC channel allocation

The FCC also made it possible for unlicensed devices to use these frequencies with the intention of supporting commercial applications (Federeal Communications Commission 2002). The American Society for Testing Materials (ASTM) developed a standard for the Physical (PHY) and Medium Access Control (MAC) layers (ASTM International 2002). This has been updated a few times (ASTM International 2010, IEEE 2010) and the current standard is the IEEE 802.11p (IEEE 2012) which is maintained by Task Group p (TGp) o the IEEE. 802.11p is actually 802.11a with adjustments to enable communications in the harsh vehicular communications environment.

The IEEE 802.11p protocol contains data transmission functionalities along with PHY and MAC layer management entities; these are the Physical Layer Management Entity (PLME) and the MAC Layer Management Entity (MLME) respectively.

Parameter	IEEE 802.11a	IEEE 802.11p
Data rates (Mbps)	6, 9, 12, 18, 24, 36, 48, 54	3, 4.5, 6, 9, 12, 18, 24, 27
Channel size (MHz)	20	10 with the option of 20
Symbol duration (µs)	4	8
Guard interval (µs)	0.8	1.6
FFT period (µs)	3.2	6.4
Preamble duration (µs)	16	32
Carrier spacing (kHz)	312.5	156.25

Table 1: Differences between the protocols 802.11a and 802.11p

The 802.11p protocol is based on the 802.11a protocol and has been adjusted to be able to handle the extremely volatile communications channel caused by the highly dynamic environment. Both protocols utilise Orthogonal Frequency Division Multiplexing (OFDM). Table 1 displays differences between the protocols IEEE 802.11a and IEEE 802.11p; the changes which help the communications to adapt to its new environment. The channel size has been halved (if 10 MHz channels are used) along with the carrier separation and data rates being halved as well. The guard interval, FFT period and preamble duration have all been doubled to help counter effects such as inter-symbol interference (ISI) and inter-channel interference (ICI). The symbol duration has also been doubled to help cope with the volatility of the radio channel.

The WAVE standard also allows higher transmitter powers to be able to cover the required 1000 m range. The FCC has introduced a maximum of 44.8 dBm (30 W) EIRP on the transmitter power levels for IVC. This maximum is not for all channels and devices though - only public devices operating on channel 178 can use this maximum, along with a public RSU using channel 184. Other devices using alternate channels can transmit with a maximum EIRP which varies from 10 dBm to 40 dBm depending on the channel and the device. There is also a maximum power which can be fed into an antenna and these details along with more information about power limits for different devices/channels can be found on (ASTM International 2010).

To complement this standard the IEEE 1609 Working Group for Dedicated Short Range Communication defined an architecture and standardised set of services and interfaces to facilitate secure vehicular communications (IEEE 2006). This group is also currently active and develops and maintains the standards, with (IEEE Vehicular Technology Society 2013) being the latest release.

If further information about the complete WAVE set of standards is required, (Kenney 2011; IEEE Vehicular Technology Society 2013) are good sources.

1.3.2 Example Applications of Vehicular Networks and the SAE Message Set

Figure 4: Example vehicular network (ERTICO 2009)

Figure 4 shows an example of a vehicular network. There are many applications which are expected of vehicular networks and these fall into three categories; 1) Active safety applications, 2) Traffic streamlining and management applications and 3) infotainment applications.

Use case	**Description**
Intersection collision warning	Vehicles approaching a road intersection are warned by an RSU if there is a chance of a lateral collision.
Head on collision warning	Early warning messages are used to reduce the chances of a head-on collision between vehicles travelling in opposite directions (e.g. while overtaking). Also known as a "Do Not Pass Warning" in (VSC-A 2011).
Emergency vehicle warning	Emergency vehicles such as police cars and ambulances can let the other vehicles know about their presence so that other cars can create an emergency lane.
Emergency electronic brake lights	If a car has to hard brake, it informs the other vehicles in the vicinity about this.

Table 2: Examples of WAVE communications use cases

The first category is the most important and is aimed at saving lives on the road. These applications will provide information and assistance to the driver so that collisions could be avoided; achieved via the sharing of information (such as vehicle position, speed, intersection position, heading, etc.) between other vehicles and roadside infrastructure. Information on hazardous road conditions can also be shared.

A handful of use cases of safety critical communications are in Table 2; these have been derived from (C2C-CC 2007; T. ETSI 2009; VSC-A 2011; Karagiannis et al. 2011). The other two categories of uses for IVC have fewer applications up to now. There are two applications described under traffic efficiency and management; speed management and co-operative navigation. The last category, infotainment applications, also has two applications identified; Co-operative local services and global internet services.

Speed management applications are aimed at assisting drivers towards fuel efficient driving habits such as informing them of the optimal speed to drive towards a junction so that they can pass through without having to unnecessarily stop and wait for the lights to change. Another application which falls into this category is co-operative navigation; this application manages multiple vehicles and their motion via cooperating between the different vehicles. A tested example of this system is the SAfe Road TRains for the Environment (SARTRE) project which managed the motion (accelerating, decelerating, turning etc.) of multiple vehicles traversing on the same stretch of road (SARTRE 2012; Robinson et al. 2010). This is also called platooning and has been proven to increase fuel efficiency of the automobiles involved, including that of the lead vehicle.

Co-operative local services will provide users/drivers with information about the locality when a vehicle enters the relevant area – e.g. when a driver enters a nature reserve, he/she could be given information about the locality, directions to attractions and parking information. Another application which falls under infotainment is being able to access the internet for a multitude of tasks ranging from software updates to streaming multimedia to entertain passengers.

The information provided in this thesis about example use cases of IVC is intended to introduce the reader to the concepts and potentials of this form of communications. The research described through the rest of the thesis is not directly about the higher layer operations of the 802.11p protocol but about the lower (PHY) layer and radio propagation characteristics. If the reader would like more information about vehicular networking use cases, their required performance levels and other information, they are directed at (Karagiannis et al. 2011; C2C-CC 2007; T. ETSI 2009).

The Society of Automotive Engineers (SAE) (SAE International n.d.) has produced a message set to be used by devices operating in the DSRC band and this has been done with cooperation with the IEEE 1609 WAVE working group. These messages are defined in their standard J2735 (SAE 2010) with more message types being developed and expected to appear in future revisions.

The most important message from this collection is deemed to be the Basic Safety Message (BSM) and its purpose is to periodically provide core status information about the transmitting vehicle; such as its position, dynamics, size and system status. The content and periodicity of these safety messages with regards to collision avoidance has been the subject of extensive research (VSC-A 2011; Xian & Huang 2012; Tielert et al. 2011; Weinfield et al. 2011; Hafeez et al. 2015) which demonstrated that despite the multiple collision avoidance applications, the state information required by the neighbouring vehicles created an overlap. BSM was thus defined to support all V2V safety applications. These authors have also reported on schemes to use dynamic and adaptive rates to transmit these messages.

A few other message types are the Common Safety Request, Emergency Vehicle Alert and Intersection Collision Avoidance. If the reader wishes to know more about remaining SAE message types, please refer to SAE (2010) and Kenney (2011).

1.3.3 European and other global ITS Developments

The IEEE standards were all designed in the US by the IEEE and other American institutions such as SAE. There have also been IVC research and development in Europe, Japan, South Korea, Australia (Institute for Telecommunications Research et al. 2011), New Zealand and China. The most significant development and standardisation outside the USA has been in Europe and Japan.

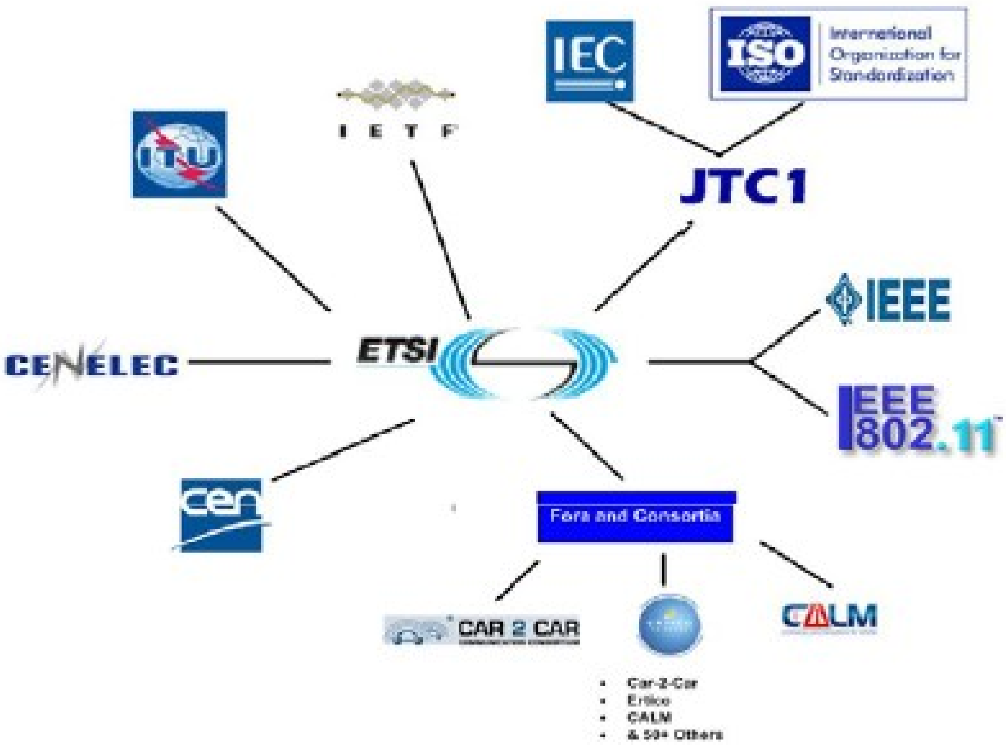

Figure 5: ETSI and its relations with regards to IVC (European Commission 2015)

European developments in vehicular communications have been done mainly by the organisations European Committee for Standardisation (CEN), European Committee for Electro-technical Standardisation (CENELEC) and European Telecommunications Standards Institute (ETSI) (Seeberger 2006). These organisations liaise heavily with other international bodies such as the International Organisation for Standardisation (ISO), IEC (International Electro-technical Commission) and the International Telecommunication Union (ITU). A map of these connections can be seen in Figure 5.

ISO/TC 204 was created to cover ITS activities and this has 16 working groups; ISO/TC 204 WG16 has its focus at the general communication system for all ITS. Communications Access for Land Mobiles (CALM) is a protocol suit standardised by this working group ISO/TC 204 WG 16 2014. This standard deals with a plethora of different wireless communication standards and technologies such as GSM, UMTS, DAB, ETSI ITS-G5 (explained subsequently), etc. and Figure 6 shows how these different communications standards will be utilised.

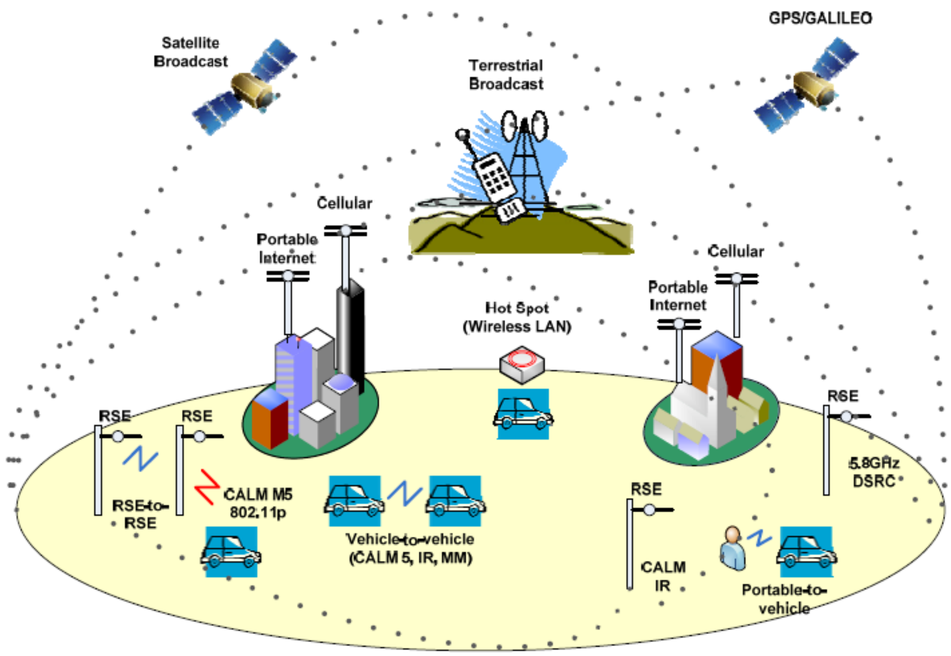

Figure 6: CALM network example (ISO/TC 204 WG 16 2014)

ERTICO ITS (ERTICO 1999) is an organisation whose main goal is to accelerate the deployment and development of ITS across Europe. It is a representation of a network of Intelligent Transport Systems and Services stakeholders in Europe and was founded at the initiative of the leading members of the European Commission, Ministries of transport and the European Industry.

The Car 2 Car Communication Consortium (C2C-CC) (C2C-CC 2007) is an organisation which cooperates closely with ETSI TC ITS and the ISO/TC 204 on the specification of the ITS European and ISO standards.

Other organisations involved in ITS and IVC in Europe are High Tech Automotive Systems (HTAS) (HTAS 2015), European Association for Collaborative Automotive Research (EUCAR) (EUCAR 2015) and eSafety (European Commission 2015). These organisations and their work is evidence that governments and transport ministries in Europe believe ITS and IVC is important when it comes to improving transport networks and saving lives.

The final draft of the ETSI ES 202 663 V1.1.0 (ETSI 2009) specifies the set of protocols and parameters to implement ITS-G5. ITS-G5 is the European profile of the PHY and MAC sub-layers of the 5.9 GHz IVC using IEEE 802.11 (IEEE 2007) as the base standard.

One of the main differences between the North American standard and the European standard is that the North American band extends beyond the upper limit of 5.905 GHz used in ITS-G5A. It is also mentioned in the ETSI standard (ETSI 2009) that the frequencies 5.905 – 5.925 GHz might be used for future ITS application. All the channels have a bandwidth of 10 MHz. The maximum transmit power when using ITS-G5 is 23 dBm.

ETSI ITS-G5 will be used in the ITS ISO CALM (ISO/TC 204 WG 16 2014) protocol which is displayed in Figure 6. CALM is used and enhanced in Europe by projects such as COMeSafety and CVIS (COMeSafety 2011; ERTICO 2009) and it is an aspect of ITS standardisation which is absent in the American architecture. CALM provides interfaces to specify how multiple wireless networking technologies can be utilised by higher networking layers. These are;

- CALM 2G/2.5G/GPRS/Cellular (ISO/TC 204 WG 16 2008a)
- CALM 3G (ISO/TC 204 WG 16 2008b)
- CALM E-UTRAN (ISO/TC 204 WG 16 2015a)
- CALM Infra-Red (IR) (ISO/TC 204 WG 16 2015b)
- CALM M5, (includes IEEE 802.11P AND WiFi (5 GHz) (ISO/TC 204 WG 16 2010a)
- CALM Millimetre (MM) (62 – 63 GHz) (ISO/TC 204 WG 16 2012)
- CALM Mobile Wireless Broadband IEEE 802.16/WiMax (ISO/TC 204 WG 16 2010b)
- CALM Mobile Wireless Broadband IEEE 802.20 (ISO/TC 204 WG 16 2011b)
- CALM Satellite (ISO/TC 204 WG 16 2011a)

1.3.4 Large Scale Projects

The Department of Transport in the United States does research and testing with connected vehicles and has a three part programme; developing architectures, developing applications and developing policies. The technical work for developing architecture for connected vehicle systems is being done and standards are being developed for this environment. The US and the EU work cooperatively to harmonise appropriate standards. When it comes to the applications perspective, development focusses on safety, mobility and the environment. V2V communication is the most advanced with a large-scale safety pilot and model deployment starting in 2012 (US DoT ITS JPO 2015d).

The Connected Vehicle Research (US DoT ITS JPO 2015b) was formerly known as IntelliDrive(sm) and VII (Vehicle Infrastructure Integration). WAVE features were verified and enhanced as part of this project and new ITS services were designed. Vehicle Safety Communications (VSC) (VSC 2006) and (VSC-A 2011), and Cooperative Intersection Collision Avoidance System (CICAS) – (US DoT ITS JPO 2015a) were projects which developed and tested traffic safety applications. The Safe and Efficient Travel through Innovation and Partnership for the 21st century (SafeTrip21) (US DoT Federal Highway Administration 2008) project accomplishes operational tests and demonstrations so that safety enhancing ITS technologies can be deployed. The Vehicle-to-Vehicle (V2V) Communications for Safety (US DoT ITS JPO 2015c) project is another project which helps towards deploying V2V based safety systems. A large scale pilot study, the Safety Pilot Model Deployment, has been implemented and details of that can be found at (University of Michigan Transportation Research Institute 2014)

These projects are mainly concerned with the development of standards and applications towards utilising wireless communications in ITS which will contribute towards improving traffic management and also for safety applications. Some of these projects stretch back to the early 2000s.

ITS projects to test the functionality of IVC have been performed in Europe where multiple academic and industrial institutions have collaborated from different European countries. A few of these projects are mentioned subsequently along with references to their respective websites and in the case of some of these projects, the references to significant literature which was produced during the process.

The COMeSafety and COMeSafety2 (Seeberger 2006), (COMeSafety 2011) projects have been involved with frequency allocation for ITS applications and also with global harmonisation. The SAFESPOT (SAFESPOT 2010) project worked towards using V2X communications to inform drivers of hazardous situations on the road. Adaptive Integrated Driver-Vehicle interfacE (AIDE) (AIDE Consortium 2006) was a project whose aim was to create an adaptable and integrated driver interface. The Cooperative Vehicle-Infrastructure Systems (CVIS) (ERTICO 2009) project designed and tested technologies to support V2X communications. Highly DEpendable IP-based NETworks and Services (HIDENETS) (University of Florence RCL 2006) was a project which analysed end-to-end resilience solutions for distributed applications and SEcure VEhicular COMmunication (SEVECOM) (Wiedersheim et al. 2009) focussed on the definition, design and implementation on VANET security and privacy requirements. The Network on Wheels (NoW) (Festag et al. 2008) project developed communication protocols for IVC and also worked towards enhancing radio communications. Connect & Drive (C & D) (Eindhoven University of Technology 2011) was a project that worked towards cooperative adaptive cruise control and one of their enabling technologies was 802.11p communications. Enhancing road safety with the use of IVC was the aim of COOPerative SystEMS for Intelligent Road Safety (COOPERS) (COOPERS n.d.). PREparation for DRIVing implementation and Evaluation of C2X communication technology (PREDRIVE C2X) (Drive C2X n.d.; Schulze 2014) is a project that worked towards future field operation tests on cooperative systems and also worked towards a common European architecture framework.

As with the projects in the US almost all of these projects have been focused on researching the feasibility of applications and their implementation. Most projects have not used commercial off-the-shelf (COTS) network devices due to vehicular networking still being a relatively young concept with only a few equipment manufacturers offering rather expensive equipment.

As previously mentioned, these projects have taken place across different European countries and this assists standardisation; they have also taken into consideration US IVC protocols which help towards having a common standard and framework. The NoW project (Festag et al. 2008) is more significant to this thesis as it does not focus on the higher layers of communications but also on the physical layer which is where all the propagation phenomena and challenges occurs.

The application focussed nature of all the projects is direct proof of how IVC can be used to improve transport systems. Improving the understanding of radio propagation enables better prediction of where these systems will fail due to radio propagation phenomena and varying channel conditions. This information in turn can be used towards improving vehicular networks using a variety of methods such as increasing infrastructure support and using different transmission powers depending on the physical environment; increased power in harsh propagation locations and decreased power in areas of high network traffic.

1.4 Challenges Faced by V2X Networks

There is an enormous complexity in the implementation of a highly dynamic network operating in environments which are unforgiving towards radio communication. VANETs will the largest wireless ad-hoc network implemented and for this to be used for critical life-saving purposes a lot of research and testing is required both, technically and sociologically.

Some of the key technical issues are listed below:

- The radio channel: The existence of several reflecting objects opens the opportunity for the signals to vary in both amplitude and frequency, and the mobility of the environment adds fading. VANETs need to be extremely robust to deliver low latency (less than 50 ms) communications and deal with the radio fading, Doppler shifts and spreads which will impact upon communications; especially in Non Line-of-Sight (NLOS) conditions where communication performance drops rapidly (Hartenstein & Laberteaux 2010).
- Decentralised network: There is no central management and coordination which leads to low efficiency and network traffic bursts. Packet collisions will be more frequent owing to the absence of a centralised transmission management system (Hartenstein & Laberteaux 2010).
- High mobility, scalability and varying environment: Maintaining a decentralised self-organising network where the nodes are moving at high speeds is challenging. Especially for optimisation algorithms aimed at making better use of the channel and the volatility of connections when it comes to forwarding packets (Hartenstein & Laberteaux 2010).
- Security and privacy: VANET security is a major concern. In-car equipment will have to be tamper-proof and inaccessible to being hacked. Trusting information packets requires increased security which reduces privacy of the sender (Hartenstein & Laberteaux 2010) and (United States Government Accountability

Office 2013). Jamming is also seen as a threat as explained by Puñal et al. (2012).

- Standardisation Vs. flexibility: Despite the dire requirement of standardising communications, original equipment manufacturers (OEMs) will want to include unique features within their VANET assets which could cause tension (Hartenstein & Laberteaux 2010).
- Network Availability: V2V communications has the potential to provide warnings to drivers in 76% of multi-vehicle accidents but only if vehicular networks are widely deployed (United States Government Accountability Office 2013).
- Spectrum Sharing: Other devices that might share the DSRC spectrum should not reduce the reliability of safety critical communications (United States Government Accountability Office 2013).

Some of the main socio-economic issues are:

- Implementation costs: It is difficult to estimate costs due to multiple ambiguous factors such as production volumes, development time frames and costs for security systems. It is unclear if security will be paid for by consumers, vehicle manufacturers, the DOT, state or local government or someone else. Limited large scale testing has also not improved the uncertainty of the required costs. Costs include initial investments to install infrastructure and then necessary maintenance and running costs (United States Government Accountability Office 2013) and (United States Government Accountability Office 2015).
- Drivers will have to react appropriately in a timely manner if V2V communications are to be efficiently utilised (United States Government Accountability Office 2013).
- Liability: Addressing the uncertainty related to potential liability issues posed by V2V communications (United States Government Accountability Office 2013).

2 Literature Review

2.1 Current Research Focusses on Vehicular Networks

This section provides a summary of the recent research being done in IVC. Different propagation environments and the effects they have on propagation are discussed first. Results of studies about radio propagation and channel conditions (which will be used to model network performance) are then presented before presenting the results of 802.11p network performance studies. Studies which have used directional antennas to enhance network performance are then discussed. Measurement based work is the most important as they provide the most realistic results. However due to costs and ease of scalability, a lot of simulation work has been performed in vehicular communications studies. Results of these are presented next and followed by brief overview of work done towards designing 802.11p transceivers.

2.1.1 How Propagation Properties Vary with the Physical Environment

Mecklenbrauker et al. (2011) states that more data is required from various environments for statistical significance; quantifying the channel differences within an environment (such as urban intersection) and comparing its variance on a global scale; a better understanding of the effects of shadowing/NLOS communication conditions.

Urban environments have higher multipath effects and delay spreads combined with reduced range caused by NLOS conditions. Alexander et al. (2011), Mangel et al. (2011) and Abbas et al. (2013) have collected data in urban environments, with the last two authors gathering data from intersections. Tan et al. (2008), Ferreira & Conceiçao (2009) and Sepulcre & Gozalvez (2012) have conducted performance evaluations in these environments.

Intersections offer an interesting mix where NLOS conditions change to Line-of-Sight (LOS) conditions which will increase the network traffic to an individual vehicle towards the centre of the intersection. Mangel et al. (2011) and Abbas et al. (2013) have collected data in suburban intersections whilst Cheng et al. (2007a 2007b), Bai et al. (2010), Paier et al. (2010), Sommer et al. (2011) and Sepulcre & Gozalvez (2012) collected data in suburban environments.

Larger Doppler spreads and shifts are expected in highways along with increased coverage in comparison to urban and suburban environments. Kaul et al. (2007), Tan et al. (2008), Bai et al. (2010), Alexander et al. (2011), Sepulcre & Gozalvez (2012) and Paier et al. (2010) also collected data in higway scenarios, with the latter focussing on the channel whilst performing an overtaking manourvre.

Tan et al. (2008), Bai et al. (2010) and Sommer et al. (2011) have collected data in a rural environments – with the latter testing a shadowing model in this environment.

2.1.2 Propagation and Channel Modelling

A very important aspect of VANET research is towards understanding the challenges presented by the variable channel conditions and characterising these conditions; which is then used in network simulations and performance evaluations. Using field trials to gather channel and network performance data, models can be created or updated to improve predictions of pathloss and packet delivery ratios.

2.1.2.1 Methods and Considerations when Gathering V2X Channel Data

Channel modelling can be approached in three main methods (Molisch et al. 2009a); deterministic (such as ray tracing), stochastic and geometry based stochastic. These methods are discussed with more detail in Molisch & Tufvesson (2004) and Molisch (2005). V2X channels include highly mobile scatterers and low antenna heights which lead to an extremely volatile and multipath rich channel in comparison with other communications channels such as indoor wireless communications. Mecklenbrauker et al. (2011) states that the channel is similar to cellular propagation channels with the addition of unique conditions due to the presence of structures such as gantries, tunnels or other low height infrastructure. However the low antenna heights reduce the number of paths which propagate over rooftops and unlike in cellular communication, both the transmitter and receiver can be mobile in IVC. Propagation channels resembling those which occur in locations of critical safety applications (such as intersections or lane change scenarios) require careful modelling as opposed to the usual environments of rural, highway, urban and suburban.

While ray tracing accounts for each site's specific geometry and also the mobile scatterers, the stochastic models do not. Stochastic models operate on the principle of previously gathered data from similar sites which is then used to model the radio channel. Accurate ray tracing thus offers the most realistic propagation model but it also requires more processing power and time. It can also provide more realistic predictions of the channel's properties such as delay spread, Doppler spread and angle of arrival which is useful when it comes to modelling MIMO systems.

Cheng et al. (2007a), Cheng et al. (2007b), Paier et al. (2010), Sommer et al. (2011), Miloslavov et al. (2011), Alexander et al. (2011a), Mangel et al. (2011) , Fernandez et al. (2012) and Abbas et al. (2013) have all made significant channel measurements to further understand and model the V2X channel – with a focus towards improving IVC network simulations.

Only the studies performed by Cheng et al. (2007a and 2007b) use channel sounding equipment at 5.9 GHz. Paier et al. (2010) and Abbas et al. (2013) have used channel sounders at 5.6 GHz which will provide results similar to propagation at 5.9 GHz but will have innacuracies – they also used SIMO and MIMO antennas. Cheng et al. (2007a and 2007b), Mangel et al. (2011), Sommer et al. (2011) and Alexander et al. (2011a) collected power loss data using 802.11p transceivers. The equipment used was commercially available and did not require custom modifications unlike the equipment mentioned in Section 2.1.6.

Using a channel sounder provides information on the power variation, Doppler spread and delay spread. A channel sounding system has higher precision and provides a snapshot of the channel at all times that the receiver is turned on, as opposed to getting an Received Signal Strength Indicator (RSSI) value from an 802.11p transceiver only upon the successful reception and decoding of a packet. When there is packet loss whilst collecting data using 802.11p transceivers, the data collected represents the channel properties only when packets are successfully received and decoded. If the packet delivery ratio (PDR) is not high, the channel properties are not measured for a significant proportion of time. This restricts finer observations on debilitating factors of V2X networks when channel properties (such as received power, delay spread and Doppler shifts and spreads) are starting to be unfavourable and creates a skew in the data as observed by Cheng et al. (2007b). Mangel et al. (2011) only uses the RSSI values when the PDR has been greater than 65%. The advantage of using 802.11p transceivers is that accurate network performance can be collected. Cheng et al. (2007a and 2007b) simultaneously use both a channel sounding system (to collect Doppler spread data) and 802.11p transceivers (to collect power and packet loss data) and hence gather both channel information and network performance. The 802.11p transceiver used by (Alexander et al. 2011) has the advantage that it could provide Doppler spreads but this data was acquired as part of the channel estimation process and not to rigourously measure the channel.

LOS or NLOS conditions are also an important factor when it comes to the IVC channel behaviour and modelling it. At 5.9 GHz NLOS conditions can cause very significant changes to the channel properties seen at the receiver, which in turn creates a significant drop in PDR. Paier et al. (2010), Alexander et al. (2011), Mangel et al. (2011), Sommer et al. (2011) and Abbas et al. (2013) have all collected data under NLOS conditions. Alexander et al. (2011) has also collected data in LOS conditions.

GPS is the most commonly used positioning system. Cheng et al. (2007a and 2007b) used a DGPS system which had the highest accuracy (1 m) of all the measurements described in this section. Abbas et al. (2013) used a combination of GPS and dash camera video.

2.1.2.2 Modelling Results

A measurement based development of 5.9 GHz IVC propagation model, VirtualSource11p, is the product of Mangel et al. (2011). Experimentally validated and with low complexity for use in NLOS conditions at intersections. The intersections chosen covered both urban and suburban environments and the influence of inter-building distance was quantified in a single path-loss equation – shown in Equation (1) with a description of the parameters provided in Table 3.

$$virtualsource11p(d_r, d_t\, w_r, x_t, i_s) = 3.75 + 2.94 i_s + \begin{cases} 10\log_{10}\left(\left(\frac{d_t^{0.957}}{(x_t w_r)^{0.81}} \frac{4\pi d_r}{\lambda}\right)^{2.69}\right), & d_r \leq d_b \\ 10\log_{10}\left(\left(\frac{d_t^{0.957}}{(x_t w_r)^{0.81}} \frac{4\pi d_r^2}{\lambda}\right)^{2.69}\right), & d_r > d_b \end{cases} \quad (1)$$

Parameter	Description
d_r	Distance from the receiver to the intersection centre
d_t	Distance from the transmitter to the intersection centre
w_r	Width of the receiver street
x_t	Distance from the transmitter to the wall
i_s	Sub-urban loss factor (0/1 for urban/suburban conditions)
λ	Wavelength (0.0508 m)
d_b	Breakpoint distance (≈ 180 m)

Table 3: Parameter descriptions for virtualsource11p

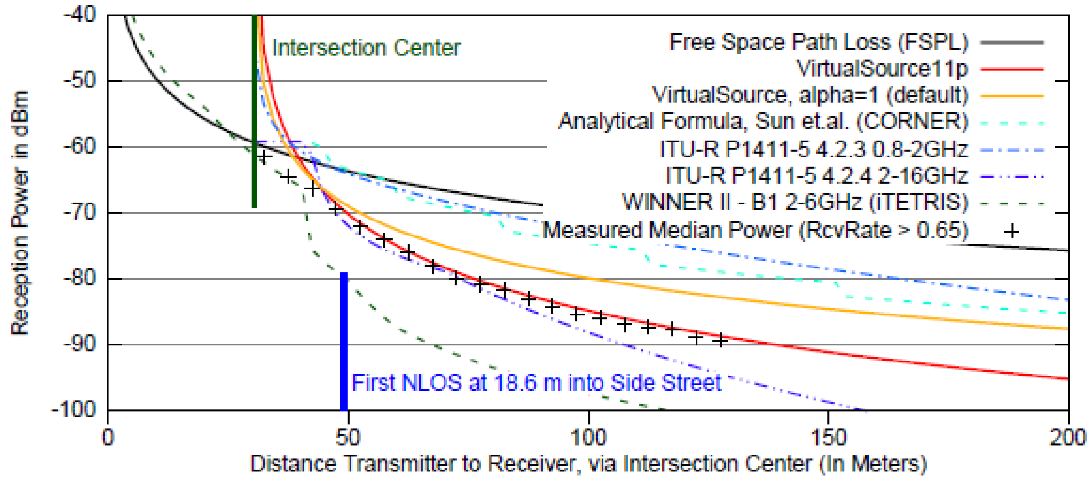

Figure 7: Example comparison of Virtualsource11p predictions with prediction from other models and measured data (Mangel et al. 2011)**.**

Compared to existing NLOS path-loss models (Figure 7) used in street canyons (including the one provided from the International Telecommunications Union – ITU (ITU 2013)), VirtualSource11p managed to correspond well with measured data when the inter-building distance varied. The other existing models are mostly for micro-cellular environments employing lower frequencies. However, only a few intersections were tested. NLOS fading was also investigated and found to be normally distributed around the average power. This model has been used in DSRC packet level IVC network simulations (Mangel & Hartenstein 2011) and the results are discussed in Section 2.1.5.2.

Virtualsource11p is tested by Abbas et al. (2013) for data collected in various environments. It is found that whilst the model produces accurate predictions in most locations, there was an instance where the prediction of received power was an underestimate because one of the buildings had large metals sheets in the corner which had assisted the received power levels. It is concluded that despite the accuracy of the model, an intersection dependent gain factor would provide improved predictions; this however requires more data to be collected from 'special' intersections which could offer variations to propagation.

$$P_r[dBm] = P_t[dBm] + 10\log_{10}\left(\frac{G_t G_r \lambda^2}{16\pi^2 d^\alpha}\right) - \beta n - \gamma d_m \qquad (2)$$

Sommer et al. (2011) developed a realistic yet computationally inexpensive simulation model for 802.11p radio shadowing by buildings in urban environments (Equation (2)). In this equation, P_r is the received power; α is the pathloss exponent; β (dB/m) is an empirically determined parameter for the attenuation experienced due to the exterior wall of a building; n is the number of times the exterior wall of a building is crossed by a transmission; γ (dB/m) is an empirically determined parameter indicative of the interior of a building; and d_m is the pathlength traversed within the obstacle. This model has some similarity with the model derived by Ibrahim & Parsons (1983) for frequencies 168, 455 and 900 MHz. Ibrahim & Parson's model contains a term (excess clutter loss - β) for the loss caused by the height of the buildings in the test area, the height difference between each antenna's position and the percentage of test area covered by buildings.

The model was validated using real world measurements in a city for different types of obstacles. The model requires building outlines which are commonly available in geodatabases and does not include reflection and diffraction. It only considers the direct line between the transmitter and the receiver and disregards obstacles and Fresnel zones.

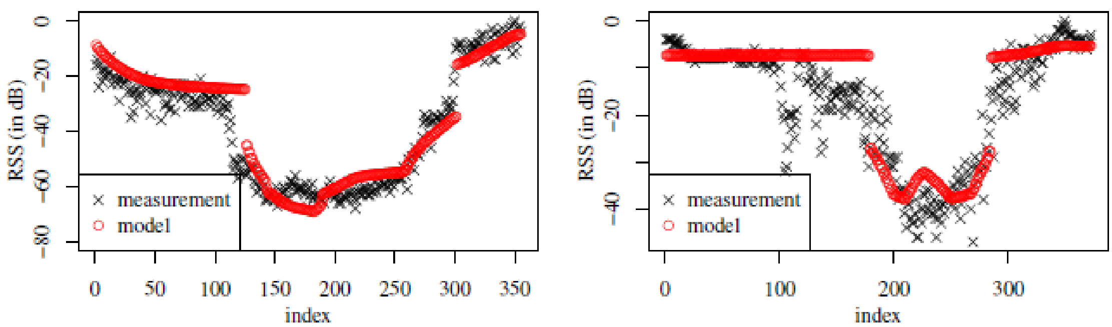

Figure 8: Model and measurement RSS comparison when NLOS is caused by a countryside warehouse (left) and suburban house (right) (Sommer et al. 2011)

A very high accuracy is seen in predictions where the buildings are not very complicated (Figure 8). Index (the x-axis title) is the location of the receiver as it goes around obstacles; no units are provided. The author states marginal overhead in computational complexity given the standard of these results.

The data collected by Cheng et al. (2007a and 2007b) most accurately fit a dual-slope piecewise-linear model shown in Equation (3).

$$P(d) = \begin{cases} P(d_0) + 10\gamma_1 \log_{10}\left(\frac{d}{d_0}\right) + X_{\sigma_1}, & d_0 \le d \le d_c \\ P(d_0) + 10\gamma_1 \log_{10}\left(\frac{d_c}{d_0}\right) - 10\gamma_2 \log_{10}\left(\frac{d}{d_0}\right) + X_{\sigma_2}, & d > d_c \end{cases} \quad (3)$$

P(d) is the received signal strength (RSS) at a distance, d; $P(d_0)$ is the RSS at a reference distance, d_0; d_c is the critical distance which is taken to be the Fresnel distance – distance where the first Fresnel zone touches the ground and is a function of the antenna heights, transmitter-receiver separation and wavelength; γ_1 and $X_{\sigma 1}$ are the pathloss exponents and zero-mean normally distributed random variable with standard deviation of σ_1 respectively up to the critical distance; γ_2, $X_{\sigma 2}$ and σ_2 are the same as their counterparts mentioned previously but for the region beyond d_c. The critical distance was allowed to vary during the fitting of the measured data with the model predictions and it was found that the best fit was when d_c was 125 m less than the theoretical value.

Similar results were also observed by Oda et al. (2000) and Masui et al. (2002). This result is explained by the multiple reflectors (pedestrians and vehicular traffic) in the propagation environment which will bring the first Fresnel zone closer than its theoretical value.

The channel (4 kHz bandwidth) is frequency swept every second to gain spectra and information about Doppler spreads. It takes 200 ms to capture a spectrum and 800 spectra were made at different distances.

In the presence of isotropic scatterers the authors confirm the model of Doppler spread as a function of the velocities of the cars using Equation (4) where V_{tx} and V_{rx} are the transmitter and receiver velocities respectively.

$$f_D = \frac{1}{\lambda}\sqrt{\frac{\left|\overrightarrow{V_{tx}}\right|^2 + \left|\overrightarrow{V_{rx}}\right|^2}{2}} \qquad (4)$$

This is further simplified to;

$$f_D = \frac{1}{\lambda\sqrt{2}} V_{eff}$$

where V_{eff} is the classed as the effective velocity and is shown in Equation (5).

$$V_{eff} = \sqrt{\left|\overrightarrow{V_{tx}}\right|^2 + \left|\overrightarrow{V_{rx}}\right|^2} \qquad (5)$$

The Doppler spread is found to be correlated to the separation distance of the vehicles – this is because when a car is travelling faster, it maintains a larger separation distance. Thus, using the vehicular separation (from the GPS receivers) the effective speed can be calculated and this is used to calculate the Doppler spread and the coherence time using the inverse relationship between them.

Alexander et al. (2011) performed real world trials to evaluate the performance of two 802.11p compliant devices (Codha Wireless MK-1 and a commercial off-the-shelf, COTS, receiver). The authors find that channel estimation just at the start of packets being received is insufficient to maintain a robust network; due to the highly dynamic conditions the channel varies in the duration of a packet being received.

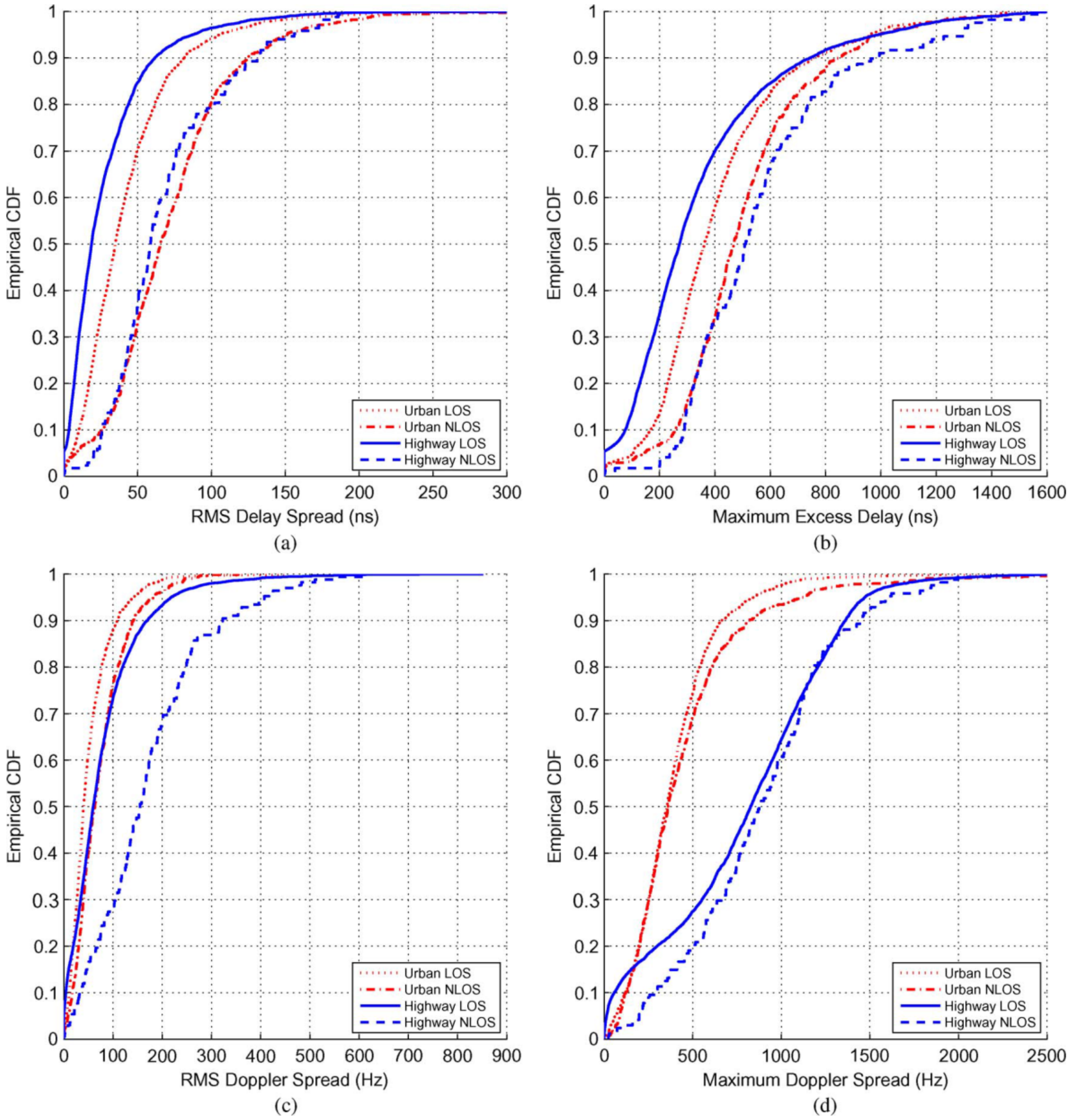

Figure 9: Doppler and delay spread graphs for data collected by Alexander et al. (2011) under LOS/NLOS conditions in urban areas and highways

Figure 9 shows the empirical cumulative distribution functions for the RMS delay spread (a), maximum excess delay spread (b), RMS Doppler spread (c) and maximum Doppler spread (d) for data measured in LOS and NLOS conditions in urban and highway scenarios. The last two panels are of special interest to this thesis as it shows the values of Doppler spreads that occurs in IVC. Under LOS conditions the RMS Doppler spreads are similar for both the urban and the highway scenarios whilst the maximum Doppler spreads have a much larger difference between the two scenarios. In the maximum Doppler spread information, LOS conditions appear to be less significant compared with the vehicular speed (which is dependent on the scenario).

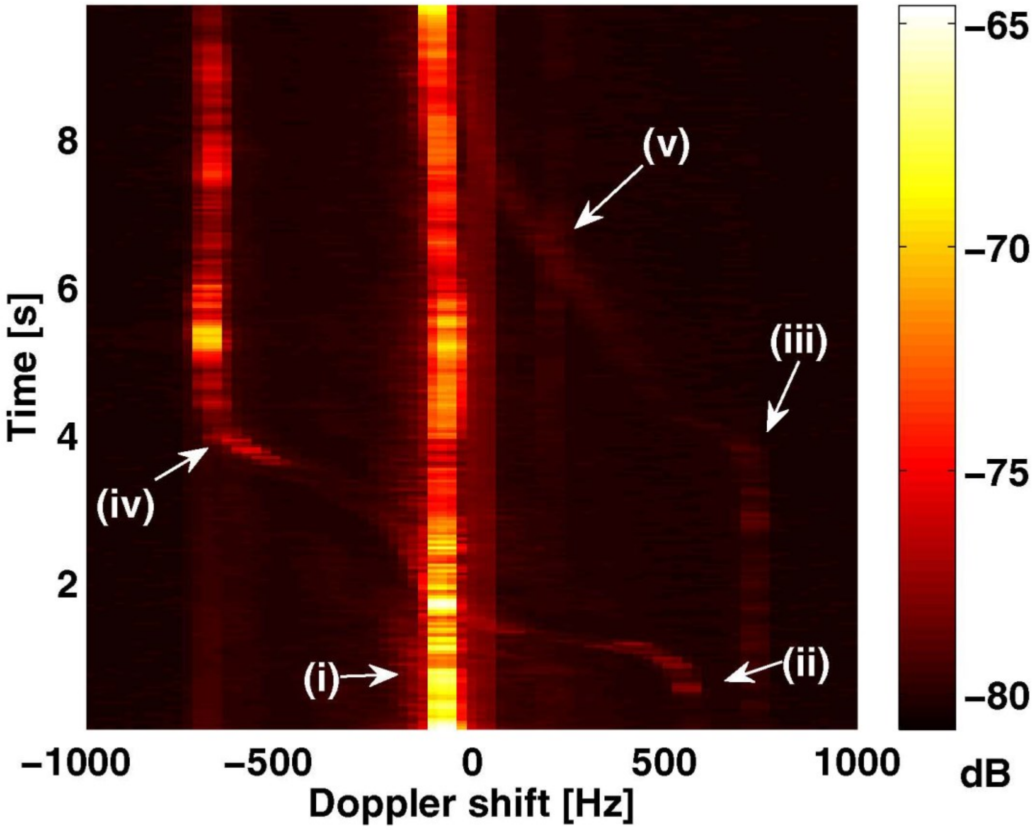

Figure 10: Doppler spectrum density in NLOS conditions for data collected in (Paier et al. 2010)

Power delay profiles and Doppler spectrum densities are collected by Paier et al. (2010) and visible multipath components can be seen in the results (labelled by roman numerals in Figure 10). Multipath effects are attributed to large scatterers such as signs, trucks and bridges. The authors conclude that their signal is detectable in NLOS conditions but this does not relate to how vehicular networks would perform under similar conditions.

Mangel et al. (2011) found that the fading (in dB) accurately fit both a Nakagami-m and normal distribution with the RMS error being less with a normal distribution (Figure 11). They recommend modelling fading under NLOS conditions using a normal distribution with $\sigma = 4.1$ dB and modelling fading in LOS conditions using a Nakagami-m = 1 distribution. However, it is not stated if the average was obtained in milliWatts and then converted to dBm or if it was the average of the data in dBm.

Cheng et al. (2007b) states that fading in vehicular environments are best modelled by a Nakagami-m distribution where 'm' is dependent on the separation distance.

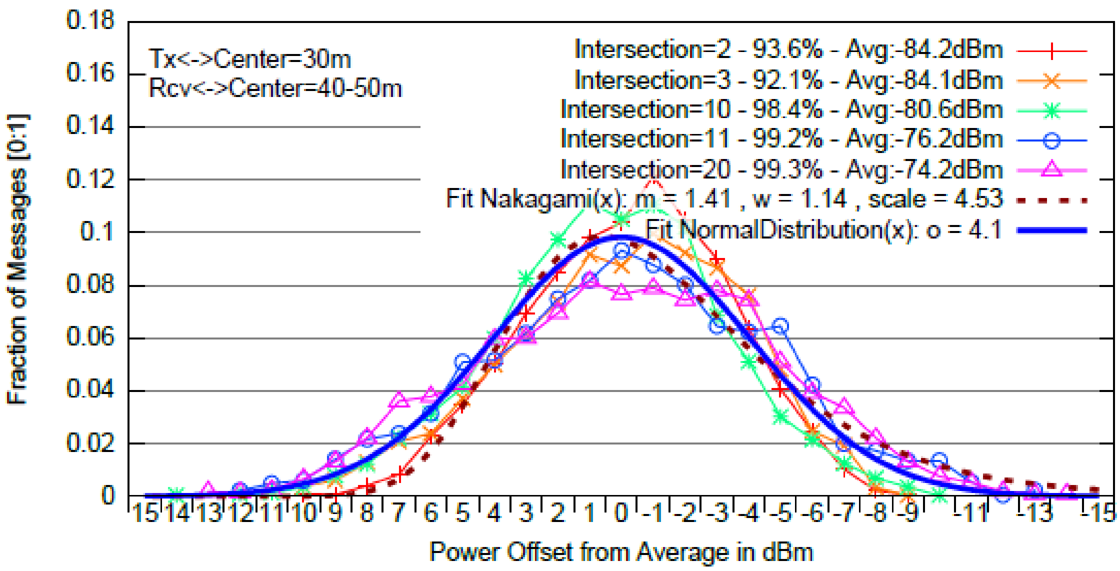

Figure 11: NLOS fading example provided in Mangel et al. (2011)

Miloslavov et al. (2011) used PDR data collected in various locations as part of the VII project (mentioned previously in Section 1.3.4) and compared it with simulated predictions using NCTUns. This includes the WAVE protocol stack and also lets users use different pathloss models. The measured and modelled PDR agreed best when the Nakagami model was used for fast fading; free space and shadowing is used for slow fading; and a shadowing correlation model is used for retransmissions.

2.1.3 Performance Evaluations

VANET research includes performance evaluations where the PDR is measured under a variety of external conditions such as different antenna placements, physical environments, speeds, antenna diversity schemes, etc. In the studies described subsequently GPS is the commonly used method for positioning.

Sukuvaara et al. (Sukuvaara et al. 2013) compares IEEE 802.11p with IEEE 802.11g and found that for vehicular environments IEEE 802.11p is the best protocol despite having lower throughput; it still satisfies IVC requirements. They also designed the WiSafeCar which is a heterogeneous network combining IEEE 802.11p (using Linkbird-MX transceivers) networking and 3G mobile services. Their pilot study proved successful despite reliance on the 3G network (which typically has higher latency) and has found an exploitable synergy between the two communications technologies.

Kaul et al. (2007) and Mecklenbrauker et al. (2011) both found out that The placement of antennas is important as it combines with the roof to produce a unique radiation pattern for each model of vehicle. Antenna patterns significantly impact the delay spread and choosing an appropriate antenna (e. g., using an array and beam steering) can reduce delay spread. A better understanding of how antennas interact with car roofs and the resulting radiation patterns is required. Equipment designers should take the joint Doppler and time spreads into consideration (Mecklenbrauker et al. 2011). Kaul et al. (2007) also say that the best performance was when the antenna was placed in the centre of a car's roof. They discuss node deafness (Choudhury & Vaidya 2004), which is when two nodes cannot communicate due to their antenna beams being formed in different directions.

Mecklenbrauker et al. (2011) says how multi-antenna systems can be used for spatial diversity and beam forming, which results in enhanced communications. Improvements in channel estimation by the receiver will also improve communications along with placing roadside equipment as high as possible. The authors note that the immediate environment of an RSU will affect its radiation pattern which will significantly impact upon its coverage, reliability and networking performance.

Maier et al. (2011 and 2012) performed experiments using multiple antennas and found that using a Single-Input-Multiple-Output (SIMO) configuration with a combining scheme provided definite improvement to the system due to the additional complication compared to using a single antenna

Kaul et al. (2007), Sepulcre & Gozalvez (2012) and Fernandez et al. (2012) all use 6 Mbps as the data rate and Bai et al. (2010) confirms the packet delivery ratio when using this data rate – an important (if not the most important) metric in IVC.

Tan et al. (2008) shows that whilst the DSRC standard accounts for Doppler and delay spreads, larger packets may face higher error rates due to channel characteristics changing during transmission. Maier et al. (2011 and 2012) and Fernandez et al. (2012) also came to this conclusion and the former states the need for an optimum message length to be chosen. Fernandez et al. (2012) also states how having just one channel estimate at the start of the packet being received is insufficient due to the highly varying channel conditions; the channel information requires updating which is not possible using just the pilot symbols. A dynamic equalisation scheme, STA (Spectral Temporal

Averaging), is implemented using an FPGA; this makes the channel estimate more robust by updating it using data subcarriers and by averaging the frequency and time. Using STA improved network performance.

Bai et al. (2010) conducted research which was inspired by the lack of literature using COTS transceivers used to study the effects that the PHY-layer had on the PDR. Numerous empirical measurements were made using an 802.11p communications system operating at 5.9 GHz; packets (of size 300 bytes) were transmitted every 0.1 s. The authors found that the environments ‘Urban Freeway’, ‘Rural Freeway’ and ‘Rural Road’ were the most affected by multipath effects and this was attributed towards the numerous reflective devices found in the environment. The PDR was relatively unaffected by relative and effective velocity (Equation (5)) variations for given separation distances which leads to the conclusion that drops in PDR as distance increases is caused by a correlation between separation distance and relative/effective velocity.

When the transmit power was reduced from 20 to 15 dBm the drop in PDR was between 2 – 5 %, which encourages spatial frequency reuse. These were the controllable parameters whose effects on the PDR were studied.

The study also analysed temporary, spatial and symmetrical correlation and found that weak temporal correlation exists despite decreasing when the separation distance increases. Spatial correlation was found to be weak and highly characteristic of the operating environment; the strongest correlations were in the open field and rural road environment, weakest correlations were in the urban freeway and rural freeway environments and with the suburban road environment being in between. Symmetric correlation was high for most of the environments apart from the open field environment. An intriguing trend in the communications symmetry was that for all the environments, symmetric correlation starts out low but rises by approximately 0.25 within 50 m and then stays there. This causes concern as IVC is expected to assist in very low latency communications at short ranges and low symmetrical correlation in short ranges means that two vehicles might not be able to share data as efficiently as they would expect to. Despite the numerous data collected in a variety of environments under different conditions, which provides an overview of how the PDR is affected in different physical environments, there is no mention of LOS/NLOS conditions which affects communications significantly.

$$f_{rms,D} = \frac{0.43 v_{eff}}{\lambda\sqrt{2}} \tag{6}$$

Using Equation (5) the root mean square (RMS) Doppler spread is shown in Equation (6) where λ is the wavelength (Molisch et al. 2009b). Considerable spread has been noticed around this along with an offset which results in a non-zero maximum Doppler spread even at zero velocity – due to Doppler spreads caused by mobile scatterers.

Three V2V safety applications were tested in Sepulcre & Gozalvez (2012) (lane change assist, overtake assist and forward collision warning) using DENSO WSUs (Wireless Safety Unit) (Robert et al. 2008) which are 802.11p transceivers.

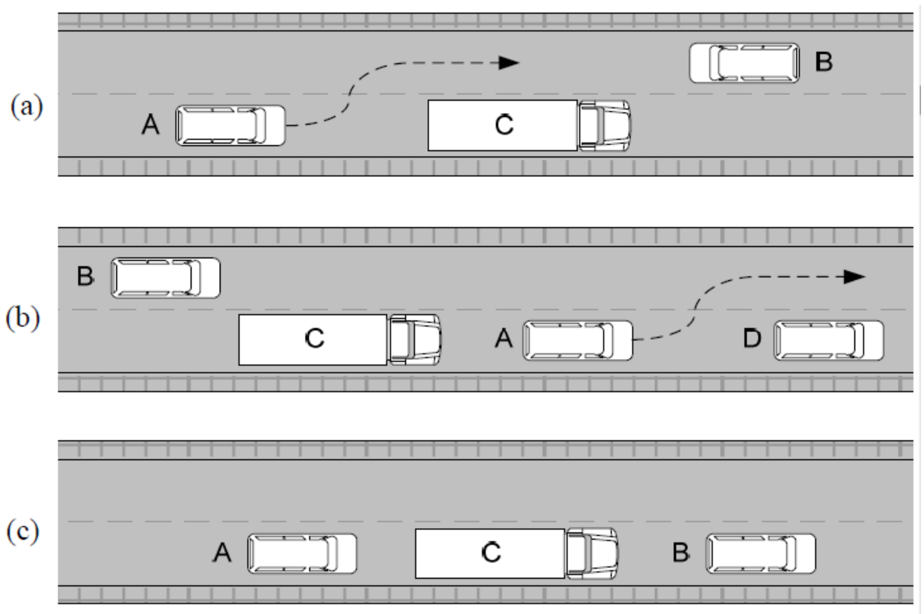

Figure 12: The three scenarios for the tests (Sepulcre & Gozalvez 2012)

Figure 12 displays the applications. Figure 12(a) is for overtake assistance, Figure 12(b) for lane change assistance and Figure 12(c) for forward collision warning. With the overtake assist application, it is tested if communication between Vehicle A and Vehicle B starts within the distance at which they must communicate to avoid a dangerous situation when the cars are travelling at speeds of 60 km/h and 80 km/h. Vehicle C was also changed between a car, a truck and freespace. These were repeated with the power level set to 10 dBm and 20 dBm. Despite using a high transmission power, the application struggled to perform satisfactorily at high speeds and when

Vehicle C was large. It is suggested that heavy vehicles should be used as relays for information packets.

In the lane change assist application (Figure 12b), similar to the previous experiment it is tested if the cars A and B communicate within the correct time frames to avoid a collision. Three experiments were run where the power was switched between 5 dBm and 10 dBm along with vehicle C being changed from a car to a truck. Vehicle B was always traveling at 120 km/h while Vehicle A was between 70 and 80 km/h. It was observed that network performance suffered when Vehicle C was large, especially at low transmission powers.

For the forward collision test, depicted in Figure 12c, the connection quality between vehicle A and B were tested when vehicle C was a bus and a truck. Transmission power was kept at 10 dBm for both runs and the truck was tested with 20 dBm as well. Using this connection data, the reliability of such an application for forward collision warning was evaluated with respect to the response time of a driver; 1 s and 1.5 s. This application's functionality depends on the vehicle's speed and the time between packets being transmitted. Transmitting packets more frequently whilst travelling at higher speeds will increase the application's reliability.

The study concluded that there seems to be limitations as the vehicles are moving at higher speeds under NLOS conditions. Adaptive and advanced communication techniques would be beneficial to dynamically adapt according to the different environments so that application requirements could be met. Examples of this would be to use heavy vehicles as communications relays and to increase the packet transmission frequency whilst travelling at higher speeds.

Ferreira & Conceiçao (2009) analyses the connectivity between vehicles using overhead stereoscopic photography. The connectivity and path availability between 10,566 cars and trucks were analysed and it was found that there are significant differences compared to mobility models used in VANET simulations.

Lin et al. (2012) capture data in a proving ground. Both static and mobile tests are performed with latency and packet success rate being measured at different distances and speeds – static tests had distance as a variable and mobile tests had speed as the variable. The transmitting power is 17 dBm with an 8 dBi omnidirectional antenna and all the data have been gathered in what appears to be a straight road in LOS conditions. The data presented is undoubtedly useful albeit being captured in what appears to be an environment which lacked a lot of important propagation affecting factors such as buildings and traffic. The mobile test data is presented against the speed of the car and does not provide any information about how the packet loss or latency will be affected by the distance between the transmitter and receiver – which is an important factor when it comes to vehicular networks. Overall, the experiments performed display that the transceivers (Savari^{tm} WAVE-BOX) function to what seems is an acceptable standard but leaves the reader asking questions about how the data displayed conveys to a real vehicular networking scenario.

2.1.4 Performance Enhancements Caused by Directional Antennas

A handful of studies have confirmed that directional antennas used for IVC can increase the coverage range: Increased throughput with directional antennas along with a reduction in adverse effects caused by other radio channel interferers was observed by Wang et al. (2004). The connection duration between an OBU and RSU was quadrupled when using a directional antenna (Timm-Giel et al. 2007). Directional antennas can also supress undesired multipath effects and frequency selective fading (Zaggoulos & Nix 2008). The coverage range with directional antennas was quadrupled in comparison to omnidirectional antennas (Xu et al. 2010). The positioning of a directional RSU antenna was found to significantly affect network performance (Shivaldova et al. 2012). They also found that directional antennas with a gain of 10 dBi provide an average 30 % increase in data transferred and triples the communications range. Mecklenbrauker et al. (2011) have found that antenna patterns significantly impact the delay spread and choosing an appropriate antenna (e. g., using an array and beam steering) can reduce delay spread.

A variety of propagation environments have been used in these measurements. Suburban environments were covered by Timm-Giel et al. (2007) and Subramanian et al. (2008). Highways were covered by Subramanian et al. (2008) and Shivaldova et al. (2012), the latter collected data in a 4 lane highway with 2 lanes each way.

Steerable antennas at the OBU were used by Timm-Giel et al. (2007) and Subramanian et al. (2008). Whilst Timm-Giel et al. (2007) performed their experiments in a V2I configuration, Subramanian et al. (2008) collected all their data in a V2V configuration. V2I communications are expected to have significant performance differences from V2V communications because the different antenna heights involved (RSU are placed on gantries much higher than a usual car's rooftop) and the increased mobility in V2V communications (both communicating nodes are mobile).

Timm-Giel et al. (2007) concludes that the strongest beams arrive in the direction of the receiver and improved network performance by steering the communicating OBUs' beams towards each other; this required knowing each other's coordinates (using GPS) and trajectory. The authors do not state if communications were done in LOS or NLOS conditions; this will impact the direction of the strongest beams as multipath propagation under NLOS conditions mean the strongest signals do not arrive in the direction of the transmitter (more work on this is presented in Chapter 7).

Signal propagation and packet loss can be predicted based on system parameters within the first 200 m, when antenna characteristics are more influential than environmental features, but not further away (Shivaldova et al. 2012). V2I experiments were performed to analyse the effect of the RSU having different types of antennas with different gains. CVIS OBUs are used with CALM M5 implementing 802.11p at 5.9 GHz. GPS is used for localisation and the communications were all simplex; from the RSU to the OBU

These experiments show how using directional antennas in V2X can vastly improve network performance. However, only Shivaldova et al. (2012) has performed experiments in the DSRC band and using 802.11p; 802.11p is designed for IVC and takes into account the harsh conditions faced by a VANET. If data is collected using other protocols (such as 802.11b or 802.11g), or outside the DSRC band (such as at 2.4 GHz), the results are not accurate from an IVC performance evaluation point of view as a network employing the 802.11p communications standard will perform better (Section 1.3.1 has information on how 802.11p is unique). None of these experiments have measured the properties of the radio channel using directional antennas nor have they collected data in urban environments which provides the richest multipath environment.

2.1.5 Network Simulation and Modelling

Most published material is done using modelling and simulation software because it is cheaper and safer compared to testing new protocols and applications using real cars on real roads. Software modelling also reduces the space required for an actual experiment which involves cars moving at high speeds. It is also more convenient to repeat and has more control over the environment.

2.1.5.1 Simulators

A review paper published in 2012 (Joerer et al. 2012) analysed papers from the conferences ACM (Advanced Computing Machines) VANET, IEEE VNC (Vehicular Networking Conference) and IEEE VTC (Vehicular Technology Conference) between 2009 and 2011; 116 simulations focussing on IVC. The authors found that the most popular network simulator to use was ns-2 and the most popular MAC protocol used was the IEEE 802.11p protocol – simulations have also been performed with other 802.11 MAC protocols. SUMO and VanetMobiSIM were the most used mobility simulators; however, their study found that most authors had not indicated the mobility simulator they had used. Manhattan grids and dual lanes roads were the most commonly investigated urban layout and road type.

2.1.5.1.1 Mobility Simulators

An important aspect of vehicular networks is the mobility of the nodes and when simulations are performed to analyse network performance, the mobility of the nodes should be taken into account. There are mobility simulators for this purpose and even though mobility is not explored in this project, the reader is provided with a very brief introduction on a few mobility simulators which can be used to simulate trajectories (traces) of a node. These traces will then be input into network simulators such as Network Simulator – 2 (NS-2) or QualNet. Descriptions of some common mobility simulators are:

SUMO – Simulation of Urban Mobility (SUMO 2015). This is an open source traffic simulator with the capability to produce mobility traces which can be used by NS-2, QualNet and Ansim. Maps can be manually input or OpenStreetMap/Topologically Integrated Geographic Encoding and Referencing (TIGER) can be used if real world maps are required.

MOVE – MObility generator for VEhicular networks (Karnadi et al. 2007). In this VANET simulator SUMO commands are run in the background with GUI support. Maps can be defined manually, generated automatically or real maps from Google Earth or TIGER can be imported.

VanetMobiSim – VANET Mobility Simulation (Eurecom 2014). VanetMobiSim can produce traces compatible with NS-2, Glosim and QualNet. It has the capability to consider road structure, road topology and traffic signs.

2.1.5.1.2 Network Simulators

Descriptions of some commonly used network simulators are provided below. They are used to predict end-to-end communication performances in different scenarios and while using different and/or altered protocols; such as an altered MAC layer protocol to establish what effects this will have on the data dissemination. Network simulators are used in conjunction with mobility simulators where the latter provides the mobility traces.

NS-2 and NS-3 – (NS-2 2011; NS-3 2011)

OMNet++ – (OMNet++ Authors 2015)

OPNET – (Riverbed Technology 2015)

QualNet – (SCALEABLE Network Technologies 2014)

TRANS – TRaffic And Network Simulator – (Laboratory for Communications and Applications 2012)

2.1.5.2 Simulations

Jiang et al. (2008) and Vinel (2012) perform network simulations focussed on finding optimal network configurations. 6 Mbps was found to provide the highest packet delivery ratio (Jiang et al. 2008). Another result is that higher data rates would result in shorter frame lengths but would also emit higher power which can cause interference and hence lower network performance. The DSRC channel is extremely volatile and higher data rates require more stable bandwidth to function efficiently. Mangel & Hartenstein (2011) also mention how a 6 Mbps data rate gives a good compromise between capacity and signal robustness.

Vinel (2012) models and compares beaconing in vehicular networks using WAVE and 3GPP LTE. The probability of successfully receiving a beacon is given for both network types and the 3GPP LTE system is modelled with extremely favourable conditions – no other traffic is considered and the latency added by the network (between receiving a beacon and sending it back out to the intended recipients) is ignored as well. The author analyses the effect of increasing traffic in each of the networks and concludes that despite the favourable assumptions taken into account when modelling the 3GPP LTE system, it is still not as efficient as a WAVE network and the probability of beacons being lost is higher in the 3GPP LTE network. Besides the significant improvement in performance, it is also worth noting that VANETs will be free to use as opposed to a 3GPP LTE network. There is also the capability of having dual radio WAVE devices which would enable having a dedicated transceiver for beaconing whilst simultaneously operating the other transceiver for information exchange.

Intersections have proven to be a complex environment for both drivers (with more than 44% of collisions happening in intersections) and also radio communications (where NLOS and LOS conditions mix) which is why there are many accidents in such areas. This has led to communications protocols designed especially for use in this environment (Azimi et al. 2013). In simulations these protocols have proven to reduce deadlock and increase VSC application reliability and throughput. These protocols have been designed to be used with autonomous cars but can also be used in driver assistance systems such as collision warning applications.

As previously mentioned, there are a lot of groups researching into the higher layers of communications such as security and routing protocols. Two interesting methods of reducing the number of hops have been studied by Amadeo et al. (2012) and Boban et al. (2014). Amadeo et al. (2012) uses Content-Centric Networking (Jacobson & Smetters 2009) as opposed to the widely used TCP/IP protocol suite. Their simulations proved an increase in network efficiency brought about by reducing the number of hops. Boban et al. (2014) performed simulations which utilised taller vehicles as the relaying nodes. It is found that after a certain distance, vehicles that are taller can transmit packets through a wider range hence making the packet forwarding process more efficient. When it came to large scale analysis, a simulation was carried out which used the knife edge propagation model. This new method is named TVR: Tall Vehicle

Relaying. Using TVR it was shown that LOS conditions are met for most of the transmissions owing to the advantage of the height the antennas would be placed at. This meant higher reception power and fewer hops in comparison to two other relaying techniques.

Islam et al. (2013) have used the variable-m Nakagami model and performed simulations comparing it with the two-ray, freespace and the dual-slope piecewise-linear (DSPL) pathloss models. They found that using simplistic models such as the freespace and DSPL resulted in underestimating bit error rates.

Other work done (analysing methods to improve network performance) looks into piggybacking data into beacon messages that each node transmits asynchronously (Klein Wolterink et al. 2012). A broadcast suppression method is described by Schwartz et al. (2012); this simulation uses the 1-hop periodic beacon message issued by each car in a VANET. This has been compared against existing delay methods and found to be more effective at controlling the number of vehicles transmitting within each time slot. The implementation of a TDM overlay on top of the MAC layer to improve packet reception performance has been simulated by Subramanian et al. (2012). The simulations found that the synchronous MAC was found to discover more neighbouring nodes as opposed to the asynchronous approach hence increasing safety in DSRC safety applications. Packet collisions involving safety related and high priority packets was reduced by modifying the EDCA (Enhanced Distributed Channel Access) mechanism (Sharafkandi et al. 2012).

Mangel & Hartenstein (2011) performed a simulation using VirtualSource11p (only in NLOS conditions) to test the functionality of 802.11p communications in intersections when the communications channel is under competition by many nodes. Low, medium and high traffic rates were simulated. It was found that the network load was highest on the street canyon which did not have the transmitting node. However, the worst case was still acceptable to receive a safety message on time and prevent an accident at the intersection centre.

2.1.6 Designing Transceivers

There are researchers who built their own 802.11p transceivers to gather information and a summary of their methods is provided below. This work is not discussed in detail as experiments performed using custom hardware is not very repeatable. The reader is directed towards the references for detailed information on their results.

In Kamal et al. (2012) a 5.9 GHz 802.11p DSRC system was designed and validated both indoors and outdoors. The devices proved to work as both a RSU and an OBU. The device was tested for its range, latency and correct operating frequency, and was proved to be successful and usable for future tests. There have been other groups that have made their own 802.11p transceivers. Fuxjäger et al. (2010) used GNURadio and USRP2 (software radio kit) to create a software radio device. In Xiang et al. (Xiang et al. 2008) a transceiver was made to work at 5.9 GHz by tuning an 802.11a chipset, which was combined with a tablet and used in V2X testing. Using a similar procedure of modifying an 802.11a chipset to create a compatible 802.11p device, Ho et al. (2010) conducted tests in a road environment where the device was used as both an OBU and RSU. Their devices were successful up to 300 m before latency and packet loss became non-negligible.

2.2 The Benefits of using a Dual Measurement System to Simultaneously Evaluate 802.11p Network Performance and Radio Propagation Characteristics

Abdelgader & Lenan (2014) mentions the importance of the PHY layer and how not a lot of research has been performed in this respect whereas a lot of research has been conducted in relation to communications security and applications.

The lack of statistically significant V2V channel data which can be used for statistical analysis is expressed in an overview of the propagation aspects in V2V communications performed by Molisch et al. (2009b). The authors also state the very low number of studies performed using directional antennas and measurements to study the impact of mobile vehicles (scatterers) between a transmitter and receiver.

Mecklenbrauker et al. (2011) states that due to the nature of the communications the channel state and statistics are very volatile and cars approaching intersections are found to face more volatile channels than cars driving in a platoon such as in a highway. The work done by Molisch et al. (2009a and 2009b), Cheng et al. (2007a and 2007b), Mangel et al. (2011), Mangel & Hartenstein (2011), Abbas et al. (2013) and other work described in Section 2.1.1 agrees that intersections appear to be challenging areas for both drivers and wireless communications due to the mix of LOS/NLOS conditions and the multipath rich environment. Cheng et al. characterised channel conditions using a very useful equipment set-up which used a narrowband wave and two DSRC radios and collected data from a variety of environments. Mangel et al used DSRC radios to develop the virtualsource11p pathloss model.

These studies have provided inspiration towards using similar equipment (a narrowband/continuous wave signal and two 802.11p radios) to collect radio propagation and network performance data at T-junctions with a focus on IVC – more information in Chapter 3. An important use of IVC is to enhance a driver’s field of view and this is done through radio communications in NLOS conditions; most of the data is collected in NLOS conditions in lieu of this. Data is gathered from three T-junctions of various layouts (presented in Chapter 4) and this data will be compared against predictions from virtualsource11p (in Chapter 5), which is for pathloss modelling in NLOS conditions. The pathloss is expected to be different from what would be expected in at a crossroads owing to how closed or open the T-junctions are.

As mentioned previously, ray tracing provides the most realistic model of a radio channel and with this in mind, a site-specific ray tracing model is programmed with an initial set of results and this is in Chapter 6

To further improve the understanding of radio wave propagation at 5.9 GHz, a sample of data is collected using a directional antenna and this will provide information on which direction the strongest multipath components are arriving from. The results for this are in Chapter 7

Chapter 8 presents an analysis of how the physical traffic appeared to assist communications and also presents Doppler spread data. A model is presented in Chapter 9 which creates a link between a vehicle’s size and the Doppler Spread it causes. The last two chapters are the conclusions and references respectively which conclude this thesis.

3 Experimental Configuration Set-up

3.1 Introduction – Vehicular Network Measurement Campaigns

Different measurement campaigns were described in Chapter 2. Based on this it was decided to use a dual measurement system similar to that used by Cheng et al. (2007). There will be a 802.11p network system (NS) to measure network performance and a continuous wave system (CWS) to measure channel parameters. The CWS is necessary because 802.11p transceivers are not designed with the focus of channel sounding and RSSI values do not have high accuracy; hence using it to model the communications channel is inaccurate. There is also a systematic error described in Section 3.4. For these reasons a signal generator will transmit a continuous wave (CW) which will be received by a spectrum analyser – this will provide an accurate measurement of the pathloss and any Doppler effects.

In addition to using this dual measurement system, the CW system will also be used with a directional antenna instead of an omnidirectional one. These equipment set-ups will be described subsequently in this chapter along with the information extractable.

3.2 Network Performance & Channel Measurement System Set-up

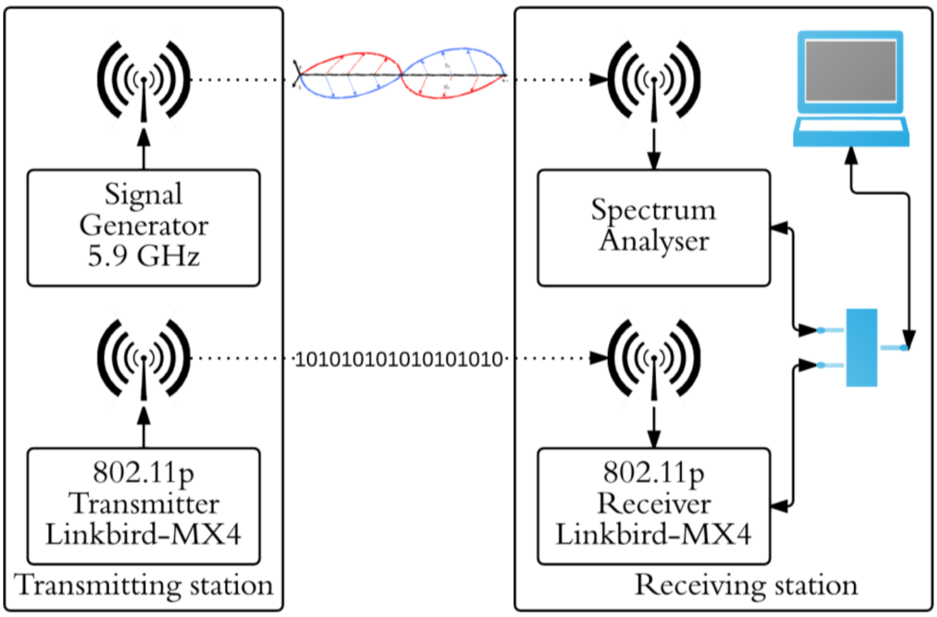

Figure 13: Schematic of equipment set up

The equipment used by both the measurements systems (the NS and CWS) and their set-up is displayed in Figure 13.

3.2.1 The 802.11p Network System set-up

This system was used to analyse packet loss in an 802.11p network operating at 5.89 GHz which is channel 178 in the FCC channel allocation system (ASTM International 2010) which is also channel ITS G5SC2 in the ETSI standard (T. ETSI 2009). One NEC Linkbird (version 4) transceiver was set up as a transmitter and a second as a receiver. The NS operating parameters are in Table 4. The data rate was chosen based on research performed by Jiang et al. (2008) and presented in Section 2.1.5.2 where 6 Mbps was proven to give the best Packet Delivery Ratio (PDR) i.e. the ratio of the number of packets received to the number transmitted. More information on data rates is in the same section. Experiments described in the same section also have packet frequencies of 10 Hz. The data in the packets was a time stamp and a collection of random numbers with a checksum; the checksum will be used at the receiver to get the PDR.

Channel	5.89 GHz
Packet size	250 bytes
Data rate	6 Mbps
Transmit power (EIRP)	16 dBm
Antennas (omnidirectional)	Mobile Mark ECOM6-5500
Antenna gain	6 dBi
Packet frequency	10 Hz

Table 4: 802.11p NS operating characteristics

3.2.2 The Continuous Wave System set-up

This system was used to analyse the signal characteristics of a continuous wave transmitted at 5.9 GHz with an effective isotropic radiated power (EIRP) of 16 dBm; which is the same EIRP as the NS's level (see section 3.2.1). This transmission power is chosen for a couple of reasons; it is expected transmitters will not always be operating with maximum transmit power (some of the equipment could not transmit at 33 dBm) and also because 16 dBm is similar to the transmit powers used in a few of the experiments described in Section 2.1.3. The signal generator (Anritsu MG3692B) produced the CW signal while the spectrum analyser (Agilent E4440A) measured the spectrum of the received signal. The antennas used were the same as those used in the NS (see Table 4). The span of the spectrum analyser was set to 500 Hz and a spectrum was saved approximately every 1.5 s. Each spectrum acquired is time stamped according to the laptop's clock.

Data collected by the spectrum analyser and 802.11p receiver were saved in a laptop which was connected to this equipment via a 100 Mbps network switch. All the equipment was loaded onto two trolleys; one being the transmitting station and the other is the receiving station. The equipment on the trolleys was powered by a deep cycle battery and a pure sine wave generator.

3.2.3 The Combined System

Figure 14: Receiving station trolley

Figure 15: Transmitting station trolley

Figure 14 and Figure 15 displays the receiving and transmitting trolleys respectively. The transmitting trolley contains the signal generator and 802.11p transmitter while the receiving trolley contains the spectrum analyser, router, 802.11p receiver and laptop. Antennas (one for each of the transmitting and receiving devices) were placed 0.508 m apart on top of the trolleys, 1m above ground level. The antenna separation corresponds to a distance of ten wavelengths at 5.9 GHz. A consequence of this deployment is that the propagation path for the CWS signal is slightly different to that of the NS signal. A set of measurements were done with the antenna positions swapped; the difference between the data collected with different antenna positions was insignificant.

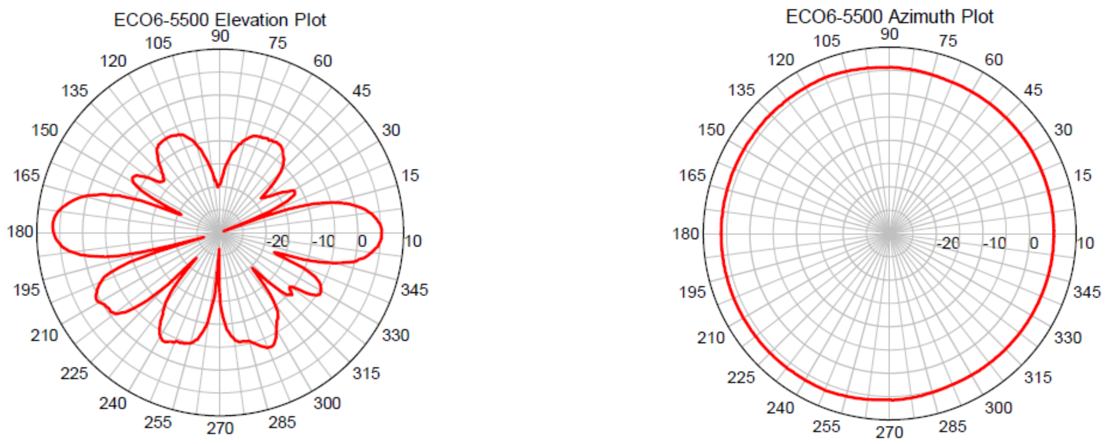

Figure 16: Radiation patterns of the ECOM6-5500 omnidirectional antennas used; 6 dBi gain, 5.0 – 6.0 GHz (MobileMark, Personal Communications)

Figure 16 displays the radiation pattern of the antennas. The antenna's omnidirectional azimuthal radiation pattern and higher equal gain at elevation angles of 0º and 180º is evident in these plots. It is worth noting that these patterns will change depending on the object/vehicle the antenna is mounted; mentioned by Mecklenbrauker et al. (2011b).

The laptop ran a script which recorded the data from both the 802.11p receiver and the spectrum analyser; a flowchart for this script is shown in Figure 17.

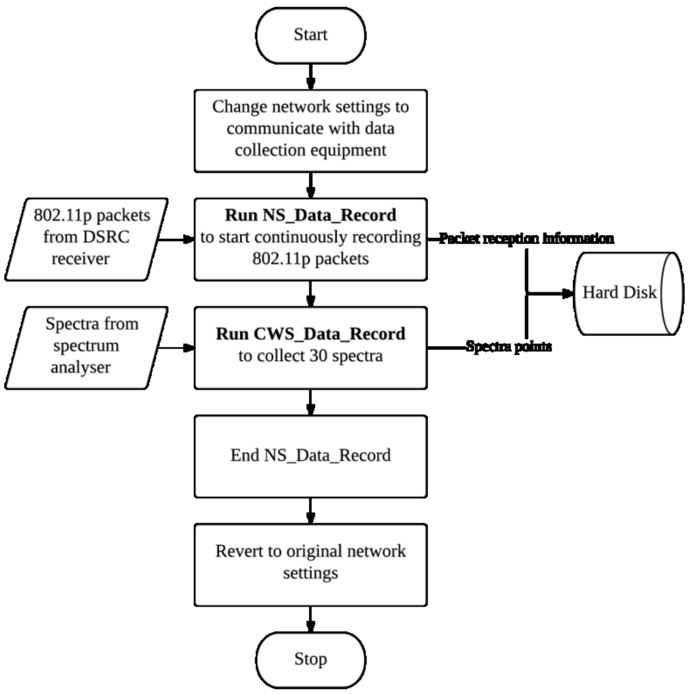

Figure 17: Flowchart describing script used to simultaneously collect 802.11p packets and spectra

For the localisation of these measurements a laser-rangefinder (Bosch GLM 80) with an accuracy of ± 0.5 mm was used. Distances are measured from fixed reference points and a path of travel is marked along the ground. The trolley is kept on this path and data is collected at regular intervals; different intervals are used depending on the experiments and this is explained in Chapter 4. GPS was not used for location information in these measurements. GPS accuracy decreases in urban environments due to multipath effects in urban canyons and GPS would also not be able to provide sub-metre accuracies.

Using this localisation technique, it was possible to gather data at 20 cm intervals which is a higher resolution than reported in literature. This high distance resolution enables any small fluctuations (caused by fast fading) in the data to be measured.

3.3 Data Output from the System

3.3.1 Data measured from the CWS and the information that can be extracted

The data collected by the CWS are spectra. At each position of the path in which data is collected 30 spectra are obtained with the bandwidth of each spectrum set to 500 Hz. This very narrow frequency setting enabled Doppler spreads caused by pedestrian traffic to be observed. A smaller bandwidth was not chosen since this meant each spectrum took too long to collect. 30 spectra were collected at each position to get a good statistical data set and so that any variations in channel conditions might not affect the data significantly over the period of data collection. Collecting 30 spectra took about 45 s. With 30 spectra collected at each position it is possible to get a statistically significant sample that would yield the median peak power and it would also provide a good indication of the variation at each position; all within 45 s. If it takes approximately 150 s to move the receiver from one position to the next and to prepare to collect data, each position requires approximately 200 s, or just less than 3.5 minutes. At this rate it is possible to cover approximately 30 positions in 105 minutes. This was a good compromise between the time to collect data before the batteries died and statistical significance which enabled analysing the variation.

Three example spectra are shown in Figure 18. The peak power of the CW can be extracted from each spectrum. For all the spectra collected at each position, the median of the CW’s peak power will be found and this can be used to analyse the pathloss against the distance from the intersection centre. The peak power was measured instead of the energy in the spectrum because the peak power is not affected by Doppler spreads as much as the energy in the spectrum and would be more accurate in determining the pathloss independent of the physical traffic. In addition to the peak power, the spectra also provide an indication of the size of the Doppler shifts and spreads that occur in the radio channel. These Doppler effects can be compared against the network performance to analyse how the NS could be affected by Doppler shifts or spreads. It was noticed during data collection that Doppler spreads were caused by pedestrians, cyclists and vehicles. When traffic frequency was extremely low, notes were made whenever traffic would cause Doppler spreads; this was only possible in two of the three experiments (see Section 4.1).

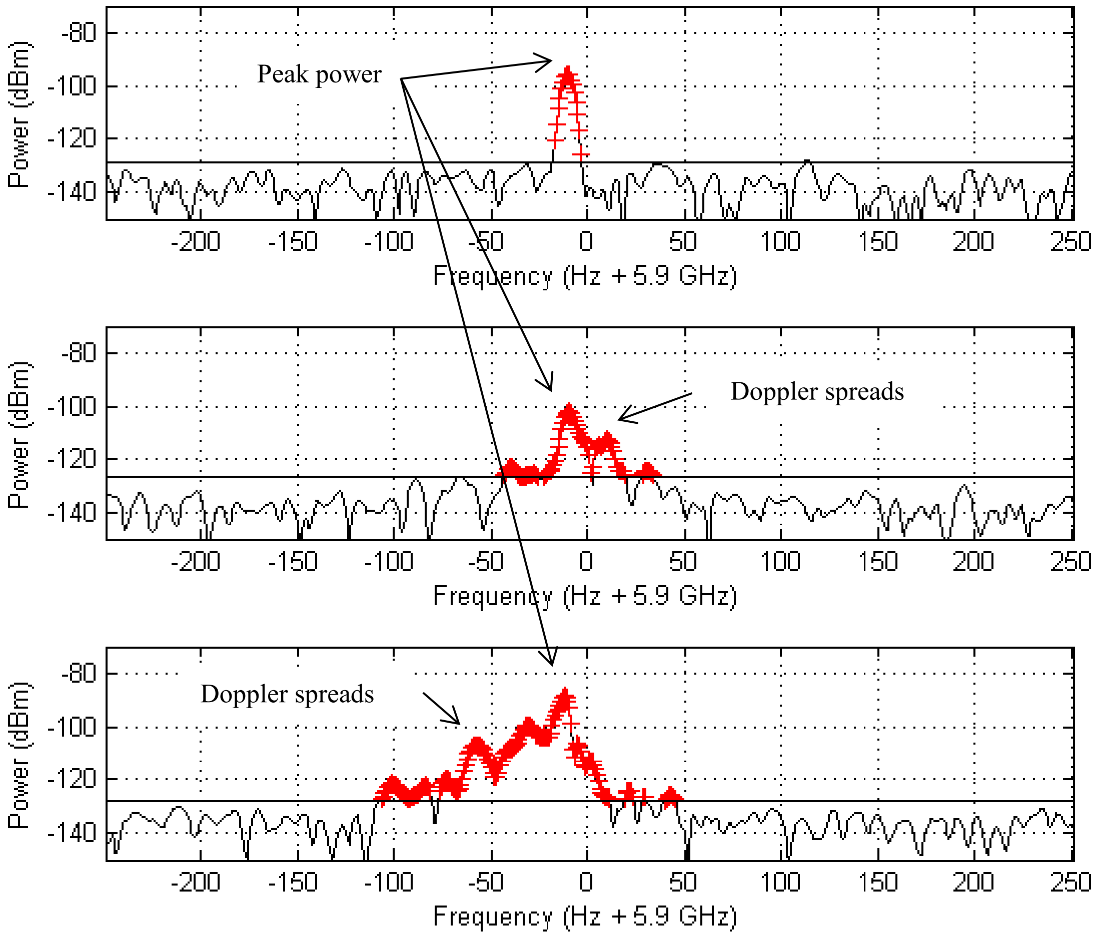

Figure 18: Three spectra showing the CW points (red crosses) affected by different sizes of Doppler spreads and power preceding a noise threshold at approximately -130 dBm

A mesh showing 30 spectra collected at a single location (which is described in Section 4.2.1) is shown in Figure 19. This figure is produced by creating a matrix using all the spectra; where the rows and columns correspond to the frequency and spectra number respectively. This matrix is then plotted as an image where the colour of each pixel corresponds to the power. Viewing spectra like this provides an indication of the Doppler spreads present and how they vary along with the power in them.

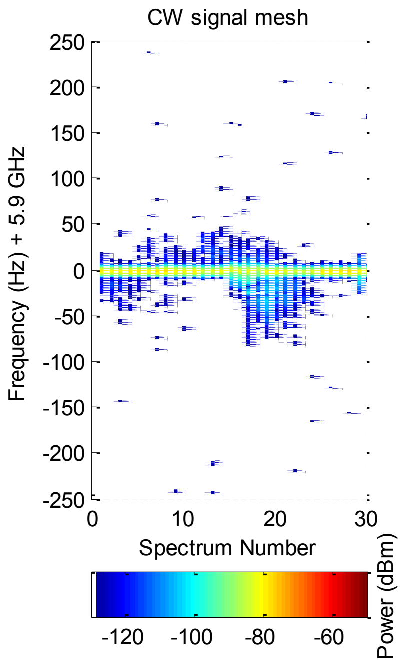

Figure 19: Plan view of mesh created by joining all the spectra collected at a certain position

3.3.2 Data measured from the NS and the information that can be extracted

Packets were continuously transmitted from one 802.11p transceiver at a rate of 10 packets per second and each packet is time stamped with the local time and a unique packet number before it is transmitted. Packets received at the receiving 802.11p transceiver are time stamped locally and the Received Signal Strength Indicator (RSSI) of each packet is also acquired. These packets are used to calculate the PDR.

At each position, data is only collected for the duration it takes to collect 30 spectra, and therefore the number of packets used to obtain the PDR varies slightly from position to position. The 45 s taken to collect 30 spectra at each position resulted in approximately 450 packets being transmitted and used to calculate the PDR. It was found at times that this method gave PDRs over 100%; approximately 105%. This is because the program to record the received packets (NS_Data_Record) was started before the program which recorded the spectra (CWS_Data_Record). NS_Data_Record was also terminated after 30 spectra had been collected by CWS_Data_Record. As NS_Data_Record ran before the first spectrum was collected and after the last spectrum was collected, a few extra packets were received. In the results all PDR values are capped at 100%.

At each point that data is collected, 30 spectra and 450 packets will be collected; 15 packets for each spectrum collected.

3.4 Indoor Power Calibration

The dual measurement system was first tested indoors and power calibrations of both the systems were performed. The trolleys were placed close to each other with the antennas 1.6 m apart and spectra and packets were collected with the transmit power (P_T) varied from 1 to 18 dBm in steps of 1 dBm. Figure 20 shows how the measured received power (P_R) varied in each system as P_T was increased. Neither of the systems have a uniform increase in their P_R (or RSSI in the case of the network system) but the CWS operates a lot more accurate than the NS. The lines of best fit for both the sets of data show that the CWS has a gradient which is only slightly higher than 1 whilst the network system's gradient is less than 0.5 and there are large differences between the measured data and line of best fit. The NS does not have a linear increase in the RSSI as P_T is increased and it was not investigated whether this was an error with the transmitter, receiver or both. Another important observation is that the RSSI is generally higher but then starts to fall once $P_T > 14$ dBm.

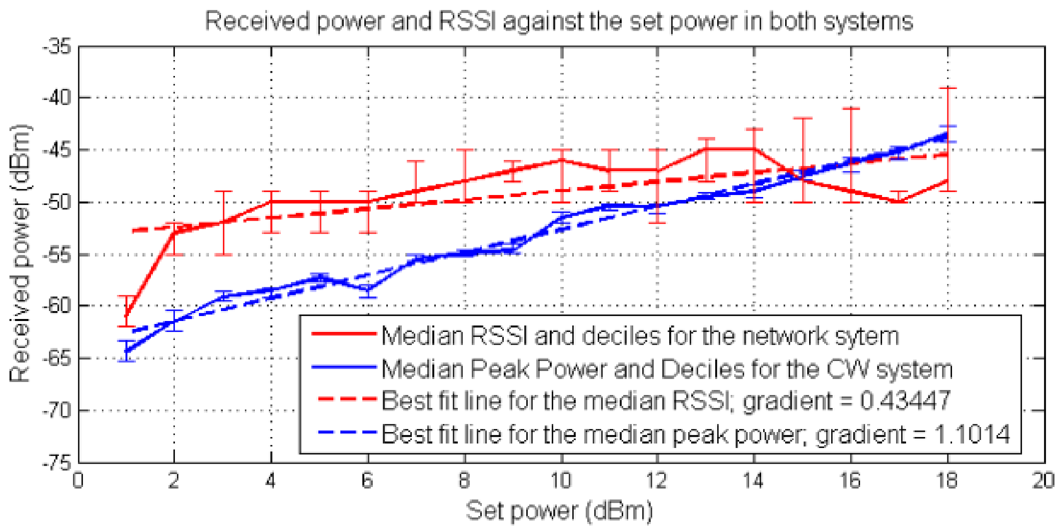

Figure 20: Graph showing how the received power of both systems varied as the transmission power was increased

The 802.11p transceivers were designed to exchange messages between each other and their primary purpose is not to measure the received signal strength with high resolution, as opposed to a spectrum analyser. The irregularity of the power increase is justifiable in this light and this is why the CW system is a very important part of this measurement system. It provides accurate data about the received signal unlike the 802.11p transceiver. It was decided not to use the RSSI data due to its non-linear power increase and high quantisation.

This simultaneous data gathering is a very important aspect of the data collected for this PhD as it provides information about the performance of an 802.11p network and how the signal varies as it propagates from the transmitter to the receiver. This system has only been used in one other study and that was in a wide variety of environments (straight roads, intersections, etc.) with the collected data not being analysed against these different environments. The data collected in this project is focussed on radio wave propagation at T-junctions in NLOS conditions. Using a laser rangefinder has also enabled highly accurate positioning which in turn enables measurements to be made with shorter distance intervals; GPS accuracy in urban areas are not as high. This is a unique feature of these measurements.

3.5 Multipath Direction Finder System

The equipment set-up for a collection of direction finding measurements (Directional Antenna System, DAS) is displayed in Figure 21.

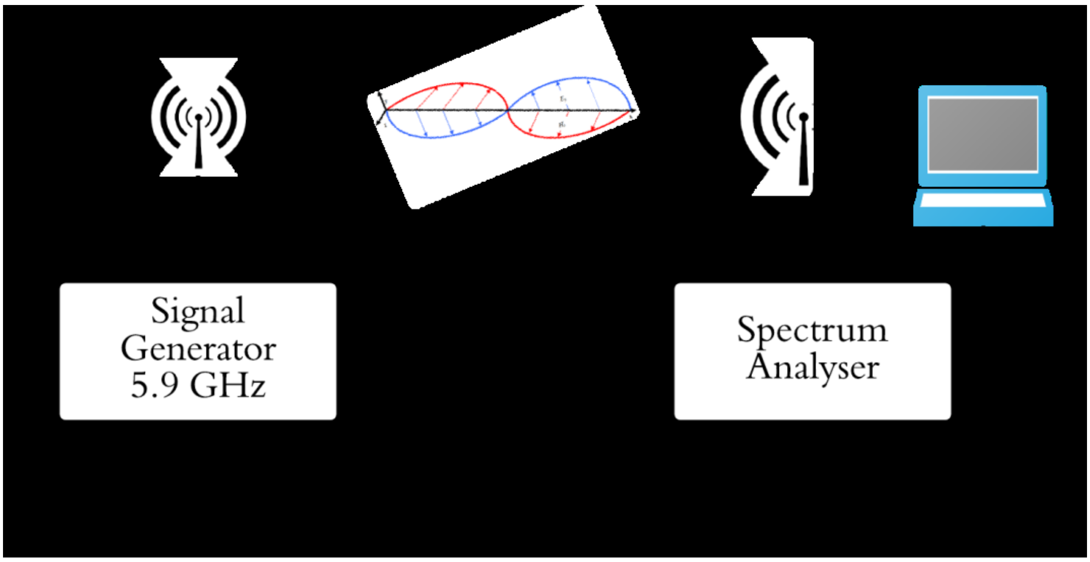

Figure 21: Directional antenna system set-up

In the DAS the NS component of the system is not used. The CWS system is altered to use a directional antenna (Mobile Mark PN18-5900) at the receiving station instead of an omnidirectional one. Radiation patterns obtained from the manufacturer for this antenna are shown in Figure 22.

The directional antenna can be used to find the directions of the strongest signal in order to obtain a better understanding of the multipath components. Like with the CWS, the main output of this system will be spectra. The DAS was only used in the urban case (explained in more detail in Section 4.2.1) since this was likely to provide the richest source of reflected signals. At each position, the antenna's azimuth angle was varied from -90º to 90º with an angular resolution of 10º; where 0º corresponds to the antenna being pointed towards the centre of the intersection. Data collected using the DAS was done with a higher distance interval compared to data collected using the dual measurement system due to time/battery constraints; 19 measurements are made at each position using the DAS as opposed to one measurement as was the case using the combined system.

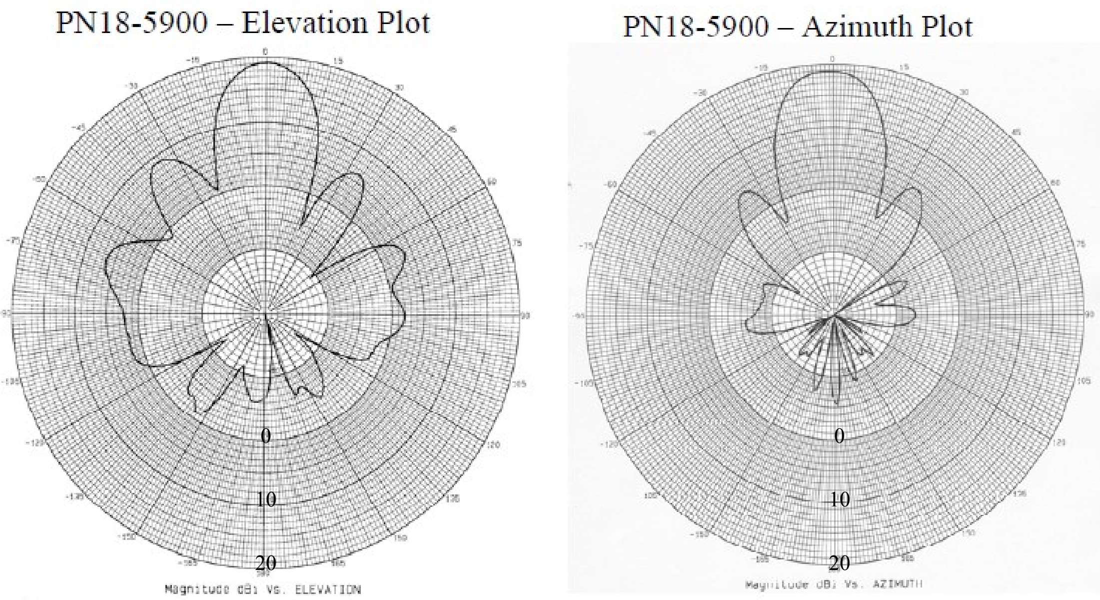

Figure 22: Radiation patterns of the MobileMark PN18-5900 directional antennas used; 18 dBi gain, 5.850 - 5.925 GHz. (MobileMark, Personal Communications)

The main disadvantage of this measurement system is the effect caused by the sidelobes; if strong Multipath Components (MPCs) arrive in line with the sidelobes whilst the signals received by the main lobe is weak, then the direction of the strongest MPCs will be wrong.

The data collected using the DAS is presented and discussed in Chapter 7. The data gathered using this system is another novel aspect of this project – data collected in an urban environment under NLOS conditions using a 5.9 GHz CW with a directional antenna at the receiver has not been seen in the literature.

4 Network Performance and Channel Measurement Data – Signal Strength Observations

4.1 Data Collection Cases and Observations in the Collected Data

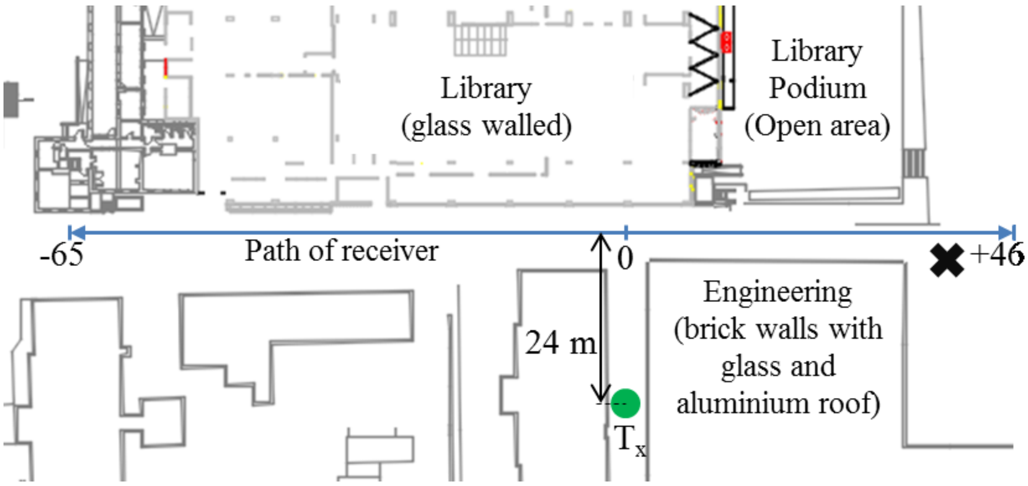

Figure 23: Plan view of the urban case

Radio propagation data and network performance is collected at three different locations; "urban" (Figure 23), "less urban" (Figure 24) and "open" (Figure 25). These three locations were picked for the different ray-path geometries, building densities and sizes they offer; the first is a T-junction which has narrow roads (single lanes) and many buildings. The locations provide NLOS propagation conditions at intersections of varying degrees of urbanisation which is a similarity with the locations used by Mangel et al. (2011). Only pedestrian and cycle traffic were present when data was collected in this area (vehicular traffic was asked to wait while data would be collected), whereas the other two cases had pedestrians, cyclists and vehicles. The less urban case has dual lane roads and fewer buildings to reflect radio waves whilst the open case comprises of wide roads and even fewer buildings. It is also not a perfect T-junction as the two roads are at acute angles and the road with the receiver sloped downwards as you moved away from the centre of the junction; this is expected to alter the ray paths in comparison to a completely perpendicular T-junction.

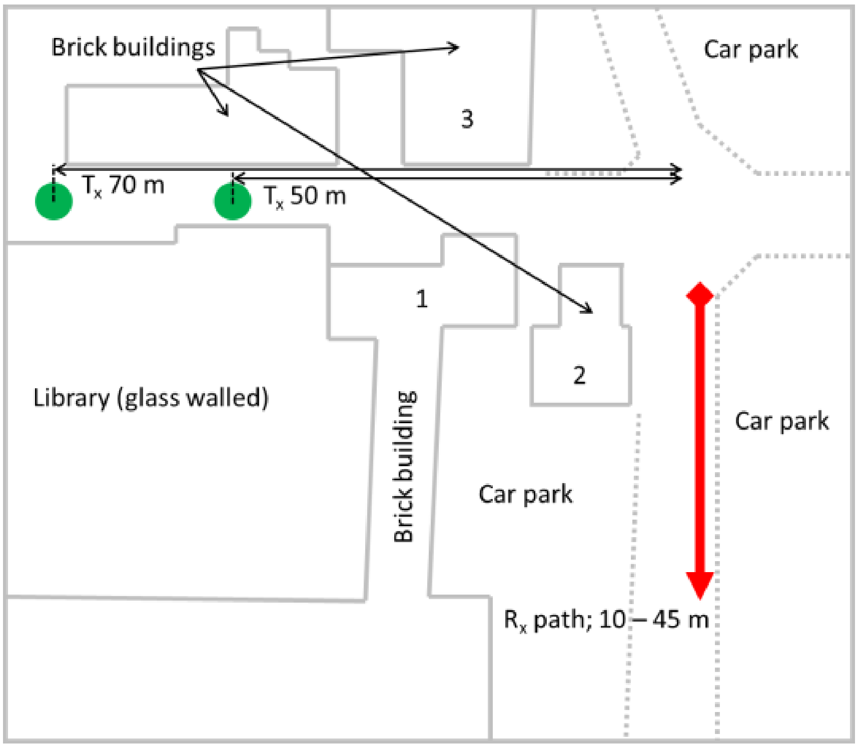

Figure 24: Plan view of the less urban case

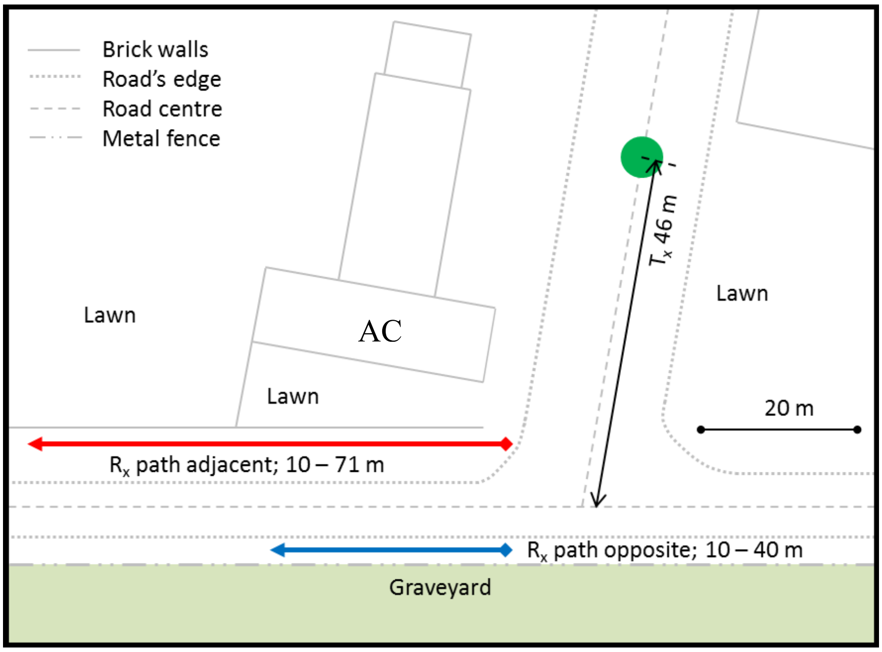

Figure 25: Plan view of the open case

The images (Figure 37 & Figure 38) of the open case were taken after data was collected; when the data was being collected there was no scaffolding or building works being done as shown in the images.

For each case, the transmitter was always at a fixed point. As explained in Chapter 3, data was collected at regular intervals (Δd) along a set path – equipment was always stationary during data collection and d is the displacement from the centre of the intersection. In the urban case Δd = 100 cm and in the other two cases Δd = 20 m.

In the urban case the receiving equipment shared the road used by vehicular traffic but traffic was restricted during data collection. Because of this it was impractical to collect data every 20 cm; vehicles were asked to wait outside the measurement area until data was collected at each position along the path and traffic would build up. Traffic would be allowed to pass once data in a particular position was collected. Also, battery time was wasted while the trolley was moved out of the way whenever a vehicle used the road.

For -15 ≤ d ≤ -10 m in the urban case, data was collected with different Δd values of 20, 50 and 100 cm and this is plotted in Figure 26. Using this data, the loss of detail due to a higher Δd can be assessed.

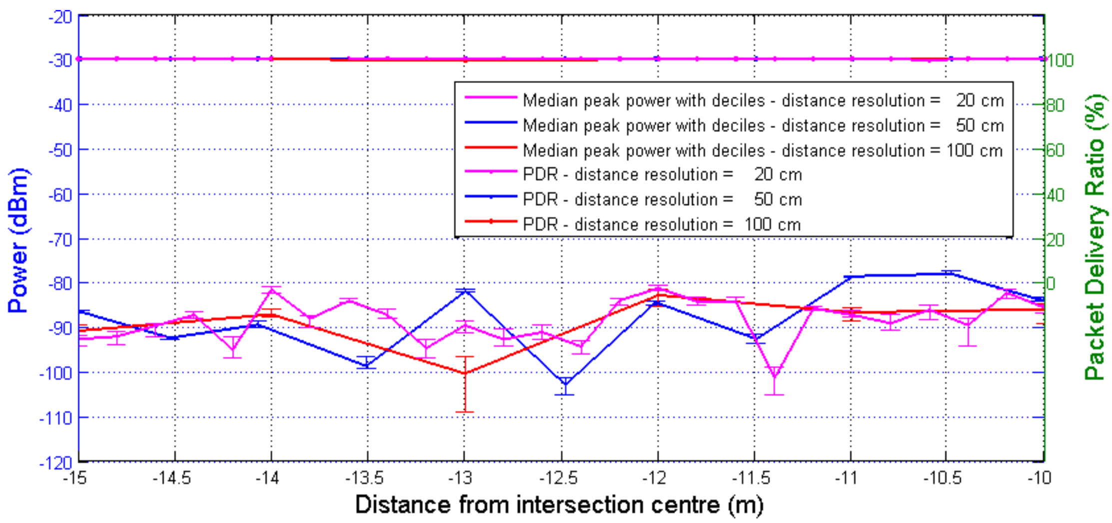

Figure 26: Median peak power with deciles and packet delivery ratio at the urban case; -15 ≤ d ≤ -10 m, Δd = 20, 50 & 100 cm

The difference in median peak power (MPP) between data collected every 20 cm and 100 cm is not large and Table 5 gives the MPP difference between their common positions. The data collected every 50 cm varies considerably more than the other two runs and also does not seem to closely track the high resolution data. However, the differences in these three measurement runs can be attributed as consequences of different propagation conditions (such as pedestrian traffic and minor changes to the physical environment) at the times data was collected. The PDR in each measurement run is almost 100%. The PDR at 13.8 m was removed as it was inexplicably low and can only be reasoned as an equipment failure.

Position, d (m)	-10	-11	-12	-13	-14	-15
Difference (dB)	0.3170	-0.5840	1.5740	10.7870	5.5530	1.8940

Table 5: Difference in MPP between the runs with Δd = 20 cm and 100 cm

In the other two cases the path of the receiver was on the pavement and as the equipment did not need moving every time a vehicle passed, data was collected in shorter distance intervals. A laser rangefinder (Bosch n.d.) was used in setting the path and also to mark the data collection points along the path. This rangefinder had an accuracy of 1 mm.

It was decided to plot the collected data against the distance from each intersection's centre. This enables comparison with the model virtualsource11p (Mangel et al. 2011).

4.2 Median Peak Power and Packet Delivery Ratio Analysis

4.2.1 The Urban Case

Figure 27: View of the urban case as seen from the 'X' in Figure 24

The urban case (Figure 23 and Figure 27) had the most buildings around it. The transmitter was placed in a narrow street canyon with the receiver moved either side of the T-junction from -65 m to 46 m. The receiver was kept in the middle of the road which was a single lane street; since this was likely to be similar to where a vehicle mounted system would be. The building geometry is different either side of the T-junction and this provides an opportunity to study the effect of buildings on the propagation. Although the Library Podium is on a raised platform with short walls (1.68 m high) on the side of the road (Figure 27), it was considered to be an open space. The data collected had a mix of both line-of-sight (LOS) and non-line-of-sight (NLOS) conditions; 6 positions with LOS and 105 with NLOS conditions.

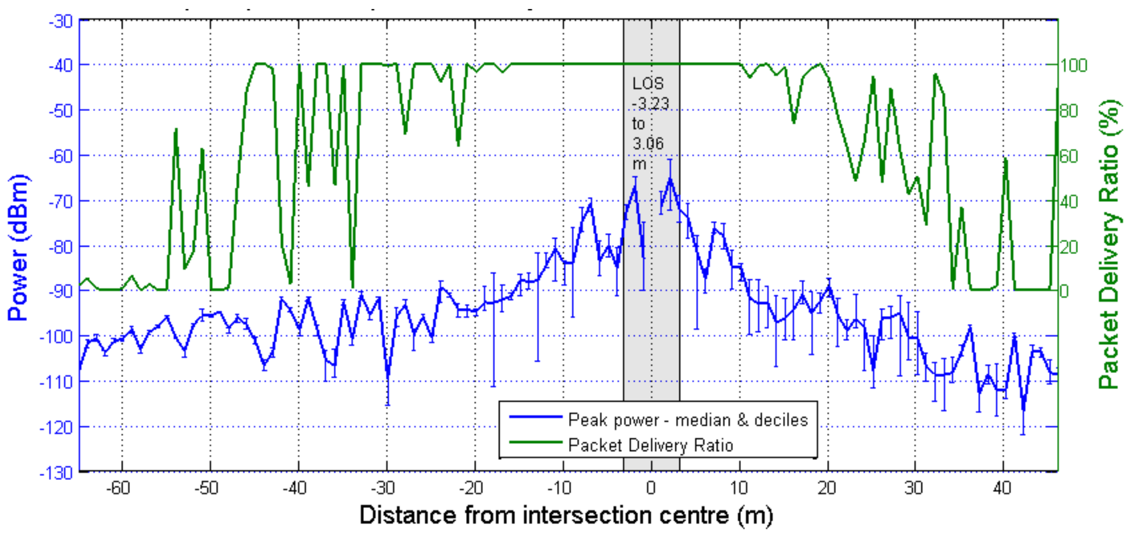

Figure 28: Median peak power and packet delivery ratio for all the data collected in the urban case - data combined from 6 runs

Figure 28 shows how the MPP and PDR varied as the receiver was moved further away from the intersection centre in either direction. Data was not collected from the exact centre of the intersection as this was in direct line of sight and the emphasis of the measurements were to focus in areas of NLOS and also the boundary between LOS and NLOS. The data shown in Figure 28 was obtained from six data collection attempts on different days; this data was combined to produce the graph, which presents the general trend of the MPP and PDR. Individual runs are discussed subsequently.

Both the MPP and PDR start high at the centre of the intersection, in the LOS region, and then decrease as the receiver was moved away from the intersection. The MPP drops sharply soon as the NLOS region is entered but rises again briefly and this can be seen on either side of the T-junction. The spacing between spikes is not easily explained by multipath but similar spikes can be seen as an output of the ray tracing program and presented in Figure 76 of Section 6.3.2. The drop in MPP is not smooth on either side and the error bars (indicating the 10^{th} and 90^{th} percentile) indicate that there is significant variation in the peak power at each position, especially at distances closer to the centre. Combining data from different runs (from different dates) can cause these variations as the radio channel is bound to have changed (e. g. the presence of parked cars in different locations provide different reflections), which leads to varied received powers. For this reason, separate plots of MPP and PDR for each run will be and provided in Figure 29 and analysed.

The MPP and PDR drop is closer to the centre on the side with fewer buildings (positive x-axis) as opposed to the side with more buildings (negative x-axis) and this is an important trend to notice; these buildings on either side of the road (represented by the negative x-axis) will reflect the radio waves and act as a waveguide which will in turn extend the coverage range. When there are fewer buildings, there will be fewer reflected waves which results in a performance drop (Chapter 6 contains a ray tracing model which supports this theory). On the positive x-axis portion of Figure 28 the PDR is 100% up to 10 m and falls below 90% within 20 m, but on the opposite side of the junction, which has more buildings, the PDR stays at 100% up to -16 m and does not drop below 90% within the first 20 m.

As the trolley is moved further away from the centre in the negative direction, the PDR is reasonably acceptable up to -33 m, apart from two drops which take it below 80%. The PDR then starts to be either approximately 0%, 50% or100%; not suitable for safety critical vehicular communications. The PDR settles around 0% at -55 m. On the side with fewer buildings, the signal goes through fluctuations after 20 m and starts to settle at 0% when the distance is beyond 36 m. The maximum distance which data could be collected in the direction of the positive x-axis was 46 m so it was not possible to see how the MPP and PDR behaved beyond that distance. Safety critical communication would not be possible beyond 15 m and despite the couple of spikes at 40 m and 46 m, beyond 36 m the system would not provide reliable communications. This extra 10 m in range that can be seen in the urban canyon half of the intersection (negative distances) is potentially caused by the multipath propagation due to the signals reflecting off the buildings either side of the road (further explored in Chapter 6).

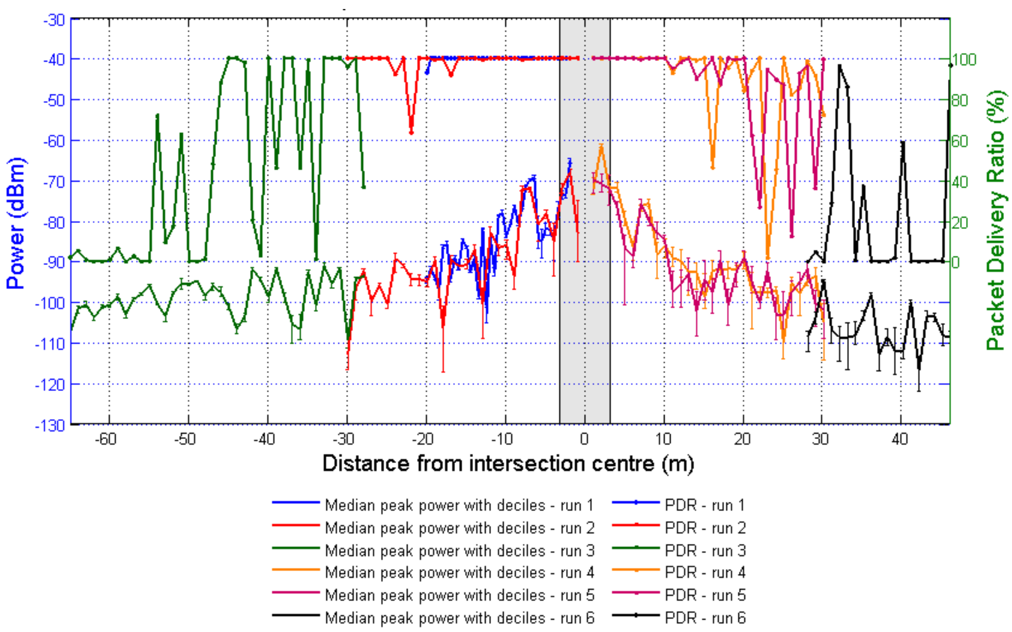

Figure 29: MPP and PDR data collected in the urban case with a separate line for each run

Figure 29 displays graphs of the data collected in the urban case from the separate runs. There are six runs which were made and details about them are listed in Table 6. The last column, Median inter-decile range (MIDR), is an indication of the variation in each run; this is the median of the inter-decile ranges of all the positions in a run.

Run No.	Start distance (m)	End Distance (m)	Distance Resolution, Δd (m)	Start time	Median inter-decile range (dB)
1	-2	-20	0.5	17:01	1.16
2	-1	-30	1	19:02	2.61
3	-28	-65	1	22:18	1.45
4	1	30	1	19:52	4.28
5	30	1	1	21:14	6.15
6	28	46	1	21:21	4.04

Table 6: Details of the different measurement runs in the urban case

Run1 was a trial measurement done to get an idea of how long the equipment could be powered using the batteries. It was started at d = 2 m because the main area of interest was the NLOS region and Δd = 0.5 m. For this (urban) case Δd was then changed to 1 m to use the battery charge time more efficiently, as explained in Chapter 3. With

$\Delta d = 1$ m it was possible to collect a reasonable amount of data at a good resolution in a single measurement run without losing much detail in how the signal degraded. The PDR throughout the data collection remained at almost 100% apart from at d = -20 m where it drops down to approximately 95%.

Run 1 showed that the peak power did not decay smoothly and there is fading present. Another run, run 2, was recorded to check if it would be similar to run 1. Despite having certain similarities between run 1 and 2, they also have some positions where the MPP differs by approximately 20 dB; e.g. at d = -18 m. The PDR in run 2 is also approximately 100% throughout with only one major dip (63%) at d = -22 m. The difference in MPP between runs 1 and 2 can be attributed to changes in the propagation environment such as parked cars and/or pedestrians which would contribute to the signal being higher in certain positions and lower in other positions due to the combination of multipath components at the receiver.

Neither measurement run showed a lot of variation (inter-decile range) at each position when it came to the MPP and this can be seen more clearly in Figure 46 and Figure 47 in Section 5.1. Run 1 has a bit of variation in the data collected closer to the junction whereas run 2 appears to have more variation in the MPP throughout.

Runs 4 and 5 were of the same portion of the path in the urban case and the data was collected on the same day. Run 4 was done first and then run 5 was the return leg starting from d = 30 m and ending at d = 1 m. Because of the relatively short times between data collected from corresponding locations, it is assumed that the radio channel did not change much and the two data sets will be similar to each other; especially in the range d = [20, 30] m as the time between collecting data from these positions at each measurement run was shorter than the data collected towards the centre of the intersection. Figure 29 shows that both the runs follow a similar pattern of decay when it comes to MPP but there is a significant difference between the data at d = 2 m, 11 m and 18 m.

When it comes to the PDR of runs 4 and 5, they only seem to be similar up until d = 13 m. After this point there tends to be a large difference in the PDR between the two runs; sometimes the difference being approximately 90% (at 23 m). The PDR and MPP do not always seem correlated as with the previously collected data and this relationship is further investigated in Section 4.3.

There was significant pedestrian traffic while collecting data in runs 4 and 5. Furthermore the receiving trolley had to be moved out of the road to avoid vehicles on 29 occasions out of the 60 positions that data was collected from. Taking the trolley off the path and then placing it back on the path has not made a noticeable difference.

The amplitude variation (signified by the higher and lower deciles given by the error bars) in Runs 4 and 5 tends to be larger than in runs 1 and 2, where the distances from the intersection centre were similar but on the other side of the junction. This larger variation is explained by the increased pedestrian traffic temporarily absorbing some of the radio wave power instead of allowing the waves to simply be reflected off the stationary reflectors/objects in the environment. Also, when the waves are subject to pedestrian traffic, their paths get altered and some ray paths, which would have previously been received, would be reflected elsewhere. The opposite of this also happens where some ray paths which would have previously not been received are now being received because these rays are being reflected off the pedestrians to the receiver. The MPP also keeps varying because as the pedestrians move, they keep altering the ray paths causing multipath propagation and the resulting received waves will add constructively/destructively depending on their phase, which depends on the ray's propagation path length, which is directly dependent on the mobile reflector; the pedestrians in this case.

Run 3 was performed to collect data from the left side of the junction until the PDR dropped consistently below 10%. Variation is relatively low at each of the positions in this run apart from at -37 and -36. The overlap of MPP data between run 2 and 3 fits almost perfectly although this is not the case with the PDR; the PDR at -28 m is less than 40% and is the lowest PDR in the range d = [-33,0]. The PDR at -28 m in run 3 remains unexplained as the MPP of data collected from the same location in run 2 is almost equal to that of the MPP at -28 m of run 3 but the PDR has dropped over 60%. Despite the propagation path not being measurably different, there is a drastic difference in the PDR, which could be a sign of the system reaching the edge of its operating capabilities (Figure 84 displays the spectra which were simultaneously collected and the CW does not appear to be affected by Doppler spreads or shifts as well).

It can be noticed again how the MPP does not have a smooth decay and this run shows the degradation of the PDR unlike the previous two runs. The PDR, along with the MPP drops as the distance increases. However, there does not seem to be a strong correlation between the MPP and the PDR; this is visible upon comparison of the data at d = -31, -35, -36 m and at d = -41, -39, -37/-44 m, respectively. Despite the MPP being approximately the same between each location pair, the PDR changes drastically. The PDR and MPP differences (in brackets) at these positions are 97% (2 dB), 53% (1 dB), 54% (1 dB) and 54% (less than 1 dB). In Figure 84 it can be seen that there is no significant difference between the Doppler shifts/spreads of these data pairs (apart from when d = -36 m). The only explanation is that the transceiver has entered a state of unreliable communications due to the low received power levels. The PDR is not high enough for reliable communications beyond -30 m as it keeps fluctuating between 100% and 0% until it reaches -55 m, where the PDR is consistently less than 10% and cannot be used for any communications. It is important to point out that this data was collected in a contention free environment and if there were more network traffic (as will be the case in a realistic deployment of a vehicular network) the distance at which the PDR drops to a percentage too low for reliable communication would be closer to the intersection centre.

Run 6 is a continuation of runs 4 and 5 (towards increasing positive d) and show how the MPP and PDR continue their degradation until what seems to be a complete loss of PDR. The data collection in this direction is also limited by a building at the end of that path which is approximately 50 m away from the intersection. The MPP for data collected in this run does not drop a lot, unlike with the other two runs on this side of the intersection. Instead, it stays within the range [-110,-100] dBm for most of the positions where data was collected.

In the positions where data was collected at distances common with runs 4 and 5, there is no clear similarity between the different sets of data. Runs 4 and 5 had differences less than 5 dB between their MPP data for two out of the three overlapping locations; with the other pair of points having a difference of 6.9 dB. Run 6 has a lot larger differences with Runs 4 and 5 when it comes to MPP; the lowest difference is 3.2 dB and the rest are all greater than 7 dB, with some differences being greater than 10 dB. The data in Run 6 has a few steep spikes/drops and it has its MPP increasing over 10 dB in the overlap range while the MPP in the other two runs decreases by approximately 10 dB. This difference can be attributed to the geometry of the propagation environment changing on different days (such as the location of parked cars and other reflective objects) altering the path length of the received waves, which in turn changes the MPP, and indicates the channel's volatility.

Vehicle traffic was very low while collecting this data and this is reflected by the very short error bars at most positions. At d = 33 and 39 m the error bars are not very short and it was noted during data recording how there was a pedestrian when data was being collected at 33 m. A car approached the system when data was being collected at 39 m. This evidence supports the theory that traffic, including pedestrians, will cause variations in the received power. More similar observations are seen and discussed in Section 8.2.

The PDR for this run does not seem to provide much conclusive data. There is a marked difference in PDR between the three runs in the overlapping regions, similar to how the MPP data was also different. Whilst there is some packet reception in the range $28 \leq d \leq 30$ m in runs 4 and 5, with some PDR levels being greater than 90%, run 6 fails to get even 5% of the packets at each position with two of the positions having a 0% PDR. The PDR briefly spikes up afterwards and reaches 95.79% at 33 m before falling down to 0% again. A few more spikes occur throughout the measurement with the last point also being a spike of 96.35%. These spikes do not correlate with spikes in the MPP and it seems impossible to explain why there is such high PDR at what seems to be random locations along the path. At 33 m there is a possibility that the pedestrian assisted the packet delivery by the changes he/she made to the radio channel, but the length of time the pedestrian would have affected the channel is less than the time during which data was collected and hence cannot be used to explain 95.79% PDR (Figure 87 shows the spectra that were affected – approximately half of those collected). In addition to that, at 39 m there was also a car which approached the receiver and would have improved the propagation conditions, as essentially, a car is a large reflective body (whose effect on the radio channel can be seen in the spectra collected at 39 m in Figure 87). However, the PDR at 39 m is almost 0% and the PDR rises at 40 m, after the equipment had been moved out of the road for the car to pass, and then moved back onto the road. The spike at 46 m also cannot be explained just using the MPP data.

What can be concluded from the PDR degradation is that once it drops below 90% the PDR could be anywhere on the scale between 0 and 100%.

Runs 1 and 2 are almost repeats of each other in terms of the positions covered whilst runs 4 and 5 are repeats of each other; with the data in the latter pair being collected within hours of each other. Despite this and not being far from the intersection centre, neither pair has similar MIDR. Most importantly, the data collected in the open half of the environment has higher MIDR in comparison to the data collected on the urban canyon part. A plausible explanation for this is that on the side with more buildings, multipath propagation assists in more rays being received in comparison to the side with lesser buildings. If the number of rays being affected by pedestrians remains approximately constant, then the proportion of rays being received, which are reflected off pedestrians, will be higher on the side with lesser buildings. There is no strong LOS component on either side of the intersection and because of the increased proportion of waves being affected by pedestrians (on the side with fewer buildings), the variation will be higher.

4.2.2 The Less Urban Case

Figure 30: Receiver path and road in the less urban case

Figure 31: Transmitter road in the less urban case

This case, shown in Figure 24, Figure 30 and Figure 31 has fewer buildings around it. Buildings were only present on one side of the junction; which also contained the transmitter hence still keeping the transmitter in a road canyon; albeit a wider road canyon. The receiving trolley was next to a car park with a hedge in between. The receiver path and the transmitter are not placed on the middle of the road but on the pavements adjacent to it.

Two sets of measurements were made; one with the transmitter 50 m away from the intersection centre ($T50_{TOT}$) and the other at 70 m away ($T70_{TOT}$). These distances were chosen because it was required to test where the system would be most vulnerable, at the edge between LOS and NLOS, and also because at closer distances the system would perform better and is not overly complicated to understand. Even though these experiments were performed with no network traffic, 802.11p networks will be working in areas of network contention and this will cause the networks to fail before the distances shown in these measurements. This is another reason why it was decided as better to start close to a point where the system would struggle to perform well; because whatever distances the system fails at, the real system will fail before that.

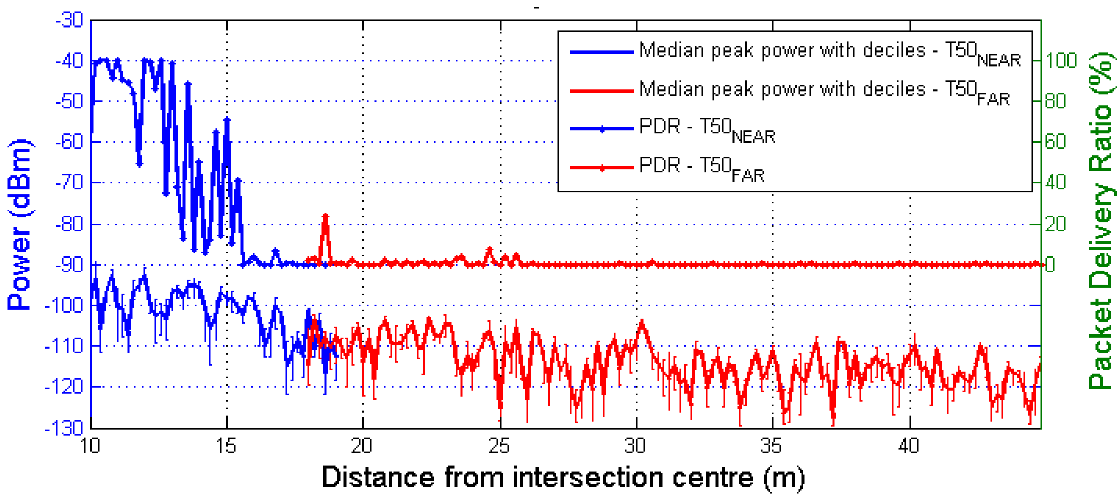

Figure 32: MPP and PDR in the less urban case with the transmitter 50 m away from the intersection centre

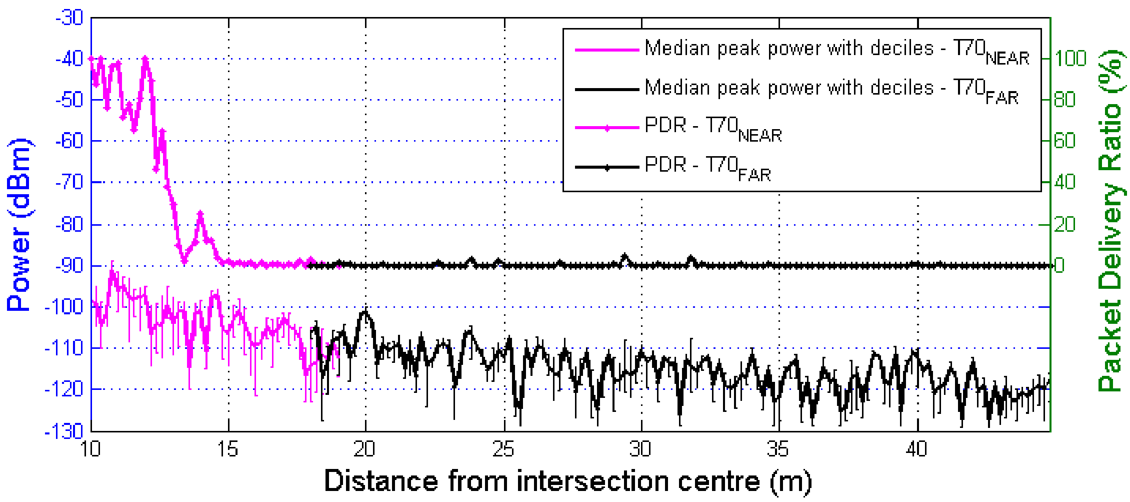

Figure 33: MPP and PDR in the less urban case with the transmitter 70 m away from the intersection centre

To get a more accurate idea of how the received signal and packet reception varied $\Delta d = 20$ cm. The distances at which the transmitter was kept meant that all the data collected was done in NLOS conditions. This case had the added effects of vehicular traffic in the vicinity along with pedestrians and cyclists; this traffic varied throughout the data collection and the presence of a vehicle was usually noted.

All the MPP and PDR data collected in this case with the transmitter 50 m and 70 m away from the intersection centre are shown in Figure 32 and Figure 33 respectively.

$T50_{TOT}$ and $T70_{TOT}$ were both completed in two sessions each; $T50_{TOT}$ comprised $T50_{NEAR}$ and $T50_{FAR}$ while $T70_{TOT}$ comprised $T70_{NEAR}$ and $T70_{FAR}$. $T50_{NEAR}$ and $T70_{NEAR}$ only contain data until it was clear that the 802.11p network has failed. $T50_{FAR}$ and $T70_{FAR}$ was an extension of $T50_{NEAR}$ and $T70_{NEAR}$ respectively, to see if there was a chance of receiving any packets which would have propagated between buildings 1 and 2 (Figure 24). The different measurement runs were done on (4) separate days and a description of each is provided in Table 7.

Measurement Run Name	Transmitter Distance (m)	Distance Range (m)
$T50_{NEAR}$	50	$10.0 \leq d \leq 19.0$
$T50_{FAR}$	50	$18.0 \leq d \leq 44.8$
$T70_{NEAR}$	70	$10.0 \leq d \leq 19.0$
$T70_{FAR}$	70	$18.0 \leq d \leq 44.8$

Table 7: Measurement runs in the less urban case

$T50_{NEAR}$ was initially stopped at 19 m because it was obvious the data network had ceased to function shortly before 16 m and data was then collected for a few metres more to make sure that a significant number of packets would not be received further away from the intersection. $T70_{NEAR}$ failed before reaching 15 m but for consistency in data collection at the same location it was decided to continue until 19 m. $T50_{NEAR}$ and $T70_{NEAR}$ had a 1 m overlap with $T50_{FAR}$ and $T70_{FAR}$ respectively and also continued far enough until it could be concluded that there is enough distance between each car so that the messages received beyond this range would not impinge on the efficiency of any safety critical messages; the cars would have over 95 and 115 m between the transmitter and the receiver when the data collection was stopped. This data collection range also provides information about how the CW wave decays far beyond the functioning limits of the 802.11p network; unlike in the previous case.

$T50_{NEAR}$ and $T70_{NEAR}$ both suffer from a drastic drop in PDR after short distances. Neither data set includes consistently high PDR at any point unlike in the previous case. This is despite the data being collected from the pavement across the road, as opposed to the pavement on the side of the road closer to the transmitter. It is expected that the power would be higher than on the oppose side of the road as the rays do not have to diffract with larger angles. In $T50_{NEAR}$ the PDR first drops to approximately 50% at 11.8 m whilst in $T70_{NEAR}$ that distance is 12.4 m; 0.6 m apart from each other. The PDR fluctuates between extremely low values and medium-high values in $T50_{NEAR}$ whereas in $T70_{NEAR}$ the PDR is above 60% until 12 m and then falls in one sharp movement apart from the spike at 12.6 m.

The 802.11p network does not seem to be reliable in this case and with the data collected it is not possible to say with certainty the limits of reliable communication. However, communications are possible until approximately 12 m away from the centre. Out of this 12 m, 7.5 m belongs to the intersection (Figure 34) with only 4.5 m belonging to the road leading to the intersection. 802.11p communications are envisaged to assist drivers in seeing beyond what the naked eye can see and in this situation it appears that the communications will not be able to greatly enhance a driver's knowledge (under NLOS conditions) if there is another automobile as close as 50 m away from the intersection. For a technology which is expected to function in an environment with high network traffic and extremely dynamic nodes which could be up to a kilometre apart (Hartenstein & Laberteaux 2010), this failure of communications in a range less than 80 m does not look promising.

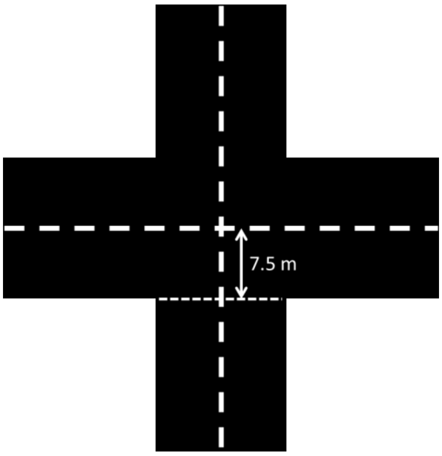

Figure 34: Junction centre size

In the overlapping region of the two measurements sets the PDR is the same apart from a spike of just over 20% at 19.6 m in $T50_{FAR}$. During $T50_{FAR}$ it was possible to maintain a rough record of the traffic, especially of a few automobiles which could have affected the data; examples of this being whenever traffic increased at the intersection centre or when a large automobile would pass through the intersection. Pedestrian traffic was not recorded as there was a steady stream in this location.

The spike (of 23.74%) in the PDR at 18.6 m (mentioned in the previous paragraph) coincides with the passing of a truck through the intersection and it was noted that this truck was previously parked next to building 2 in Figure 24. At 21.2 m an SUV was noted to have passed but this has not affected the PDR. An increase in traffic was noted at 23.4 m and this has given rise to a 2.80% increase in PDR but nothing of any significance in the MPP. At 24.6 m there is a spike of 7.35% but there is nothing noted which could be used to explain this spike. What is also more interesting is that at the same distance, there is also an increase in the MPP data. It is possible that a stationary reflector combined with the ray path geometry contributed in an increase in the received power and performance. Confirmation of this would be possible using a ray-tracing model, similar to the one described in Chapter 6.

Distance (m)	PDR (%)	Noted traffic
25.2	3.55	Truck
25.6	4.33	Truck
26.2	0.51	
29.4	0.27	
30.6	1.07	
32.8	0.29	
34.6	0.21	Car present within a minute before measurement
36.0	0.24	Bike, van and car
36.4	0.25	SUV present within a minute before measurement
38.0	0.32	Truck
39.6	0.25	Light traffic
40.2	0.50	
42.4	0.86	Car present within a minute before measurement
42.8	0.74	Slight traffic
44.6	0.55	

Table 8: Positions beyond 25 m in $T50_{FAR}$ where the PDR was non-zero and noted visible traffic

Between 20 and 25 m in $T50_{FAR}$ the PDR remains extremely low; between 0 and 10%. Beyond this the PDR then drops to a near constant 0% with a few exceptions. Each of the occurrences of non-zero values in PDR is shown in Table 8.

There is a total of 15 non-zero PDR values after 25 m and even though they are almost insignificant in percentage, 6 of these values coincide with the recording/sighting of some form of vehicular traffic which was within the visible (from the receiver) part of the propagation environment. In addition to this, there are 3 non-zero values which arose within a minute after a car passed through the propagation environment. There is a barrier between buildings 1 and 3 in Figure 24 which stops all traffic on the road between these buildings. The increase in PDR at those three positions could have been caused via reflections off these vehicles as they were waiting for the gates to open. Unfortunately, this is not extremely conclusive evidence to prove that those passing cars assisted a few packets to reach the receiver.

Even if the passing traffic assisted a few packets, there are still 6 more non-zero PDR values which have no explanation yet; with the PDR values not being too different from the PDR values of those positions where there was traffic. Because of these reasons, it is not possible to confidently say that passing traffic can significantly improve packet reception, or that it is the only cause which increased the PDR.

Besides the data shown in Table 8, there were 4 instances where a car was recorded to have passed through the propagation environment but there was no rise in PDR noticed; more evidence that every passing vehicle will not assist the communications network. This could also be due to the reduced range in this case which limits the interference levels.

There was less traffic information recorded during the collection of $T70_{FAR}$; light traffic at the start with an increase around 31.6 m. This is not enough data to make any conclusions of the PDR depending on the traffic.

The MPP of either measurement pair does not have a smooth decline, similar to how it was in the urban case. There are a lot of peaks and troughs which appear throughout both sets of data as the MPP decreases. Due to this irregular decline, it is not possible to precisely say how much the received power has dropped from the start to the end of data collection in both $T50_{TOT}$ and $T70_{TOT}$.

Measurement	Median inter-decile range (dB)	Start time
$T50_{NEAR}$	5.27	16:58
$T50_{FAR}$	5.54	12:38
$T70_{NEAR}$	9.04	11:42
$T70_{FAR}$	5.66	14:59

Table 9: Table showing the average inter-decile range for the different runs in the less urban case

The variation at each position in $T50_{TOT}$ and $T70_{TOT}$ also appear greater than what was usual in the previous case. Table 9 displays the MIDR for the four measurements done in this case. These values are similar to the highest MIDR in the urban case albeit that there is one MIDR in this case that is markedly higher (9.04 dB). The highest MIDR in the urban case (6.15 dB) was for measurements made in the right side of the T-junction; which had less buildings and more open space, similar to this case. These two similarities in MIDR (in the building-less parts of both cases) imply that when the receiver is not in a street canyon – where more signals can be received through reflections off stationary objects such as buildings or other street furniture – the variation in the received signal power is higher due to the relatively higher proportion of waves reflected off mobile scatterers e.g. traffic. These reflected waves have constantly varying phases due to their constantly varying lengths; the varying phases results in the received signal power fluctuating (at the receiver) as the waves contribute constructively or destructively.

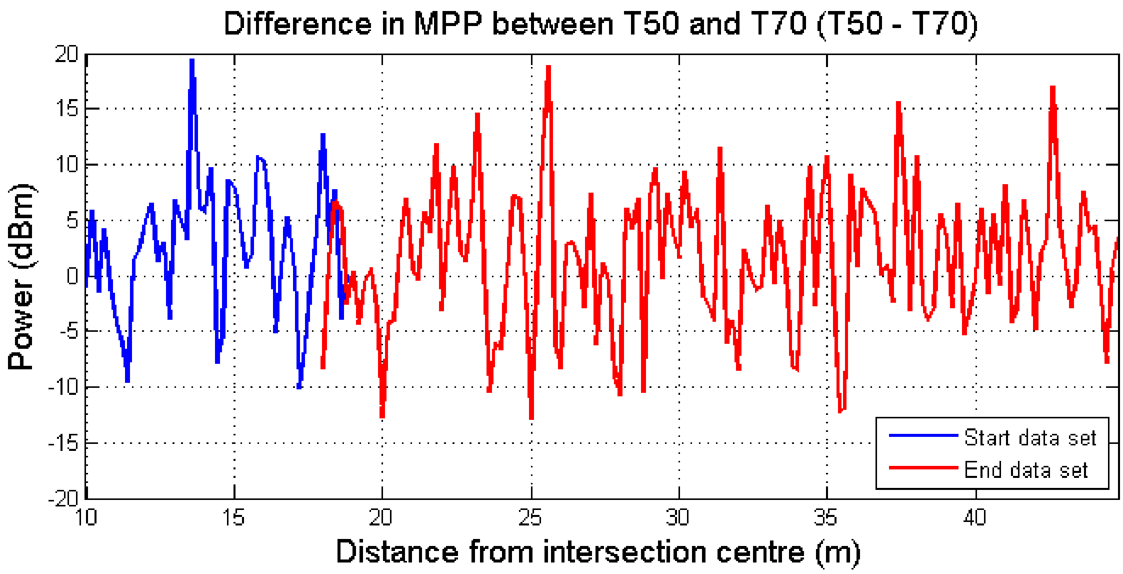

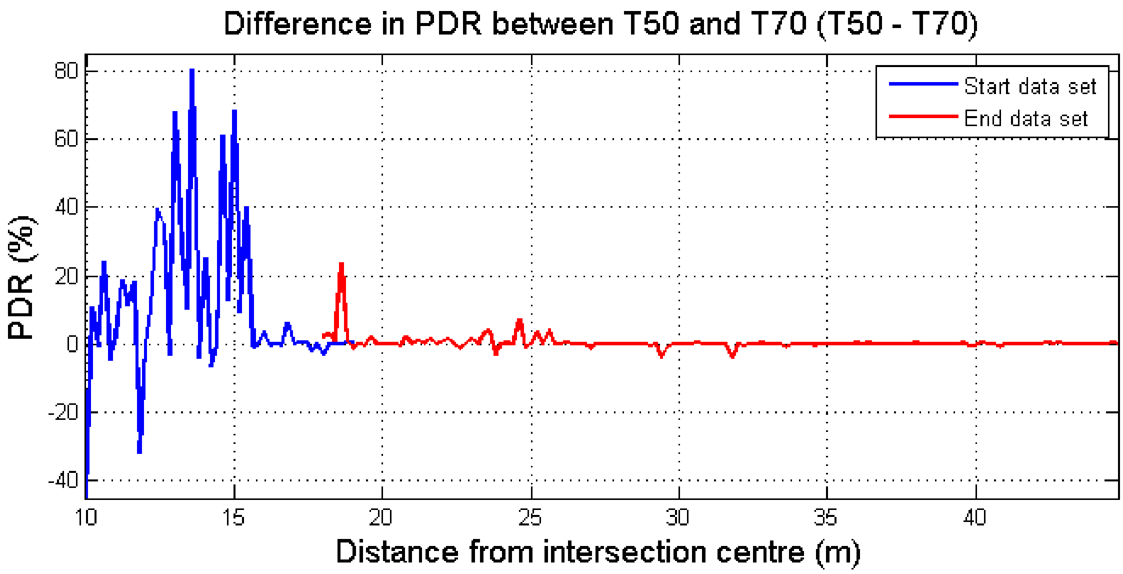

Figure 35: Difference in the median peak power (top) and packet delivery ratio (bottom) between data collected with different transmitter positions

Figure 35 displays the difference in MPP and PDR between $T50_{TOT}$ and $T70_{TOT}$; this case is the only one where there are datasets with different transmitter positions. The MPP of $T50_{TOT}$ does not always seem to be higher than that of $T70_{TOT}$ despite this being expected (Chapter 5 compares the collected data against the model Virtualsource11p (Mangel et al. 2011) and the expected difference between $T50_{TOT}$ and $T70_{TOT}$ is calculated to be 3.8 dB). $T50_{TOT}$ even starts with a MPP less than that of $T70_{TOT}$ by 0.9 dB.

Between the 181 receiver positions shared between $T50_{TOT}$ and $T70_{TOT}$, which includes the overlap between 18.0 m and 19.0 m, on 74 instances the MPP of $T70_{TOT}$ is higher than that of $T50_{TOT}$ and this equates to 41% of the total number of positions data was collected from. Out of these 74 instances, 16 (out of 46) happen between $T50_{NEAR}$ and $T70_{NEAR}$ while 58 (out of 135) happen between $T50_{FAR}$ and $T70_{FAR}$.

It was then decided to see if such a trend was present with the PDR and the graph produced is in the second panel of Figure 35. Visually, there does not seem to be such a trend between the PDRs of the measurements with different transmitter locations. Table 10 shows more numerical information related to this.

Data sets	**Both differences > 0**	**MPP has a positive difference while PDR = 0**	**Differences have opposite signs**	**MPP has a negative difference while PDR = 0**	**Both differences < 0**
$T50_{NEAR}$ & $T70_{NEAR}$	17 (37%)	4 (9%)	18 (39%)	2 (4%)	5 (11%)
$T50_{FAR}$ & $T70_{FAR}$	21 (15%)	48 (36%)	16 (12%)	40 (30%)	10 (7%)

Table 10: Table showing the synchronicity of the MPP and PDR differences

For $T50_{NEAR}$ and $T70_{NEAR}$ (where 35% of the time T70's MPP is greater than T50's) the difference in the two MPP and PDR values have the same sign for 48% of the time while on 39% of the time their differences are of opposite signs. On 13% of the positions the PDR is 0% on both $T50_{TOT}$ and $T70_{TOT}$ whilst there is a change in the MPP. Between $T50_{FAR}$ and $T70_{FAR}$ there are a lot of instances where the difference in the PDR is 0%; 65.19%. Out of the remaining data, in most cases the difference between the two MPP and PDR values are either both positive or both negative.

Judging from the numbers in Table 10, it can be concluded that in most of the cases (where a PDR difference of 0% is not taken into account) where the MPP of $T50_{TOT}$ was higher or lower than the MPP of $T50_{TOT}$, the difference between the PDR of the two data sets also changed similarly. It is important to note that these 'synchronised differences' do not occur significantly more than when the differences have opposite signs. Another important observation in Table 10 is that the number of times both differences (in MPP and PDR) are positive is higher than the number of times where both differences are negative; this is a direct consequence of $T50_{TOT}$ having a higher MPP or PDR than that of $T70_{TOT}$ for most of the positions that data was collected from.

In conclusion, in this case it was observed that despite having 20 m between the two different transmitter positions, the received power and the PDR for the data with the transmitter positioned closer is not always higher than that of the data collected with the transmitter 20 m away. The model Virtualsource11p (Mangel et al. 2011) predicts that the power received in T50 should be 3.76 dB higher than that of T70. T70 being greater than T50 for such a significant number of positions could be due to temporary factors (such as vehicular traffic and the position of parked vehicles) which affect the propagation positively or negatively.

4.2.3 The Open Case

Figure 36: Arial view of the junction used in the open case (enclosed in the white circle); red line showing receiver paths and green circle showing the transmitter's location.

This is the case with the least buildings and Figure 25 and Figure 36 displays its layout, surroundings and the paths of the receiver. The white circle in Figure 36 encircles the relevant junction with the red lines and green circle showing the path of the receiver and position of the transmitter respectively. The scaffolding seen in these images were not present during data collection. This T-junction does not have the intersecting roads meeting perpendicular to each other, but at an angle less than 90º. Further to this, both the paths of the receiving equipment are on a road sloping downwards as the distance increases from the centre of the intersection. There were no street canyons in this propagation environment at all, unlike in the previous sets of measurements.

Only one building is in between the transmitter and the receiver at most times but there was a medium (non-metallic) sized road sign in between for a brief length of the data collection path and this is shown in Figure 37 and Figure 38. This building was not situated at the edge of the junction hence reducing the angle that the radio waves needed to be diffracted off its edge, for successful propagation between the transmitter and the receiver. There was also a wall running next to the adjacent path and as the path sloped downwards away from the intersection centre, the height of this wall in relation to the path also rose – the wall had a flat top. This wall is next to the sign and can be seen in Figure 37 and Figure 38. Next to the opposite path there was a steel fence dividing the pavement from the cemetery next to it and it is believed that this will have influenced the radio propagation as each metal bar on the fence is an extra surface for the radio waves to reflect off. These features (fence, wall and sloping road) are marked in Figure 38 and are also mentioned in Figure 25.

Figure 37: Road sign in the open case which caused brief NLOS conditions

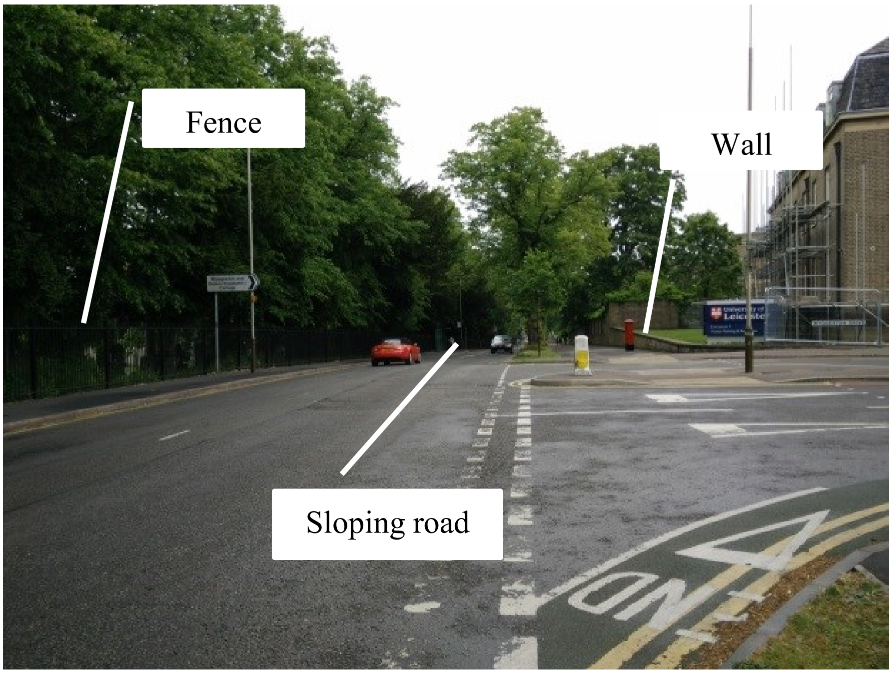

Figure 38: Centre of the intersection in the open case - shows where the road sign is placed

In this case the transmitter was kept on the middle of a four lane road which only had the two inner lanes open for most of the time. The transmitter was 46 m away from the centre of the intersection for all the data collected and the receiver was moved along two paths in this case as shown in Figure 25 – the adjacent path (same side of the road as the transmitter) and the opposite path (on the other side of the road from the transmitter). Both paths were on the pavement instead of being on the road and $\Delta d = 20$ cm.

The traffic in this case was the fastest as data was collected next to a public road – University Road. There were also a higher occurrence of larger vehicles which used this road such as busses and trucks. No attempt was made to record any traffic data as this was too complicated to do along with running the equipment. However, it was noticed that whenever busses passed by there was a change in the signal width caused by Doppler spreads. In both the other cases data was collected until the PDR consistently dropped to single digits if not zero. In this case data collection was stopped before that; 40 m on the opposite path and at 70 m on the adjacent path. There was a mix of LOS and NLOS conditions on both paths with data being collected over 10 m into the NLOS region in the opposite path and over 50 m into the NLOS region of the adjacent path.

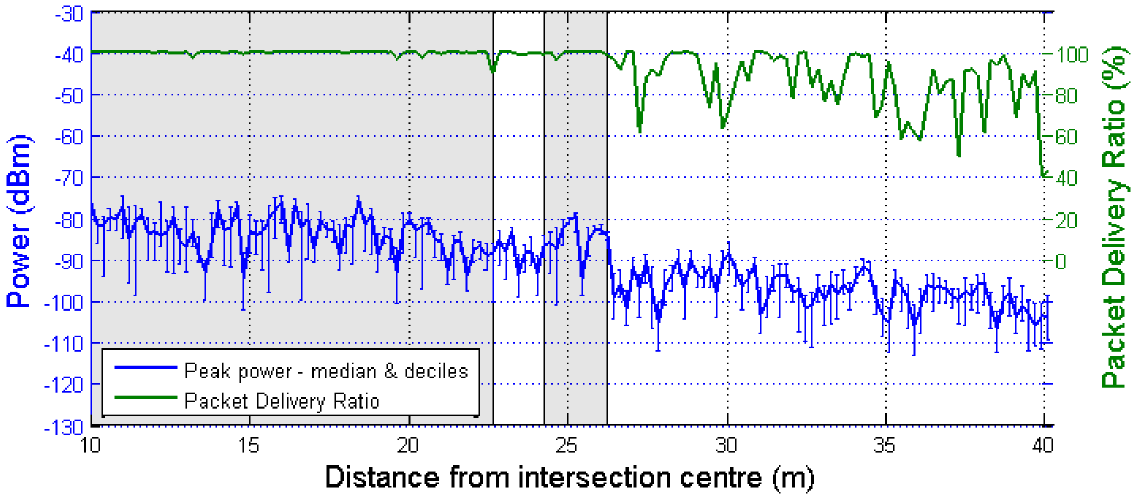

Figure 39: Median peak power and packet delivery ratio when the receiver was on the opposite path of the open case

Figure 39 displays the PDR and MPP for the data collected in the opposite path of this case with the shaded parts of the graph denoting where LOS communications existed. All the data was collected in one attempt and the receiver was always 5 m away from the centre of the road. The short NLOS portion seen just before 25 m is caused by the road sign mentioned previously.

The PDR is unaffected by the sign causing NLOS communications; the sign seemed to be mostly made of plastic. The first significant drop in PDR happens at 27.2 m where it drops approximately 40% over 0.20 m. From 27.2 m onwards there is considerable fluctuation in the PDR and it swings between 100% and 60% for the majority of the rest of the data collected until the last two points, where it drops to 40%. It can be said that until 40 m there is an acceptable level of communications even though after 27 m it might not be suitable for safety critical operations.

The MPP decays slowly and is mixed with fading. There is also considerable variation of the MPP at each point as displayed by the long error bars which denote the upper and lower deciles. The LOS region after the road sign (about 25 m) encompasses some interesting MPP data; the MPP appears to rise (by approximately 5 dB) compared to the data on either side (NLOS conditions) of that LOS region. Even though this would be expected, it also appears that the MPP in this LOS region is marginally higher than that of the data in the LOS region just before the road sign – between 20 and 22.60 m. This region also contains positions where the variation is very low compared to all the other data collected in the opposite path. Both these occurrences could either be due to the variable conditions in the environment (such as a dip in vehicular traffic) being favourable to the communications or an improvement due to the geometry of the environment causing multipath propagation which has increased the received power; propagation modelling would provide an answer.

Figure 40 displays a combination of all the data collected in the adjacent path; this path also runs on University Road but is on the same side of the road as the transmitter. NLOS conditions are reached earlier in this path compared to the opposite path and in this path the data collection extends a lot further, up to 70.80 m, in comparison to the 40.00 m in the opposite path. The receiver was kept on a line parallel to the centre of the road and 8 m away from it.

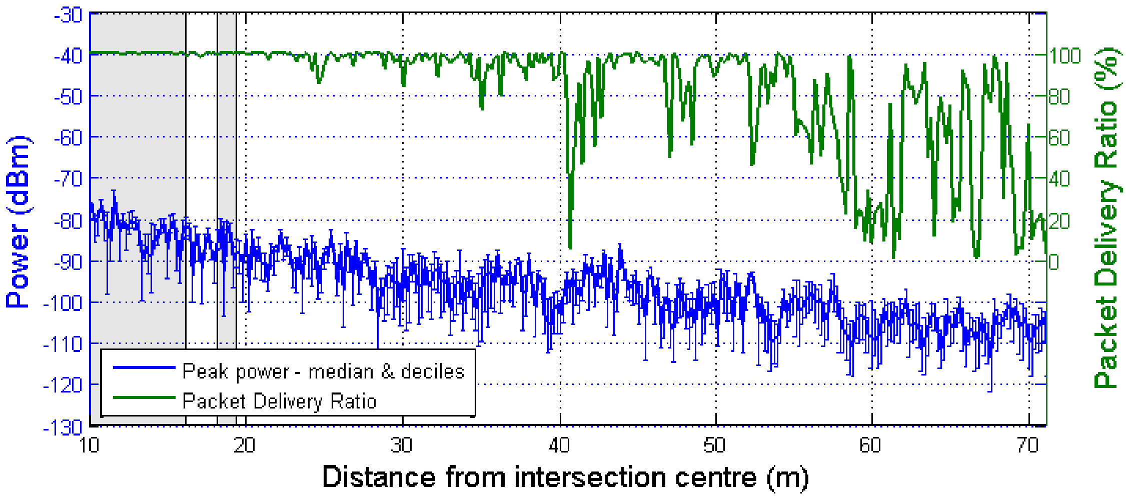

Figure 40: Median peak power and packet delivery ratio when the receiving station was on the adjacent path - different runs combined to get one line for the PDR and MPP

The lines on Figure 41 are from all the data collected in the range 0 – 40 m in the open case – both sides of the road. The grey and green shaded areas represent the LOS regions in the opposite path and the adjacent path respectively. The black lines are used to represent the data collected in the opposite path while the blue, red and green lines display data collected in the adjacent path, hence making it possible to compare the data on either side of the road.

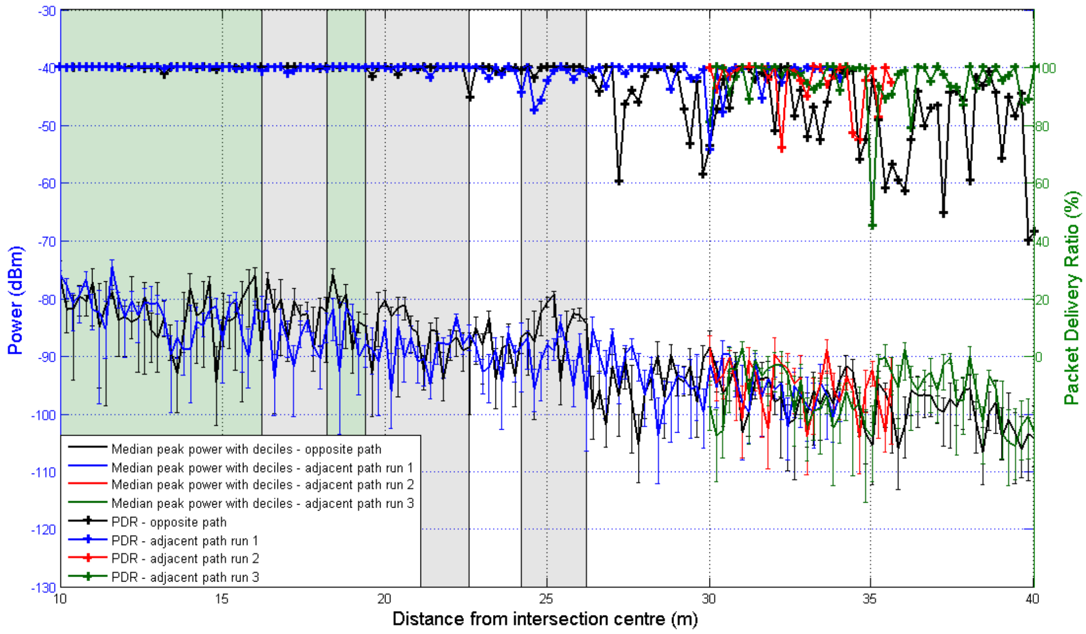

Figure 41: MPP and PDR for data collected on both paths in the open case up to 40 m

An important observation is that despite there being 13 m between the two paths (Figure 25), the MPP (of both paths) is very similar to each other closer to the intersection centre. At 13.80 m the MPP of the opposite path is significantly higher and stays higher for most of the distances until 26.20 m. It cannot be argued that this increased power is due to the opposite path maintaining LOS conditions for most of the distances until 26.20 m; the opposite path has higher power in most positions where both paths have the same conditions, LOS or NLOS. In the region after 26.20 m, where both paths have NLOS conditions, the opposite path's MPP is less than that of the adjacent path's for a short while before rising above it and then mixing with the MPP of the different measurement runs.

The region $30.0 \leq d \leq 34.0$ m shows 3 runs from the adjacent path as opposed to the single run from the opposite path. In this region, the opposite path's MPP is not consistently lower than the other measurements. There are positions where it has the lowest power out of the four lines but there are also a significant proportion of positions where data collected on the adjacent path have lower MPP values, despite being closer to the transmitter. Between 35.00 and 40.00 m the opposite path's MPP is consistently lower than the MPP of data collected in the adjacent path; with a handful of exceptions.

The cause for the opposite path's MPP to be greater for such a significant proportion is not clear. It is expected that the opposite path would naturally have a lower MPP because it is both further away from the transmitter and also because there is a road between the transmitter and the receiver which had vehicles. These vehicles are expected to block the CW and hence reduce the MPP in the opposite path whilst also assisting propagation in the adjacent path by reflecting the CW off them and towards the receiving equipment. However this does not seem to be the case. There could be two factors why the MPP is higher than expected in the opposite path. One of these factors could be that the metal bars which make the fence next to the opposite path reflects some waves back towards the receiver. The other reason could be that the required diffraction angle (off the edge of the building AC in Figure 25) to reach the opposite path is less than the required diffraction angle to when the receiver is on the adjacent path; hence enabling more waves to reach further down the opposite path and increase coverage.

The MPP in both paths appear to start and end at similar values; starting in the range [-80, -70] dBm and then reaching the interval [-110, -100] dBm at 40 m. In the opposite path a significant drop is noticed when the receiving equipment moves from the LOS to NLOS conditions. The variation of the data in the adjacent path (Figure 40) in the interval $30.0 \leq d \leq 36.0$ m appears to be high and this is caused by multiple (3) measurement runs being combined in that interval.

In comparison with the data collected in the opposite path, the PDR for the data in the adjacent path remains above 80% in the interval $10.0 \leq d \leq 40.0$ m apart from six instances where there are dips; most of them still greater than 70% with one going down to 45%. This is unlike in the opposite path where the PDR started swinging between 60% and 100% after 27 m and then drops down to 40% at 39.80 m.

Moving past 40 m in Figure 40 the PDR starts to show signs of not being able to maintain reliable communications; it drops down to 5% at 40.60 m and regularly drops below 80%. This trend of the PDR dropping continues until the interval $55.0 \leq d \leq 61.60$ m, during which it appears that the system has an inherently low PDR with a few regular spikes boosting it. After 61.80 m the PDR swings through its entire range for the rest of the data collected.

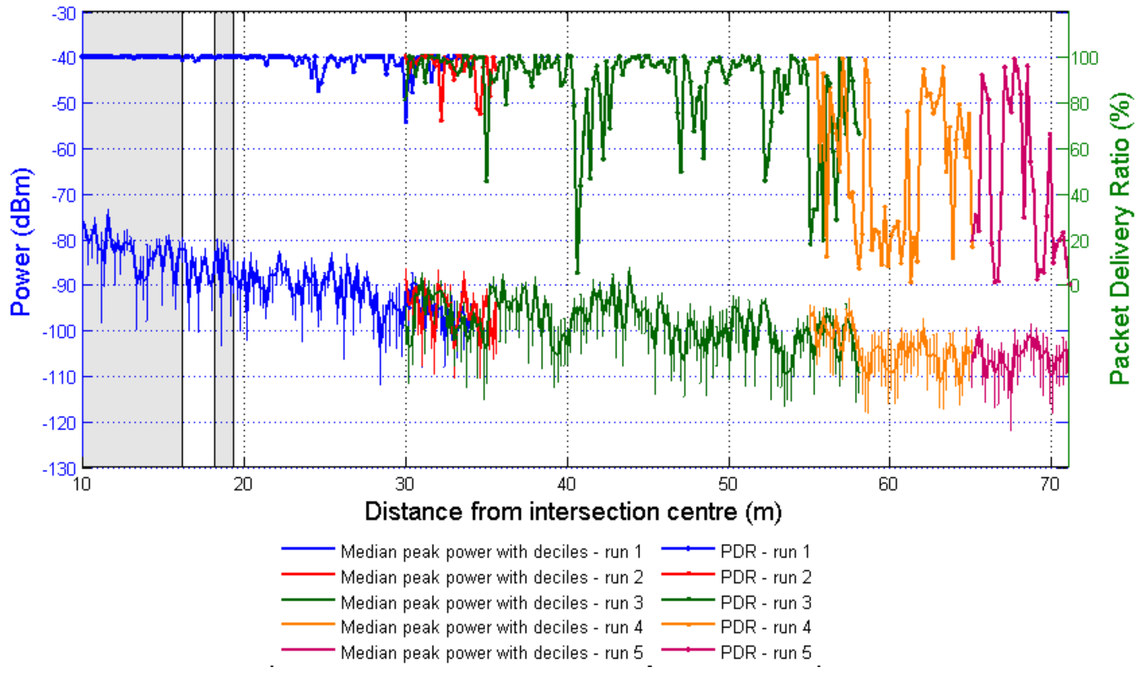

Figure 42: MPP and PDR of all the individual runs in the adjacent path of the open case

The MPP in Figure 40 increases after 40.00 m whilst the PDR does the opposite. Judging by the MPP data the region around 39.40 m is unfavourable for communications but the PDR data is contradictory. The MPP continues its slow and extremely variable decay until the end of the measurement; after 57.60 m the MPP decays even slower and remains in the interval [-110, -100] dBm for the next 13.40 m.

Figure 42 displays the MPP and PDR for all the separate runs made in the adjacent path, which have been combined to create the lines in Figure 40. There are only two short intervals where the different data runs overlap each other; $30.0 \leq d \leq 35.8$ m and $55.0 \leq d \leq 58.00$ m.

In the first overlap region there are three runs overlapping each other for most of the time and then two sets of lines. The shortest line which goes from $30.0 \leq d \leq 35.60$ m is from a run which had to be cancelled due to the batteries dying soon afterwards. Despite the MPP lines being within 10 dBm (and also in the range [-100, -90] dBm) for most of the time, they do not always appear to rise or fall synchronously. However, when there are three lines, more often than not there are two lines with extremely similar values of MPP. After 34 m the (only) two lines rise and fall synchronously for a couple of points before appearing to go completely out of sync for the rest of their overlapping range. All this variation can be attributed to varying propagation conditions on the different days and shows the scale of variation possible at the same location but at different days and times.

The PDR does not vary much between the three lines as well. There are a few positions where the PDR drops below 90% but for most of the time it is between 90% and 100%. Beyond 34 m, when there are only two runs, the PDR is not similar for most of the positions. It is believed that propagation conditions were significantly different on the days that these two sets of data was collected, hence the noticeable differences in both PDR and MPP. The PDR difference at 35 m is approximately 50% which is very significant and would not be able to support reliable vehicular communications.

The second overlap region between runs in the adjacent path is 3 m long. The MPP data measured in run 4 appears to be similar to run 3, but with a 0.20 m lag. The MPP values seem most closely linked, with the difference between them being less than 10 dB apart from at 55.20 m. The PDR values seem fairly different, but they rise and fall together most of the time; this is also if run 4 is shifted to the left by 0.20 m. It is highly improbable that the receiving equipment was placed wrongly along the path as the path was always marked; especially at the end of each run so that the next run's starting point is easy to find. Based on this, the only explanation available for this apparent shift in MPP and PDR is that the radio channel or the propagation environment must have altered in between the two sets of data being collected.

4.3 Relationship between the PDR and MPP

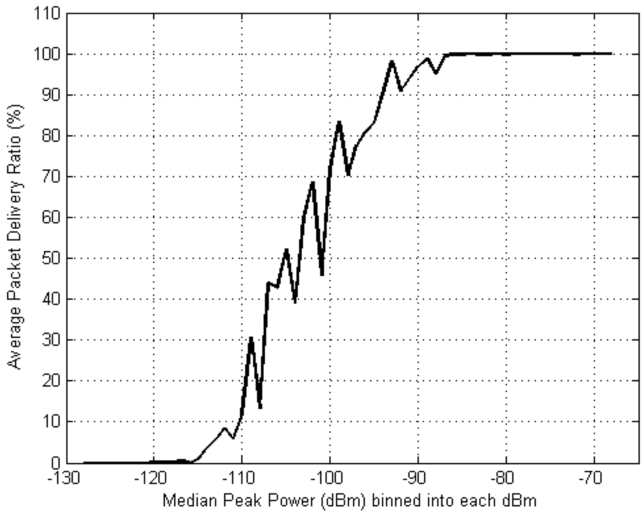

Figure 43: Plot showing the relationship between the average PDR and MPP for all the data collected. The MPP is binned into whole numbers

Figure 43 shows how the PDR varies with the MPP for all the data collected. The MPP has been binned every dBm and the mean PDR at each bin is plotted. When MPP > -90 dBm the PDR is highly likely to support safety critical applications. There is a transition region when -110 < MPP < -90. The network can be used for data transfer in this region but safety critical features will not perform as efficiently. In the region MPP < -110 dBm the network cannot be used at all. This conforms with the IEEE 802.11p standard (IEEE 2012).

4.4 Conclusions

To conclude this chapter, the data collection rig described in Chapter 3 was used to gather data at three junctions which presented different propagation environments; a narrow T-junction with pedestrian-only traffic during data collection, an open roundabout where NLOS conditions started very close to the centre of the roundabout and a very open T-junction which was a public road and had relatively fast moving traffic. The data was collected with very high distance accuracy and resolution (every 20 cm) which is unique to this study. Another unique aspect of the data collected is the combination between the measurement rig and the focus on the environment (T-junctions). Data collection was focussed on NLOS conditions which are where vehicular networking is required to increase driver awareness beyond what he or she can see.

The collected data showed the difference in how the median peak power and packet delivery ratio degraded at each junction as the receiving equipment was moved further away from the centre of the junction. This data shows the distances at which vehicular networks would operate reliably for safety critical messages in similar environments, which in turn can be useful in network planning.

In the urban case it was seen that pedestrians increase the variation in the peak power in a path with fewer buildings. This is because there are fewer rays being received (due to fewer buildings to reflect waves) compared to an urban canyon. If there are fewer rays being received while the number of rays reflected off a pedestrian remains constant on either side of the intersection, then the proportion of rays being influenced by a pedestrian increases. At the receiver this causes higher variation as the waves combine constructively or destructively depending on their phases.

In the less urban case it was noticed that the MPP with the transmitter 50 m away from the intersection centre was less than the MPP when the transmitter was 70 m away for a significant number of positions from which the data was collected from. In this case the main difference between the data collected with different transmitter positions was that the PDR dropped to 0% earlier when the transmitter was further away.

The open case has the best PDR performance furthest from the intersection centre. The urban case had its PDR drop to zero at least once by 40 m from the centre of the intersection and this happened on both sides of the intersection. In the less urban case the PDR was in single digits long before the receiving equipment was 40 m away from the intersection.

However, the emphasis of the analysis should be on the performance of the data network in the NLOS region and if the NLOS region (in the open case) caused by the sign is ignored, data collected from 26.20 m onwards in the opposite path are in NLOS conditions which provides 13.80 m of data collected in NLOS conditions. Throughout this 13.80 m the PDR lies between 60% and 100% (Figure 39) for most of the times. If this is compared with the data collected on either side of the T-junction in the urban case (shown in Figure 29), the NLOS region starts at -3.23 m on the urban canyon portion and at 3.06 m on the open part, and 13.80 m into the NLOS regions would be at -17.03 m and 16.86 m. The PDR only fluctuates between 80% and 100% with the exception of a dip below 60% at 16 m. One of the main factors behind this improved PDR can be due to the transmitter being 22 m closer to the intersection centre. But if the total distance that the radio wave has propagated along both streets is considered, at the point of NLOS conditions starting in the open case the waves have to propagate 46.00 m to the centre of the intersection and then a further 26.20 m, adding up to 72.60 m. At the equivalent point in the urban case (48.60 m away from the intersection) the PDR is almost zero and cannot reliably support an 802.11p network.

The data can also assist in finding out the speed at which a vehicle can travel at and also stop safely if it gets to know of an oncoming vehicle which might need to pass straight through, such as an emergency services vehicle. Figure 44 from the Highway Code (Department of Transport n.d.) shows the typical stopping distances for different speeds.

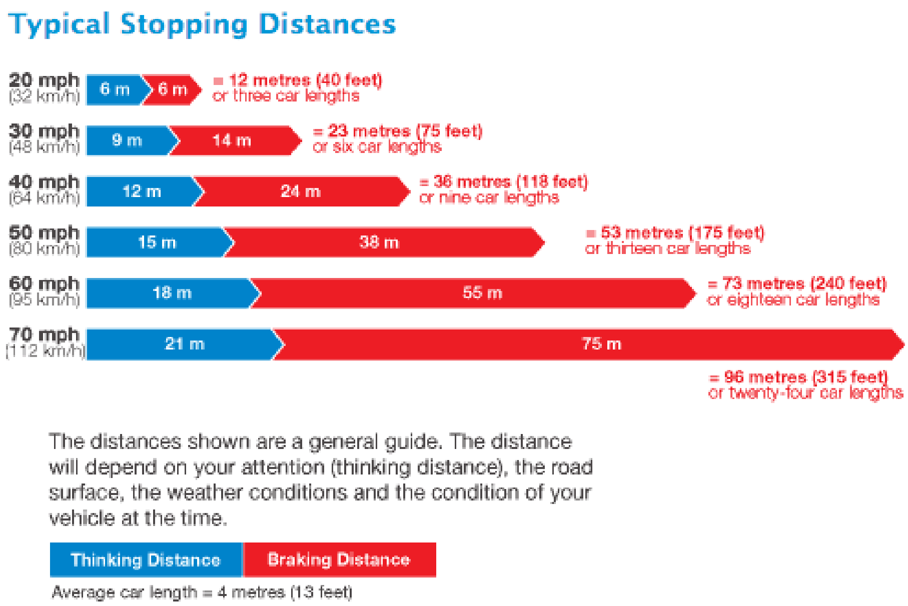

Figure 44: Stopping distances at different speeds according to the highway-code (Department of Transport n.d.)

Table 11 shows the maximum distance along each path where the PDR is above 90% and can therefore be used by safety critical messages. The table also shows the speeds that a car can be travelling at, if it is to be able to stop by the junction. The less urban case is not used in this table because the PDR on all its paths were not consistently above 90% for far enough.

Case and Path	**Critical Usage Distance (m)**	**Maximum Potential Speed**
Urban case – built up path	21.00	Less than 30 mph (48 km/h)
Urban case – open path	15.00	Less than 20 mph (32 km/h)
Open case – opposite path	27.00	Less than 30 mph (48 km/h)
Open case – adjacent path	24.40	Less than 30 mph (48 km/h)

Table 11: Table showing the distances along each path (of the urban and open case) up to which the PDR can support safety critical systems. The table also shows the maximum potential speed a vehicle can travel at when it enters this high PDR zone.

The maximum potential speed is approximated depending on the speeds and distances available in Figure 44. It is also dependent on the distance between the transmitter and the intersection centre. If the transmitter was closer the distance would increase and hence increase the maximum potential speed. If the transmitting vehicle was too far beyond, like in the less urban case when the transmitter was 50 m away from the intersection, and if we assume that the receiving vehicle was 20 m away from the intersection centre. The receiving car can safely pass through the intersection unless the transmitting car is travelling at approximately 2.5 times the speed of the receiving car, which would mean they meet at the intersection simultaneously. In such a situation however the critical usage distance would be extended by the transmitting car moving towards the intersection centre which increases the chances of packet reception. However, to determine a maximum potential speed for the receiving car, more data will have to be collected with the transmitter moved gradually closer to the intersection centre.

In the urban case another observation was that the MPP closer to the intersection on both sides of the intersection were very similar when they were plotted against the distance that LOS conditions were lost. Further away from the intersection centre the difference in MPP started to show as the path with fewer buildings had a lower MPP than the path with buildings on both side. The PDR did not show similar patterns and started to drop earlier in the path with fewer buildings whilst it stayed high in the path with more buildings; despite corresponding MPP values being similar in both sides of the intersection. This implies an importance in the building geometry along with the MPP. The open case also displays how the propagation geometry affects the PDR as well as the MPP. The PDR in the open case does not drop below 40% despite the MPP being less than -90 dBm and in the urban case this was not observed. Having wider roads and no buildings on the edge of the intersection in the open case has assisted vehicular communications; the angles that the waves have to diffract (off the corners of buildings surrounding the intersections) to get from the transmitter to the receiver are smaller in the open case.

5 Comparison of Observations of Signal Strength with Prediction

In this section the data collected using the dual measurement system will be compared against predictions from the model virtualsource11p (Mangel et al. 2011).

There is more information about this model in the Literature Review chapter (Section 2.1.2.2). The ITU also has a model to predict the path loss in this frequency range. However, it has not been tested at 5.9 GHz and the authors of virtualsource11p have shown how their model is more accurate at predicting the path loss in the DSRC band (compared to the ITU model and various other models). Because of this high prediction accuracy in comparison to the other models, the collected data will only be compared against predictions produced using the virtualsource11p model.

The equation of this model is Equation (7) and Figure 45 shows the geometry related parameters. λ and d_b are the wavelength and breakpoint distances (≈ 180 m) respectively while i_s is the sub-urban loss factor (0/1 for urban/suburban conditions).

$$\begin{aligned} &virtualsource11p(d_r, d_t\, w_r, x_t, i_s) \\ &\quad = 3.75 + 2.94 i_s \\ &\quad + \begin{cases} 10\log_{10}\left(\left(\frac{d_t^{0.957}}{(x_t w_r)^{0.81}}\frac{4\pi d_r}{\lambda}\right)^{2.69}\right), & d_r \le d_b \\ 10\log_{10}\left(\left(\frac{d_t^{0.957}}{(x_t w_r)^{0.81}}\frac{4\pi d_r^2}{\lambda}\right)^{2.69}\right), & d_r > d_b \end{cases} \end{aligned} \tag{7}$$

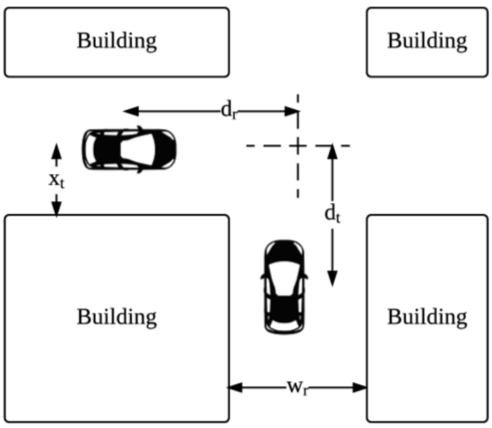

Figure 45: Geometric parameters used in the virtualsource11p model

5.1 Comparisons for the Data Collected in the Urban Case

Figure 46 to Figure 51 display graphs of the median peak power (MPP) with deciles (solid lines with error bars) for all the data collected in the urban case along with the prediction given by the model virtualsource11p (dashed lines). The shaded areas in each graph denote the areas of LOS communications conditions.

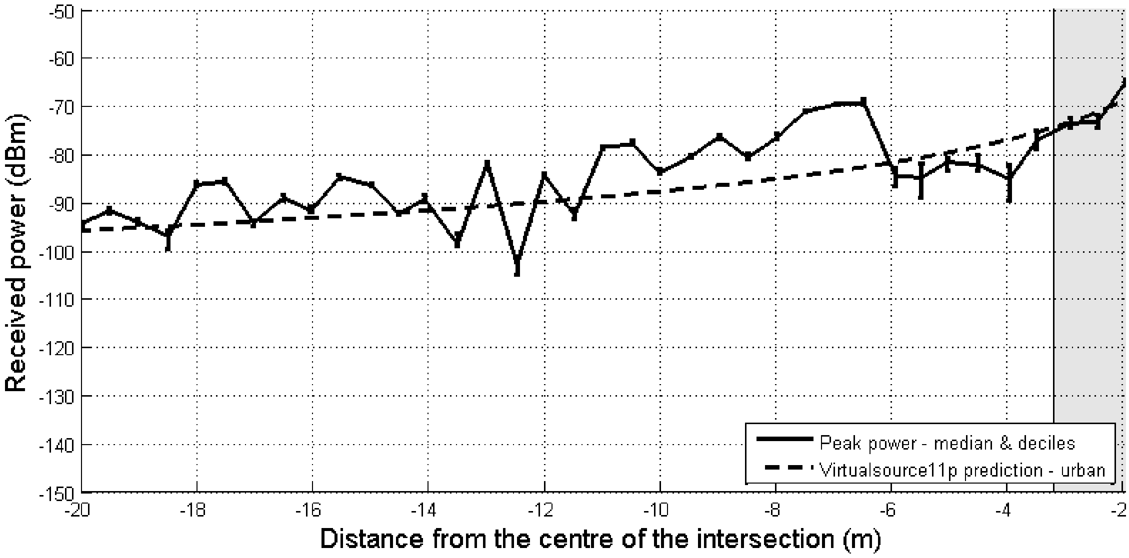

Figure 46: MPP with deciles and received power predicted using virtualsource11p; run 1 in the urban case

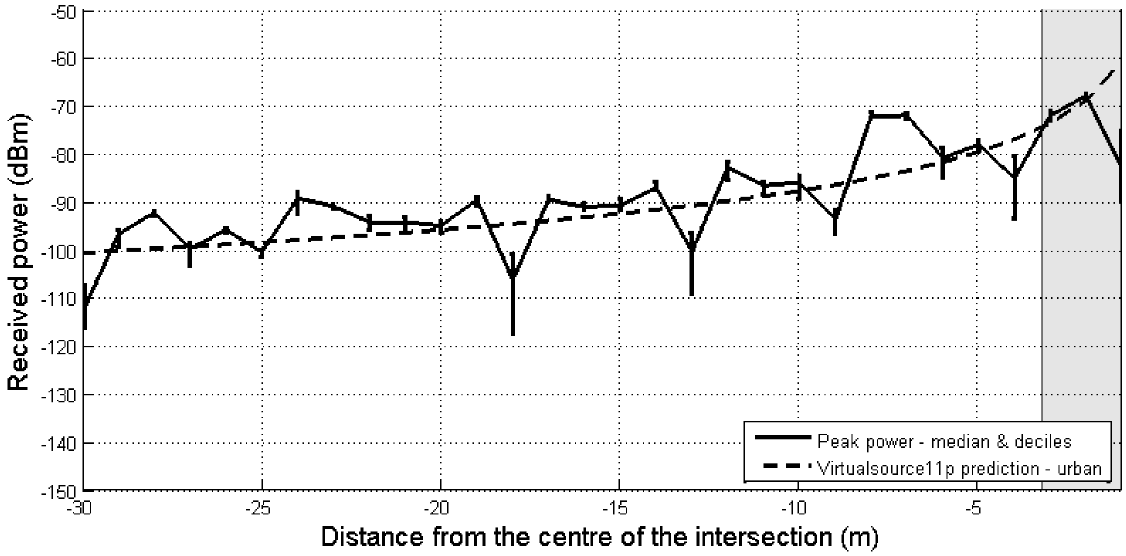

Figure 47: MPP with deciles and received power predicted using virtualsource11p; run 2 in the urban case

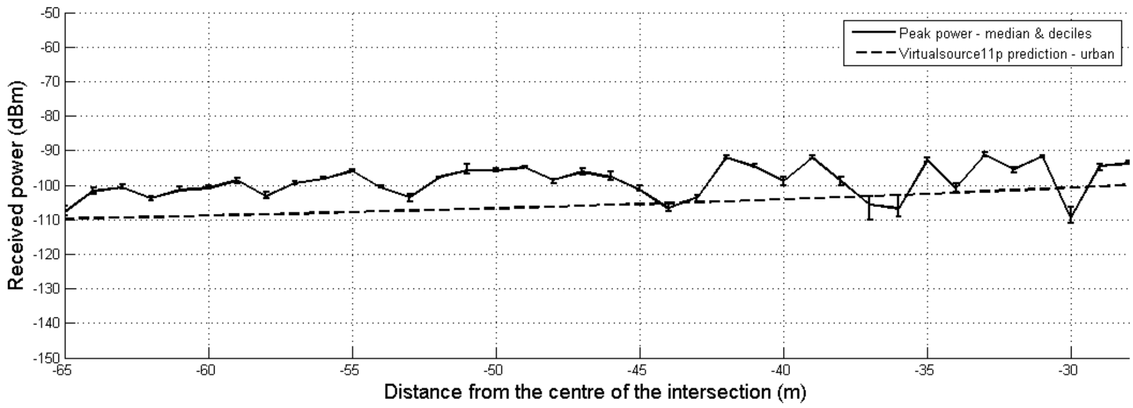

Figure 48: MPP with deciles and received power predicted using virtualsource11p; run 3 in the urban case

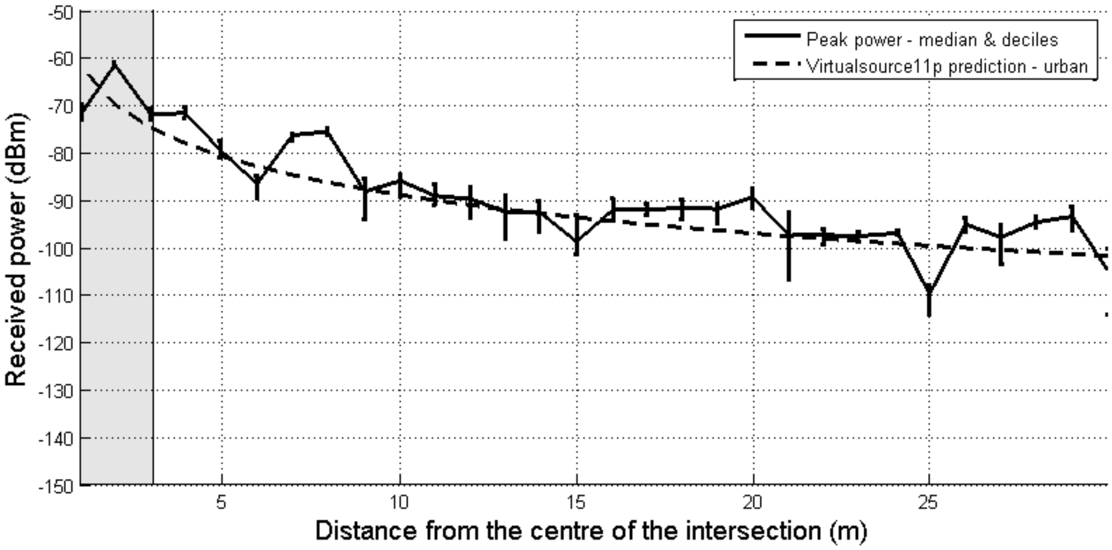

Figure 49: MPP with deciles and received power predicted using virtualsource11p; run 4 in the urban case

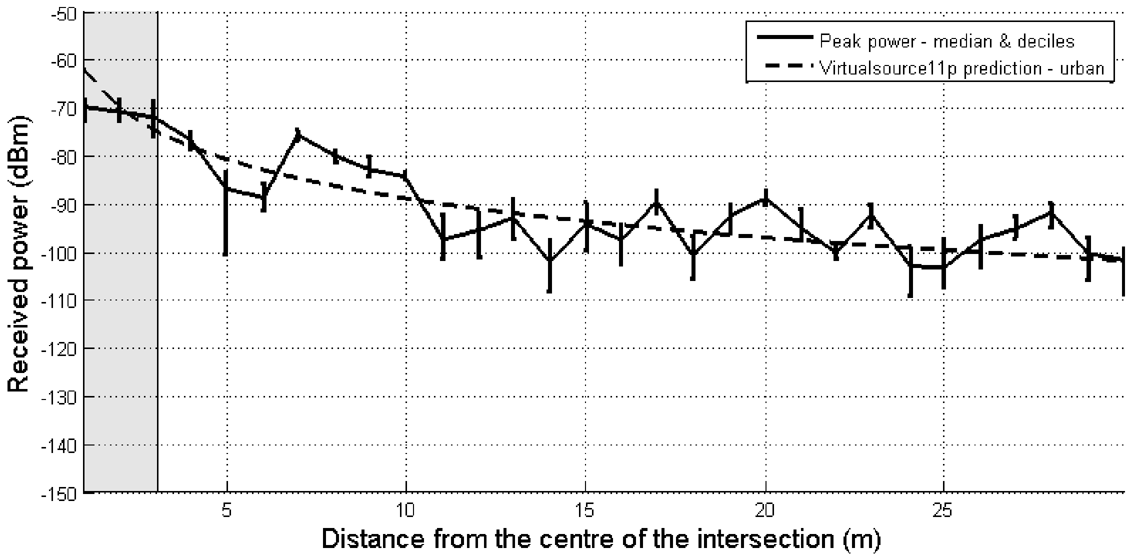

Figure 50: MPP with deciles and received power predicted using virtualsource11p; run 5 in the urban case

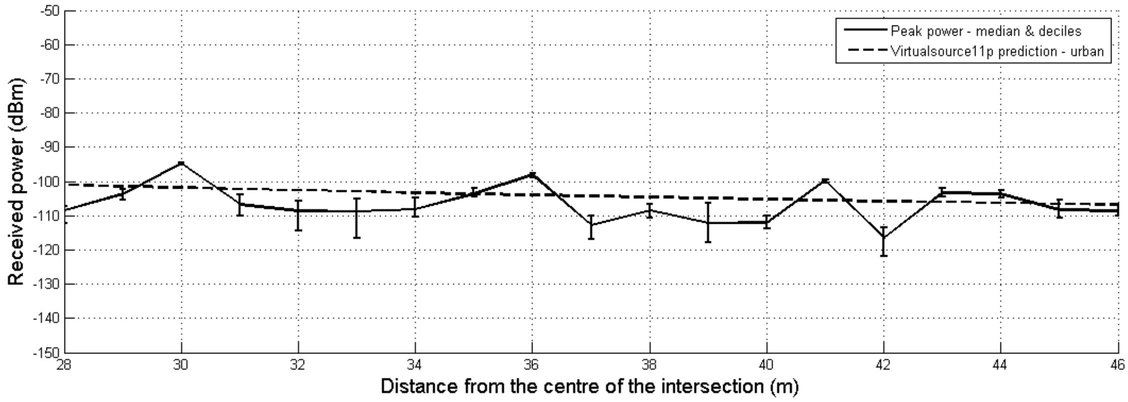

Figure 51: MPP with deciles and received power predicted using virtualsource11p; run 6 in the urban case

The graphs show good fit with the model when the path loss is predicted for urban locations. This is despite the variation at each position (shown by the error bars) and also the varying nature of the signal decay.

Measurement Run	Distance Range (m)	Median Error, E_m (dB)	Figure
1	$-20 \le d \le -2$	4	Figure 46
2	$-30 \le d \le -1$	2	Figure 47
3	$-65 \le d \le -28$	8	Figure 48
4	$1 \le d \le 30$	0	Figure 49
5	$1 \le d \le 30$	-1	Figure 50
6	$28 \le d \le 46$	-6	Figure 51

Table 12: Median error and distance range for each run in the urban case

Table 12 shows the median error (E_m = median(MPP – virtualsource11p prediction)) and the distance range for each of the runs in the urban case. There is a significant difference in E_m between the data collected closer to the intersection (runs 1, 2 4 and 5) in comparison to the runs which contain data from further away from the intersection (runs 3 and 6). It is also interesting to see that in general, E_m for the runs which were in the urban canyon portion of the urban case (runs 1, 2 and 3) are higher than those from the runs (with corresponding distances) in the more open part of the urban case (runs 4, 5 and 6). A very strong reason for this higher E_m on the urban canyon side could be due to the increased multipath propagation causing fades of larger magnitude, which causes the received power to vary more along the path (Figure 47). The largest error was in Run 3 (Figure 48) which was further away from the intersection centre and a continuation of Runs 1 and 2, into a part of the street which had fewer buildings on either side. There is a systematic difference between the collected data and the prediction which contributes towards the relatively large E_m value.

5.2 Comparisons for the Data Collected in the Less Urban Case

Figure 52 and Figure 53 show how the MPP of the data collected in the less urban case compares with the predictions provided by virtualsource11p. Figure 52 and Figure 53 have the transmitter placed 50 and 70 m away from the intersection centre respectively. In this case the model output was from the suburban mode as this was more accurate reflection of the experimental situation. However, there is still a significant difference between what the model has predicted and the observations.

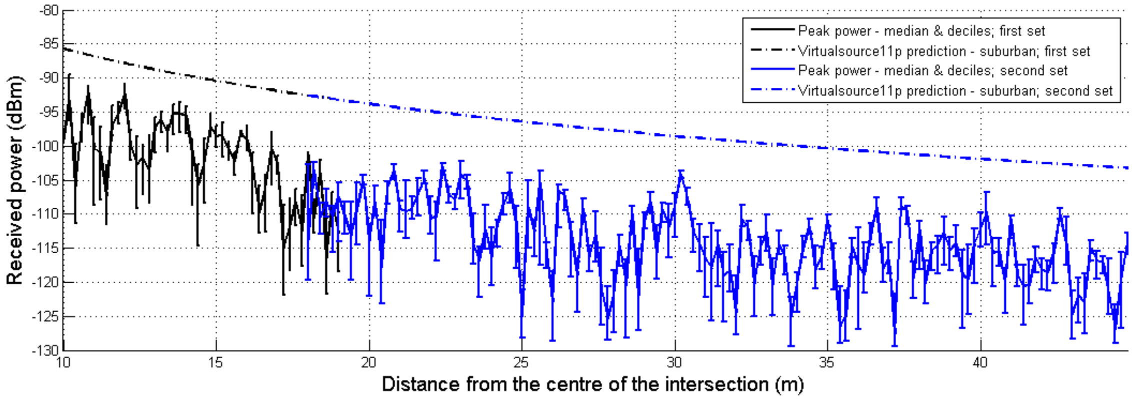

Figure 52: MPP with deciles and received power predicted using virtualsource11p; transmitter 50 m away from the intersection centre in the less urban case

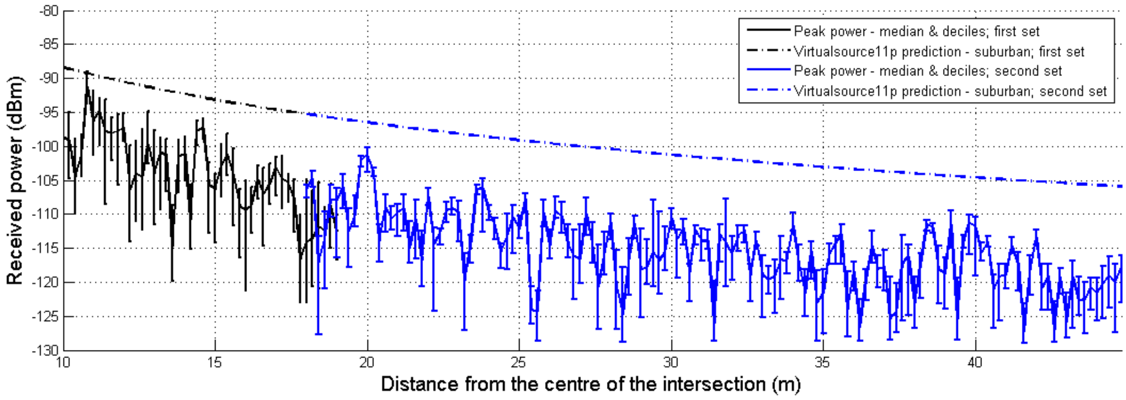

Figure 53: MPP with deciles and received power predicted using virtualsource11p; transmitter 70 m away from the intersection centre in the less urban case

Table 13 shows E_m for the data collected in the different runs at the less urban case and these values are very high compared to those from the urban case. The prediction is an overestimate and this is because virtualsource11p was derived with data collected in an urban environment. Such an environment would have more reflective surfaces which will increase the signal strength at the receiver because of more signals being reflected towards the receiver. Similar to data from the urban case, results are more consistent with observations for the predictions closer to the intersection.

Measurement Run	Distance Range (m)	Median Error, E_m (dB)	Figure
$T50_{NEAR}$	$10 \leq d \leq 19$	-11	Figure 52
$T50_{FAR}$	$18 \leq d \leq 45$	-15	Figure 52
$T70_{NEAR}$	$10 \leq d \leq 19$	-11	Figure 53
$T70_{FAR}$	$18 \leq d \leq 45$	-14	Figure 53

Table 13: Median error and distance range for each run in the less urban case

5.3 Comparisons for the Data Collected in the Open Case

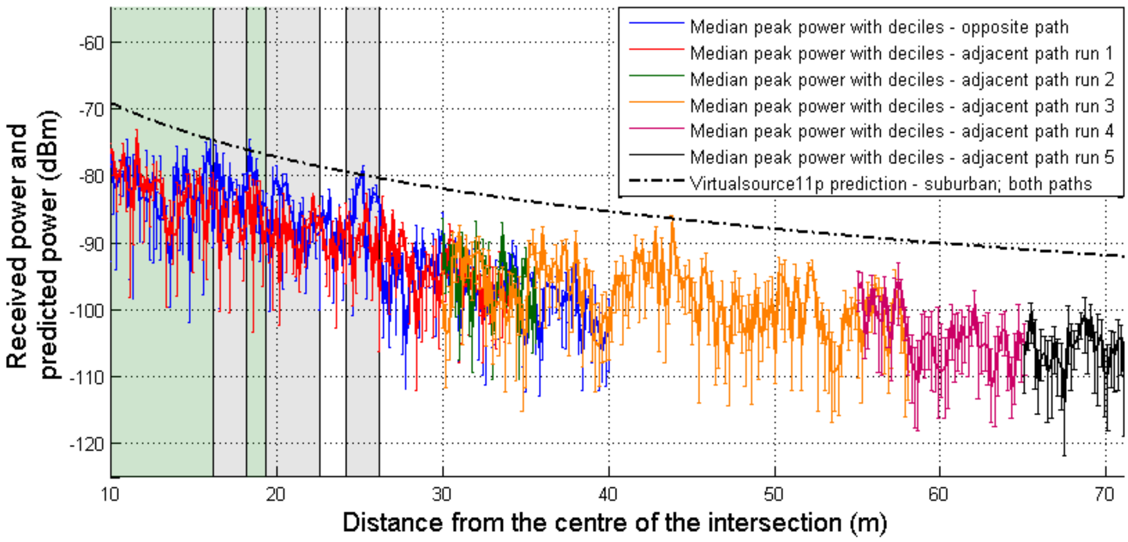

Figure 54: MPP with deciles and received power predicted using virtualsource11p for all the data collected in the open case

Figure 54 shows how the MPP for data collected in the open scenario compares with the predictions from virtualsource11p. The predictions were from using the model in suburban mode as the environment was very open and the predictions were also more accurate in this mode. There is a significant difference between the measured and the predicted data again, similar to the less urban case. The reason for this difference is the same as previously explained; there are fewer buildings to reflect signals towards the receiver.

Table 14 shows the E_m for data collected in the open case. These values are similar to some of the values seen in the less urban case.

Another recurrent observation is that the accuracy decreases for predictions further away from the intersection centre and this is seen in all the three cases.

Measurement Run	Distance Range (m)	Median Error, E_m (dB)
Opposite path	$10.0 \leq d \leq 40.0$	-11
Adjacent path run 1	$10.0 \leq d \leq 34.0$	-11
Adjacent path run 2	$30.0 \leq d \leq 35.6$	-12
Adjacent path run 3	$30.0 \leq d \leq 58.0$	-12
Adjacent path run 4	$55.0 \leq d \leq 64.8$	-14
Adjacent path run 5	$65.0 \leq d \leq 70.8$	-14

Table 14: Median error and distance range for each run in the open case

5.4 Assessment of the Model

The model produces results consistent with observations when used in an urban canyon and when the receiver is close to the intersection centre. The accuracy of predictions drops for distances further away from the intersection. The main weakness of the model was in environments where the receiver was not in an urban canyon despite being in NLOS conditions. In such environments the prediction from the model differed from the observation by more than -10 dB.

In Section 4.3 it was seen how the packet delivery ratio (PDR) goes from high to low once the MPP falls below -90 dBm. If network simulation software is to use virtualsource11p to predict the path loss and then the typical PDR, the value of the PDR would be overestimated in less urban and open cases.

In (Abbas et al. 2013) experiments were performed to validate the accuracy of virtualsource11p and despite these experiments performed in mobile vehicles the results showed that in some environments there is a significant difference between the predicted data and the measured valued. However in these experiments the model underestimated the signal strength.

If the model is to be used in environments such as the less urban or the open case, it would be useful to add an extra term to compensate for the lack of buildings in the environment.

There is also another solution to increase the accuracy of the predictions; a ray tracing model can be used which will provide more accurate predictions. Such a model will take into account the geometry of the environment in the ray casting process which will enhance the accuracy of the model. In addition to that, a ray tracing model will provide a better indication of the fading caused by all the multipath components – especially important in environments with multiple possibly mobile reflective surfaces. In the urban case it was seen how the MPP had deep fades and this can be accurately modelled using a ray tracing model. Delay and Doppler spreads can also be calculated more accurately using a ray tracing model; a ray tracing model is described in the next chapter.

6 Site Specific Ray Tracing Model for the Urban Case

6.1 Introduction

In the data collected in the urban case (Section 4.2.1) it was seen that the median peak power (MPP) in the urban canyon portion of the street was generally higher than the MPP in the open side of the intersection for corresponding distances. In this chapter a site specific ray tracing model is developed to consolidate the theory that the buildings in the urban canyon portion of the urban case contributed towards a higher MPP in comparison to the open portion of the intersection.

This model only deals with the geometry of the rays and does not deal with any power calculations – power can be incorporated into a more mature version of this model. Other enhancements which could increase the accuracy of the model would be the inclusion of diffraction, non-specular reflections, signal phase (calculated using the pathlength or randomly allocated) and tracing the rays in all three dimensions. These features could not be incorporated due to the lack of time.

6.2 Methodology and output

Figure 55 displays an overview of the different scripts used by the model and the information exchanged between them. The scripts are numbered according to their usage order. Scripts 1.0, 2.0 and 4.0 are the main scripts used to produce predictions whilst scripts 3.0, 5.0 and 6.0 are functions used by the main scripts. The rest of this section is a description of how the model works along with the assumptions made, limitations and scope for improvement

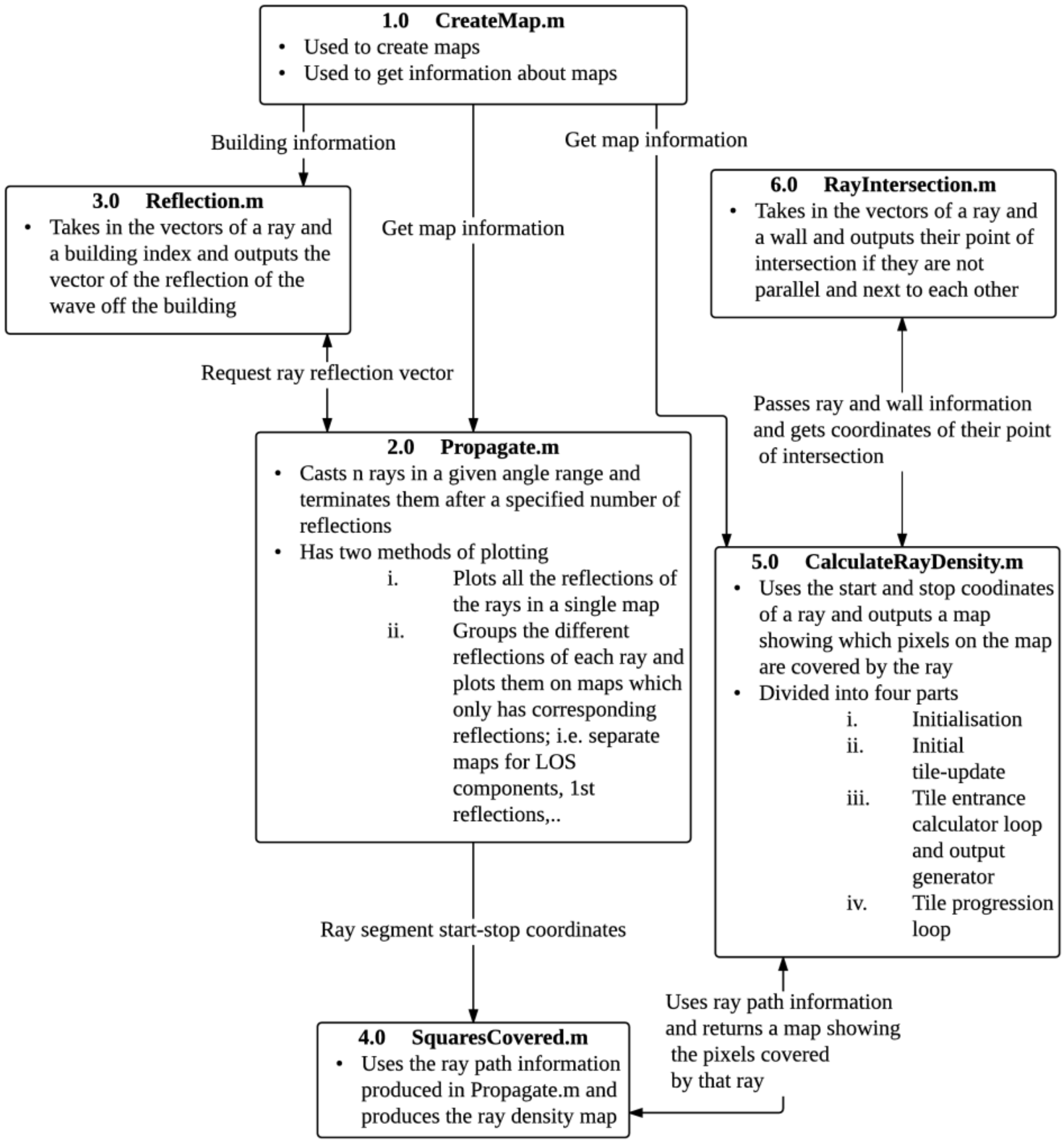

Figure 55: Overview of scripts used in the model and how they are related to each other

6.2.1 Maps

An assumption of the model is that all walls are flat surfaces perpendicular to the ground plane and majority of the relevant signals all propagate in the horizontal plane which contain the antennas. Based on this the model requires a 2-dimensional map on which the rays propagate; the map is in the form of a matrix where each element represents a point on the ground – similar to a grid or Cartesian coordinates. A building on the map is represented by an integer whilst a ‘0’ indicates that the point is not occupied by a building. Each building has its own integer assigned to identify which building is covering a certain point; the reason for this will be explained in

Section 6.2.2. A sample map containing a wall/building is shown in Figure 56 with its relevant matrix superimposed over it.

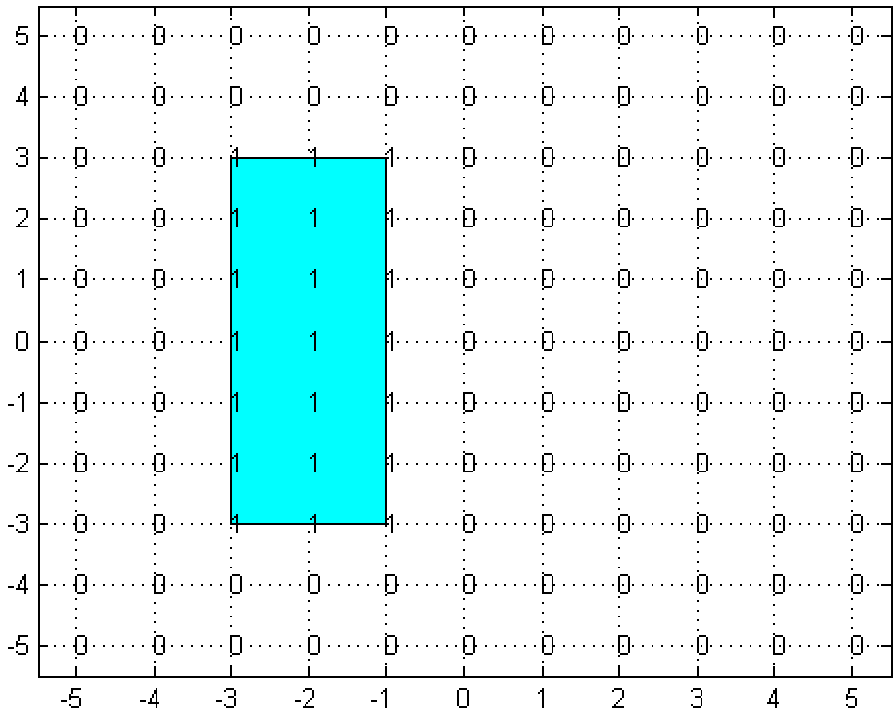

Figure 56: Example map showing a building represented by its building index matrices

The program *CreateMap* is used to display and create maps along with get information about individual buildings in the map. All this information has been previously input using drawings of the environment; the user can request a map using the map's reference number.

A flowchart of this function is shown in Figure 57. The function is called with two inputs; RequiredOutput and PlotRequirements whose purpose will be explained later as they become used. For each map, the number of buildings it contains is stored and the coordinates of the vertices of each building in each map is stored in a structure. If RequiredOutput is 0, then the output of the function is the coordinates of the building vertices of the building with the same ID as PlotRequirements; this is how other functions will obtain the coordinates of an individual building's vertices.

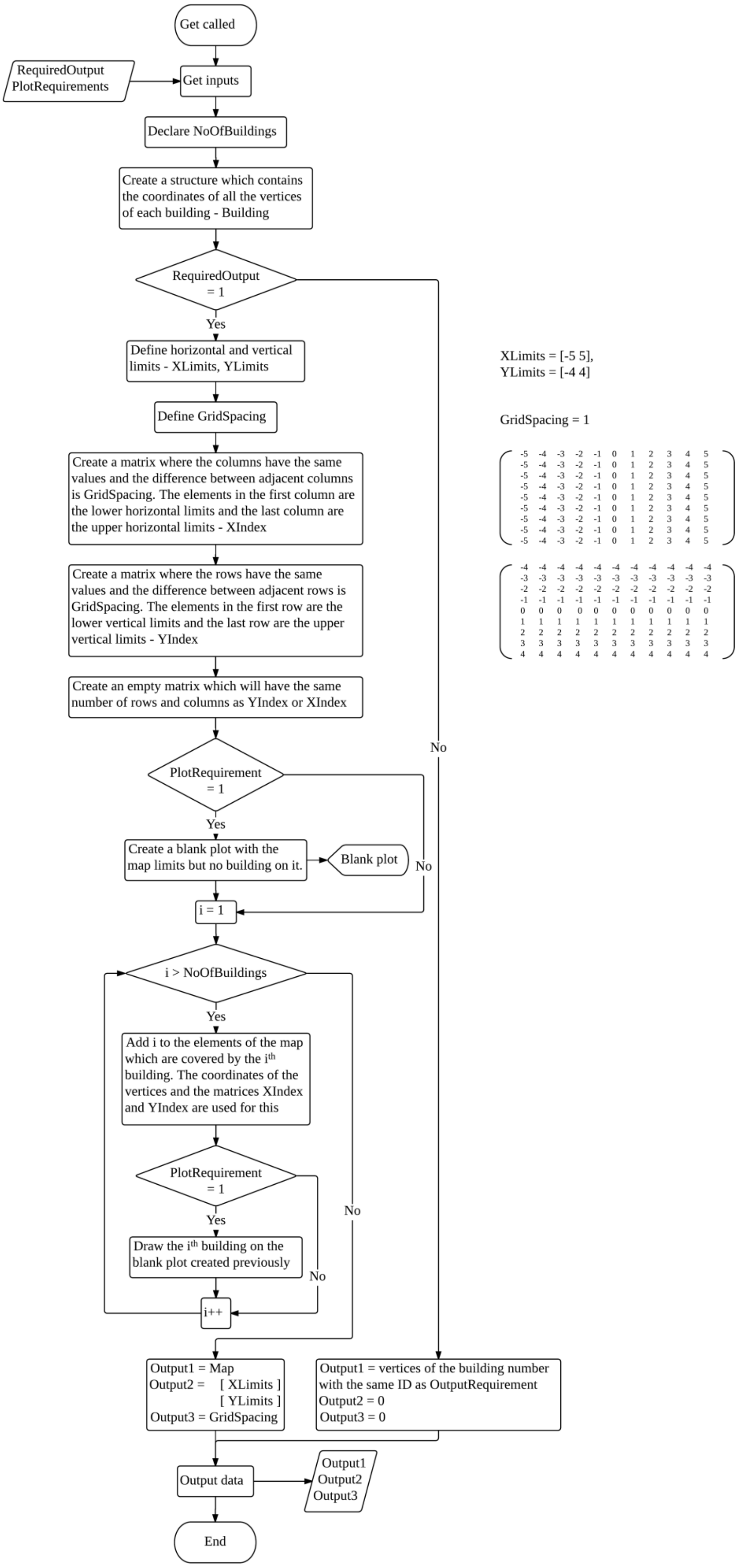

Figure 57: Flowchart of the function CreateMap.m

If the RequiredOutput is 0, then the output of the function is the matrix which describes the map, the x and y limits of the map and the size of the grid; GridSpacing. The Limits and Gridspacing are stored in the program but the map matrix creation requires going through all the building information. Two matrices are first made; XIndex and YIndex. Examples of these matrices are in the flowchart next to the actions that create them. The next step is to create a matrix the same size as XIndex or YIndex which will have all its elements set to 0; this will be the matrix which will have information about the map and is called Map.

If PlotRequirement is 1, then the map will be produced on screen after creation. At this stage a blank map is displayed and the buildings are added individually. To find which elements are covered by a building, XIndex and YIndex are used along with the coordinates bounding a building. A matrix the size of XIndex is made where each of the columns bound by the building's x-coordinates are 1, and the rest of the columns are 0. A similar process is performed to the y-coordinates using YIndex; where the rows which fall within a building's y-coordinates are set to 1 with the rest of the matrix being 0. Each of the corresponding elements from both these matrices are then multiplied with each other to obtain the elements which are bound by the building. This resulting matrix is then multiplied by the building ID and added to the map matrix; multiplying by the building ID enables identifying which building is covering a group of. This process is repeated for all the buildings and as the OutputRequirement was set to 0, the completed matrix, x and y limits and the spacing of the grid is output.

This method of map creation works in the urban case as the buildings are all modelled as rectangles which are not next to each other. However for a more universal approach, if buildings are next to each other or if they are not rectangular, a check will have to be performed before the matrices of each building are added. This will prevent the addition of building indices from different buildings which will occupy the same map matrix element.

For simplicity each map is designed with the transmitter's coordinates in mind and the transmitter always has the coordinates (0, 0). This will be changed when the model is to be used for multiple transmitters which could be mobile.

6.2.2 Propagation of Waves

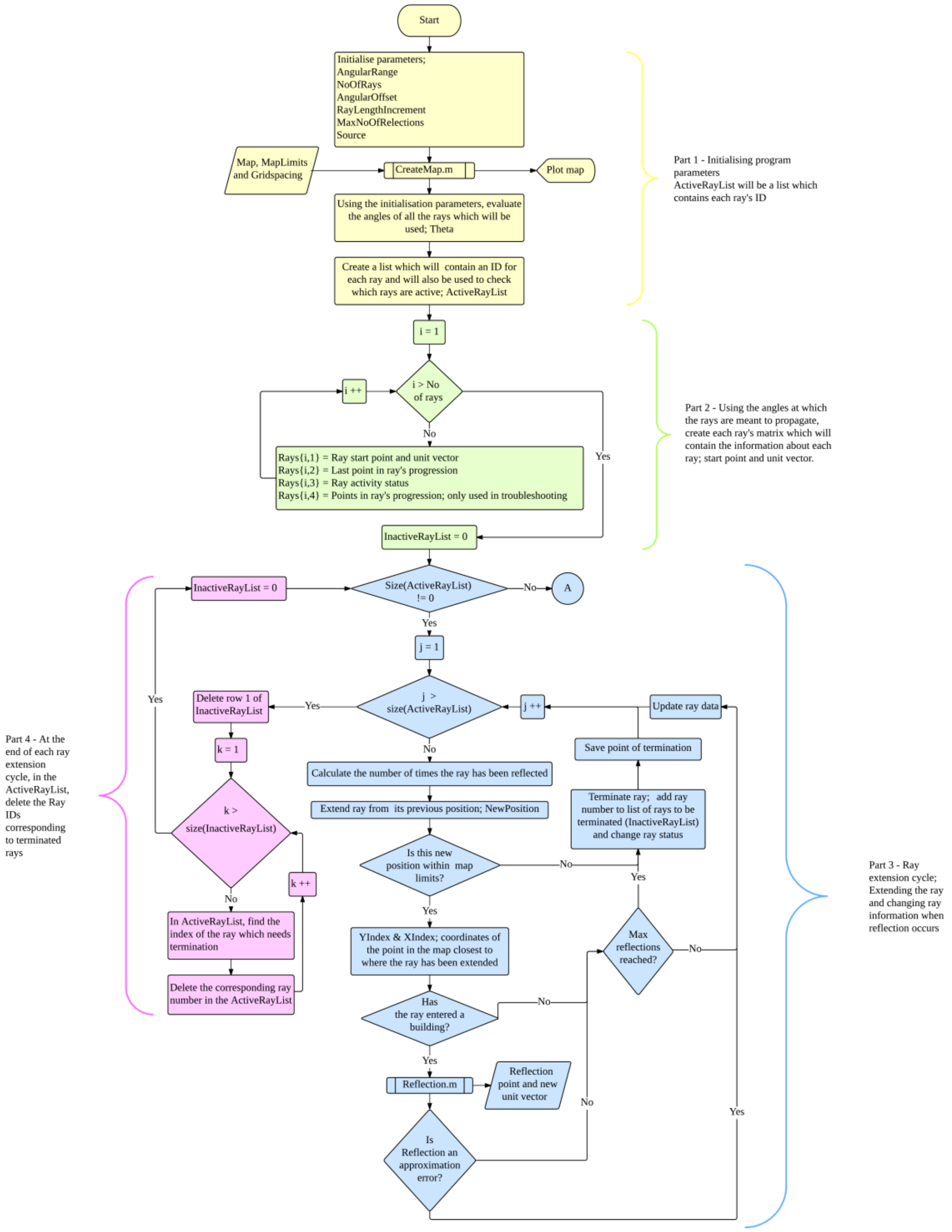

Figure 58: Flowchart for the program Propagate.m

The program *Propagate.m* is the main program which casts the rays onto the map (described in the last section) and a flowchart for this is presented in Figure 58. The ray propagation is done by first assuming the transmitter is a point source. The user can specify how many rays should be cast and the range of angles (where 0º is parallel with the vector $\boldsymbol{i}$) the rays should be cast in. For example, the user can state that he/she wants 1000 rays with all of them propagating in the range of 60º to 120º. The rate at which each ray grows (RayLengthIncrement) is then defined – this is a compromise between the computation time and accuracy. As RayLengthIncrement reduces, the ray extends by smaller lengths and hence requires more checks for interactions, which increase computation time. As RayLengthIncrement increases the chances of a ray jumping over a building's edge are increased – as shown in Figure 59.

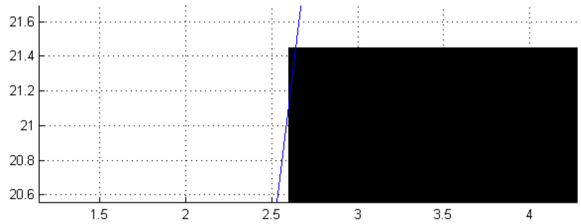

Figure 59: Ray propagating over a building edge instead of being reflected

RayLengthIncrement = 0.05 m when the results shown in Section 6.3.1 were produced; this distance was the longest which did not produce errors as shown in Figure 59. The maximum number of times each ray is allowed to reflect is then defined. *CreateMap* is run to obtain the matrix of the map to be used, the gridspacing and also the limits of the map. The map is displayed on screen without any of the rays. Using the information provided previously, the bearings that each ray makes is calculated and stored in an array called Theta. Another array is created which contains each active ray's ID – ActiveRayList. These steps conclude part 1 of *Propagate.m*.

Part 2 of the program creates a structure, called Rays, which will contain all the data about each ray. The program goes through each value in Theta (the bearings of the rays) and creates a matrix which contains each ray's start point (in the first row) and direction (in the second row). The direction is stored as a unit vector and the format of each matrix is as shown in Equation (8). The rays are modelled as vectors used to represent a line using $\boldsymbol{i}$ and $\boldsymbol{j}$ vectors and α which is the length of the ray; Equation (9) shows an example of how to represent a line using this method and also how the matrix holding information about a ray relates to this equation.

$$RayMatrix = \begin{bmatrix} X_{Start} & Y_{Start} \\ X_{Direction} & Y_{Direction} \end{bmatrix} \quad (8)$$

$$Ray = X_{Start} * \boldsymbol{i} + Y_{Start} * \boldsymbol{j} + \alpha * (X_{Direction} * \boldsymbol{i} + Y_{Direction} * \boldsymbol{j}) \quad (9)$$

The structure also stores each ray's last coordinates as it propagates, along with its activity status; 1 if a ray is active and 0 if the ray has been terminated. For troubleshooting purposes, it is also possible to store (inside the Ray structure) all the points a ray has propagated through. Plotting this enables the user to see the exact path a ray would have taken before an error occurs.

To conclude part 2 a vector called InactiveRayList is created and set to 0. This vector will contain information on which rays should be deleted from the ActiveRayList as they have been terminated.

In part 3 of the program, if active rays exist they are all extended. A while-loop goes through all the active rays and extends them from their previous position by RayLengthIncrement m. If the ray has gone out of the map's limits, the ray is terminated by adding the ray's ID to the array InactiveRayList. This ray's last position is also saved.

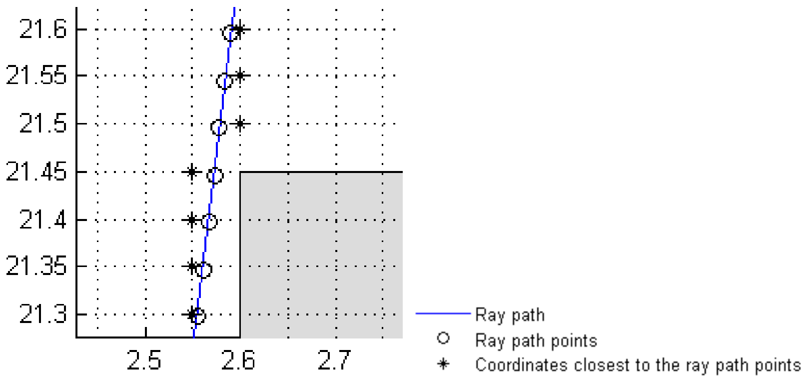

Figure 60: Ray's propagation and approximations

If the ray is still within the map, it is checked if the grid point (on the map matrix) closest to the newly extended ray has a building on it. This is done by evaluating the indices of the map matrix closest to the end of the ray and then using these indices to check if that point on the map matrix is nonzero; Figure 60 displays an image which helps visualise this process. The circles correspond to the actual path of the ray whereas the asterisks display the closest coordinates to the ray's extension. The dotted lines represent the grid lines.

If the closest coordinate on the map is a '0' then the ray keeps on extending. If the point had a non-zero value that means that the ray has potentially gone into a building and it is now required to find the equation of the reflected segment of the ray along with the coordinates of the point of reflection. When there is a building (see Section 6.2.1 on page 94), the element of the matrix representing that point has a number corresponding to the building number. This is where that number comes useful; once a ray gets approximated to a non-zero element, the program will use this value (this value is the same as the building number) to run the function *Reflection.m*; which calculates the point of reflection and also outputs the new equation of the ray. The way *Reflection.m* works is described in the next section.

Sometimes the element closest to where the ray ended is covered by a building despite the ray not entering the building; tends to happen when a ray passes close to the corner of a building. To detect these false reflections caused by approximation errors, once *Reflection.m* has been used to get the new ray's start point and direction, the output is checked to see if the reflection actually happens or if it was an error caused by approximations. The output of *Reflection.m* will be a 4 x 4 matrix of NaNs if no reflection occurs.

If no reflection has occurred then the ray data is updated with the new point the ray has extended to. If a reflection has occurred it is checked if the ray has reflected beyond its maximum number of reflections and if this is true, the ray is terminated after saving its intersection point. If the ray has not gone beyond its maximum number of reflections the ray's information is updated on the ray matrix to say that the ray has reflected and has a new direction.

$$RayMatrix = \begin{bmatrix} X_{Start} & Y_{Start} & X_{NewStart} & Y_{NewStart} \\ X_{Direction} & Y_{Direction} & X_{NewDirection} & Y_{NewDirection} \end{bmatrix} \quad (10)$$

The modified matrix for the ray is shown in Equation (10). By concatenating the new information onto the old information, it is possible to count the number of reflections a ray has gone through by dividing the number of columns by 2.

Part 3 and Part 4 are each run within the same while loop; after the script in Part 3 has been run for each ray, before extending the rays again the script in Part 4 is run. Part 4 is where all the rays which have been terminated have their ray IDs removed from the ActiveRayList. It starts with deleting the first entry of the InactiveRayList, which is a 0 – this 0 is what the array gets initialised with. The program then goes through each of the entries in the InactiveRayList – these entries have been put here in Part 3 whenever a ray was terminated. For each of the entries, the corresponding ray ID is removed in the ActiveRayList array. Once all the ray IDs of the terminated rays has been removed from the ActiveRayList, InactiveRayList is reset to 0 and the while-loop starts again to extend each of the rays – Part 3 of the flowchart.

Upon all the rays being terminated, the data can be plotted in two distinct ways which will be described on page 105 – Plotting Rays.

6.2.2.1 Reflections – Reflection.m

Figure 61 shows the flowchart for *Reflection.m;* the function used to calculate and output the point of intersection between a ray and a wall and the ray's reflected direction as a unit vector. The inputs for the function are the ray matrix and the building number which the ray has entered. This function will then call *CreateMap.m* and request for the coordinates of the building's vertices. Using the vertices, data about the four walls of each building is stored in a structure (Walls). These data are the start point, unit vector in the direction of the wall and the x and y directions' limits of the wall.

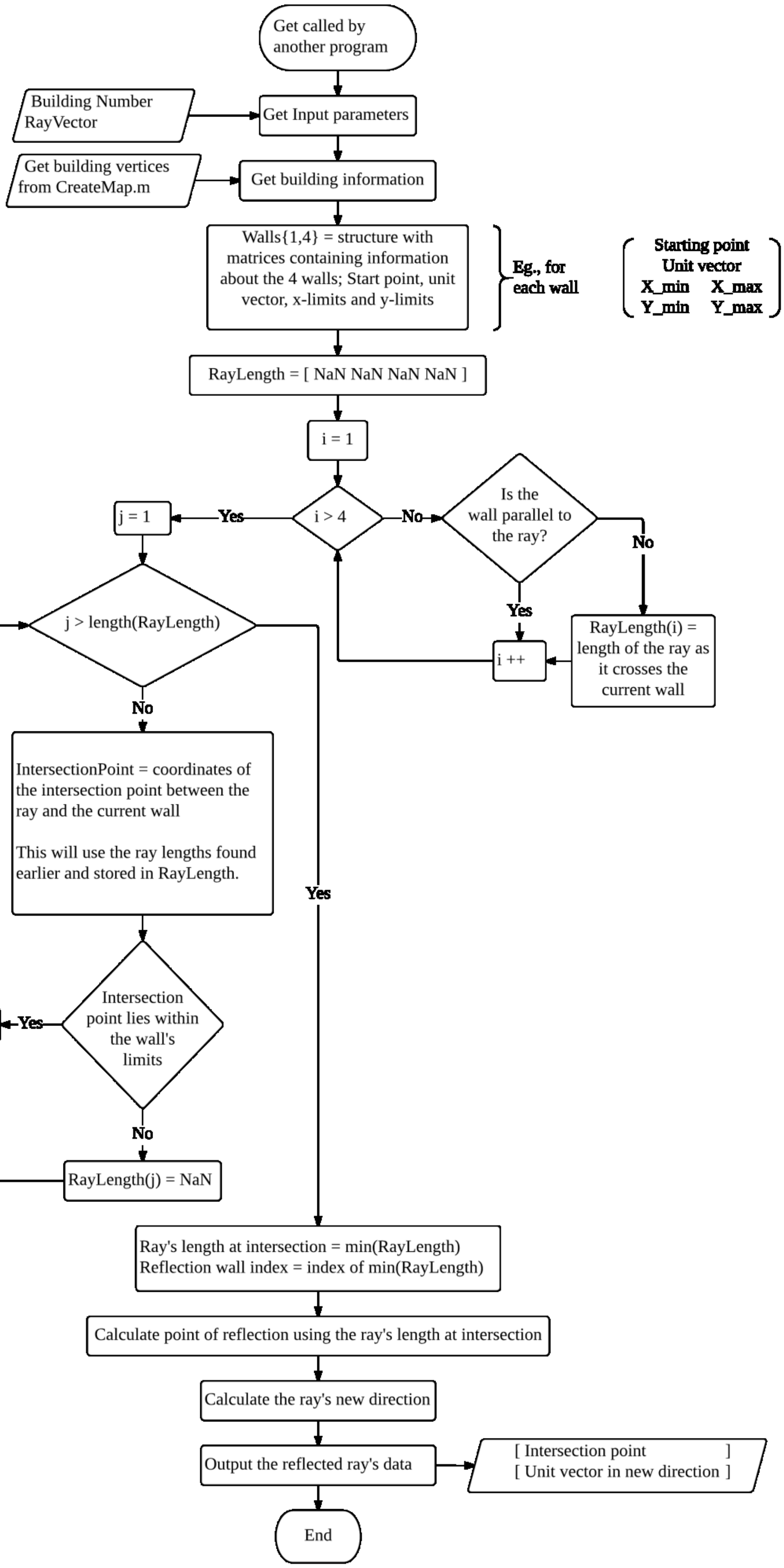

Figure 61: Flowchart for the function Reflection.m

A four element array (RayLength) of NaNs is created to hold the displacement of the ray (from its start point) as it intersects with each of the walls of the building. It is checked to make sure the ray is not parallel to the wall as this would mean the ray would never intersect the wall and reflect off it. When a line is found to be parallel and next to a wall, its entry in RayLength is left as it is; a NaN. If the ray is not parallel to the wall the displacement along the ray vector at which the ray intersects the wall is calculated and stored in the RayLength array. Table 15 contains definitions of all the terms found in Equations (11) and (12).

$$WallVector = w_{stx} * \boldsymbol{i} + w_{sty} * \boldsymbol{j} + \alpha * (w_{dx} * \boldsymbol{i} + w_{dy} * \boldsymbol{j}) \qquad (11)$$

$$RayVector = r_{stx} * \boldsymbol{i} + r_{sty} * \boldsymbol{j} + \beta * (r_{dx} * \boldsymbol{i} + r_{dy} * \boldsymbol{j}) \qquad (12)$$

Term	Description
w_{stx}	x-coordinate of the starting point of the wall
w_{sty}	y-coordinate of the starting point of the wall
w_{dx}	x-component of the unit vector of the wall
w_{dy}	y-component of the unit vector of the wall
α	Length of the wall vector
r_{stx}	x-coordinate of the starting point of the ray
r_{sty}	y-coordinate of the starting point of the ray
r_{dx}	x-component of the unit vector of the ray
r_{dy}	y-component of the unit vector of the ray
β	Length of the ray vector

Table 15: Definitions of the terms in Equations (11) and (12)

At the coordinates where the ray reflects, the right hand sides of Equation (11 **)** and Equation (12) will be the same which means the ***i***-terms and ***j***-terms can be grouped together to form Equation (13) and Equation (14). These can be solved to find β; the ray's length at the reflection point.

$$\boldsymbol{i} - terms \rightarrow \alpha * w_{\mathrm{dx}} - \beta * r_{\mathrm{dx}} = r_{\mathrm{stx}} - w_{stx} \qquad (13)$$

$$\boldsymbol{j} - terms \rightarrow \alpha * w_{\mathrm{dy}} - \beta * r_{\mathrm{dy}} = r_{\mathrm{sty}} - w_{sty} \qquad (14)$$

With the ray lengths calculated, the program goes through each of these values and evaluates the point of intersection between the ray and the walls. These intersection points are checked to see if they are within the locus of points which represent the respective wall and if not, the corresponding value in RayLength is changed to a NaN. The smallest value of the leftover elements in RayLength is the length of the ray as it enters a building and using this, the coordinates of this intersection point is found.

With the intersection point, ray direction and wall direction known, it is now possible to find the direction of the reflected wave using Snell's Law (Weisstein n.d.). Figure 62 displays an example where a vector, $\boldsymbol{v}$, is reflected off a surface and Equation (15) provides the method of obtaining the vector describing the reflected wave. This same method is used to calculate the unit vector of the reflected wave. The unit vector of this reflected wave is coupled with the starting coordinates (the intersection point) of the vector to provide the matrix describing the reflected ray; which is output by the program.

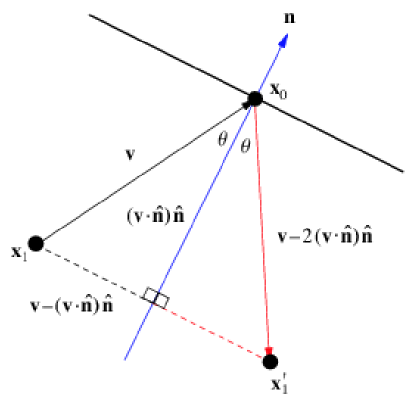

Figure 62: Vector reflection

$$\boldsymbol{x_1'} - \boldsymbol{x_0} = \boldsymbol{v} - 2(\boldsymbol{v}.\boldsymbol{\hat{n}})\boldsymbol{\hat{n}} \quad (15)$$

6.2.3 Plotting rays

There are two ways that the rays can be plotted and each method provides its own advantages. The first method plots all the rays onto the map and the second method plots multiple maps showing the corresponding reflections on each graph, i.e. the first map will only have the LOS rays, the second graph with only the first reflection, the third graph with the second reflection and so forth. The first method of plotting is useful to have an overview of where all the rays have propagated whilst the second method is useful to see the reach of the different reflections of the rays.

6.2.3.1 Plotting Complete Rays from Start to Stop in One Map

The first method is very straight forward; it plots all the rays (including all its reflections) as a line onto the map. The flowchart in Figure 63 shows how this is performed and Figure 64 displays an example of the output with the rays plotted as lines.

As mentioned previously, this method is useful to get an overview of where the rays propagate to. However, because of the overlapping of all the different reflections with the LOS rays, it is hard to say where the signals might be stronger or weaker; depending on how many times the ray has been reflected.

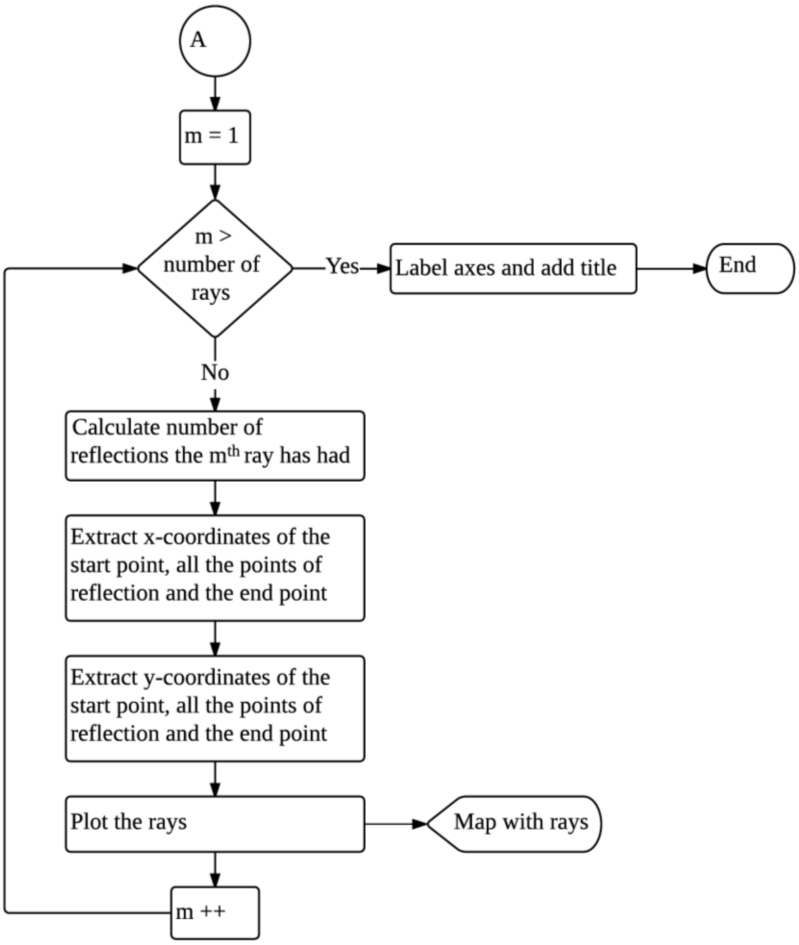

Figure 63: Flowchart to plot all the rays in one map

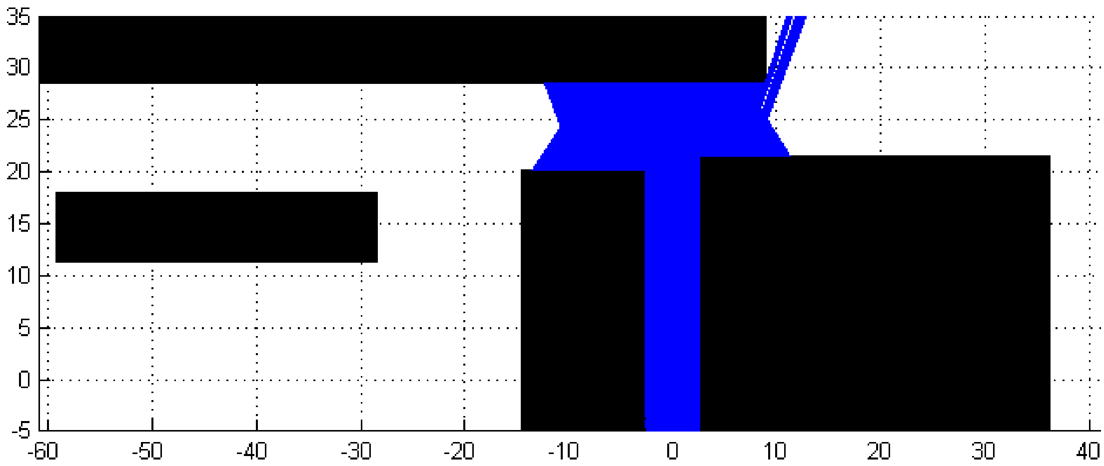

Figure 64: Example propagation of 1000 rays from (0,0) in directions 0 – π^c with a maximum of 3 reflections; RayIncrement = 0.05m.

6.2.3.2 Plotting Corresponding Ray Segments Together in Separate Maps

The second method of plotting the rays provides a clearer image of where the different reflections propagate to. Figure 65 is a flowchart of how the rays are plotted in segments; where a segment means a reflection or the LOS ray.

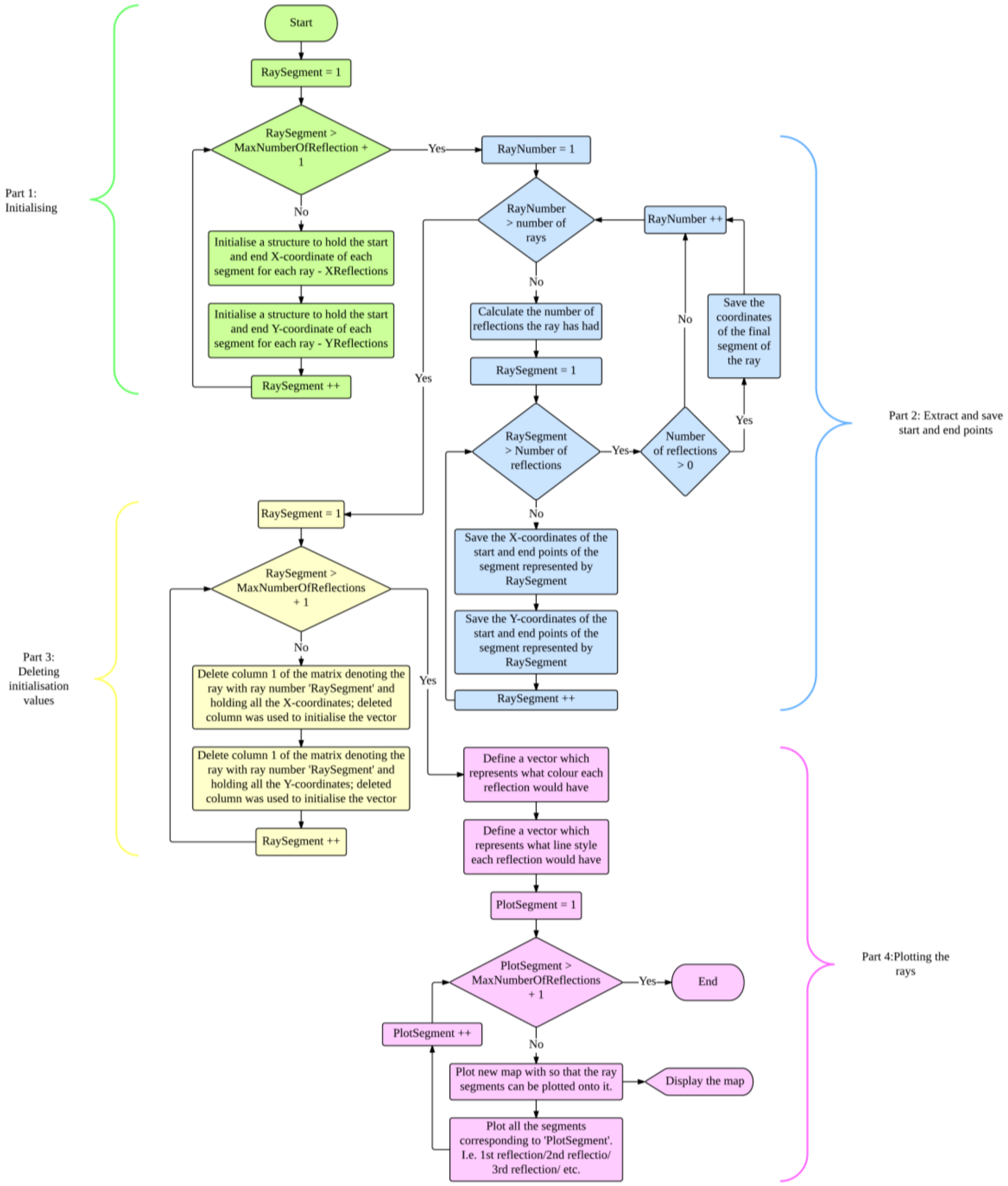

Figure 65: Flowchart to plot rays in separate maps grouped by their segment

The program creates and initialises two structures in Part 1; XReflections and YReflections. Both these structures will store the x-coordinates and y-coordinates respectively, of the starting and ending points of each segment of each ray. The structure is organised by the segment number. Once these two structures are created and initialised with zeros, Part 2 of the program starts and in this part, the program goes through each of the rays, extracts the coordinates of each of the segments and stores them in the appropriate structure.

Once all the start and end coordinates have been extracted the entries used to initialise the structures are deleted – this is what Part 3 does.

Part 4 is where the ray segments get plotted into their respective maps. To help distinguish the different segments, each segment is plotted with a different colour or line style. These styles and colours are defined first. The program then goes through the two structures and plots all the corresponding segments into a map.

Figure 66 shows the same rays as in Figure 64 but where the different segments of each ray are plotted in maps with only corresponding segments of other rays. This provides information on the coverage provided by the different segments. It is worth noting that in all the coverage maps the rays still exist as lines which are densely clumped to the extent that the background is not visible; they do not form shapes as Figure 66 might appear to show.

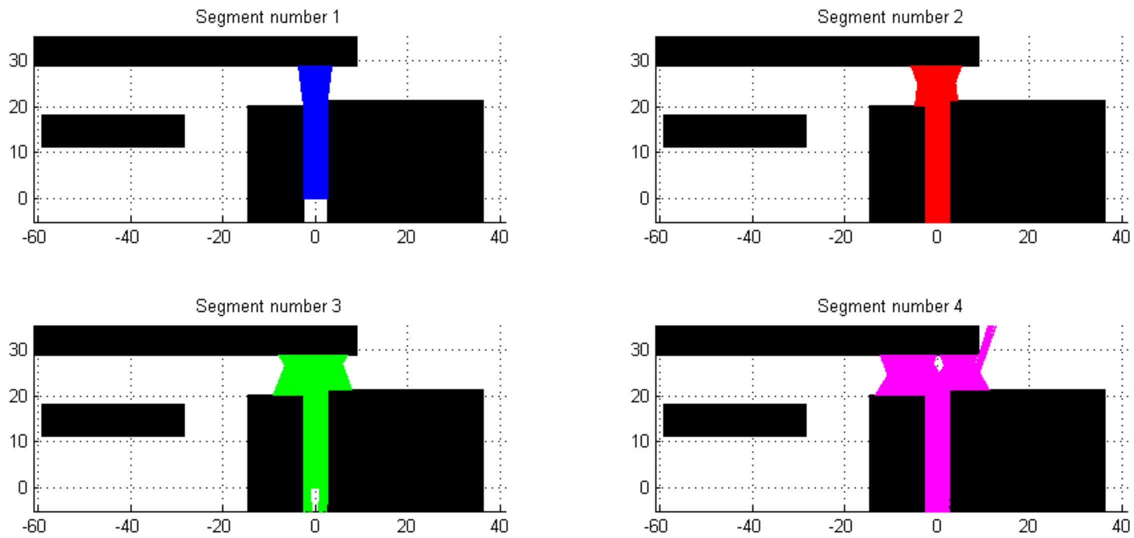

Figure 66: Graphs showing the different segments plotted individually; 1000 rays transmitted from (0,0) in directions 0 – π^c with a maximum of 3 reflections; RayIncrement = 0.05m

Storing the information about the rays in the two structures XReflections and YReflections will also be useful with the processing and analysis performed in the next section.

6.2.3.3 Calculating Ray Density

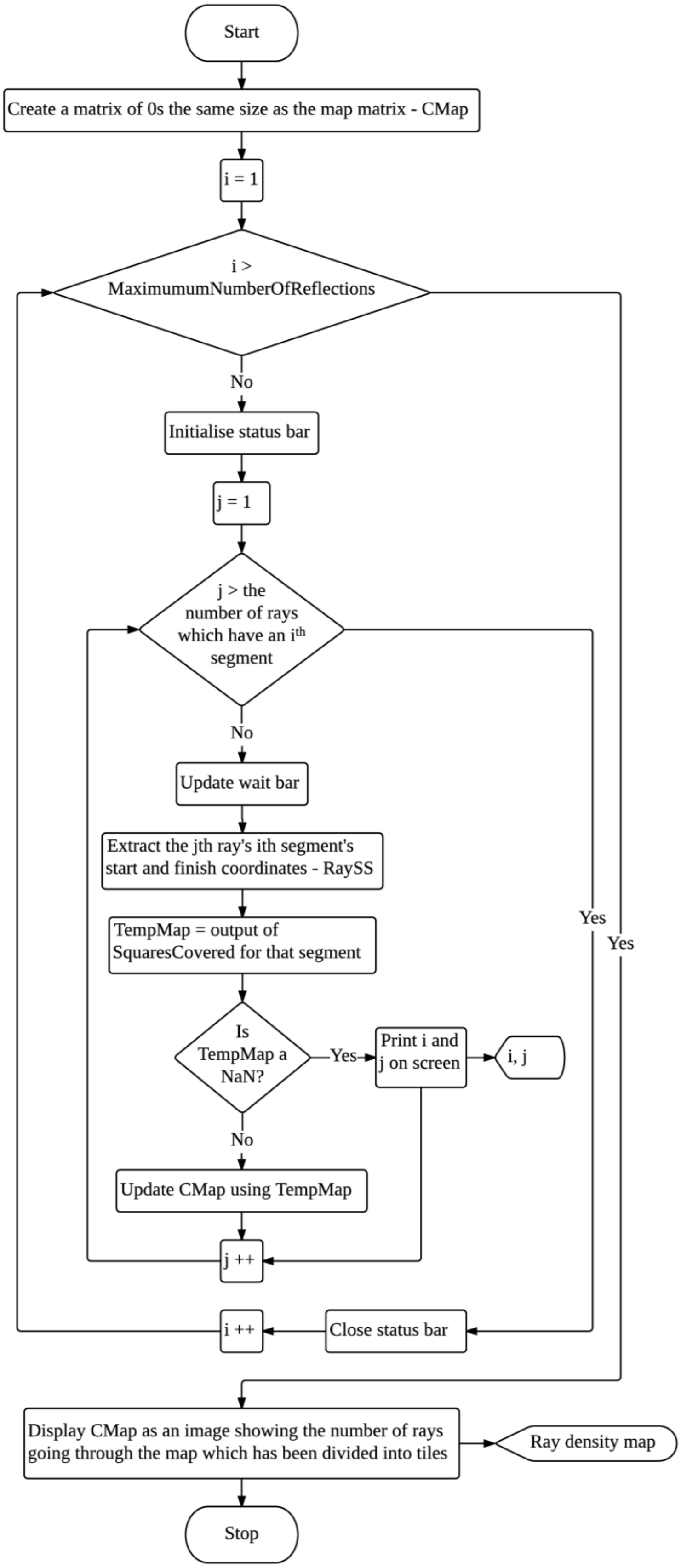

Figure 67: Flowchart showing how the program CalculateRayDensity.m works

Despite the visual information provided by both of the plotting methods previously described, it is not possible to get any numerical data about the ray density at any particular point from either of these plots. To get this information, a program, *CalculateRayDensity.m*, was written which divides the map into tiles and then counts how many rays go through each tile. This program uses the same map as *Propagate.m* but here each ray was processed to see which tiles in the map it passed over. A flowchart of how *CalculateRayDensity.m* works is in Figure 67, with Figure 68 showing the output produced for the map displayed in Figure 64.

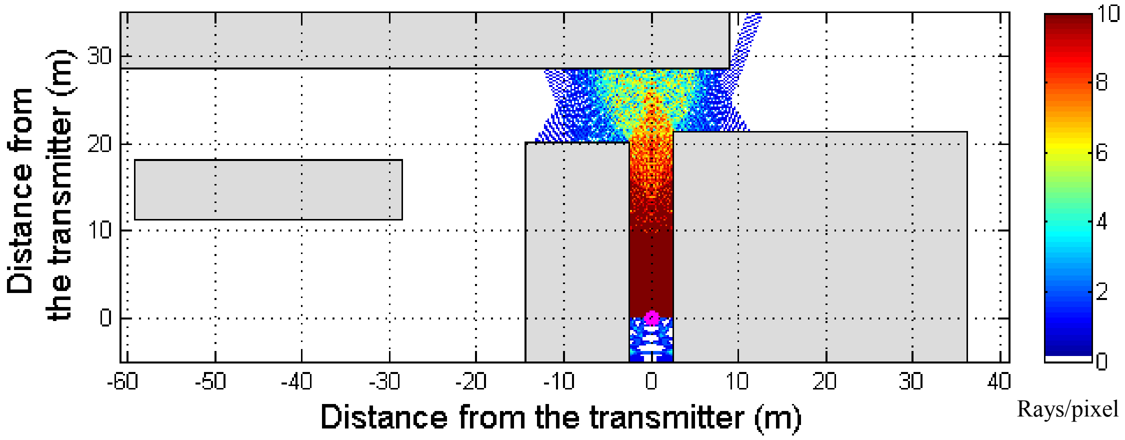

Figure 68: Map showing the rays per pixel (pixel size = 5 x 5 cm) for 1000 rays transmitted from (0,0), magenta circle, in directions 0 – π^c with a maximum of 3 reflections; RayIncrement = 0.05m

Before *CalculateRayDensity.m* can be run, the two structures used to plot the rays in segments are required; XReflections and YReflections. For this purpose it is required to run the previous program (with flowchart presented in Figure 65) before running this program and then save the two structures. This program first creates a matrix, CMap, the same size of the map matrix but full of zeros which will be used to hold all the ray density information.

The program goes through XReflections and YReflections, and for each ray's individual segment, extracts the start and end coordinates and makes a matrix out of this as shown in Equation (16).

$$RaySS = \begin{bmatrix} X\_Start & Y\_Start \\ X\_End & Y\_End \end{bmatrix} \qquad (16)$$

This matrix is then passed on to a function called SquaresCovered.m whose output is a matrix the same size as CMap but has its elements changed depending on the segment's path. This matrix has a constant, RayWeighting, added to the elements whose locus on the map the ray covers. RayWeighting will depend on the number of times the ray has been previously reflected – it will be higher for any LOS rays and will decrease for subsequent reflections. Currently all predictions are collected with RayWeighting = 1; calibration work is required to accurately allocate ray weightings to the segments depending on how many times the ray has been reflected and the material that the ray has reflected off.

CMap is updated using the output of *SquaresCovered* and once this process has been done for all the rays, CMap is plotted as an image where the colour of the pixels in the image represents the number of rays going through it; as shown in Figure 68.

6.2.3.4 Mapping a Ray to the Squares it Covers – SquaresCovered.m

6.2.3.4.1 Part 1 – Initialisation

This function tracks each ray segment and produces a matrix showing the elements (on the map matrix) whose locus the ray propagated through; a flowchart for the first part of this function, the initialisation stage, is in Figure 69.

The inputs to this function are the RaySS matrix (which was described in the previous section) and a scalar value named RayWeighting. RayWeighting is what is added to the elements of the map matrix if the ray passes through its locus. The elements of RaySS are rounded off to 4 decimal places to prevent errors caused by floating point precision problems. The length of the ray is then calculated so that the ray segment can be represented by a matrix similar to the one in Equation (8); the elements of this matrix is also rounded up to four decimal places for the reason previously mentioned. Map data is also extracted by running *CreateMap*.

If the segment starts on a gridline (the boundary between two elements) its start point is moved 0.001 m away from the original start point and in the direction of the segment. This assists in choosing the square (pixel on the map represented by an element in the matrix) which the segment starts on. The segment's initial coordinates are then stored in StartPoint.

An empty matrix the same size as the map is made and filled with zeros. Two arrays are then created to store the x-coordinate and y-coordinate of the y and x directions' gridlines respectively. The ray start and end points are converted to map coordinates. As part of the tracking process, the program tracks which squares the ray passes through from its starting square to its ending square. At this stage, the indices of the segment's starting point are the same as the indices of CurrentSquare.

Other data about the segment are also extracted – all of which will be useful later in the program as it tracks the squares the ray propagates through. These data include whether the segment is horizontal, vertical or diagonal and if it starts in the middle of a square. If the segment is diagonal and starts at the centre of the square then it will pass through the corners of the square as opposed to the sides and knowing this will simplify the processing. Using the segment's start and end points, the direction of the ray is evaluated before setting the value of RequiredIndex.

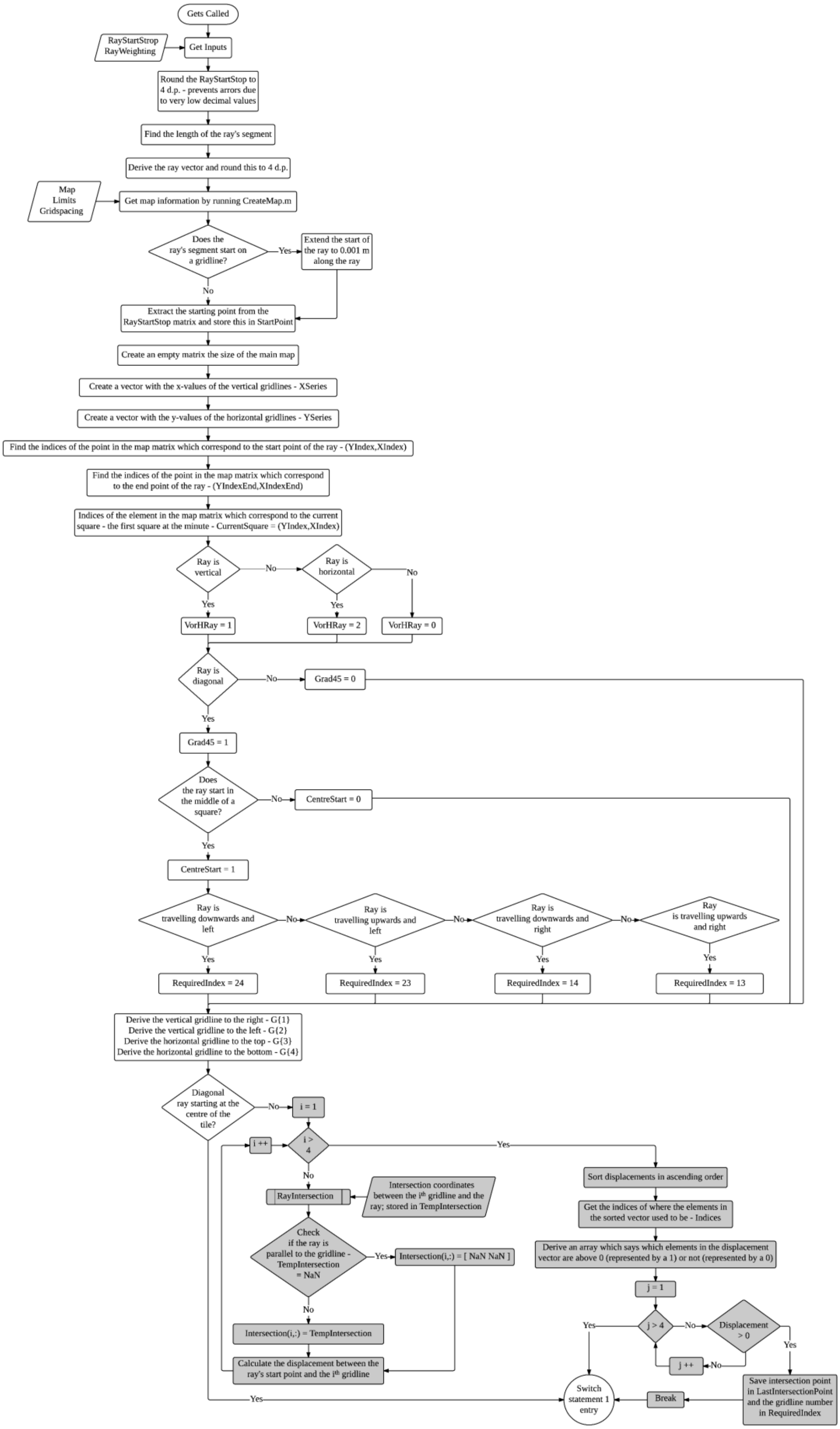

Figure 69: Flowchart for the initialisation stage of function SqauresCovered.m

RequiredIndex is used to store the direction of the next square the segment will propagate to, depending on which gridline the segment exits the current square by. If the segment exits from a side of the square then the RequiredIndex is the index of the relevant gridline in the structure holding the gridline. If the segment exits from a corner, then the RequiredIndex is set to be the combination of the gridlines which it goes through. Figure 70 displays a square with its gridlines labelled.

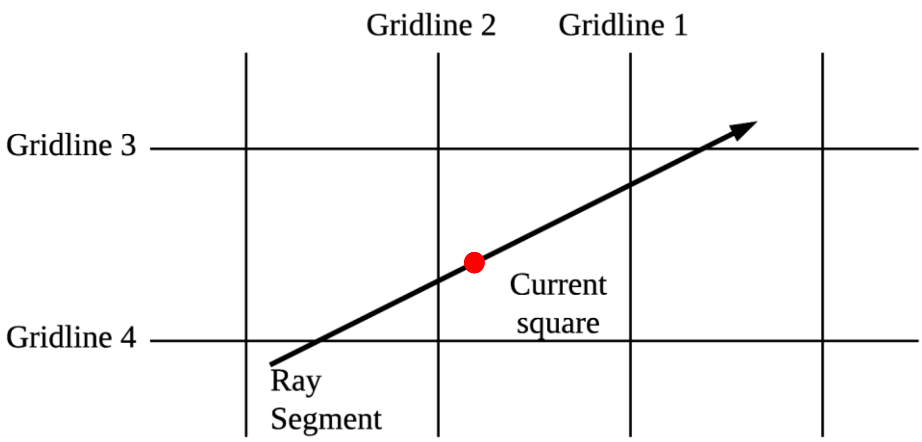

Figure 70: Ray passing through a square

The segment's starting square's gridlines are calculated next and stored in a structure; each gridline is represented by a matrix similar to the one presented in Equation (8). It is then checked if the ray segment is diagonal and starting in the centre of a square. If this condition is satisfied, the program goes to a switch statement shown in Figure 71.

The grey part of the flowchart in Figure 69 is processed if the ray segment is not diagonal and starting at the centre of a square. The program goes through each gridline and using the function *RayIntersection.m,* gets the coordinates of the point of intersection between the ray segment and the gridline. These coordinates are used to find the displacement of the segment from its start point. When calculating this displacement it is required to know if the ray is horizontal; if the ray is horizontal the ***i***-terms will have to be resolved instead of the ***j***-terms (usually the ***j***-terms are resolved). This is why it is previously determined if a ray was horizontal or vertical.

The program goes through the displacement list and finds the lowest positive value because this happens when the ray crosses the next gridline in its path. This can be seen in Figure 70; the displacements (where the red dot denotes the start point) of the ray segment at the intersection points with gridlines 2 and 3 are negative. Of the remaining two, the intersection with gridline 3 happens outside the squares limits. Once the next gridline is found, the coordinates of the intersection are stored in LastIntersectionPoint and RequiredIndex is updated to reflect the direction of the square the ray segment will next go into. The program then goes into the switch statement shown in Figure 71; This is one instance where knowing if the segment is diagonal and starting in the middle of the square, will reduce the processing required.

6.2.3.4.2 Initial Square Updater

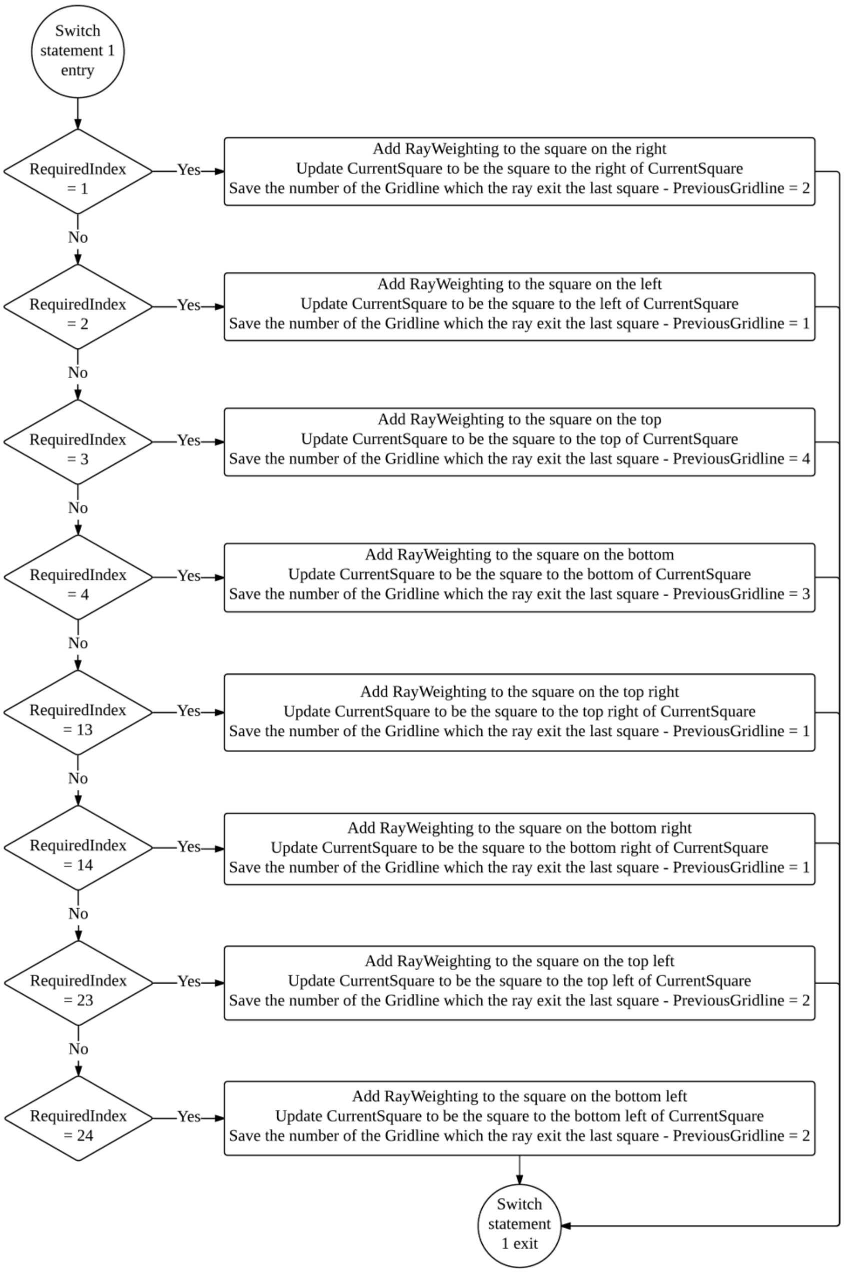

Figure 71: Flowchart for the initial tile updater stage of function SquaresCovered.m

Figure 71 is a flowchart for the initial square updater part of SquaresCovered. The purpose of this part is to add RayWeighting to the next square the ray segment will be going into, update the value of CurrentSquare to the next square and the save the number of the gridline which the ray segment crosses to enter the next square. For the last task, the gridline number saved is the gridline number of the gridline crossed, as seen from the next square. This means that if the ray segment exits through gridline 1, then it enters the next square through gridline 2 and so gridline 2 is saved.

6.2.3.4.3 Intersection Calculation Loop and Output Generator

Part 3 of SquaresCovered.m is the intersection calculation loop and output generator; shown in Figure 72. This mainly comprises a loop which tracks the ray and the squares whose locus it passes through. The loop will continue until a variable, EndLoop, been changed to 1 upon the ray being successfully tracked or if an error has been detected and the loop gets aborted.

The matrices representing the gridlines for this square are calculated using the indices provided by the variable CurrentSquare, which was updated in the initialisation part. It is then checked if the ray is diagonal and starting at the centre of the square. If this condition is met the program goes to its fourth part; the square progression switch (Figure 73). Before entering this part, a variable (error) is set to 0; explained in more detail in Section 6.2.3.4.4.

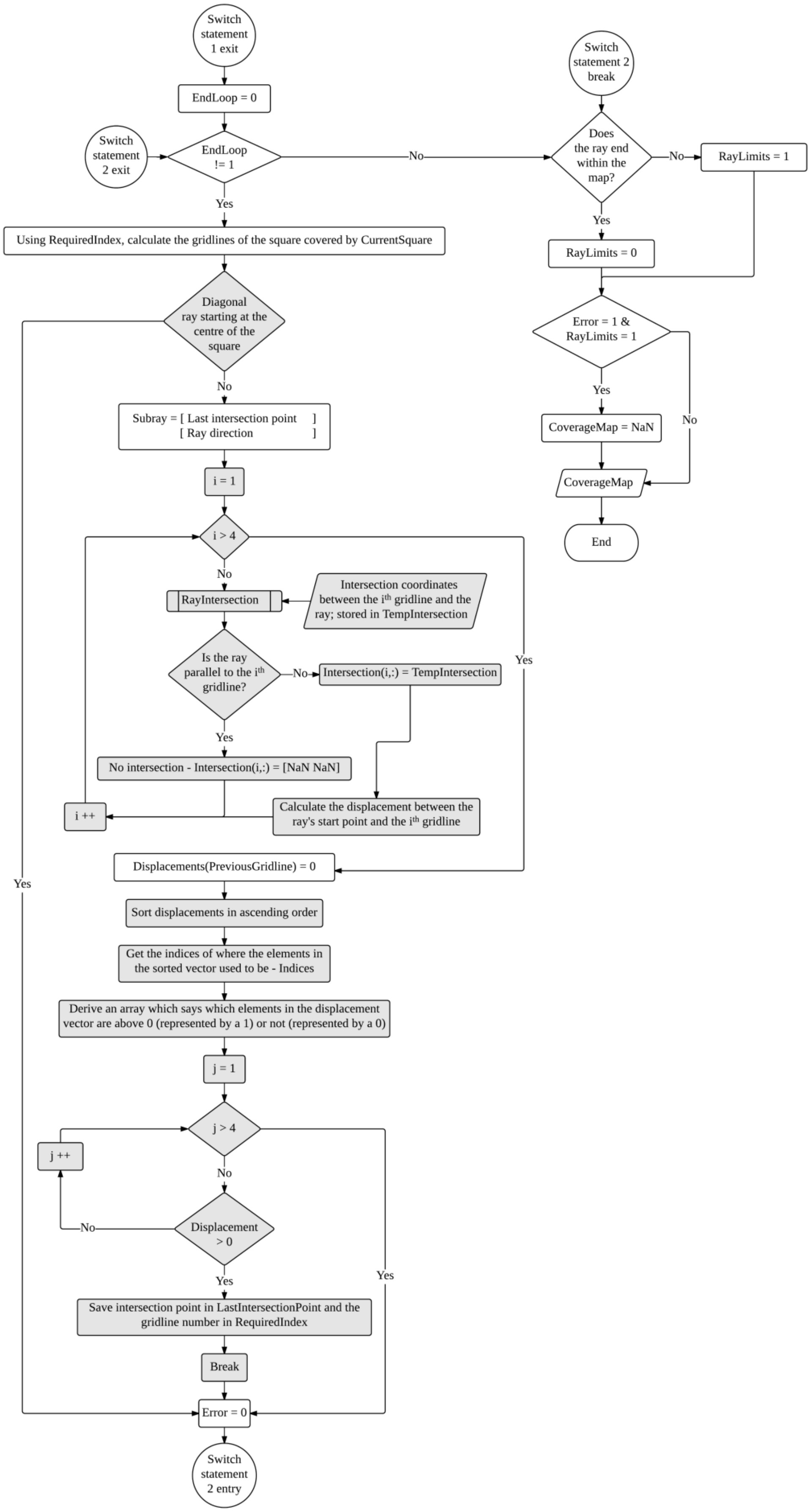

Figure 72: Flowchart for the intersection calculation loop and output generator of function SquaresCovered.m

If the segment is not diagonal and does not start in the centre of the square, then the coordinates of the exit point from the square along with which gridline the ray segment exits the square through (the RequiredIndex) are found. The processing that happens is similar to the grey part of the flowchart in Figure 69. One of the two differences in these two sequences is that the ray segment's matrix is altered and the start point is changed to the coordinates of the last intersection point.

Tile tracking fails at times due to floating point precision problems and to prevent this, the displacement between the start point and the entrance gridline is set to 0 by the program – this is the other difference. Once the exit coordinates and the RequiredIndex has been found, the variable error is set to 0 and the square progression switch is entered.

6.2.3.4.4 Square Progression Switch

This part (flowchart in Figure 73) is similar to the initial square updater part (in Section 6.2.3.4.2). There are two more actions being performed in this part which do not get performed in the previous one; changing the loop condition (EndLoop) to exit the loop once the ray segment has been completely tracked and tracking error detection.

The loop continues until the ray segment has been tracked to its end square; whose matrix element was found earlier (see Figure 69) and stored in (YIndexEnd, XIndexEnd). After calculating the coordinates of the next square, the program will check if this square will be the final square of the ray segment. If this is true, the loop condition (EndLoop) is set to 1 which will cause the program to come out of the while-loop and finalise the tracking. RayWeighting is not added because in most cases, the ray reflects and this means RayWeighting will be added to the same square while tracking the reflection (as the reflection starts from the same square) hence duplicating the action.

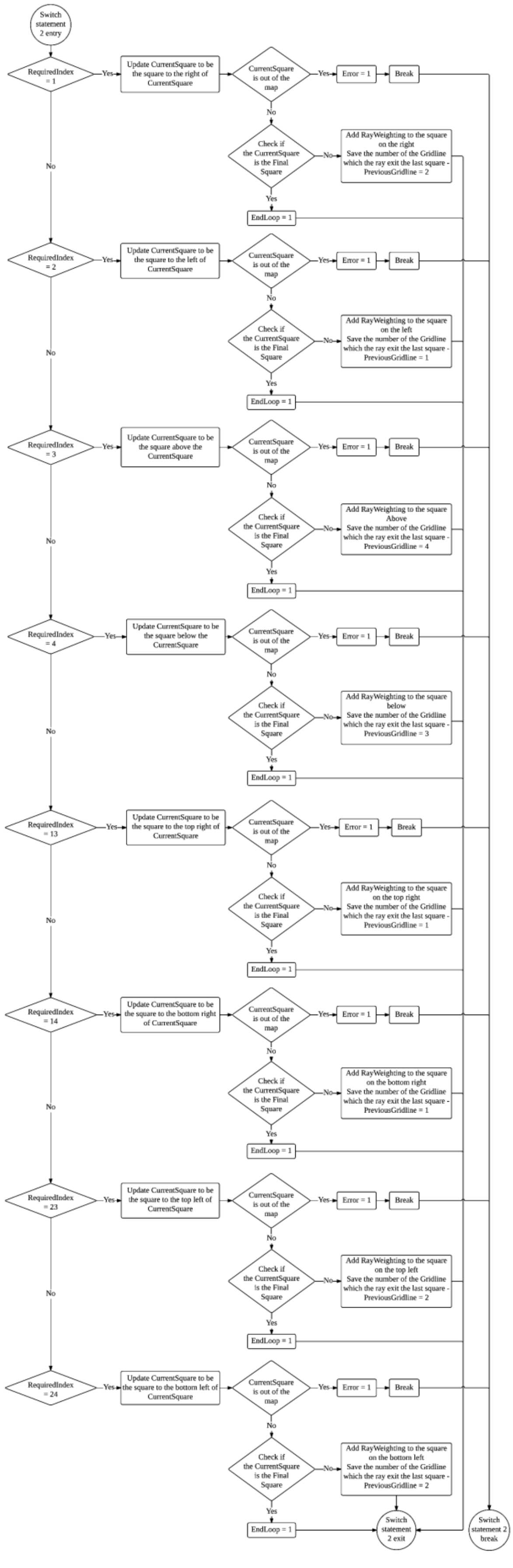

Figure 73: Flowchart for the square progression switch of function SquaresCovered.m

It was noticed that at times certain rays do not get completely tracked as the program fails to find the correct gridline which the ray segment exits through. Upon investigation this was found to be largely due to the displacement between the ray segment's starting coordinates and the entrance gridline not being calculated to zero but extremely small (in the order of 10^{-22}) positive values which misled the program; this is why the ray matrix is rounded to 4 decimal places at the start of the program and also why the program sets the displacement with the entrance wall to 0 despite calculating this displacement (explained a few paragraphs earlier). This was not a frequent occurrence and happened less than 20 times while 1000 rays were propagated with a maximum of 9 reflections.

The tracking error would cause the program to enter the wrong square and continue along that line until it went out of the map and then caused an error resulting in the program ending while trying to access a matrix element outside the matrix' index. By breaking the loop upon detection of indices out of bounds, it was possible to continue tracking the other rays instead of the program stopping. When an error is detected, the variable error is also changed from 0 to 1.

These were the only two extra tasks performed in this part (Figure 73) compared to the initial square updater (Figure 71). The switch statement can lead to two exit points; back into the while loop and out of the while loop. As long as no error is detected the switch statement leads back into the start of the while loop in Figure 72 at the connector named, 'Switch statement 2 exit'. If an error is detected, the program comes out of the while loop and also back into the flowchart in Figure 72 but at a different entry point; the connector named, 'Switch statement 2 break'.

Upon the ray segment being successfully tracked (the correct elements of the map matrix altered) and the program having exit the while loop, it then finalises the output. The program checks if the ray segment's final coordinates were out of the matrix; this can happen if the ray segment was initially terminated (in *Propagate.m*) due to going outside the map's limits.

The program then checks if there was an error and if the ray segment's end coordinates are within the map limits. If this condition is true, that means a tracking error has occurred and the coverage map is changed from a matrix to a NaN. If an error was detected and the end coordinates were outside the map, then the ray segment has been correctly tracked and the coverage map is left unchanged. The coverage map is now output from the function.

6.2.3.5 Calculating the Intersection Point Between two Rays or a Ray and a Gridline – RayIntersection.m

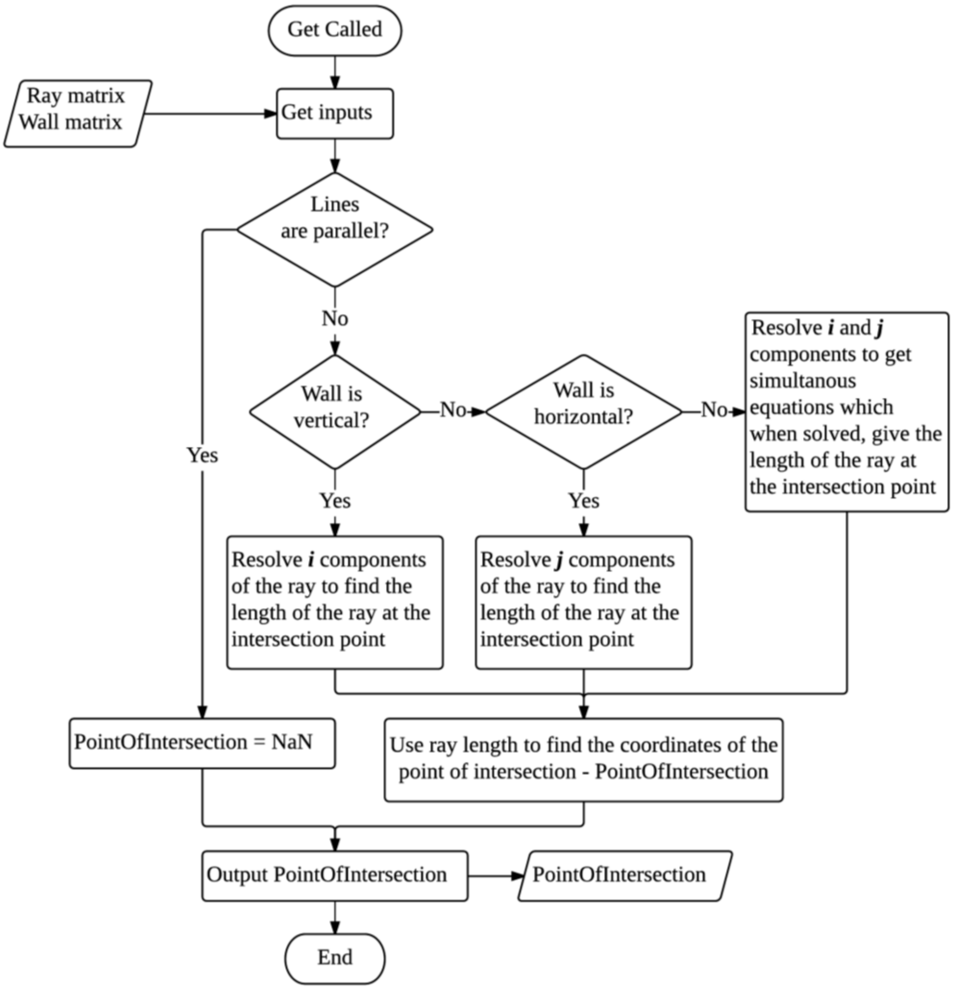

Figure 74: Flowchart for RayIntersection.m

This function is used to find the coordinates of the intersection between two lines and works in a similar way to *Reflection.m* but this function takes two lines as its input instead and the only output is the coordinates of the point of intersection. A flowchart for this function is displayed in Figure 74. Once the function gets called, it gets passed two inputs; two matrices containing information about the two lines which are checked for an intersection. These matrices could represent two lines or a line and a wall.

The lines are checked if they are parallel and if so, the output (PointOfIntersection) is set to a NaN. If the lines are not parallel then there is an intersection and to get the coordinates of this point, the ***i*** and ***j*** vectors can be resolved. If one of the lines is vertical or horizontal, it's ***i*** or ***j*** component is 0 which means that only the ***i*** or ***j*** terms need to be resolved, respectively. If the one of the lines is not vertical or horizontal, then both the ***i*** and ***j*** terms are resolved which provides two simultaneous equations (similar to the Equations (13) and (14)) which can be solved to find the length of the ray at the intersection point. Once this is known, the ray's equation can be used to find the coordinates of the point of intersection which is then output by the program.

6.3 Interpreting Data

6.3.1 Ray Density Map

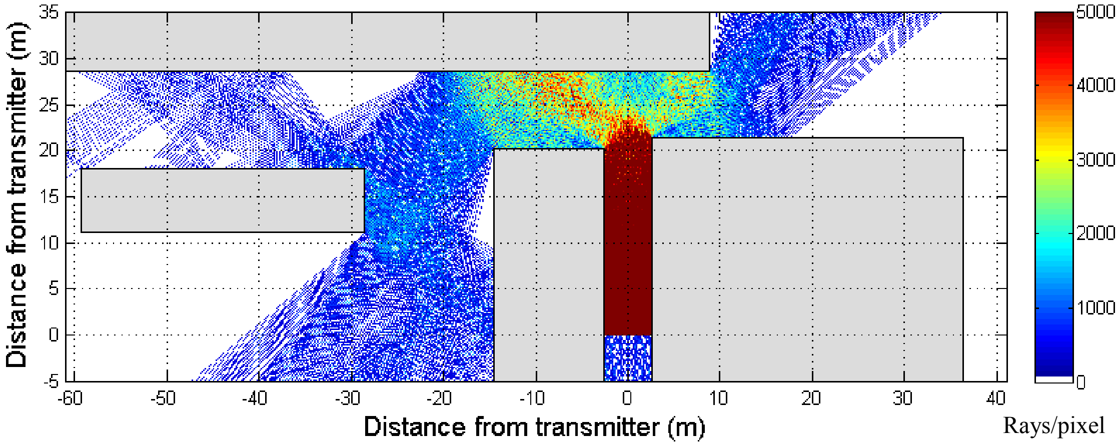

Figure 75: Ray density for 1000 rays transmitted from (0,0) in directions 0 – π^c with a maximum of 9 reflections

Figure 75 displays the ray density for the urban case; obtained by dividing the rays per pixel by the area covered by each ray. The rays were allowed to reflect nine times before they were terminated and this provided a good coverage range. RayWeighting = 1 irrespective of the reflection number which reduces the accuracy but the model still provides an accurate image of where the signals would propagate to when only considering reflection and no diffraction. The accuracy would be improved by including diffraction and it is expected that the model would produce accurate predictions with less reflections.

Using the ray density shown in Figure 75 it is possible to get an indication of the signal strength at a given point; more rays depict more power being received.

6.3.2 Ray Density for the Path that Data was collected on

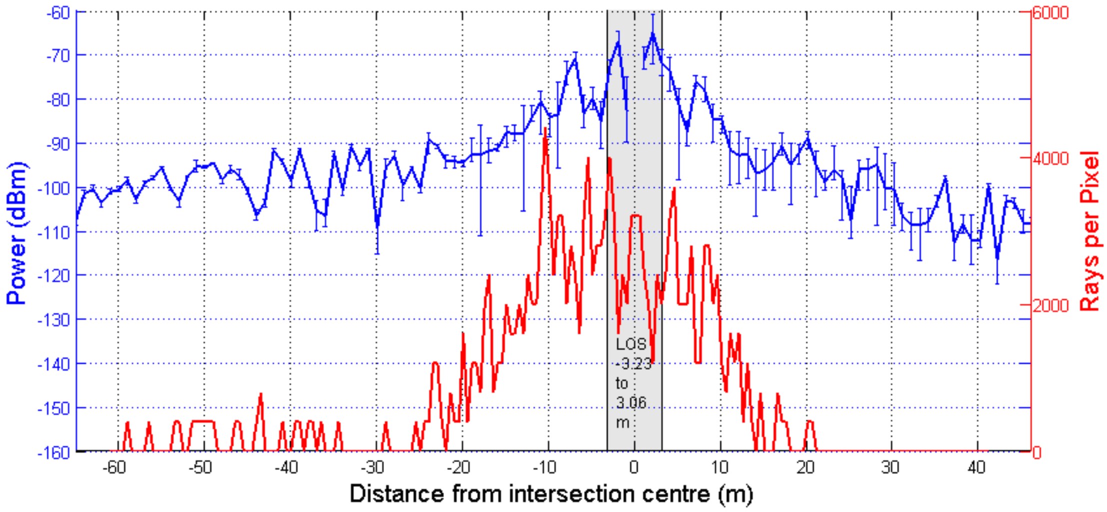

Figure 76: MPP and rays per pixel for the data collection path in the urban case

Figure 76 shows the MPP and rays per pixel (RPP) for the path that data was collected in the urban case. The RPP is higher in the negative portion of the x-axis (urban canyon part of the environment) in comparison to corresponding distances in the positive portion (open part of the environment). It can also be seen that the RPP increases in the NLOS region on either side of the intersection in comparison to the LOS region (shaded in grey); caused by multipath propagation in the urban canyon. The RPP changes will be smoother with an appropriate scheme to allocate RayWeighting.

The MPP for the data collected in this case follows similar trends; The MPP rises just outside the LOS region and is higher in the urban canyon in comparison to the open region. The model supports the theory that urban canyons increase MPP due to more multipath components adding up at the receiver. Due to restrictions on time it was not possible to fine-tune the model but the current output is promising.

6.4 Further Improvements that can be made to the Model

Currently the model can only reflect rays off buildings and in a horizontal 2-dimensional plane. There is no diffraction involved and the model does not work in 3 dimensions. Getting the program to operate in 3 dimensions would involve changing the map to 3-dimensional matrix and each ray vector also having a ***k***-component to its vector. This would enable coverage analysis when the antennas are placed at different heights and also the effect of reflection off buildings with non-uniform walls can be investigated.

Calibration is required to relate the ray density with the power; the number of rays cast, n_r, will then be a function of the transmit power, P_t, and the received power, P_r, can be calculated using the ray density. This can be performed theoretically using a pathloss equation (such as the 2-ray ground or freespace loss) and then building a relationship between the ray density and P_r at different distances. Another method would be to gather signal strength data under LOS conditions in an open field (minimised multipath effects) and then building a relationship between P_r and ray density. Combinations of P_r and n_r will have to be used to obtain the best relationship. The calibration will enable comparing the output of the model with predictions from other models and most importantly, the data that was collected.

Calculations which use building material information can be used to calculate the percentage power loss due to reflections. Suitable RayWeighting values can then be calculated for the different segments of the rays.

Diffraction has not been implemented in this model and there is scope for its inclusion. This will require finding all the rays that propagate within a certain range of a building's corner and then creating a family of rays (children rays, C_r) to be produced from the individual rays (parent rays, Pa_r). This family of rays will have a cumulative RayWeighting which equals the Pa_r's RayWeighting. In this case the RayWeighting of each C_r will be a function of the angle of diffraction; similar to the power in a diffracted wave.

It is highly unlikely to incorporate the effects of refraction as this would require accurate building plans to be used in the model and acquiring these plans.

The effect of physical traffic on the propagation of waves is a matter of significance in this project. The model can be improved to analyse the effects of these mobile reflectors on the coverage; especially as traffic had an effect on the data collected (described in Chapter 8) at the site being modelled in this section. Doppler shifts and spreads are a function of the change in a signal's path length (Parsons 2000). The model can be improved to calculate the change in path length of the rays being received which in turn can be used to calculate the Doppler shift and spread at the receiver – related work can be found in Chapters 8 and 9.

Another enhancement to the model would be to enable the use of multiple transmitters which could be mobile – this requires a shift from the condition where the origin of the map is the location of the transmitter.

6.5 Conclusions

A ray tracing model was developed to successfully explain certain MPP trends in the urban case; specifically the higher power in the urban canyon portion in comparison to the open portion of the path and the MPP being higher in the NLOS regions just past the LOS regions. Despite being able to shed light onto these trends, the model still requires more work to increase its accuracy and to output the received power instead of the ray density.

Improvements to the model involves the incorporation of diffraction, non-specular reflections, signal phase (calculated using the pathlength or randomly allocated), tracing the rays in all three dimensions, outputting power instead of ray density (which requires calibration work), insertion of mobile traffic enabling calculations of Doppler shifts and spreads at the receiver. These features could not be incorporated due to the lack of time. The model will also require more validation which will be performed by making measurements in a variety of environments (open, suburban, urban, etc.) and comparing these with the output of the model.

7 Investigating the Directional Characteristics of Multipath Components

7.1 Introduction and Data Collection Environment

An increased understanding of radio propagation at 5.9 GHz can be expected from the information about multipath components (MPCs) and their paths, which in turn will be useful towards improving propagation models.

The directional antenna (radiation pattern in Section 3.5) has a 22º beamwidth for the main lobe which has a gain of 18 dBi. The main side lobes are 33º either side of the main lobe and they are 16 dB below the main lobe in power. This strong directionality gives a strong indication of the relative strength and direction of the different multipath components which add up at the receiver.

The directional antenna system (DAS) is only used in the urban case which is pictured in Section 4.2.1. This case provides the richest multipath environment due to the numerous buildings and reflective surfaces present. There was no vehicular traffic in the environment whilst data was being collected; only pedestrians and cyclists whose presence was noted in most cases.

7.2 Data Collected

The distance separation (Δd) in these measurements is 5 m, with the distance from the intersection centre (d) varying from 5 m to 25 m. The azimuthal angular separation (Δa) is 10º to get the best compromise between angular resolution and time spent gathering data.

$$P_{NORM} = \frac{P_{MEDIAN} + 125}{60} \tag{17}$$

The data is first plotted for all the positions in the urban case with a map in the background. Polar plots of the data collected are plotted at the positions of collection. This is similar to a radiation pattern of the signal being received at a particular position;

an example is displayed in Figure 77 for d = -5 m where the solid line is the normalised power (P_{NORM}) from the different angles. This is calculated from Equation (17).

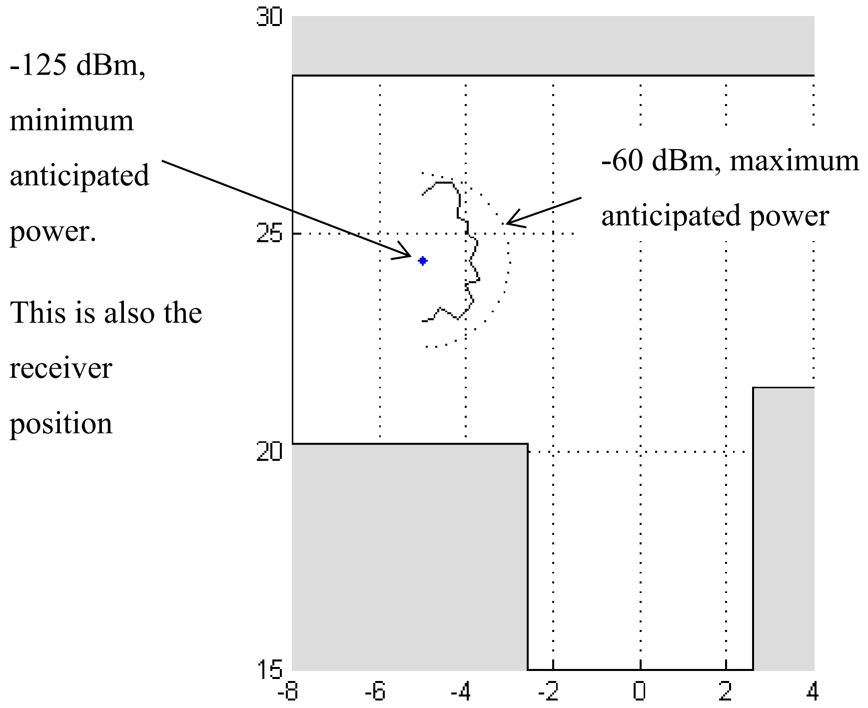

Figure 77: Example plot showing the relative strengths of the MPCs received, d = -5 m, Tx at (0,0)

P_{MEDIAN} is the median peak power of all the spectra collected at a particular angle of a particular distance. 125 dB is added to each of the P_{MEDIAN} values as they are all negative and this cannot be plotted in a polar plot. None of the P_{MEDIAN} values were less than -125 dBm and subtracting anything lower would have made the lowest P_{MEDIAN} values too large. In addition to adding 125, this sum is also divided by 60 to get a normalised value; P_{NORM}.

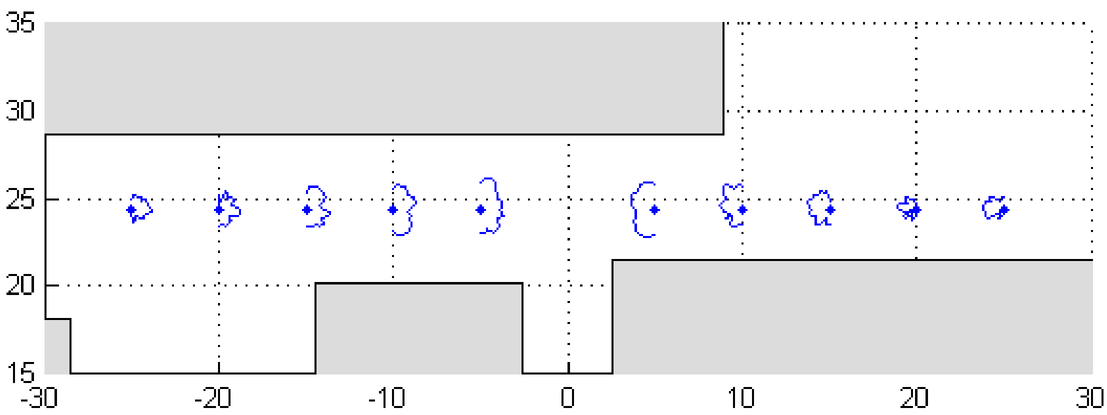

Figure 78: Relative strengths of the MPCs at all positions, Tx at (0,0)

Figure 78 shows P_{NORM} for all the data collected in the urban case. The range of angles decreases as |d| increases and when |d| ≥ 20 m P_{NORM} has relatively larger spikes implying stronger signals were received from some directions. P_{NORM} also displays its inverse relationship with distance and is higher in the data collected in the urban canyon portion (negative x-axis); similar to what is seen in Figure 28 in Section 4.2.1.

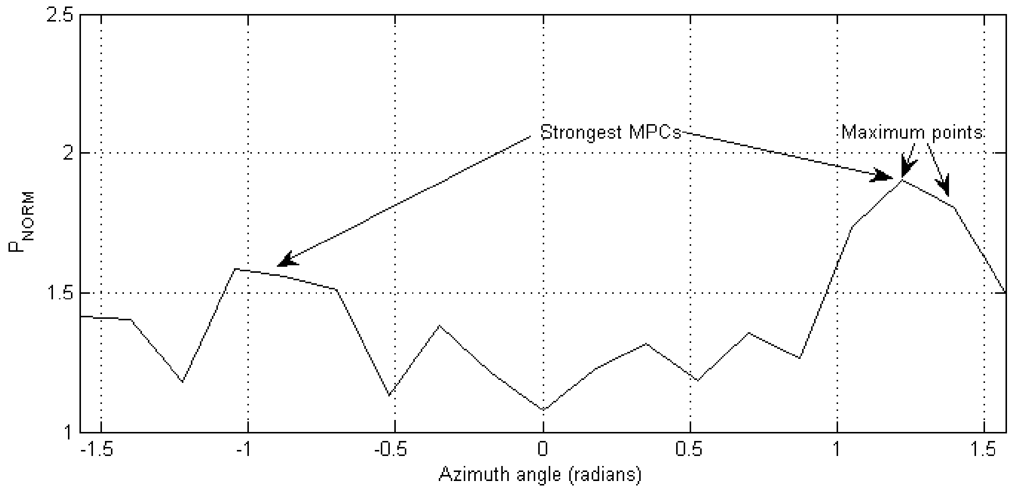

Figure 79: P_{NORM} for different azimuth angles at d = -5 m

To further understand the multipath components and their paths, it was decided to select the two highest peaks in the P_{NORM} values at each position and then cast rays outwards in these directions. The two highest peaks in P_{NORM} was chosen instead of the two highest P_{NORM} values because it is possible that adjacent points could have the two maximum values caused by the same (strong) multipath component; as shown in Figure 79. By using the two peaks instead it is possible to find the main beam and the second strongest beam received.

From the MPCs seen in Figure 79, the difference in power between the main MPCs and the power at other azimuthal angles is not high enough for the antenna's sidelobes to combine with MPCs and give erroneous directions for the strongest MPC. This is due to the main beam having a 22° beamwidth with a gain greater than 16 dB compared with the sidelobes.

The ray casting method is described in Section 6.2.2. Eleven rays are cast with a beam width of 10º and uniform Δa; this will display where the strongest multipath components arrive from. The main beam formed from the highest P_{NORM} peak at each position is plotted using solid lines and the dotted lines denotes the secondary beam.

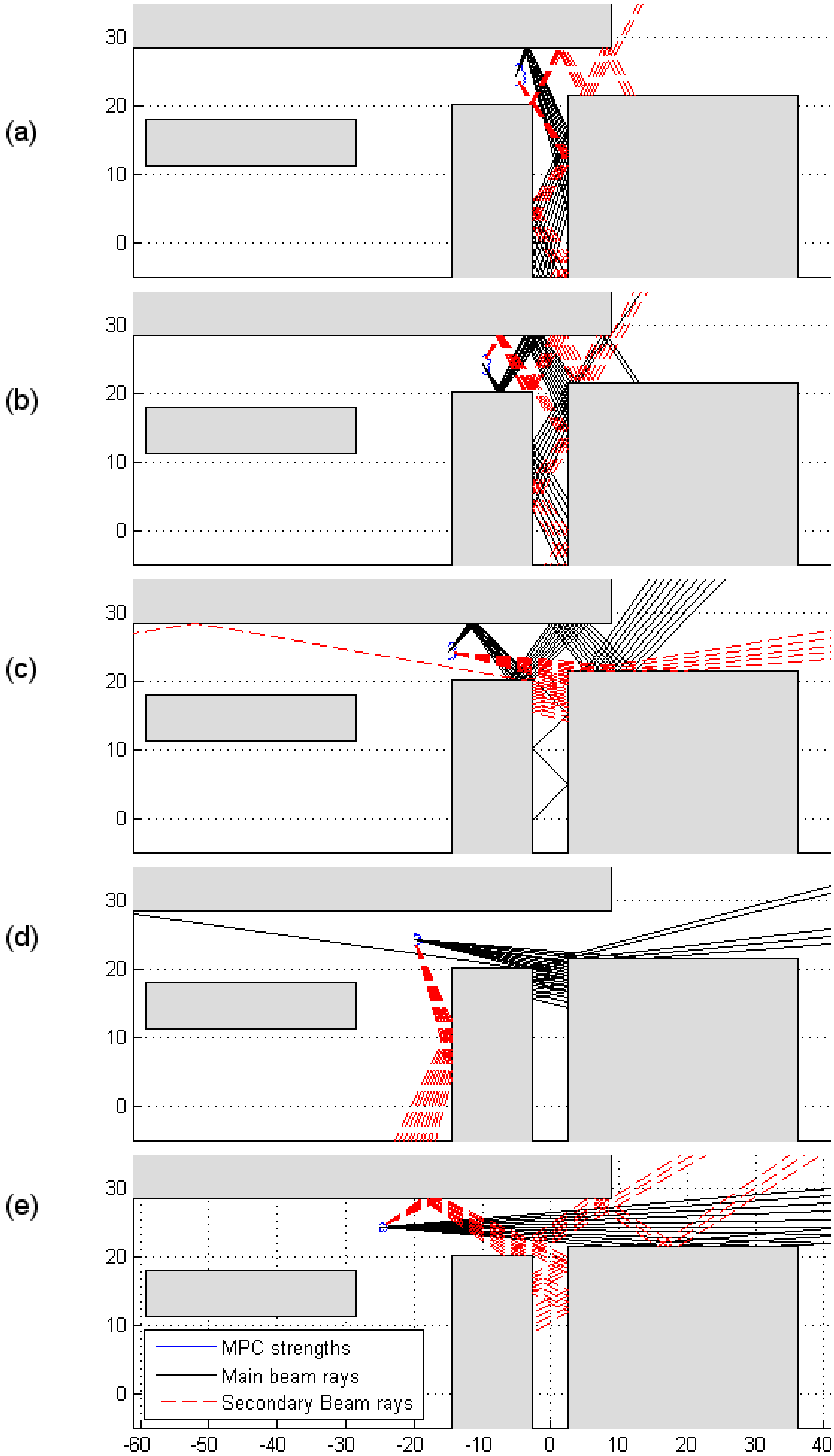

Figure 80: Projected main and secondary beams for data collected in the urban canyon part of the urban case. Panels (a) – (e) are for receiver positions -5, -10, -15, -20 and -25 m.

Figure 80 and Figure 81 shows rays projected from the main and secondary beams in the urban case; maximum of 4 reflections before termination with no diffraction considered. The normalised power plots which shows the relative strengths of the MPCs is in blue. These are the same as those from Figure 78, but they only appear in the relevant panel of the plots in Figure 80.

Figure 80 is for the urban canyon part of the urban case. When $|d| < 10$ m (panels (a) and (b)) it is clear that the strongest MPCs come via reflections off the buildings. However, from panel (c) onwards this changes and the beams do not trace to the transmitter at (0,0). If the secondary beam in panel (c), main beam in panel (d) and the secondary beam in panel (e) are not terminated after 4 reflections, there is a chance that they will go through the points of the transmitter. These rays will be very weak though due to the loss in power caused by the multiple reflections.

Something that these beams and the main beam in panel (c) have in common is that they all point towards the corner of a building, where rays get diffracted from. When $|d| > 10$ m, the behaviour of the ray paths displayed are consistent with the strongest rays arriving from the transmitter via diffraction off the edge of a building and then being received after at least one reflection.

In panel (d) the secondary reflection comes from a rather strange location. This is a rather interesting observation; when the data was being collected there were a few cars parked around the coordinates (-17,17), which is where the secondary beam is heading towards. This signifies the importance of accurate maps when using ray tracing to model propagation behaviour. Modelling reflections off vehicles is expected to take extra time and computation resources, but would be extremely beneficial.

In panel (e) the main beam appears to come directly from the right, where there is no transmitter. There was no traffic or any objects in the middle of the intersection which could have caused the rays to reflect in this direction. The behaviour is consistent with strong MPCs arriving at one or both of the strongest sidelobes; the secondary beam has an angle coincident with one of the larger sidelobes and there appears to be a relatively strong MPC arriving approximately in the direction of the other large sidelobe. The combined strength of the MPCs arriving in line with the sidelobes is larger than the MPCs arriving in line with the main beam when the azimuth angle = 0º. This is one of the drawbacks of this system as explained in Section 3.5.

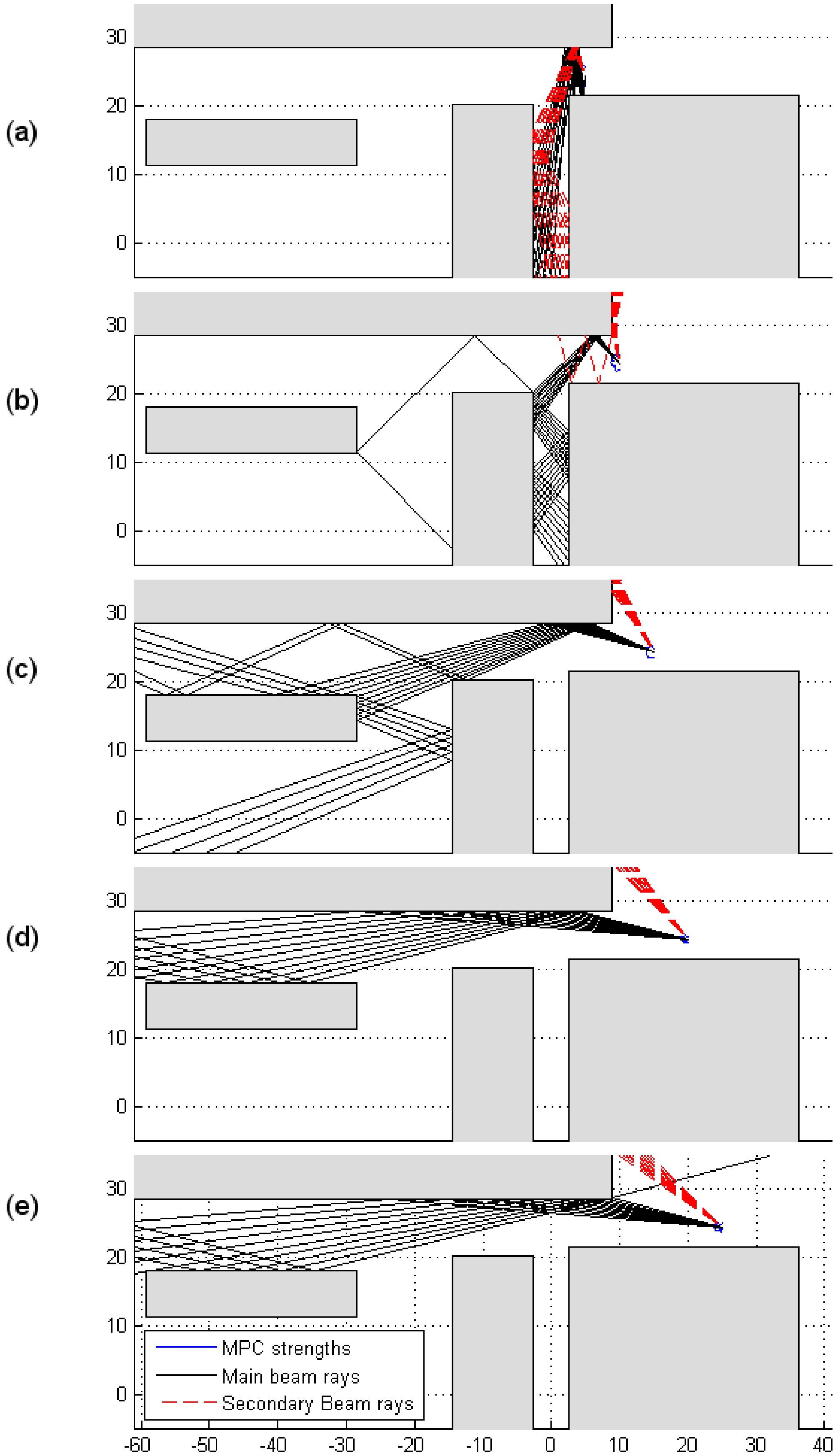

Figure 81: Projected main and secondary beams for data collected in the open part of the urban case. Panels (a) – (e) are for receiver positions 5, 10, 15, 20 and 25 m.

Figure 81 displays the projected main and secondary beams for data collected in the open half of the urban case. In panel (a) the main MPCs can be traced back to the transmitter and this applies to the main beam in panel (b) as well. The secondary beam in panel (b) appears from the corner of a building and this is consistent with diffraction.

Panels (c), (d) and (e) display some unexplainable sources for the main beam. Neither the main or secondary beams can be traced back to the transmitter at (0,0) and nor do they point towards the edge of a building, hence eliminating diffraction as an explanation. The main beam is the strangest as it appears to place the transmitter in the far left part of the map. The secondary beam points towards an angle which the transmitter would find near impossible to reflect rays off. Upon re-inspecting the area it was seen that there is a relatively high wall and multiple large metallic bins with irregular surfaces in the range 10 – 20 m on the x-axis and at 30 m on the y-axis. The tracing of these secondary beam rays are consistent with signals being reflected off the bins.

7.3 Conclusions

Data collected using the directional antenna confirms that shortly after LOS is lost in a T-junction, the strongest beams are the ones that are reflected towards the receiver. However, this changes as d increases; the strongest beam appears to involve diffracted waves as well as well reflected waves. This can provide a useful insight towards how many reflections and diffractions to incorporate into a model.

This set of measurements also proves the importance of map accuracy. The secondary beam in panel (d) of Figure 80 and the secondary beams of panels (c), (d) and (e) in Figure 81 all appear to point to a direction which cannot be traced back to the receiver. What the map does not show is that these rays do point towards reflective objects found irregularly placed in the area. As mentioned in Section 2.1.2, ray tracing is the most accurate prediction method for radio propagation. This does require extremely detailed maps which would have to be constantly kept up to date.

This experimental set-up was used to gain an improved understanding of the ray paths of the strongest beams being received in an urban environment. In the urban canyon portion of the measurements it is safe to say that reflections combined with diffractions comprise the main propagation paths. In the open half of the urban case this fact does not hold true for when d > 10 m, the main ray cannot be traced back to the receiver. Currently there is no explanation for this and more measurements would be beneficial to get a clearer understanding of where signals arrive from. The DAS is useful and can be used for further data collection in similar locations. It can also be useful towards verifying a ray tracing propagation model; to check if the model agrees with where the strongest rays arrive from.

8 Network Performance and Channel Measurement Data – Frequency Analysis

Chapter 4 displayed how the MPP and PDR varied for the data in collected in all the cases. This chapter delves into the Doppler spreads caused by mobile reflectors during the collection of data presented in Chapter 4.

8.1 Mesh Plots of the Data Collected in the Urban Case

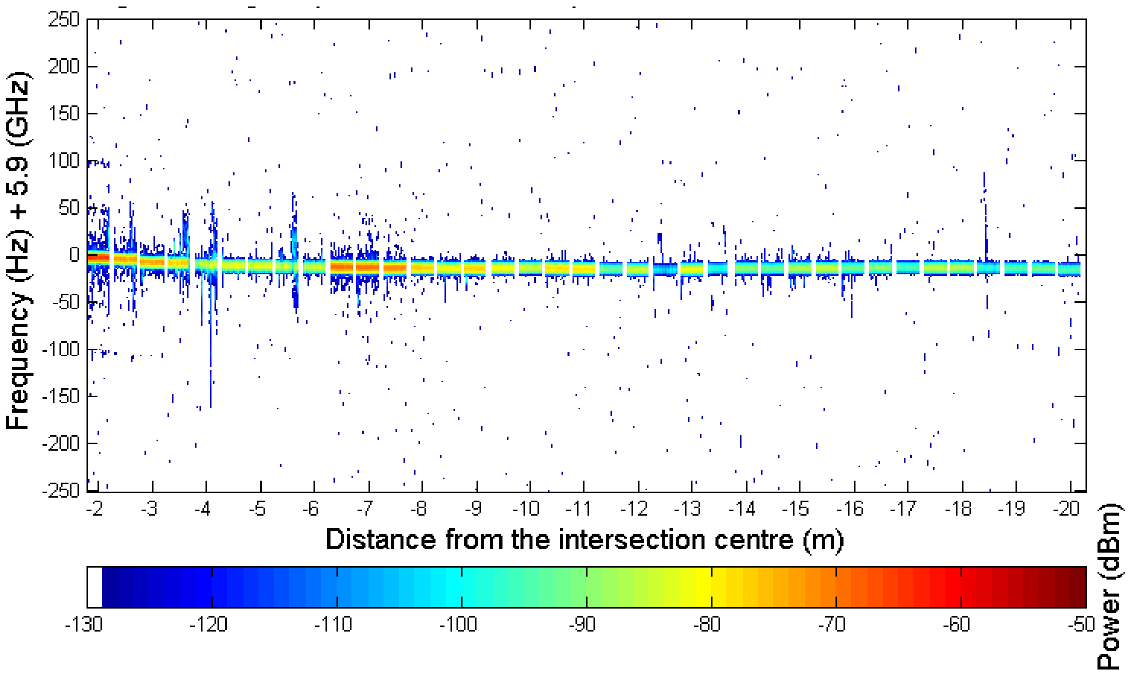

Figure 82: Plan view of all the spectra collected in run 1 of the urban case

Figure 82 shows a mesh of all the spectra collected in run 1. The spectra collected at each position are grouped together and the power in the continuous (CW) wave is shown by the horizontal coloured band which goes through the middle of the image. The gaps in the coloured band are five blank spectra inserted to distinguish the position boundaries that the spectra were collected from. This is how all the mesh plots are presented. Using these mesh plots it is possible to see all the spectra collected during data collection along with visualising the Doppler spreads caused by traffic.

The images also show how the power in the CW varies at each position. A feature visible in each of the meshes is that the frequency of the CW drifts by a few Hertz. This is due to the transmitter being moved outdoors and taking some time to get to a steady operating temperature which in turn causes a slight drift in the frequency. Because the equipment used a battery and data had to be collected as quickly as possible, it was not feasible to first let the equipment reach a stable operating temperature. The information extracted from each spectrum is the MPP and Doppler spread neither of which are not affected by this frequency drift. Frequency drifts are seen in most meshes where the data was collected for more than 30 minutes.

A small amount of power from the sidelobes is visible in the data collected closer to the intersection centre and there are minute bursts of noise spread across randomly in most spectra. The lowest value plotted is -130 dBm and some noise can be omitted if this is raised, but that would get rid of some details on Doppler spreads/shifts.

The Doppler spreads shown in Figure 82 does not have a large range and is within 100 Hz of where the peak of the CW. There are relatively longer Doppler spreads closer to the centre of the intersection and these are all caused by pedestrians; this was noticed on the spectrum analyser screen during data collection. On some runs it was simply not possible to maintain accurate information about pedestrian numbers whilst on some runs it was possible to record whenever small numbers of pedestrians would be present in the environment. In this measurement run there were three recordings of traffic which was made and this was towards the end of the acquisition at 2 m and 2.5 m. At 18.5 m it was noted that a cyclist passed through the road being used and this is visibly shown on the image as one of the largest Doppler spread.

The largest Doppler spreads (large in terms of both frequency shift and the power in these frequency shifted waves being received) were caused by pedestrians when they walked through the intersection centre and this was noticed while data was being collected. It also suggests the previous statement made about pedestrians altering the path geometry of the waves which causes variations in the received signal power. Another noticeable trend is that as the receiver gets moved further away from the intersection centre, the frequency span of the Doppler spread becomes smaller. The is because the received power in the main CW component greater than the background noise is also less at this point and so the rays which are Doppler spread having enough power to rise above the background noise is also reduced. It would be possible to see relatively similar ranges in Doppler spread throughout the measurement run if the background radio noise also decreased as the trolley moved away from the centre, but this does not happen in reality.

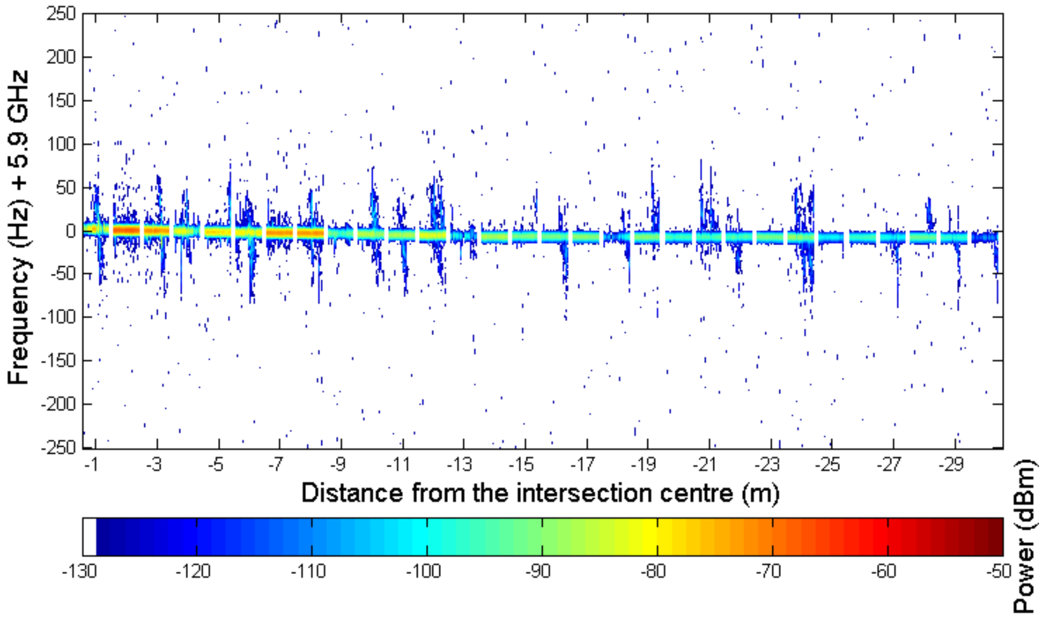

Figure 83: Plan view of all the spectra collected in run 2 at the urban case

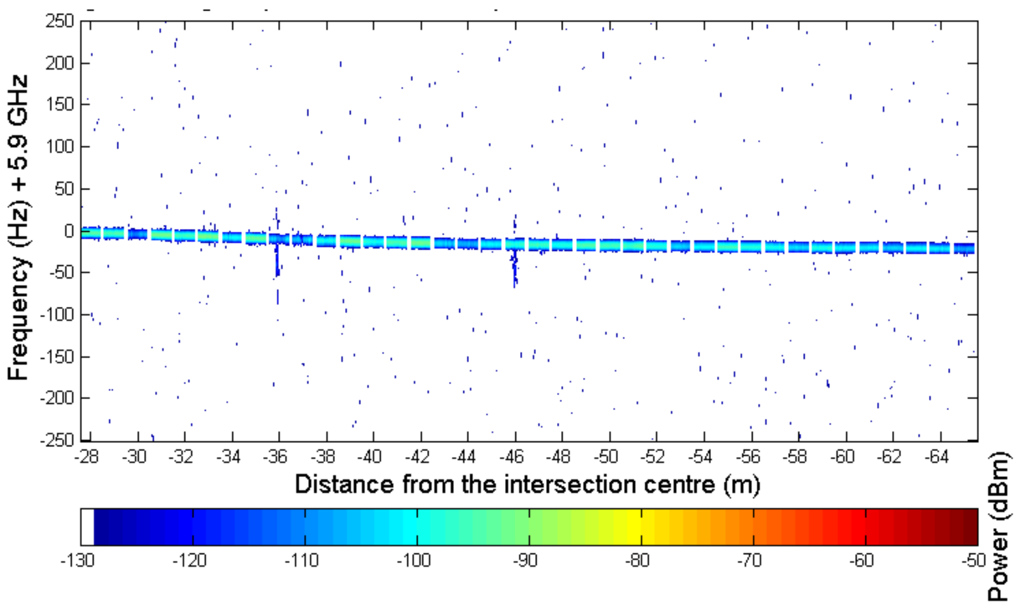

Figure 84: Plan view of all the spectra collected in run 3 at the urban case

Figure 83 displays the mesh made of spectra collected in run 2. During this run it was possible to keep a better record of the pedestrian traffic and unsurprisingly, every Doppler shift seen in the image happened when a pedestrian was noted to interfere with the propagation by passing through the intersection. The frequency drift in this set of measurements is lower than in the previous case and the range of the Doppler spreads is similar to that in run 1.

Figure 84 shows the mesh plot made from spectra collected during run 3 and it is instantly recognisable that there is less power being received at these distances compared with the two previous runs, which were both closer to the intersection centre. Only one pedestrian was recorded to have passed through the area that data was being collected and this can be seen clearly in the mesh at -46 m; despite the received power being lower than in the previous measurements, thus displaying the sensitivity of the equipment to Doppler spreads caused by humans.

The meshes generated from spectra collected in runs 4 and 5 are shown in Figure 85 and Figure 86. As previously mentioned, this data was collected in one session with run 4 being done first and then run 5 being done afterwards, starting from 30 m and coming back to the centre of the intersection. The data was collected on the right side of the intersection where there were more open spaces compared to the other side of the intersection and both these sets of data can be classed as being close to the intersection centre. The transmitter stabilised pretty fast without varying a lot from its original frequency.

There are considerably more Doppler spreads in these data sets as there was a lot of pedestrian traffic during the time of data collection. It was not possible to have a clear record of pedestrian traffic as there was a steady flow throughout the data collection. The sidelobes of the CW can be seen on data collected closer to the intersection and this is strongest in these two measurement sets; there is no explanation as to why this is strongest only on these sets. From all the data collected up to now, these sets have the largest Doppler spreads and these can be found at distances of 9, 12 and 10 m; the latter of those being in run 5. These Doppler spreads have extended beyond 150 Hz and in the case of data collected at 12 m, the Doppler spread is greater than 200 Hz (which corresponds to a velocity of over 36.61 km/h). This range of Doppler spread is hard to be connected with pedestrians and was likely caused by a cyclist or an automobile in the vicinity – whose presence was not recorded at the time as it was not in the immediate propagation environment.

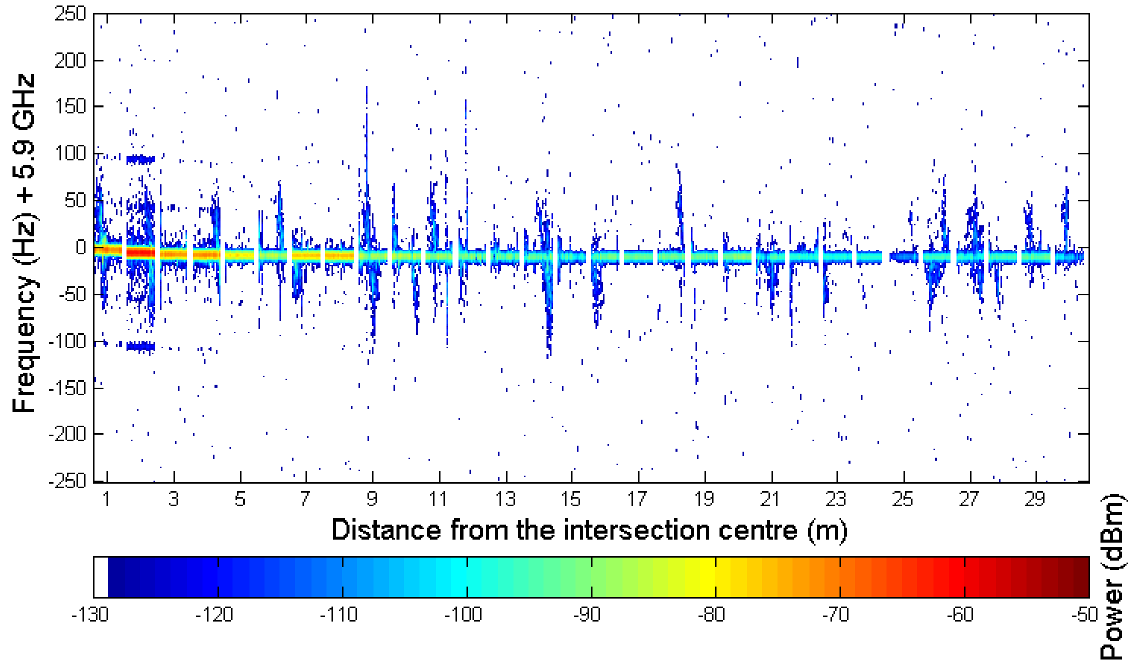

Figure 85: Plan view of all the spectra collected in run 4 at the urban case

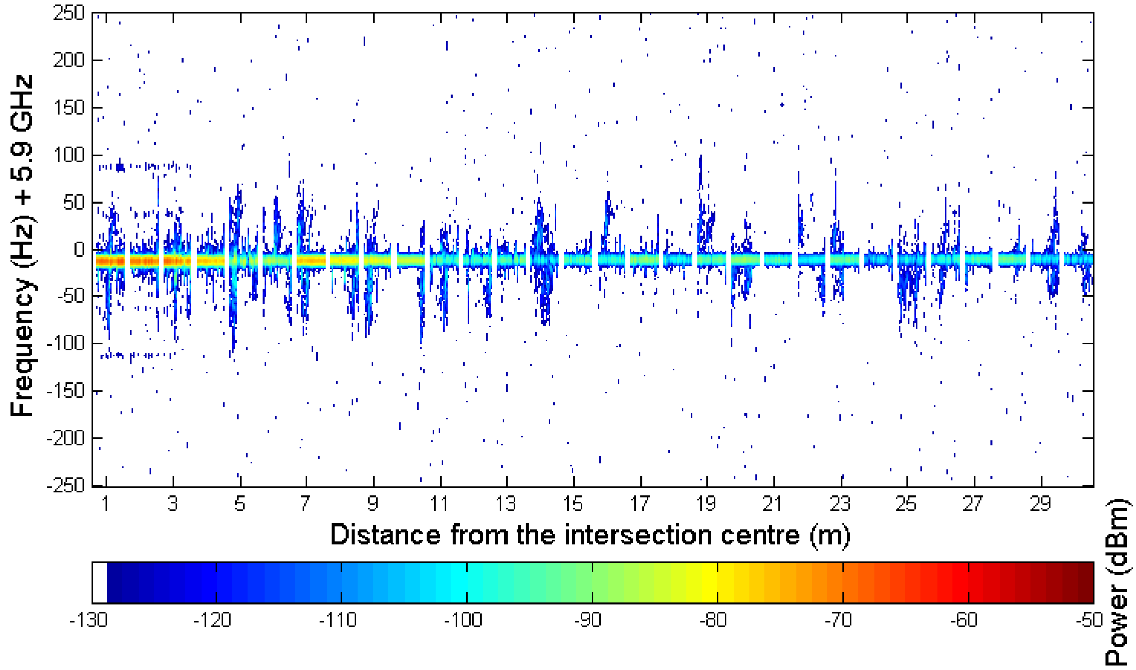

Figure 86: Plan view of all the spectra collected in run 5 at the urban case

Figure 87 displays the mesh created by all the spectra collected in run 6; which is a continuation of runs 4 and 5 and is not close to the intersection centre. Pedestrian traffic was low again as can be seen from the lack of Doppler spreads. Each Doppler spread can be associated to a pedestrian apart from the one at 45 m where there was no noted cause for the Doppler spread seen during data collection. Due to the short distance range for which the data was collected, less time was required and the CW frequency did not drift as much as in previous experiments.

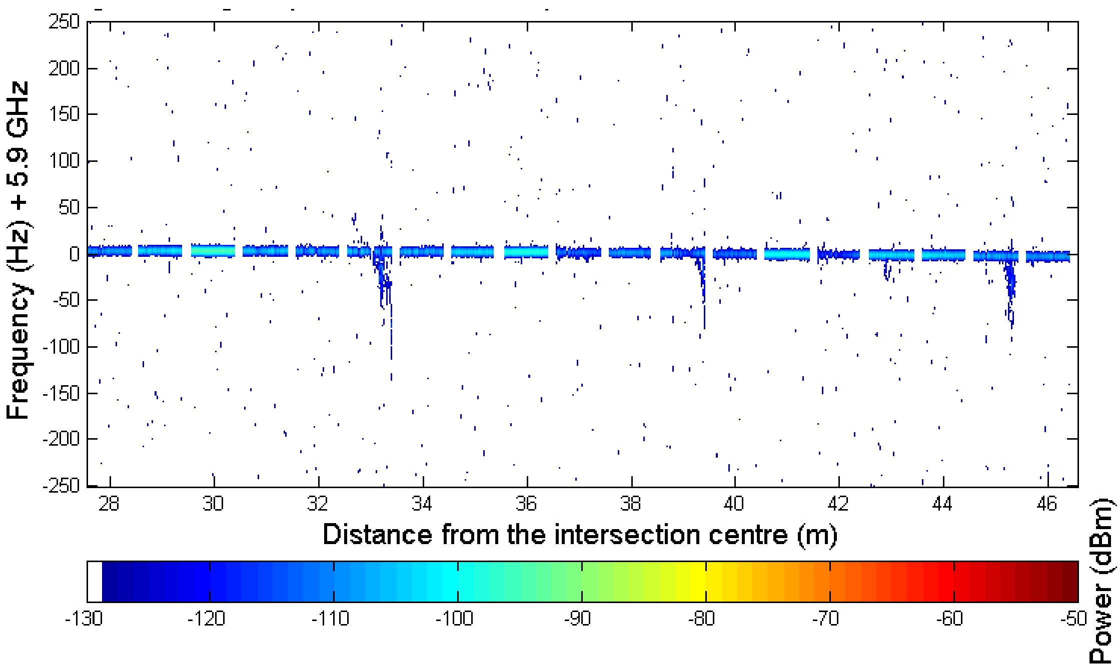

Figure 87: Plan view of all the spectra collected in run 6 at the urban case

In conclusion, the mesh plots provide a good overview of all the spectral data collected even though detailed or numerical information are harder to obtain. However, the information in the mesh can be processed to get more useful numerical information such as the median peak power which was plotted and displayed in Section 4.2.1. Mesh plots are a good indicator of the size and frequency of Doppler spreads which occurred during the data collection, which in turn is a good indicator of the traffic which was present along with its speed. There are instances where pedestrian information was collected but there are Doppler spreads when they are not expected. This could be due to pedestrians moving in the propagation environment (closer to the transmitter), but where they could not be seen at the receiver. These pedestrians would not be in sight for most of the time that the data was being collected as the main aim was to collect data in NLOS regions.

8.2 Mesh Plots of the Data Collected at the Less Urban Case

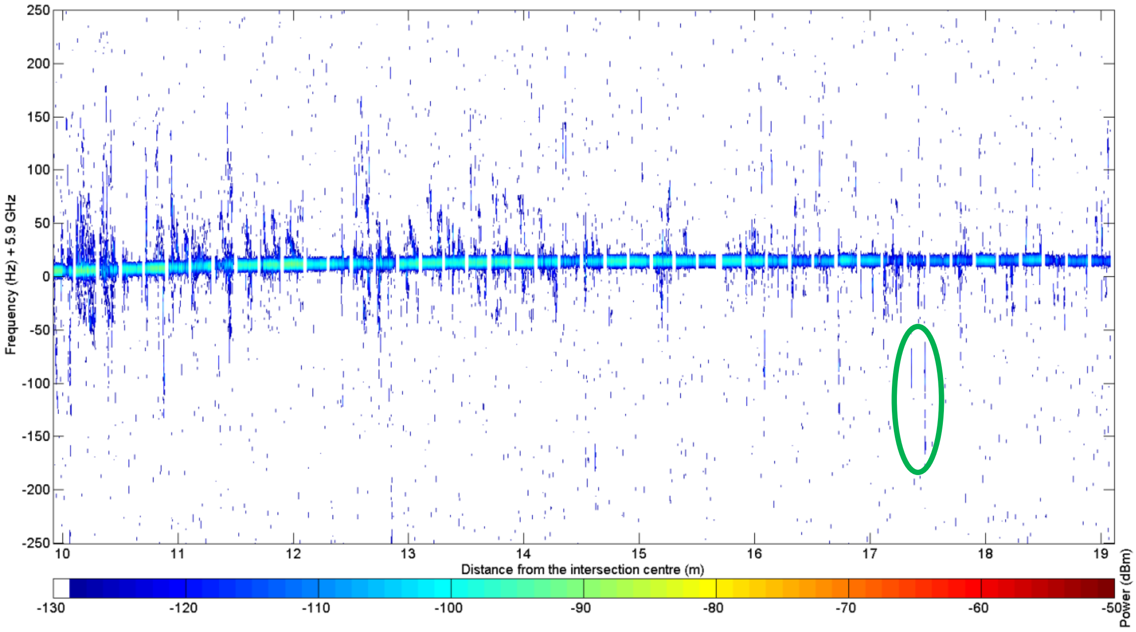

Figure 88: Mesh plot showing all the spectra collected in T50$_{NEAR}$ of the less urban case

Figure 88 and Figure 89 display the mesh plots created by the data collected in the less urban case with the transmitter 50 m away from the intersection (T50); the presence of the red bands in Figure 89 will be explained shortly. The CW frequency is within 10 Hz throughout both data collections due to equipment temperature variations - as with the previous mesh plots. The CW signal in Figure 88 shows clear gaps between the positions where the data was collected but in Figure 89 these gaps are relatively shorter, along with the length of each segment in the CW wave. This is because Figure 88 only shows data in the range $10.0 \leq d \leq 19.0$ m whereas Figure 89 shows data in the range $18.0 \leq d \leq 44.8$ m; these shorter segments in Figure 89 are caused by the increased data being displayed.

These two data sets have a markedly increased occurrence of Doppler spreads visible, along with larger Doppler spreads, in comparison with the previously collected data. These larger spreads are probably caused by the presence of vehicles passing through/near the radio propagation path instead of just pedestrians and cyclists – unlike in the previous case. Doppler shifts of reflected waves reach values close to 200 Hz (equivalent to velocity differences of 36.61 kmph) in these measurements, mostly visible in the data being displayed in Figure 88 which was data acquired closer to the intersection centre; where the CW signal has more power, resulting in the ability to detect larger Doppler spreads.

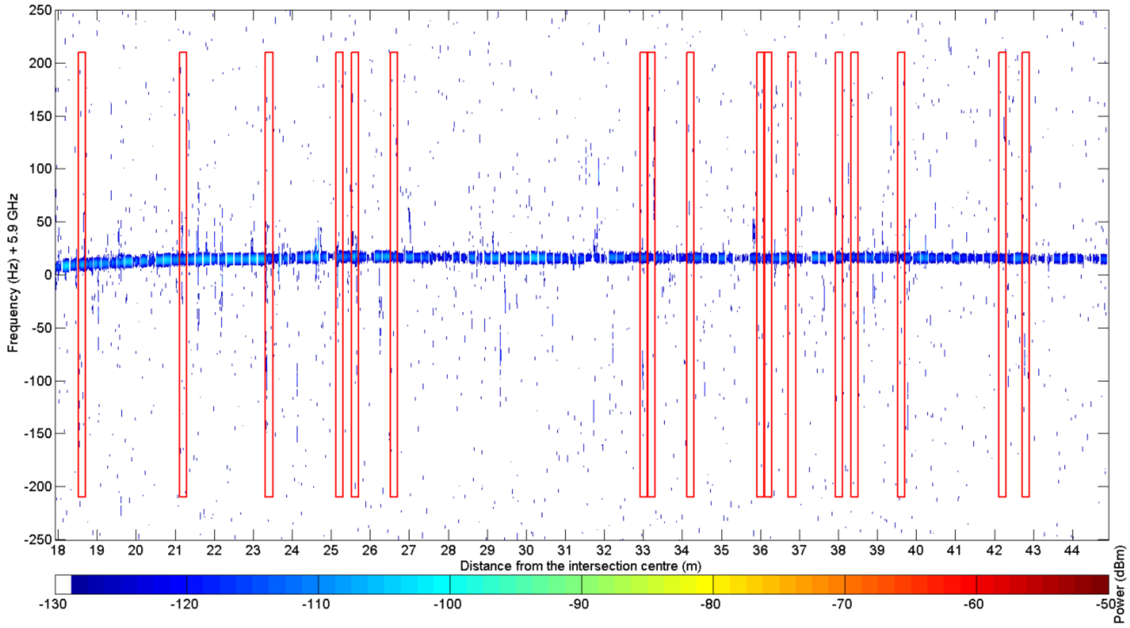

Figure 89: Mesh plot showing all the spectra collected in $T50_{FAR}$ of the less urban case

There is no record of traffic data for $T50_{NEAR}$ (Figure 88) but for $T50_{FAR}$ (Figure 89) a partial written record was kept of what was visible at the receiving station. The number of Doppler spreads and their ranges is a direct indication of the increased traffic present, along with the increase in speeds of these mobile reflectors, in comparison with the data collected in the urban case. There were more pedestrians who moved in all directions in this case compared to the open case; where pedestrians only moved along the path due to the layout of the environment. This made it more complicated to keep a rigorous record of their motion and presence.

In Figure 88 and Figure 89 there are also an increased presence of waves which are Doppler shifted away from the centre frequency, but there are no waves with frequencies in between these Doppler shifted reflections and the CW; isolated Doppler shifts. An example is encircled in green in Figure 88. This is due to reflections of the CW off a vehicle which is moving at a higher speed and is not within (or close to) the main propagation path, but is further away and only reflects the CW for a very short amount of time; less than a second. This distant and short interaction explains why the Doppler shifted wave has considerably less power and also why it is isolated from the CW's frequency.

The red bands in Figure 89 encapsulate the spectra that were collected at the positions where traffic was noted. The traffic notes are shown in Table 16 along with the potential affect they have had on the radio propagation. The information seen in Table 16 required zooming in on Figure 89 as it was not possible to see such detail otherwise.

d (m)	Observed traffic	Observed affect in mesh
18.6	Truck	Doppler spreads present; < 100 Hz
21.2	SUV	Doppler spreads present with more power in Doppler shifted rays; < ±50 Hz
23.4	Traffic burst	Doppler spreads and shifts present; < -100 Hz
25.2	Truck	Doppler spread present with more power in Doppler shifted rays; < ±50 Hz
25.6	Truck	Doppler spreads present with more power in the Doppler shifted rays; < ±50 Hz
26.6	Car	No significant Doppler spread or shift
33.0	Car	Some Doppler shifted rays visible; ≈ -100 Hz
33.2	Car	Some Doppler shifted rays visible with more power in the Doppler shifted rays; 50 – 100 Hz.
34.2	Car	No significant Doppler spread or shift
36.0	Slight traffic through the measurement	Doppler spread detected with more power in the Doppler spread rays; < ±50 Hz
36.2	SUV	No significant Doppler spread or shift
36.8	Large van	No significant Doppler spread or shift
38.0	Large truck	Doppler spread detected with more power in the Doppler spread rays; < ±50 Hz
38.4	SUV	No significant Doppler spread or shift
39.6	Slight traffic at the start	No significant Doppler spread or shift
42.2	Car	No significant Doppler spread or shift
42.8	Slight traffic at the start	Doppler Spreads present with more power in Doppler spread rays; ≈ ±50 Hz

Table 16: Table showing the Doppler shifts involved with non-zero PDR positions after the network failed.

Significant Doppler spreads have occurred even when there was no traffic visible from where the receiver was; which can be seen outside the red bands. These Doppler spreads are on occasion larger than the Doppler spreads which are suspected of being caused by vehicular traffic. The effects of pedestrian traffic are unknown in these measurements as mentioned previously because pedestrian traffic was not noted due to its random and fluctuating nature.

When the receiver is closer to the intersection centre, the Doppler spreads caused by traffic have a larger effect, which was also noticed in the previously collected data. Larger vehicles have caused larger and stronger Doppler spreads as well and this is because they have a larger area to reflect the radio waves (further details in Chapter 9). An important observation is that on a few instances, rays which were Doppler shifted had more power in them rather than the rays which were not Doppler shifted; the yellow rows in Table 16. There were also instances where the passing vehicles did not cause any detectable Doppler spreads; pink rows in Table 16. This happened more often as the receiving station was further away from the intersection centre and when the vehicle was a car; smaller vehicle with a smaller reflective area to reflect radio waves.

Figure 90 shows some of the spectra affected by Doppler spreads and shifts in $T50_{FAR}$ at d = 25.6 m. The first panel is an unaffected spectrum – the red vertical line shows the CW frequency at that time. The second panel's peak has dropped by 12.9 dB and there is more power spread either side of it. The third panel is an example of when the Doppler affected rays have 1.9 dB more power compared with the CW. The fourth panel has Doppler spread rays while the fifth panel appears to show the CW Doppler shifted by 4.16 Hz, which is rather insignificant

Upon zooming into the mesh it was noticed that there were more Doppler spreads and spikes in the power which are not visible in Figure 89. In Figure 32 (which shows the PDR of for the data collected in Figure 89) it was noticed how there were instances where there were extremely low non-zero PDR values after the receiving equipment was past 25 m from the intersection centre and how these happened to occur when there was no traffic noticed – this information was also displayed in Table 16. Based on the information seen there and also how Figure 32 shows Doppler spreads where no vehicles were reported to be seen, it was decided to highlight the spectra collected when a non-zero PDR is seen in $T50_{FAR}$ (data collected in the range $18.0 \leq d \leq 44.8$ m).

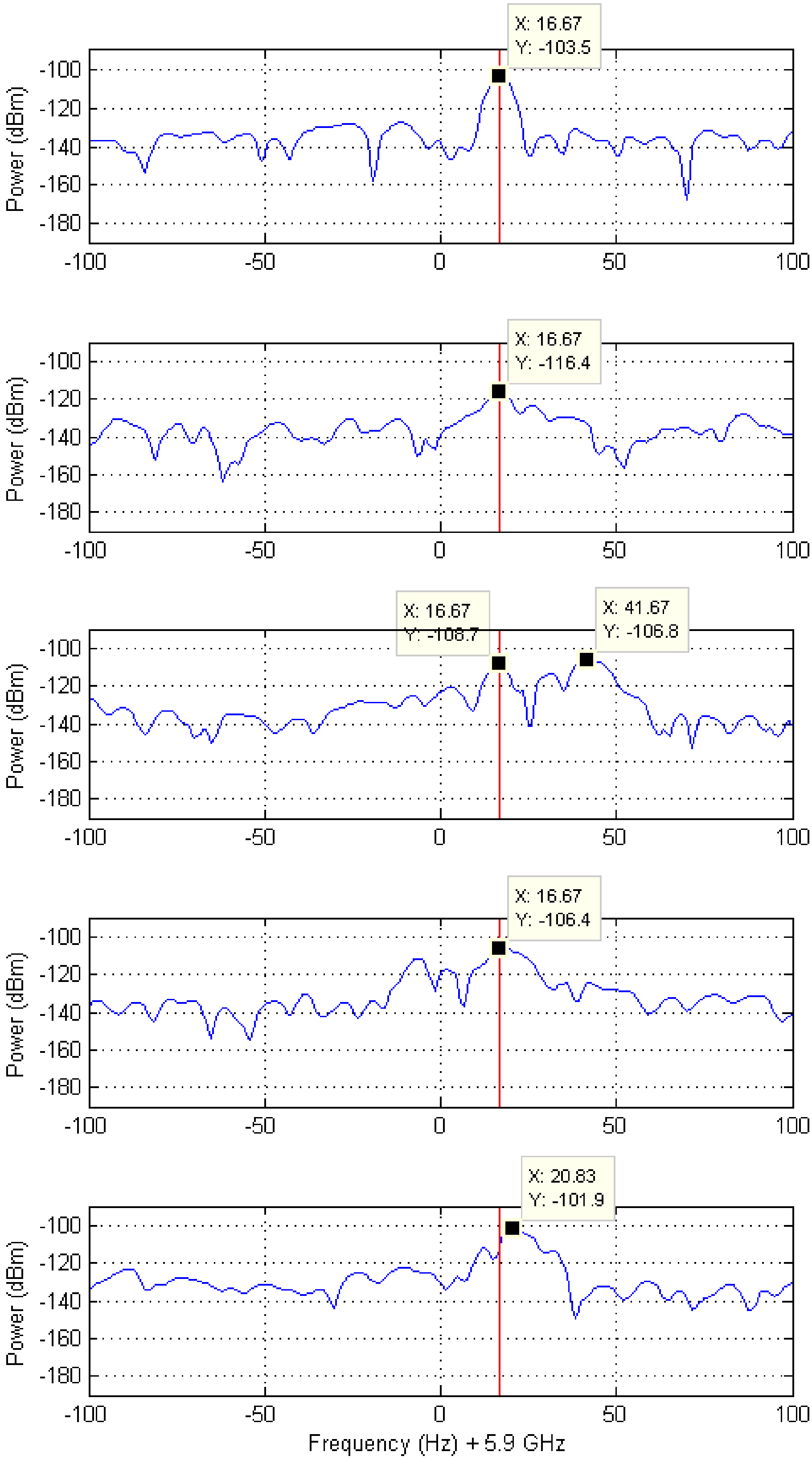

Figure 90: Doppler spreads and shifts as seen on spectra collected in T50$_{FAR}$, d = 25.6 m

Figure 91 to Figure 95 are enlarged portions of Figure 89; the solid red bands are the same as previously described and the dashed black bands encompass all the spectra which are from positions where the PDR is greater than zero, albeit being less than 10%. Table 17 contains all these positions with non-zero PDRs, in the range $18.0 \leq d \leq 25.0$ m, along with their PDR value; these positions were omitted in Table 16 which was displayed previously. Almost all the Doppler spreads are now enclosed within the black and red bands and this is a common feature amongst all the figures. There are a very small number of Doppler spreads/shifts which are not captured in these bands and they all have very low powers.

Distance from intersection centre (m)	PDR > 0% (%)
18.00	2.29
18.20	2.82
18.40	0.73
18.60	23.74
18.80	0.73
19.00	0.24
19.20	0.24
19.60	2.17
20.80	1.93
21.20	1.09
21.60	1.44
22.00	0.59
22.20	1.57
22.60	0.30
23.00	1.62
23.40	2.80
23.60	3.96
24.20	0.29
24.60	7.35
24.80	1.09

Table 17: Table showing the positions between 18 and 25 m which had a non-zero PDR

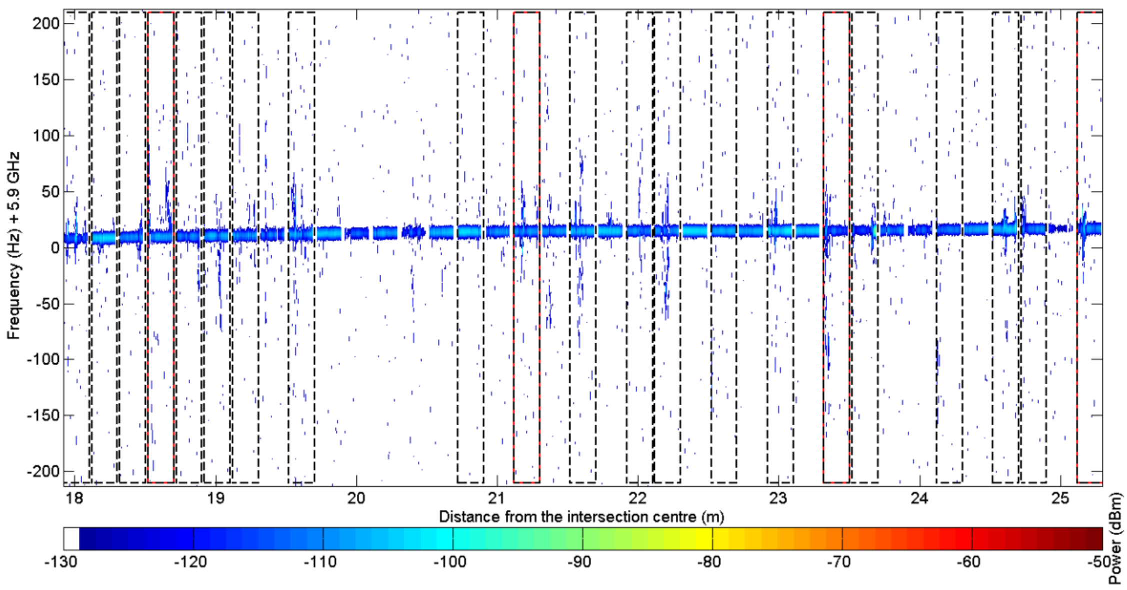

Figure 91: Enlarged plan view of spectra from $T50_{FAR}$; $18.0 \leq d \leq 25.0$ m

Doppler spread rays are seen to have more power in them yet again, similar to what was seen previously. The last few spectra collected at 23.6 m have a very small Doppler spread and also have considerably more power in comparison to the other spectra collected at the same position. Coincidentally, this position has the third highest PDR in the range [18, 25] m; one of the other two positions being closer to the intersection centre and the other is when there was a truck passing through the propagation environment and at 24.6 m.

At 24.6 m two Doppler spreads have occurred; at the middle and at the end of the data collection. Both these Doppler spreads, which comprise rays with more power, imply that the rays propagating from the transmitter to the receiver at that time were assisted by the object they were being reflected off. As mentioned previously in Chapter 3, there are 15 packets for every spectrum collected. 28 packets were received and this falls within the number of packets which would be received within an interval of collecting two spectra; more than two spectra display Doppler spreads. It can be said with confidence that the received packets coincide with the spectra which show Doppler spreads.

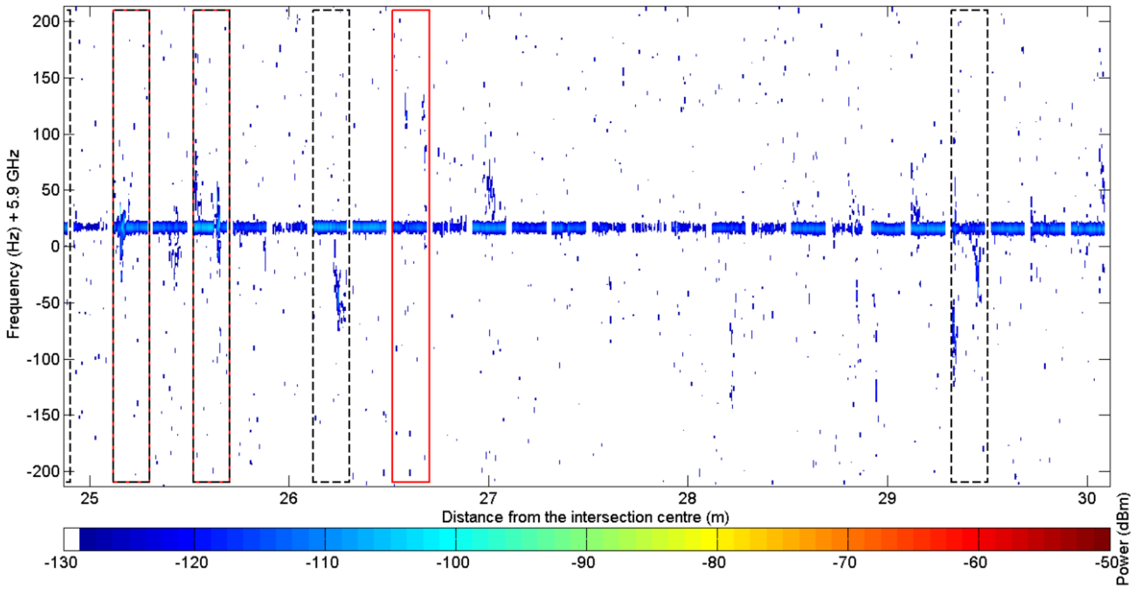

Figure 92: Enlarged plan view of spectra from $T50_{FAR}$; 25.0 ≤ d ≤ 30.0 m

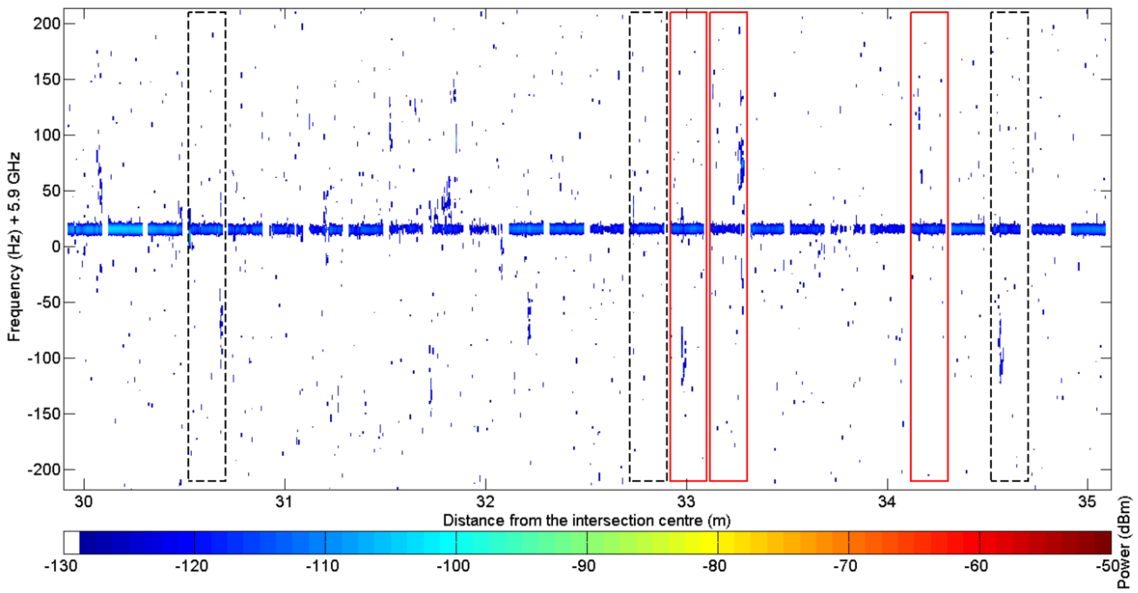

Figure 93: Enlarged plan view of spectra from $T50_{FAR}$; 30.0 ≤ d ≤ 35.0 m

It is no coincidence that almost all of the positions which have Doppler spread spectra also have a non-zero PDR and it can be concluded that the road traffic (irrespective of visibility at the receiver) has directly improved the 802.11p network's performance, albeit for a very short amount of time (takes approximately 1.5 s to collect a spectrum and 15 packets would be transmitted in this time) which in turn only contributes to a very small increase in PDR (less than 5% in most cases). Despite not seeing (or being able to record) the traffic which has improved communications, the Doppler spreads imply that the waves were reflected off moving objects – the pedestrian and vehicular traffic present in the propagation vicinity.

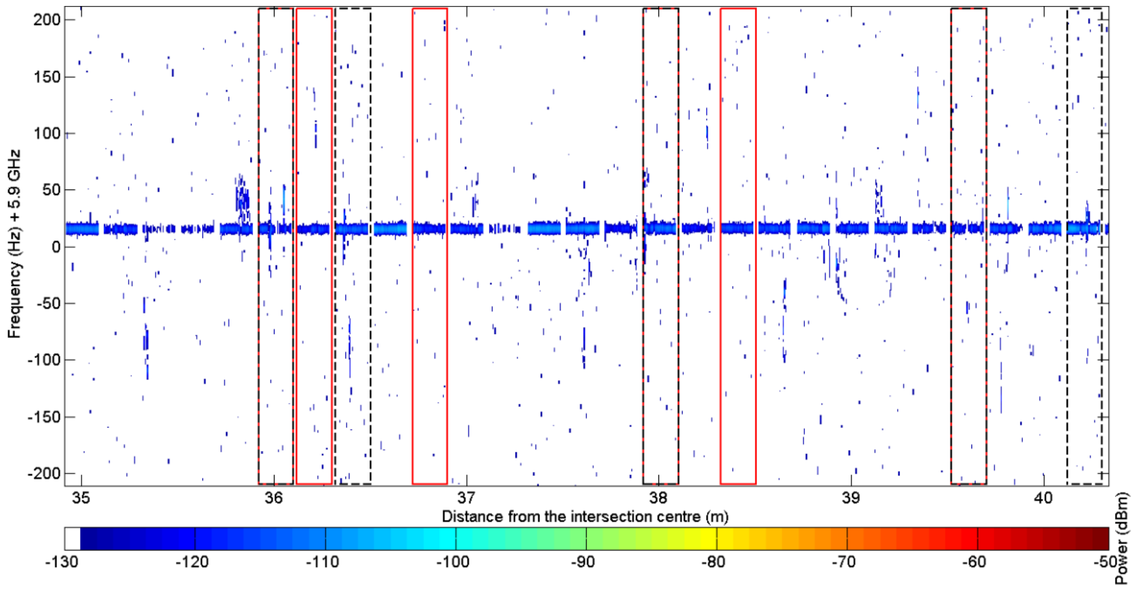

Figure 94: Enlarged plan view of spectra from T50$_{FAR}$; 35.0 ≤ d ≤ 40.0 m

802.11p networks will be deployed in areas with dense vehicular traffic which will in turn assist the PDR. However, if each of these vehicles were to also contribute towards increasing the network traffic, another study will have to be performed to find out where the advantages of vehicular traffic become overcome by the disadvantage of increased network traffic.

Figure 96 and Figure 97 display the mesh plots obtained from the spectra collected in the less urban case with the transmitter 70 m (T70) away from the intersection centre.

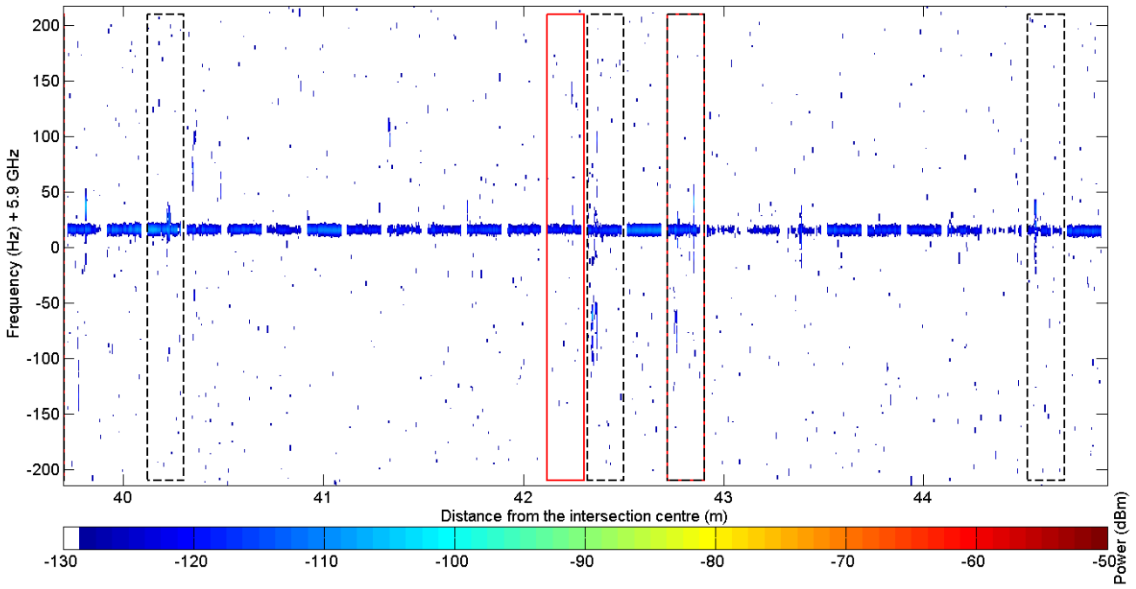

Figure 95: Enlarged plan view of spectra from T50$_{FAR}$; 40.0 ≤ d ≤ 44.8

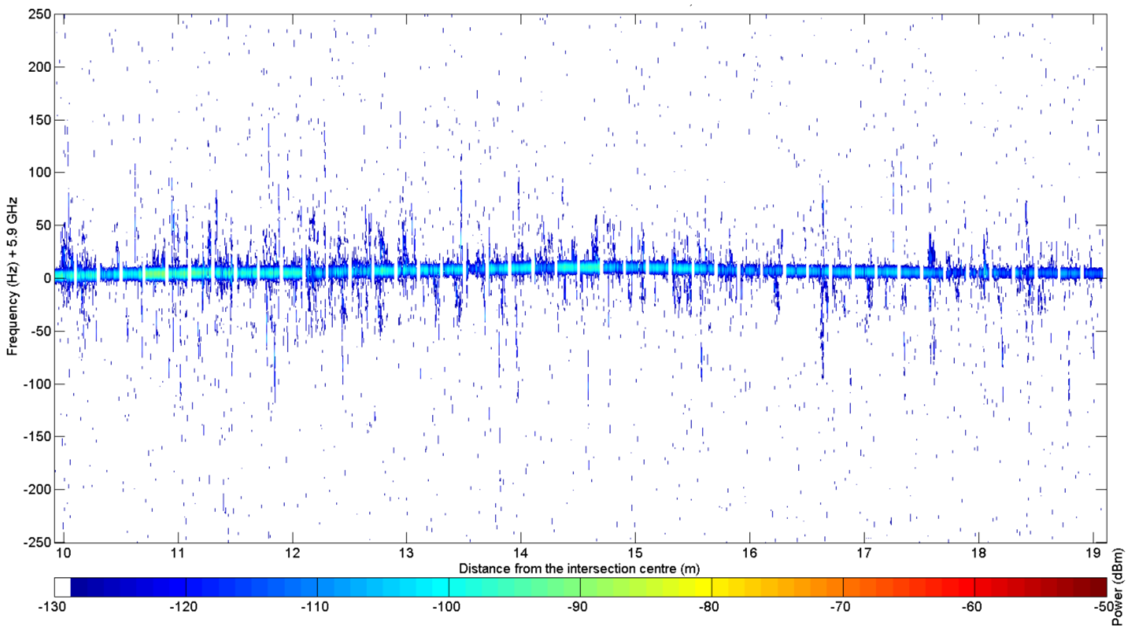

Figure 96: Plan view of all the spectra from $T70_{NEAR}$ in the less urban case

No specific traffic data was recorded during $T70_{FAR}$ but it was noted that there was low amounts of traffic during both the measurements.

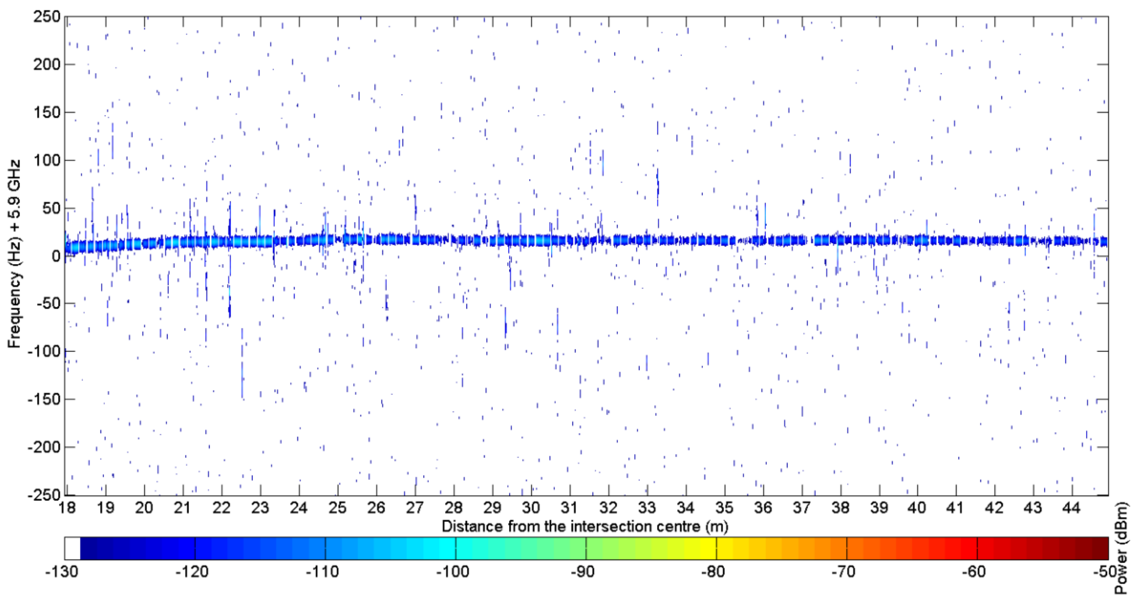

Figure 97: Plan view of all the spectra from $T70_{FAR}$ in the less urban case

In comparison with $T50_{NEAR}$ (at a glance) there appears to be a similar number of Doppler spreads in the data. However, $T70_{NEAR}$ appears to have smaller Doppler spreads than those seen in $T50_{NEAR}$; the Doppler spreads seen in $T70_{NEAR}$ appears to have a maximum magnitude of approximately 100 Hz while those in $T50_{NEAR}$ have Doppler spreads with magnitudes almost reaching 200 Hz. These smaller Doppler spreads can be explained from the reason that there are 20 extra metres in $T70_{TOT}$, which causes the Doppler spread rays with less power to get buried in the background noise; similar to the data in $T50_{FAR}$.

According to the model VirtualSource11p the difference in the power should only be 3.76 dB and the maximum size of the Doppler spread has been halved in this drop. To further investigate, the number of spectra (in $T50_{NEAR}$) with more than -130 dBm at +50 and 50 Hz away from the centre frequency was found to be 155 and 78 respectively. Out of this, only 31% and 22% of the spectra had more than -126.24 dBm; which explains the reduction in the size of Doppler spreads between $T50_{NEAR}$ and $T70_{NEAR}$.

When analysing the data from $T50_{FAR}$ it was seen how the Doppler spreads coincided with non-zero PDR values and with traffic in the propagation environment; some of which was not seen but assumed to be traffic as this was the only viable explanation to the Doppler spreads.

Based on this analysis and conclusion, it was decided to find out all the positions with non-zero PDR values in $T70_{FAR}$. These distances were then used to highlight the spectra collected from non-zero PDR positions in the mesh.

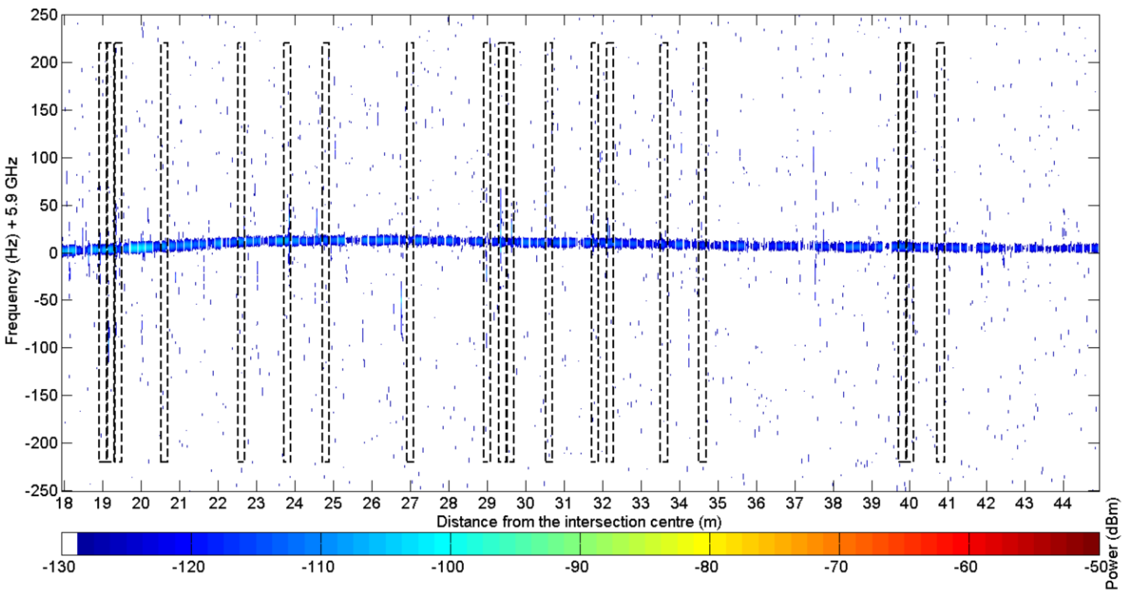

Figure 98: Plan view of all the spectra from $T70_{FAR}$ in the less urban case; positions with non-zero PDR are enclosed in the black bands

Figure 98 displays the same mesh as Figure 97 but with the dashed black bands denoting the positions where there were non-zero PDR values. A lot of the Doppler spreads fall within the black bands as it was noticed in T50; thus consolidating that moving objects in the propagation environment (such as traffic) temporarily assisted packet delivery albeit the PDR increase usually being less than 5%. There are three locations on the mesh which appear to have higher power in their spectra compared to the rest of the spectra. These positions are at 29.4, 31.8 and 33.6 m and coincidentally they have relatively high PDR values compared to their surroundings; 4.09, 3.95 and 0.70. These spikes in PDR can be seen quite clearly in Figure 33.

In conclusion to the data collected in this case, it can be said with confidence that vehicles in the propagation environment can be helpful towards improving the data network as these vehicles reflect the radio waves which in turn extend the wave's coverage range, enabling the reception of packets which would otherwise be lost. It is also clear that the presence of a vehicle, cyclist or pedestrian does not always result towards increasing the PDR and this is because not every visible Doppler spread has an increase in PDR attached to it. It is believed that the larger vehicles, such as trucks (which have a larger reflective surface), will be better at improving the PDR as opposed to small cars or sports utility vehicles.

8.3 Mesh Plots of the Data Collected at the Open Case

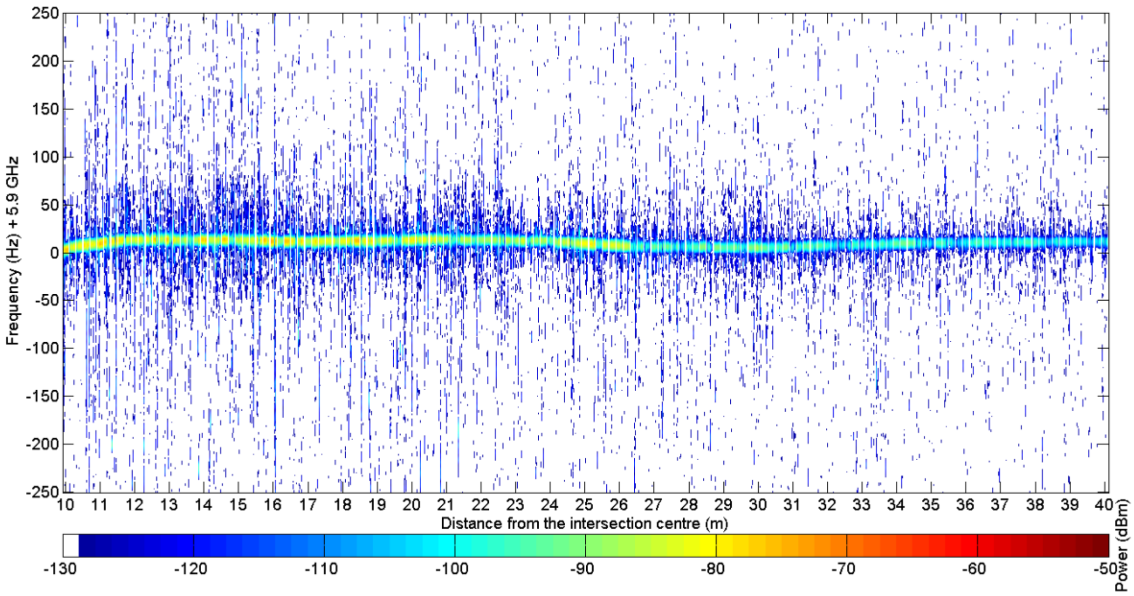

Figure 99: Spectra collected in the opposite path of the open case

Figure 99 shows the mesh created by all the spectra collected in the opposite path of the open case. As with previous meshes the main CW wave which runs along the middle is seen to rise and fall before settling at approximately 25 Hz higher than it should be. The

Doppler spreads and shifts are much larger and more frequent in this set of data and this is because the data was collected with a public road in between the transmitter and the receiver; where the received signals at each position have been influenced more by the many moving vehicles of all sizes/shapes and also the pedestrians in the vicinity. The Doppler spreads/shifts seen in Figure 99 regularly reach ±200 Hz and probably go beyond 250 Hz as well, but cannot be seen due to the span of the spectrum analyser being set to 500 Hz. Such large Doppler effects were not seen in any of the previous cases due to the traffic not moving as fast.

There is also an increased presence of signals which appear to be simply Doppler shifted; these are the signals which appear to have higher (than the background radiation) power levels and are located away from the main CW, with only background radiation between these signals and the CW. These signals are also a consequence of faster moving traffic further away from both the transmitter and receiver – a small fraction of signals get reflected by these vehicles as they are moving with higher speeds and in relative isolation. At the receiver these Doppler shifted rays combine with all the other rays and if there are no rays with lower Doppler shifts, the rays which were affected appear isolated from the main CW. The maximum Doppler shifts seen correspond to velocities of approximately 46 km/h (29 m/h).

In the urban case this was barely seen because the common type of traffic was pedestrians, who move a lot slower, and were also closer to the system. Because the reflective surfaces were closer to the propagation environment, the rays being reflected off surfaces moving at lower relative velocities were also detected as they did not lose their power in the process of travelling far, to reach the receiver. In the other two cases, it is believed that not a lot of rays are detected if they have been reflected off portions of the moving object which were moving at lower relative velocities and this is due to the distances and speeds involved.

The next few figures of mesh diagrams comprise of spectra collected on the side of road which had the transmitter; the adjacent path. Five data collection runs were made on this side of the road and more distance was covered; up to 71 m away from the centre of the intersection. These five runs will be referred to as run 1 to 5 in the next figures and the distances covered by each measurement run are in Table 18.

Run Number	Distance range (m)
1	10.00 – 34.00
2	30.00 – 35.60
3	30.00 – 58.00
4	55.00 – 64.80
5	65.00 – 71.00

Table 18: Table showing the distances covered by each run in the open case

Figure 100 shows the mesh made of the spectra collected in the first run on the adjacent path; there are some similarities with the mesh comprising of spectra collected on the opposite of the road (Figure 99). The Doppler shifts and spreads appear to occur in similar frequency and size. Both images show Doppler shifted rays with more than -100 dBm of power; in the PDR and MPP graphs, this level of MPP corresponded with PDRs which enabled vehicular communications, albeit not to a standard to satisfy safety critical communications. Both the measurements made on either side of the road have spectra with larger Doppler spreads and shifts. The data in Figure 100 also shows the CW frequency rise and fall throughout the data capture.

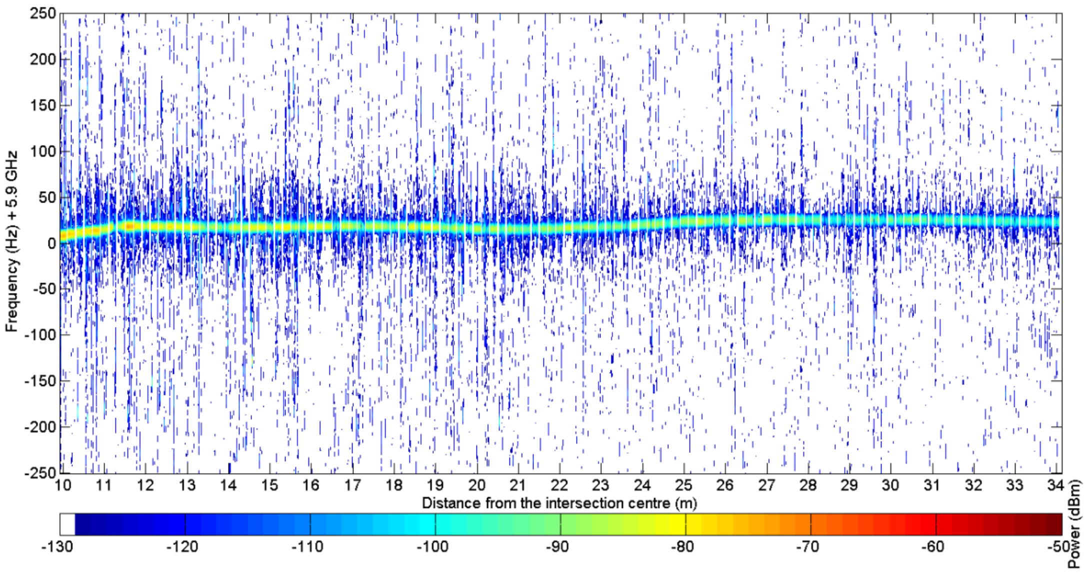

Figure 100: Plan view of all the spectra collected in the 1st run of the adjacent path in the open case

Figure 101 and Figure 102 shows the meshes created from run 2 and 3 in the open case; run 2 is a shorter version of run 3. In the common distances the Doppler spreads and shifts occur in similar numbers and frequency ranges. Figure 102 however shows that as the receiver is moved away from the intersection centre, the Doppler spreads and shifts reduce in both size and frequency of occurrence. This reduction in occurrence of

Doppler spreads and shifts is a trend that continues along the path and can be seen in Figure 103 and Figure 104; this also keeps with the trends seen at the other cases where the effects of Doppler spreads and shifts reduce as the receiver is moved away from the intersection centre.

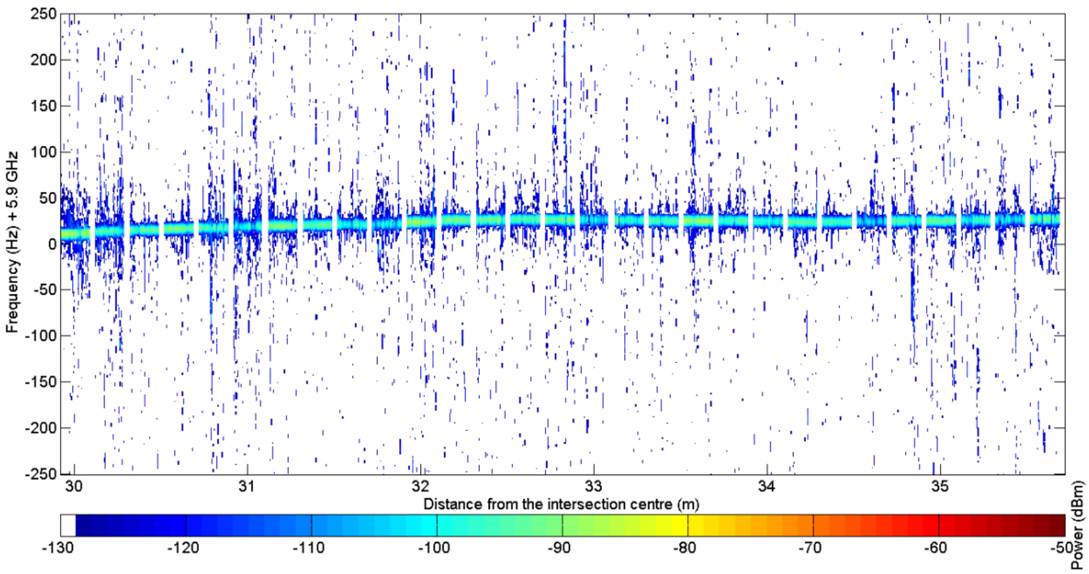

Figure 101: Plan view of all the spectra collected in the 2nd run of the adjacent path in the open case

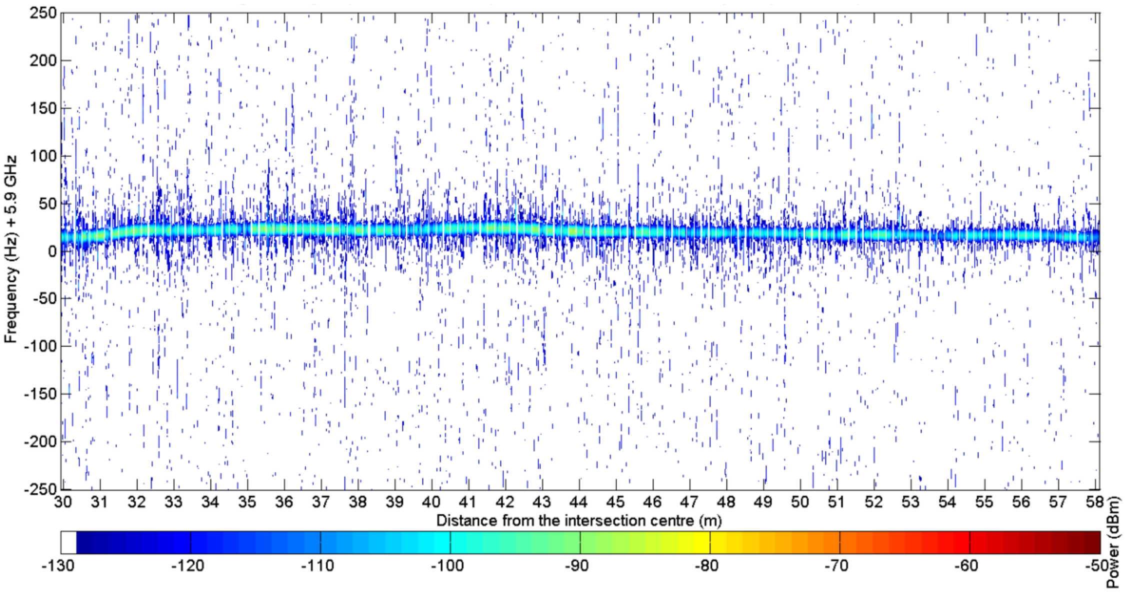

Figure 102: Plan view of all the spectra collected in the 3rd run of the adjacent path in the open case

In the last two measurement runs (shown in Figure 103 and Figure 104) the CW frequency does not appear to vary a lot throughout the experiment. As mentioned previously, this variation is not expected to have an effect on the conclusions drawn from the data.

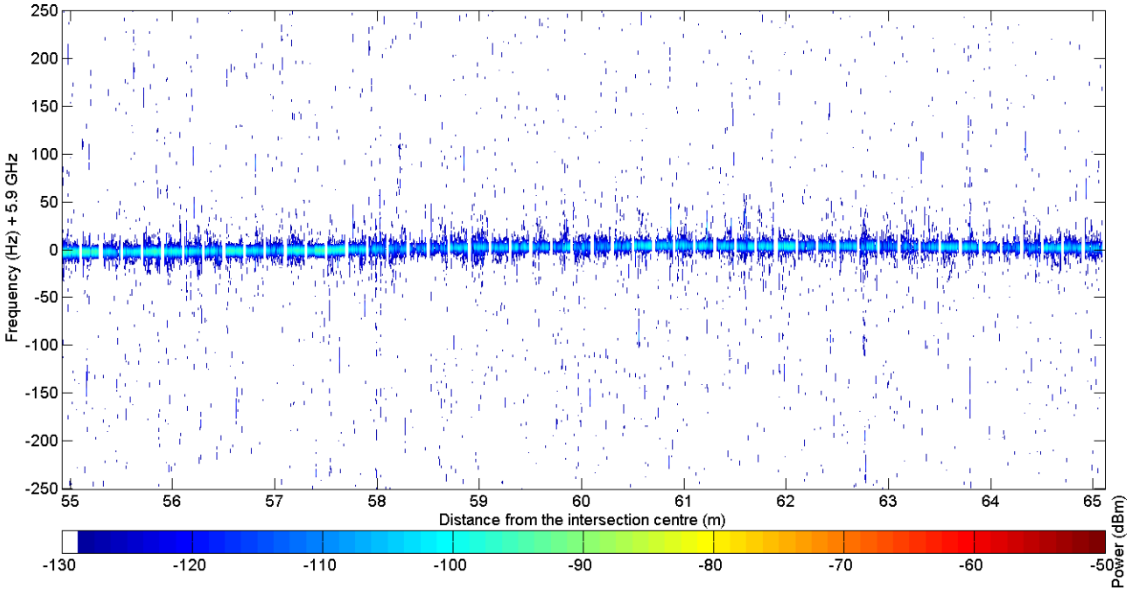

Figure 103: Plan view of all the spectra collected in the 4th run of the adjacent path in the open c

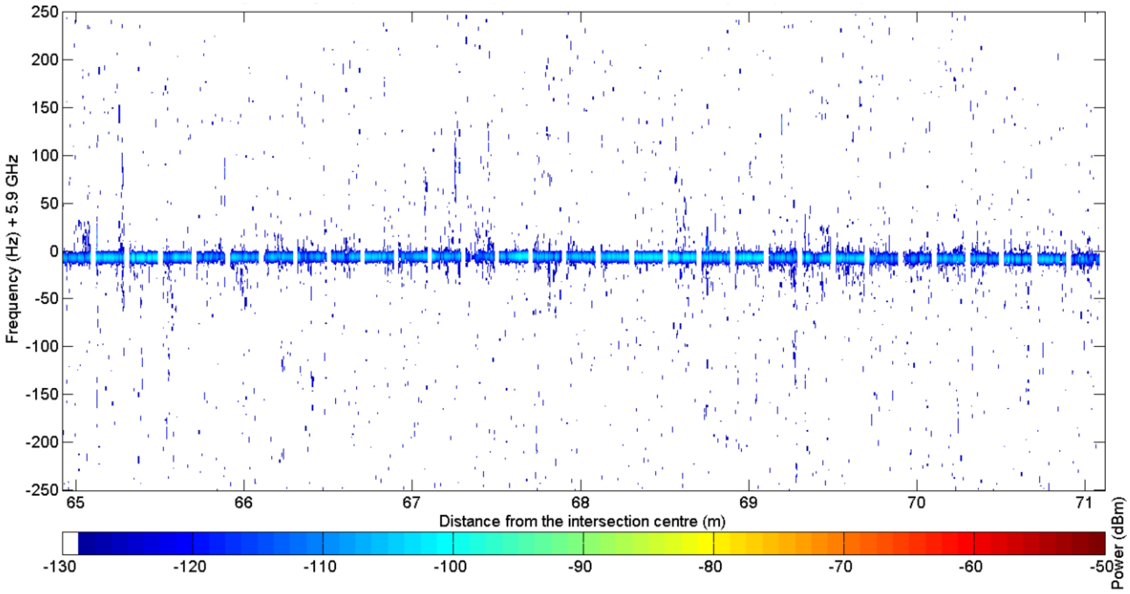

Figure 104: Plan view of all the spectra collected in the 5th run of the adjacent path in the open case

8.4 Conclusion: Effect of Traffic on the PDR and MPP

Traffic affected the MPP and PDR in each of the cases and the different types of traffic had their individual influence on the data; increasing speeds caused larger Doppler spreads and when there was more traffic, more Doppler spreads and shifts were seen. Apart from these expected effects, a couple of other effects were also noticed. In the urban case where there were two paths it was observed that on the path with less buildings the traffic had a more significant effect on the variation of the MPP because the proportion of waves being influenced by pedestrians were higher.

In the less urban case there were both pedestrian and vehicular traffic and the PDR dropped to 0% within 16 m of the intersection centre. Considerably more data was collected beyond the point where the vehicular network failed and as larger vehicles went through the intersection centre, the PDR increased by a small percentage; usually less than 5%. Traffic was not high when these observations were made and it is expected that if traffic were to be higher in an environment with similar building geography, a small number of rays which would have propagated into open areas would be reflected towards the receiver and assist vehicular networks. There were very slight increases in PDR at distances (further from the intersection centre) where no packets were usually received and these PDR spikes coincided with Doppler spreads/shifts on the spectra which prove that the traffic has assisted message throughput. It was also noticed that larger vehicles had the most impact as they had an increased surface area to reflect the waves.

Another important observation in the data collected in the less urban case was that the size of the Doppler spread appears to have a link with the size of the vehicle reflecting the signal. This is because larger vehicles have a larger surface to reflect more signals. These reflected signals will be Doppler shifted and as more rays are received, the range of Doppler spreads in the signals received increases. This causes an increase in Doppler spread. This hypothesis is modelled in the next chapter.

9 Vehicle Size and Doppler Effects

9.1 The Dependencies of Doppler Spread on Vehicle Size – A Simple Model

In Chapter 8 it was explained how larger vehicles appeared to cause larger Doppler Spreads. In this section a simple method for simulating this is presented. The assumptions made in this model are as follows (see also Figure 105).

- The single vehicle is modelled as a rectangle.
- The transmitter and receiver are stationary while the vehicle moves past them in a line parallel to a line drawn between the transmitter and the receiver.
- The vehicle will only reflect waves from the side facing the transmitter and receiver and all points will reflect signals from the transmitter to the receiver (essentially scattering rather than reflecting).
- All 'reflected' signals are assumed to have equal power irrespective of the ratio between its incidence and reflection angles.
- No Line-of-Sight component is considered

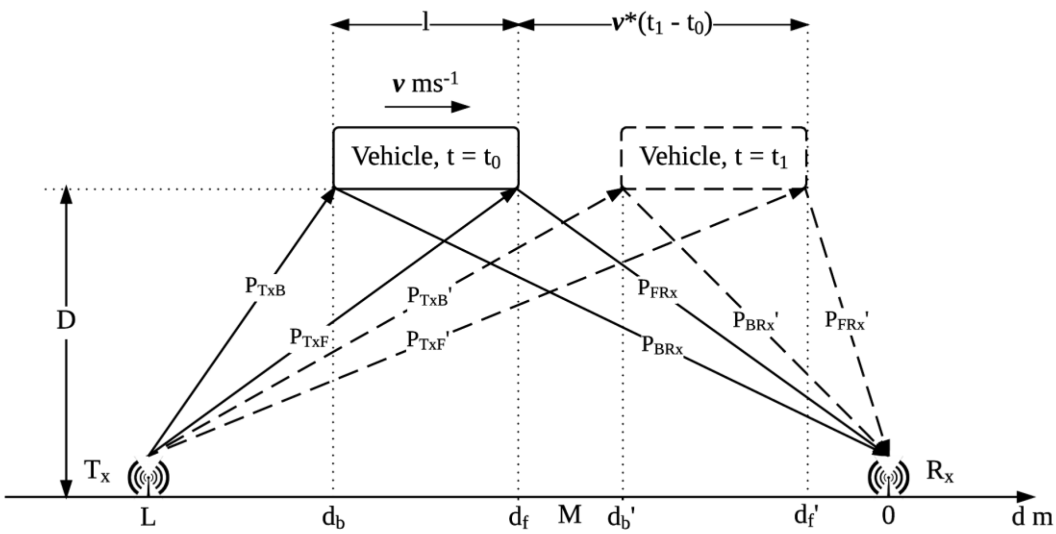

Figure 105: Diagram showing the rays reflected off the front and back of the side of a moving vehicle from the transmitter to the receiver at times t_0 and t_1

Table 19 lists the definitions of the various parameters in Figure 105. The receiver is kept at the origin and $t_1 - t_0$ is assumed to be very small.

Parameter	Description
T_x	Transmitter
R_x	Receiver
D	Normal distance between the vehicle and a line drawn from the T_x to R_x.
L	$T_x - R_x$ separation
M	Midpoint of the $T_x - R_x$ separation
l	Length of the vehicle
$\boldsymbol{v}$	Velocity of the vehicle
t_0	Initial time
t_1	Small amount of time during which the vehicle has moved
d_b	Horizontal distance between the back of the vehicle and the R_x at t_0
d_b'	Horizontal distance between the back of the vehicle and the R_x at t_1
d_f	Horizontal distance between the front of the vehicle and the R_x at t_0
d_f'	Horizontal distance between the front of the vehicle and the R_x at t_1
P_{TxB}	Path-length between T_x and the back of the vehicle at t_0
P_{BRx}	Path-length between the back of the vehicle and R_x at t_0
P_{TxF}	Path-length between T_x and the front of the vehicle at t_0
P_{FRx}	Path-length between the front of the vehicle and R_x at t_0
P_{TxB}'	Path-length between T_x and the back of the vehicle at t_1
P_{BRx}'	Path-length between the back of the vehicle and R_x at t_1
P_{TxF}'	Path-length between T_x and the front of the vehicle at t_1
P_{FRx}'	Path-length between the front of the vehicle and R_x at t_1

Table 19: Symbols used in Figure 105 and text

A signal undergoes a Doppler shift due to its phase varying as the pathlength varies (Parsons 2000). The relationship between the phase (*Φ*) and pathlength (*l*) is shown in Equation (18) while Equation (19)shows the relationship between a signal's Doppler shift (Δ*f*) and its phase.

$$\Delta\Phi = \frac{-2\pi}{\lambda}\,\Delta l \qquad (18)$$

$$\Delta f = \frac{-1}{2\pi}\,\frac{\Delta\Phi}{\Delta t} \qquad (19)$$

Combining Equations (18) and (19), the Doppler shift can be represented as a function of the change in pathlength; Equation (20).

$$\Delta f = \frac{\Delta l}{\lambda \Delta t} \tag{20}$$

Since we assume that the reflective surface of the vehicle is a series of scatterers which will reflect a signal from the transmitter to the receiver, there will be multiple waves of different rate of change of pathlengths at the receiver and hence different Doppler shifts, which causes a Doppler spread at the receiver.

The signals reflected off the side of the vehicle at the front (S_F) and back (S_B) are most likely to have the highest pathlength difference between them and hence the highest difference in Doppler shifts. The difference between these Doppler shifts describes the Doppler spread, F_{SP}.

Equation (20) can be applied to the situation shown in Figure 105. Only two paths are considered in the equation; the path of the S_B (P_B) and the path of S_F (P_F). At time t_0 the back and the front of the car is at d_b and d_f respectively. At t_1, a very small amount of time (Δt) has elapsed and the vehicle has moved to have its back and front at d_b' and d_f' respectively, which are both vΔt m away from their original positions. At t_1 the path of S_B and S_F is P_B' and P_F' respectively. Each of these four paths can be split into two segments, which helps determine their length using Pythagoras Theorem (Equations (21) - (28)).

$$P_{TxB} = \sqrt{D^2 + (L - d_r)^2} \tag{21}$$

$$P_{BRx} = \sqrt{D^2 + d_r^2} \tag{22}$$

$$P_{TxF} = \sqrt{D^2 + \left(L - d_f\right)^2} \tag{23}$$

$$P_{FRx} = \sqrt{D^2 + d_f^2} \tag{24}$$

$$P'_{TxB} = \sqrt{D^2 + \left(L - (d_r + v)\right)^2} \tag{25}$$

$$P'_{BRx} = \sqrt{D^2 + (d_r + v)^2} \tag{26}$$

$$P'_{TxF} = \sqrt{D^2 + \left(L - (d_f + v)\right)^2} \tag{27}$$

$$P'_{FRx} = \sqrt{D^2 + \left(d_f + v\right)^2} \qquad (28)$$

The change in pathlength for both these paths is thus given by the Equations (29) and (30).

$$\Delta P_B = P_{TxB} + P_{BRx} - P'_{TxB} - P'_{BRx} \qquad (29)$$

$$\Delta P_F = P_{TxF} + P_{FRx} - P'_{TxF} - P'_{FRx} \qquad (30)$$

The Doppler shifts for both these paths are as shown in Equations (31) and (32).

$$\Delta f_B = \frac{\Delta P_B}{\lambda \Delta t} \qquad (31)$$

$$\Delta f_F = \frac{\Delta P_F}{\lambda \Delta t} \qquad (32)$$

Therefore Equation (33)gives the Doppler spread.

$$f_{sp} = \Delta f_B - \Delta f_F \qquad (33)$$

9.2 Model Output

In this section results from the model described above are presented.

9.2.1 Interpretation of the Phase Change, Doppler Shift and Maximum Doppler Spread Graphs

D, v and L are kept constant. The first two panels of Figure 106 and Figure 107 show plots of the phase change and Doppler shifts (Δf) for S_B (blue line) and S_F (green line). The third panel displays the Doppler spread (f_{sp}) that would be caused. The difference between the figures is that one is for a vehicle length (l) of 3 m while the other is for l = 5 m; both of which are similar to standard sizes of cars. Compared to Figure 106, Figure 107 has an increase in the gap between the ΔΦ lines which leads to an increase in the gap between Δf lines. This increased frequency range results in a larger Doppler spread for the larger vehicles.

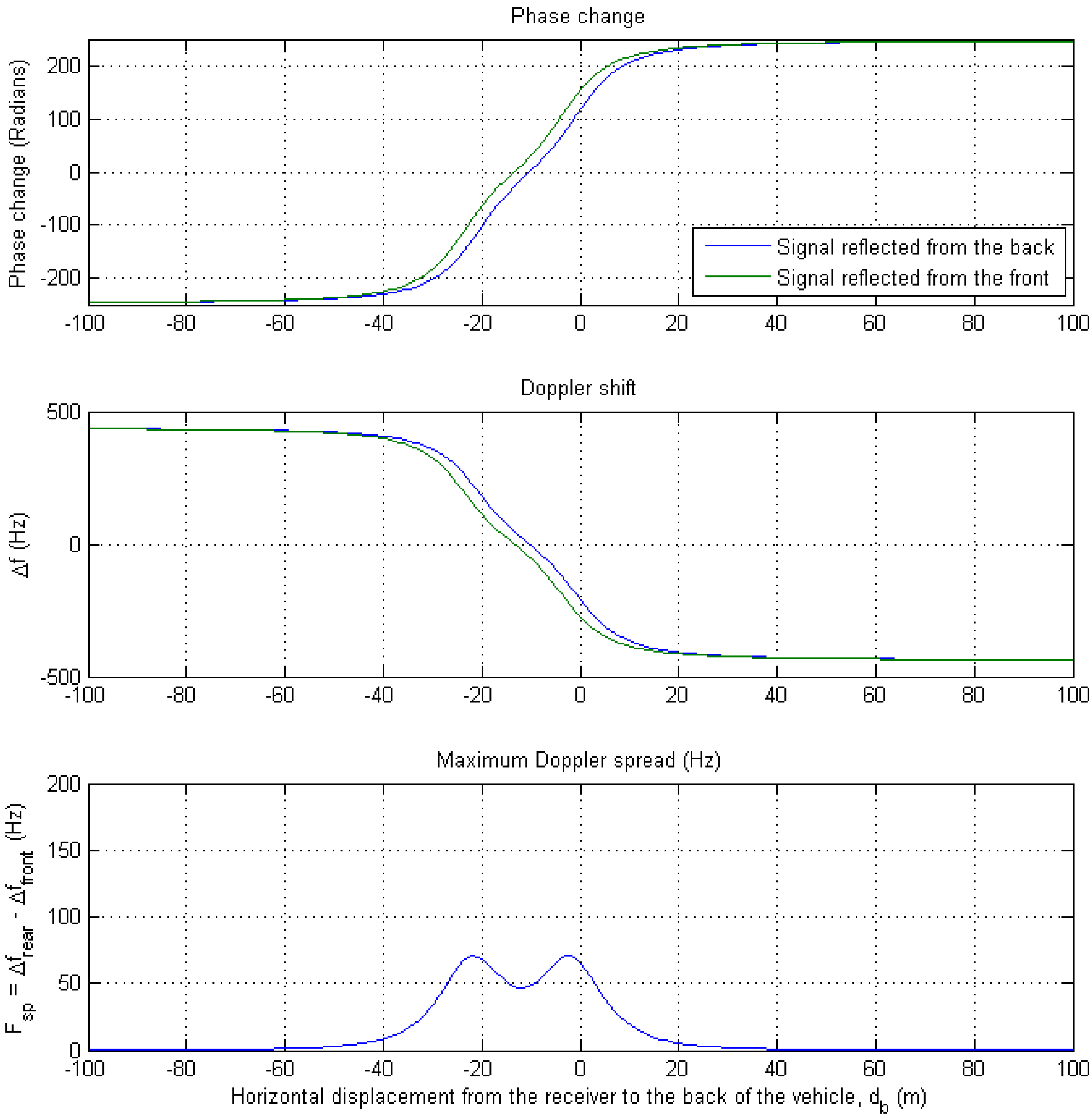

Figure 106: Phase change and Doppler shift for S_B and S_F and the resulting Doppler spread for a vehicle of length 3 m moving at 40 kmh^{-1}, 10 m away from the transmitter and receiver line, with 20 m between the transmitter and the receiver

At greater distances ($d_b < 60$ and $d_b > 40$) $\Delta\Phi$ and Δf are almost constant because the vehicle is far enough for $P_{TxB} \approx P_{BRx} \approx P_{TxF} \approx P_{FRx}$ – so the vehicle is approximately in line with the transmitter and the receiver.

In both Figure 106 and Figure 107 $\Delta\Phi$ and Δf do not have a gradual decrease/increase; the transition zone ($-40 < d_b < 20$) contains two inflexions. P_B and P_F each comprises two components; P_{TxB} and P_{BRx}, and P_{TxF} and P_{FRx}. P_{TxB} and P_{BRx} change at different rates which causes the variation in the rate at which $\Delta\Phi$ and Δf vary; the same applies for P_{TxF} and P_{FRx} which is just shifted to the left by 1 m, Section 9.2.2 further explores the reason behind having two peaks.

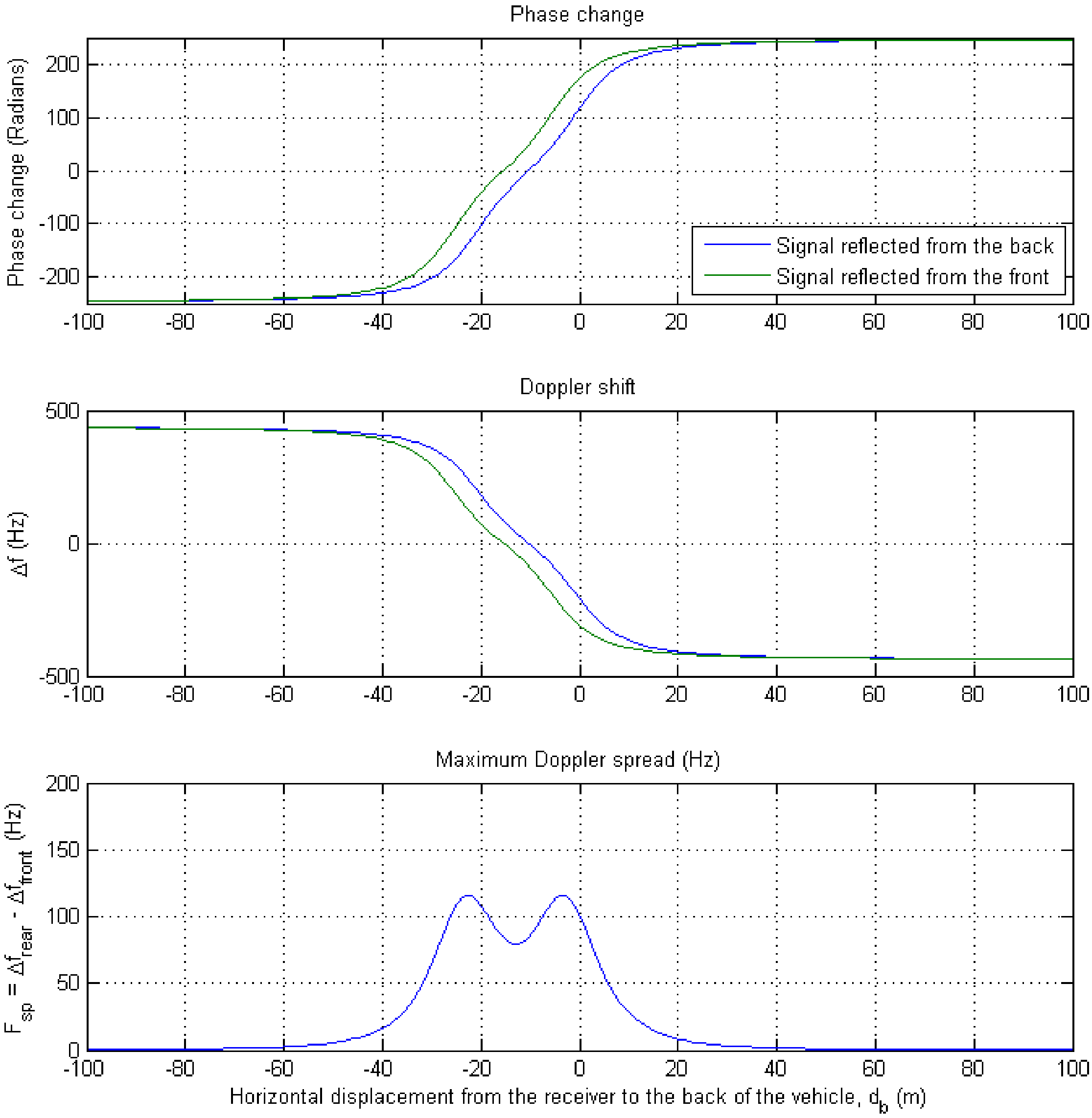

Figure 107: Phase change and Doppler shift for S_B and S_F and the resulting Doppler spread for a vehicle of length 5 m moving at 40 kmh-1, 10 m away from the transmitter and receiver line, with 20 m between the transmitter and the receiver

For a transmitter or receiver operating at 5.9 GHz and moving with a velocity of 40 kmh^{-1} relative to each other, Δf is expected to be 219 Hz. However, Δf has a maximum of 431 Hz which is almost double that of signals received directly from a mobile receiver or transmitter. This is because each path between the transmitter and the receiver comprises two paths, whose rate of change of pathlength adds up and hence gives a higher ΔΦ and Δf.

9.2.2 The Dual Peaks Phenomena

The two peaks in f_{sp} are when P_F and P_B change the most – as they pass the transmitter and the receiver. Figure 108 shows a diagram of the vehicle just before it goes past the transmitter.

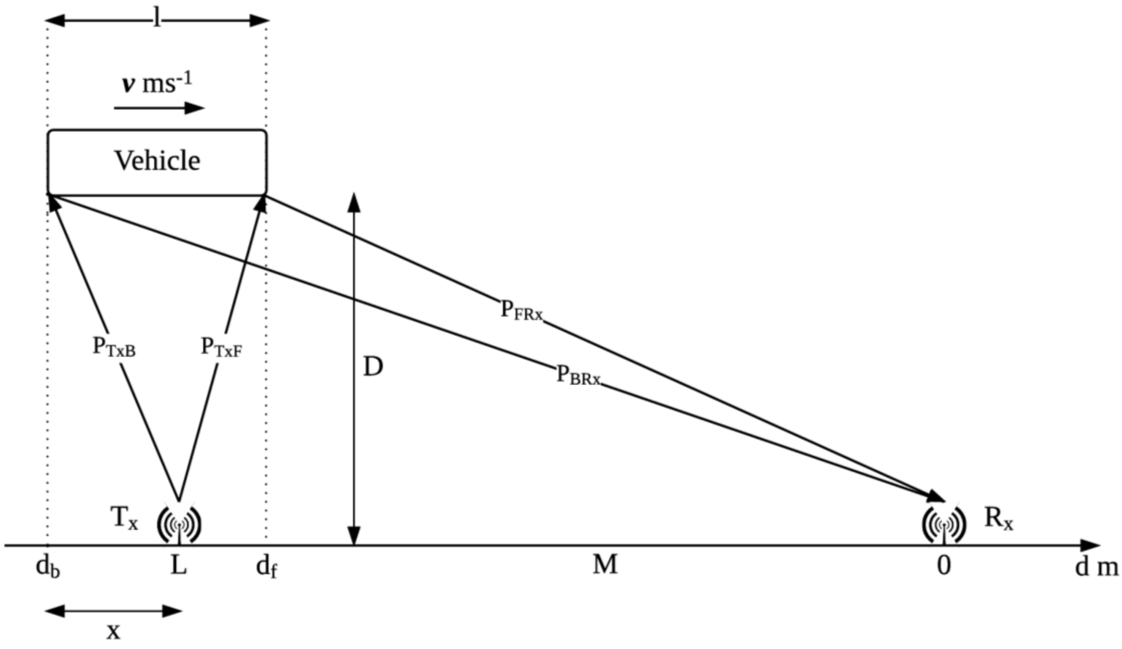

Figure 108: A vehicle in line with the transmitter

If the receiver is far enough from the transmitter such that $P_{FRx} \approx P_{BRx}$ and the variation in the path length is entirely down to P_{TxB} (Equation (34)) and P_{TxF} (Equation (35));

$$P_{TxB} = \sqrt{D^2 + x^2} \tag{34}$$

$$P_{TxF} = \sqrt{D^2 + (x+l)^2} \tag{35}$$

As the front passes the transmitter P_{TxF} is at its minimum value and changes from decreasing to increasing; the same applies to P_{TxB}. The Doppler spread is a function of the differences of the Doppler shift between S_B and S_F, which is reliant of the rate of change of P_{TxB} and P_{TxF}. Therefore, the maximum f_{SP} is when

$$\max f_{sp} \rightarrow \max\left\{\frac{d(P_{TxB} - P_{TxF})}{dx}\right\}$$

and

$$\max\left\{\frac{d(P_{TxB} - P_{TxF})}{dx}\right\} = \frac{d^2(P_{TxB} - P_{TxF})}{dx^2} = 0$$

$$\frac{(x+l)^2}{\sqrt{(D^2+(x+l)^2)^3}} - \frac{x^2}{\sqrt{(D^2+x^2)^3}} = 0$$

$$\frac{(x+l)^2}{\sqrt{(D^2+(x+l)^2)^3}} = \frac{x^2}{\sqrt{(D^2+x^2)^3}} \tag{36}$$

In Equation (36) as D and l are constants, the roots to the equation is when $x^2 = (x + l)^2$. Which can be solved to get $x = -l/2$. This is when the middle of the vehicle is in line with the transmitter. The same applies when the vehicle moves past the receiver; which explains the two peaks seen in Figure 106 and Figure 107.

9.2.3 Doppler Spread as a Function of Vehicle Length

Figure 109 shows how the maximum Doppler spread varies as l increases; small cars are approximately 3 m long while longer trucks can be approximately 25 m.

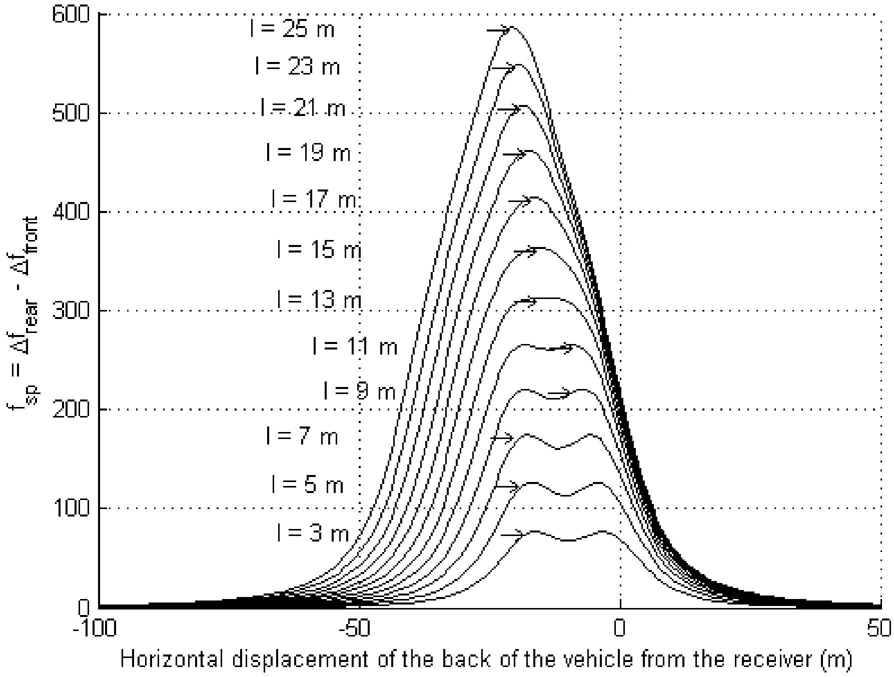

Figure 109: Family of curves showing how the Doppler spread changes as the length of the vehicle varies between 3 and 25 m. The vehicle is travelling at 40 kmh^{-1}, 10 m away from the line of the transmitter and the receiver, which are 15 m apart

As the l increases the width of the f_{sp} peak also increases. This is because as l increases, the front of the vehicle reaches the transition zone (where P_F starts to undergo significant change in size) while the back of the vehicle is further away from the transition zone and hence P_{TvB} is not varying significantly.

The dual peaks in f_{sp} are separated by a distance of L m because the highest Doppler spreads are caused as a vehicle's middle passes in line with the transmitter and receiver.

The dual peaks are seen for l ≤ 15 m, after which point there is only one peak. Vehicle lengths greater than this are longer than the distance between the transmitter and the receiver (L). As mentioned previously, large Doppler spreads occur as the middle of the vehicle is vertically over the transmitter or receiver (shown by the red and blue dashed lines in Figure 110). However when l = L (as shown in Figure 110) and the back and the front of the vehicle is in line with the transmitter and receiver respectively, both P_F and P_B have fast varying components; components which are almost vertical. These variations are opposite to each other with P_B decreasing while P_F starts to increase. This increases f_{sp} beyond what it would be as the vehicle passes just the transmitter or the receiver.

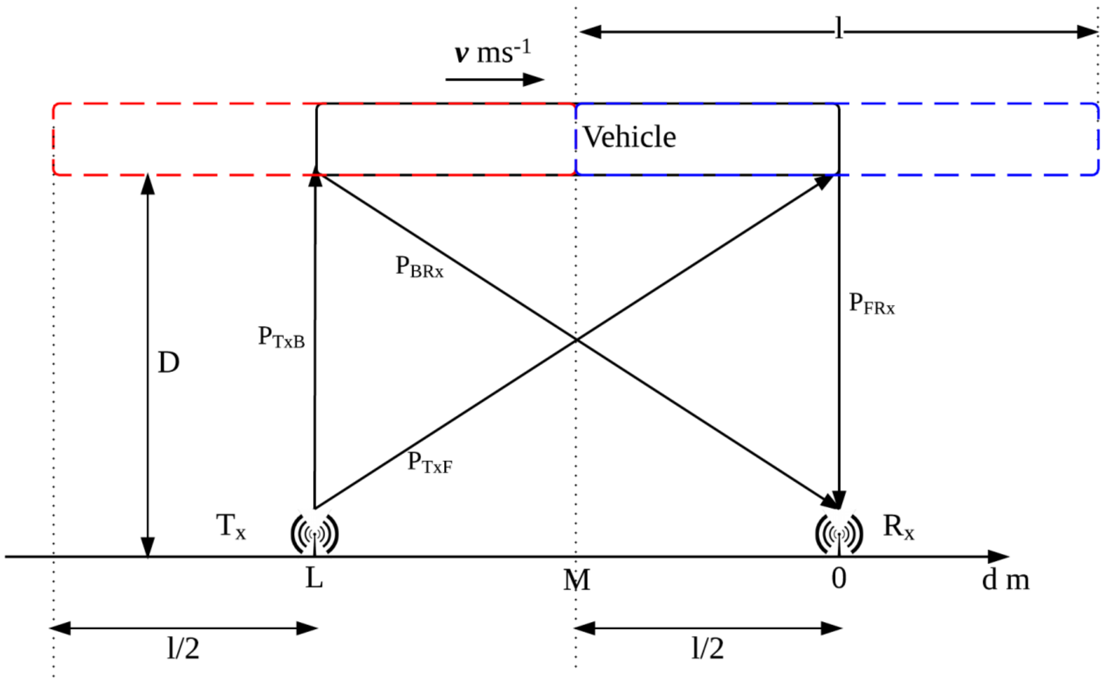

Figure 110: Vehicle passing between the transmitter and the receiver when l = L

As $l \geq L$, when the vehicle's midpoint passes the midpoint between the transmitter and the receiver (M), P_{TxB} is shortening while P_{FRx} is extending. This combined with the significant shortening and extending of P_{BRx} and P_{TxF} respectively contributes to larger differences between the rate of change of P_B and P_F, which gives a larger Doppler spread.

9.2.4 Doppler Spread as a function of the Vehicle Size as D Varies

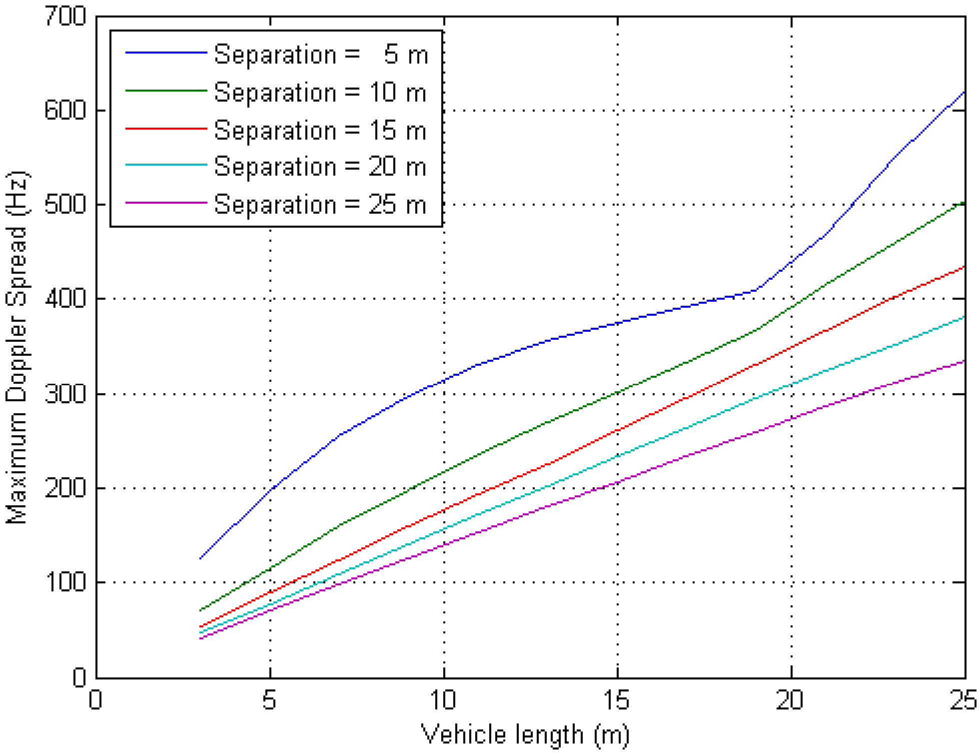

Figure 111: Maximum Doppler spread as a function of the vehicle's length as D varies

Figure 111 shows how the maximum Doppler spread (pointed by the arrows in Figure 110) varies as a function of vehicle length, for different values of D (marked as separation in the figure). As D increases so does the max f_{sp}, for a given vehicle length. However, there is an interesting trend seen – f_{sp} appears to increase uniformly for larger values of D but as D gets shorter, f_{sp} loses the uniformity that it increases with.

As D becomes shorter, it brings the vehicle closer to the transmitter and the receiver which increases the differences between the variations of the paths. This in turn increases the range of Doppler shifts of the different signals being received which result in a higher Doppler spread experienced at the receiver.

It was also found that when D was significantly larger than L and l, there would only be one peak in the Doppler spread which was not as high if D was smaller. This is because L and l becomes small enough (in relation to D) for all the components of P_B and P_F to vary synchronously; as opposed to one part varying rapidly while the other one stays approximately constant. With all the parts in both paths varying at a similar rate to each other, ΔP_F and ΔP_B have gradual transitions which lead to just one peak in f_{sp}.

9.3 Conclusions

In this chapter a model was developed to analyse how the Doppler spread varies as a function of the size of a moving vehicle. The model showed that the Doppler shifts of the received signals were larger than the expected Doppler shift from a moving transmitter or a receiver. This is because the Doppler shift is a function of the rate of change of pathlength and in a path which has reflected components which varies; the total pathlength's variation is the sum of all these variations.

The most important result from this model is that the Doppler spread varies as a function of the vehicle's length and also the proximity of the vehicle to the transmitter and the receiver. For short vehicle lengths which are closer to the transmitter and receiver, the Doppler spread has two peaks which coincide with the points where the vehicle passes in line with the transmitter or the receiver. As the vehicle length becomes larger than the distance between the transmitter and the receiver, there is only one peak in the Doppler spread which occurs as the vehicle is equidistant from the transmitter and the receiver. The Doppler spread also increases as the vehicle moves closer to the transmitter and receiver as a result of the increased differences between the rates at which the pathlengths vary.

10 Conclusions

It is likely that radio communications systems will be used to share information between vehicles as part of a drive towards autonomous systems. The widely adopted communications standard for this is currently IEEE 802.11p which operates at 5.9 GHz. However, the volume of research for radio wave propagation at 5.9 GHz with a focus on inter-vehicular communications is not very large and this leaves a lot of questions about the performance of such communications. Different physical environments (such as urban and suburban intersections, and highways and rural areas) offer challenging channel properties (such as increased Doppler and delay spreads caused by multipath propagation and mobile transmitters, receivers and reflectors). The work in this thesis has focussed on propagation at an urban, less urban and open T-junction.

Signal strength, Doppler spreads and network performance has been measured simultaneously using the equipment configuration described in Chapter 3. Such a configuration and the data it produces is a unique aspect of this study – Cheng et al. (2007) used similar equipment but did not measure power loss using a spectrum analyser. Another unique feature is the type of locations used for data collection – T-junctions with the transmitter placed on the branched road hence causing NLOS conditions. Whilst studies have been performed to model propagation at intersections this is the first that entirely focusses on radio propagation at 5.9 GHz at T-junctions.

Measurements of signal strength and packet delivery ratio presented in Chapter 4 showed that network performance suffers a dramatic loss under NLOS conditions in single and dual lane roads. When the transmitter was 24 m away from the intersection centre in a single lane T-junction (urban) and transmitting a CW with EIRP of 16 dBm, 90% PDR (which would be marginal in supporting safety critical communications) was consistently observed only for 20 m and 10 m (from the intersection centre) on the perpendicular roads which were under NLOS conditions. The road with the larger coverage was an urban canyon (which acts as a waveguide) whereas the other road had a relatively open space which led to less power being received in that part of the junction. An unexpected observation was that the signal strength increased by approximately 10 dB after its initial dip soon after entering NLOS conditions. These ranges are short compared to the coverage of 100s of metres on highways or open areas.

The network performance was worse in a second intersection (less urban) which had fewer buildings to reflect signals (this intersection had double lane roads). A consistent PDR greater than 90% was not observed at all with the transmitter being 50 or 70 m away from the intersection centre and the receiver collecting data from 10 m away from the intersection centre. The PDR was consistently less than 10% once the receiver was beyond 15 m from the intersection centre.

The PDR was consistently greater than 90% for just over 25 m in the open junction (fewer buildings and a dual lane road with a 4-lane road joining it). The PDR was also consistently greater than 60% up to a distance of 40 m away from the intersection centre.

To support safety critical systems designers may have to consider using a communications repeater at the centre of single/dual lane intersections with buildings at the edges assuming that the increased latency and network congestion does not adversely affect the system more.

The pathloss predictions from a recent model, VirtualSource11p (Mangel et al. 2011) were compared against the signal strength measurements (Chapter 5). For the urban T-junction (single lane roads with multi-storey buildings either side) it was found that the median error was within 5 dB for measurement runs up to 30 m away from the intersection centre. The median error then increased for the measurement runs made further away from the intersections. In the less urban and open junction the median error for measurement runs within 20 m of the intersection centre was greater than 10 dB and this increased up to 15 dB for runs as they approached 50 m away from the intersection. Users of this model should be aware that the model works best in urban environments which have lots of surfaces to reflect the waves.

It will be useful to collect more data from junctions of different layouts and then use this data to derive a loss factor depending on an intersection's layout, and possibly building material.

The virtualsource11p model is a site generic model which does not consider the layout of buildings surrounding a junction.

Another solution to finding the signal strength is to use ray tracing. This will potentially produce more accurate signal strength, Doppler and delay spread predictions for different layouts and can also reflect the effect of physical traffic. The ray tracing model described in Chapter 6 successfully provides a qualitative explanation as to why the power levels are higher on the urban canyon half (as opposed to the open half) of the urban case. The model's results are also congruent with the spike in signal strength shortly after LOS conditions are lost. Both these observations are caused by signals being reflected off the surrounding buildings.

The directions of the strongest multipath components in the urban case were found using a directional antenna and presented in Chapter 7. The results show the importance of accurate maps when it comes to ray tracing – parked cars and large bins contributed towards the received power. The data also showed that shortly after LOS is lost, the strongest signals arrive via reflection. But as the distance from the intersection centre increases the strongest signals arrive through a combination of both reflection and diffraction.

Chapter 8 shows another unique contribution of this study – the effect of vehicles on communications. Larger vehicles in the propagation area were seen to cause a small but noticeable increase in network performance under NLOS conditions during periods when the network was otherwise not functional. The most likely explanation is that the vehicles reflected waves around the corner from the transmitter to the receiver. It was also found that larger vehicles led to larger Doppler spreads with stronger amplitudes. This was further explored in Chapter 9 where a model was developed that demonstrated the relationship between a vehicle's size, the distance between it and the transmitter and the receiver, and the Doppler spread it causes. The information provided here would be useful towards V2X communications channel modelling – such networks will have many of mobile reflectors (such as cars and trucks) in close proximity and the Doppler spreads caused by them cannot be ignored.

To further the work done in this study:

- More data from other intersections with different layouts can be collected. This will then be used to develop an intersection and building material dependent loss factor, which will improve the accuracy of models such as Virtualsource11p. The data can also be used to verify the accuracy of ray tracing models.

- A more rigorous method of recording traffic density during measurements would be beneficial. This can be used to create relationships between physical traffic and the network performance, signal strength and the Doppler spread.
- The ray tracing model presented in Chapter 6 will also require improvements to incorporate diffraction and to relate its output to the pathloss. A planned addition to this model is to incorporate physical traffic and then use it to analyse the effect of physical traffic on the signal strength and Doppler spread.
- There are also improvements which can be made to the Doppler spread analysis model – the current model is based only on the change in pathlength of the signals. For more accurate results the reflection angle of the scattered waves should be taken into account because the received power is also dependent on the angle that a signal reflects through.

11 References

Abbas, T. et al., 2013. Validation of a non-line-of-sight path-loss model for V2V communications at street intersections. In *2013 13th International Conference on ITS Telecommunications (ITST)*. IEEE, pp. 198–203.

Abdelgader, A.M.S. & Lenan, W., 2014. The Physical Layer of the IEEE 802 . 11p WAVE Communication Standard : The Specifications and Challenges. *World Congress on Engineering and Computer Science 2014*, II, pp.22–24.

AIDE Consortium, 2006. AIDE - Adaptive Integrated Driver-vehicle Interface. Available at: http://www.aide-eu.org/ [Accessed November 24, 2015].

Alexander, P., Haley, D. & Grant, A., 2011. Cooperative Intelligent Transport Systems: 5.9-GHz Field Trials. *Proceedings of the IEEE*, 99(7), pp.1213–1235.

Amadeo, M., Campolo, C. & Molinaro, A., 2012. Content-centric networking: is that a solution for upcoming vehicular networks? In *VANET12 Proceedings of the 9th ACM International Workshop on VehiculAr InterNETworking Systems and Applications (2012)*. pp. 99–101.

ASTM International, 2002. *ASTM E2213-02, Standard Specification for Telecommunications and Information Exchange Between Roadside and Vehicle Systems — 5 GHz Band Dedicated Short Range Communications (DSRC) Medium Access Control (MAC) and Physical Layer (PHY) Specifications*,

ASTM International, 2010. *ASTM E2213-03(2010), Standard Specification for Telecommunications and Information Exchange Between Roadside and Vehicle Systems — 5 GHz Band Dedicated Short Range Communications (DSRC) Medium Access Control (MAC) and Physical Layer (PHY) Specifications*,

Azimi, S. et al., 2013. Reliable intersection protocols using vehicular networks. In *Cyber-Physical Systems (ICCPS), 2013 ACM/IEEE International Conference on*. pp. 1–10.

Bai, F., Stancil, D.D. & Krishnan, H., 2010. Toward understanding characteristics of dedicated short range communications (DSRC) from a perspective of vehicular network engineers. In *Proceedings of the sixteenth annual international conference on Mobile computing and networking - MobiCom '10*. New York, New York, USA: ACM Press, p. 329.

Boban, M. et al., 2014. TVR - Tall Vehicle Relaying in Vehicular Networks. *IEEE Transactions on Mobile Computing*, 13(5), pp.1118–1131.

Bosch, GLM 80 Professional Laser Measure Laser measures | Bosch Professional. Available at: http://www.bosch-professional.com/gb/en/glm-80-26171-ocs-p/ [Accessed October 2, 2015].

C2C-CC, 2007. *CAR 2 CAR Communication Consortium Manifesto: Overview of the C2C-CC System*,

Cheng, L. et al., 2007a. A fully mobile, GPS enabled, vehicle-to-vehicle measurement platform for characterization of the 5.9 GHz DSRC channel. In *IEEE Antennas and Propagation Society, AP-S International Symposium (Digest)*. pp. 2005–2008.

Cheng, L. et al., 2007b. Mobile Vehicle-to-Vehicle Narrow-Band Channel Measurement and Characterization of the 5.9 GHz Dedicated Short Range

Communication (DSRC) Frequency Band. *IEEE Journal on Selected Areas in Communications*, 25(8), pp.1501–1516.

Choudhury, R.R. & Vaidya, N.H., 2004. Deafness: a MAC problem in ad hoc networks when using directional antennas. In *Proceedings of the 12th IEEE International Conference on Network Protocols, 2004. ICNP 2004.* IEEE, pp. 283–292.

COMeSafety, 2011. *COMeSafety2 Newsletter, June 2011, Issue 1*,

COOPERS, Coopers: Project. Available at: http://www.coopers-ip.eu/index.php?id=project [Accessed November 25, 2015].

Department of Transport, 2015a. Average number of trips made and distance travelled (NTS01) - Statistical data sets - GOV.UK. Available at: https://www.gov.uk/government/statistical-data-sets/nts01-average-number-of-trips-made-and-distance-travelled [Accessed October 12, 2015].

Department of Transport, General rules, techniques and advice for all drivers and riders (103 to 158) - The Highway Code - Guidance. Available at: https://www.gov.uk/guidance/the-highway-code/general-rules-techniques-and-advice-for-all-drivers-and-riders-103-to-158#rule126 [Accessed October 7, 2015].

Department of Transport, 2015b. NTS factsheets - Publications - GOV.UK. Available at: https://www.gov.uk/government/publications/nts-factsheets [Accessed October 12, 2015].

Department of Transport, 2015c. Road accidents and safety: statistical tables index - Statistical data sets - GOV.UK. Available at: https://www.gov.uk/government/statistical-data-sets/road-accidents-and-safety-statistical-tables-index [Accessed October 13, 2015].

Drive C2X, Project - DRIVE C2X. Available at: http://www.drive-c2x.eu/project [Accessed December 29, 2012].

Eindhoven University of Technology, 2011. Connect & Drive. Available at: https://www.tue.nl/en/university/departments/industrial-design/research/research-groups/user-centered-engineering/research/projects/explorations-in-interactions/connect-drive/ [Accessed November 24, 2015].

ERTICO, 2009. CVIS Objectives. Available at: http://web.archive.org/web/20100620000634/http://www.cvisproject.org/en/about_cvis/objectives/ [Accessed November 24, 2015].

ERTICO, 1999. ERTICO - ITS Europe. Available at: http://ertico.com/ [Accessed November 16, 2015].

ETSI, 2009. *ES 202 663 - V1.1.0 - Intelligent Transport Systems (ITS); European profile standard for the physical and medium access control layer of Intelligent Transport Systems operating in the 5 GHz frequency band*,

ETSI, T., 2009. ETSI TR 102 638 V1.1.1 Intelligent transport systems (ITS); vehicular communications; basic set of applications; definitions. , 1, pp.1–81.

EUCAR, 2015. EUCAR | European Council for Automotive R&D. Available at: http://www.eucar.be/ [Accessed November 17, 2015].

Eurecom, 2014. VanetMobiSim - Newcom | Institut Eurecom | Politecnico di Torino. Available at: http://vanet.eurecom.fr/ [Accessed December 11, 2015].

European Commission, 2015. EC initiatives on eSafety - European Commission.

Available at: http://ec.europa.eu/transport/road_safety/specialist/knowledge/esave/ec_initiatives_on_esafety/index_en.htm [Accessed November 17, 2015].

Federeal Communications Commission, 2002. *Amendment of the Commission's Rules Regarding Dedicated Short-Range Communication Services in the 5.850-5.925 GHz Band*,

Fernandez, J.A. et al., 2012. Performance of the 802.11p Physical Layer in Vehicle-to-Vehicle Environments. *IEEE Transactions on Vehicular Technology*, 61(1), pp.3–14.

Ferreira, M. & Conceiçao, H., 2009. Urban connectivity analysis of vanets through stereoscopic aerial photography. ... *Conference Fall (VTC ...*, pp.3–5.

Festag, J.A. et al., 2008. 'NoW – Network on Wheels': Project Objectives, Technology and Achievements. In *Proceedings of 5rd International Workshop on Intelligent Transportation (WIT)*. pp. 211–216.

Fuxjäger, P. et al., 2010. IEEE 802.11p Transmission Using GNURadio. *Spectrum*, 94, pp.1–4.

Gruteser, M., 2012. VANET ' 12 Keynote Address : A Mobile Systems Perspective on Vehicular Networks. In *VANET12 Proceedings of the 9th ACM International Workshop on VehiculAr InterNETworking Systems and Applications (2012)*. p. 1.

Hafeez, K., Anpalagan, A. & Zhao, L., 2015. Optimizing the Control Channel Interval of the DSRC for Vehicular Safety Applications. *IEEE Transactions on Vehicular Technology*, 9545(c), pp.1–1.

Hartenstein, H. & Laberteaux, K.P., 2010. *VANET* H. Hartenstein & K. P. Laberteaux, eds., Chichester, UK: John Wiley & Sons, Ltd.

Ho, K.-Y. et al., 2010. Implementation of WAVE/DSRC Devices for vehicular communications. In *2010 International Symposium on Computer, Communication, Control and Automation (3CA)*. IEEE, pp. 522–525.

HTAS, 2015. High Tech Automotive Systems. Available at: http://www.htas.nl/ [Accessed November 17, 2015].

Ibrahim, M.F. & Parsons, J.D., 1983. Signal strength prediction in built-up areas. Part 1: Median signal strength. *IEE Proceedings F Communications, Radar and Signal Processing*, 130(5), p.377.

IEEE, 2012. *802.11-2012 - IEEE Standard for Information technology--Telecommunications and information exchange between systems Local and metropolitan area networks--Specific requirements Part 11: Wireless LAN Medium Access Control (MAC) and Physical Layer (PHY) Spec*,

IEEE, 2010. *802.11p-2010 - IEEE Standard for Information technology-- Local and metropolitan area networks-- Specific requirements-- Part 11: Wireless LAN Medium Access Control (MAC) and Physical Layer (PHY) Specifications Amendment 6: Wireless Access in Vehicular En*,

IEEE, 2006. IEEE SA - 1609 WG - Dedicated Short Range Communication Working Group. Available at: https://standards.ieee.org/develop/wg/1609_WG.html [Accessed October 21, 2015].

IEEE, 2007. IEEE Standard for Information Technology - Telecommunications and Information Exchange Between Systems - Local and Metropolitan Area Networks

- Specific Requirements - Part 11: Wireless LAN Medium Access Control (MAC) and Physical Layer (PHY) Specificatio. *IEEE Std 802.11-2007 (Revision of IEEE Std 802.11-1999)*, pp.1–1076.

IEEE Vehicular Technology Society, 2013. *IEEE Guide for Wireless Access in Vehicular Environments (WAVE) Architecture*,

IHS, 2015. Slower, Not Lower: IHS Automotive Forecasting 88.6 Million Unit Global Light Vehicle Market in 2015 | IHS Online Newsroom. Available at: http://press.ihs.com/press-release/automotive/slower-not-lower-ihs-automotive-forecasting-886-million-unit-global-light-v [Accessed October 12, 2015].

Institute for Telecommunications Research et al., 2011. ConnectSafe. Available at: http://www.connectsafe.org/ConnectSafe/ConnectSafe.html [Accessed November 16, 2015].

Islam, T. et al., 2013. Realistic simulation of IEEE 802.11p channel in mobile Vehicle to Vehicle communication. In *2013 Conference on Microwave Techniques (COMITE)*. IEEE, pp. 156–161.

ISO/TC 204 WG 16, 2015a. *ISO 17515-1:2015 - Intelligent transport systems -- Communications access for land mobiles (CALM) -- Evolved Universal Terrestrial Radio Access Network (E-UTRAN) -- Part 1: General usage*,

ISO/TC 204 WG 16, 2008a. *ISO 21212:2008 - Intelligent transport systems -- Communications access for land mobiles (CALM) -- 2G Cellular systems*,

ISO/TC 204 WG 16, 2008b. *ISO 21213:2008 - Intelligent transport systems -- Communications access for land mobiles (CALM) -- 3G Cellular systems*,

ISO/TC 204 WG 16, 2015b. *ISO 21214:2015 - Intelligent transport systems -- Communications access for land mobiles (CALM) -- Infra-red systems*,

ISO/TC 204 WG 16, 2010a. *ISO 21215:2010 - Intelligent transport systems -- Communications access for land mobiles (CALM) -- M5*,

ISO/TC 204 WG 16, 2012. *ISO 21216:2012 - Intelligent transport systems -- Communication access for land mobiles (CALM) -- Millimetre wave air interface*,

ISO/TC 204 WG 16, 2014. *ISO 21217:2014 - Intelligent transport systems -- Communications access for land mobiles (CALM) -- Architecture*,

ISO/TC 204 WG 16, 2010b. *ISO 25112:2010 - Intelligent transport systems -- Communications access for land mobiles (CALM) -- Mobile wireless broadband using IEEE 802.16*,

ISO/TC 204 WG 16, 2011a. *ISO 29282:2011 - Intelligent transport systems -- Communications access for land mobiles (CALM) -- Satellite networks*,

ISO/TC 204 WG 16, 2011b. *ISO 29283:2011 - ITS CALM Mobile Wireless Broadband applications using Communications in accordance with IEEE 802.20*,

ITU, 2013. *ITU-R P.1411-7 Propagation data and prediction methods for the planning of short-range outdoor radiocommunication systems and radio local area networks in the frequency range 300 MHz to 100 GHz P Series Radiowave propagation*,

Jacobson, V. & Smetters, D., 2009. Networking named content. *Proceedings of the 5th international conference on Emerging networking experiments and technologies CoNEXT 09 (2009)*, 178(1), pp.1–12.

Jiang, D., Chen, Q. & Delgrossi, L., 2008. Optimal data rate selection for vehicle safety communications. In *Proceedings of the fifth ACM international workshop on VehiculAr Inter-NETworking - VANET '08*. New York, New York, USA: ACM Press, p. 30.

Joerer, S., Dressler, F. & Sommer, C., 2012. Comparing Apples and Oranges ? Trends in IVC Simulations A Position Paper. In *VANET12 Proceedings of the 9th ACM International Workshop on VehiculAr InterNETworking Systems and Applications (2012)*.

Kamal, F., Lou, E. & Zhao, V., 2012. Design and validation of a small-scale 5.9 GHz DSRC system for vehicular communication. In *2012 25th IEEE Canadian Conference on Electrical and Computer Engineering: Vision for a Greener Future, CCECE 2012*. IEEE, pp. 1–4.

Karagiannis, G. et al., 2011. Vehicular Networking: A Survey and Tutorial on Requirements, Architectures, Challenges, Standards and Solutions. *IEEE Communications Surveys & Tutorials*, 13(4), pp.584–616.

Karnadi, F.K., Mo, Z.H. & Lan, K., 2007. Rapid Generation of Realistic Mobility Models for VANET. In *2007 IEEE Wireless Communications and Networking Conference*. IEEE, pp. 2506–2511.

Kaul, S. et al., 2007. Effect of Antenna Placement and Diversity on Vehicular Network Communications. *2007 4th Annual IEEE Communications Society Conference on Sensor, Mesh and Ad Hoc Communications and Networks*, pp.112–121.

Kenney, J.B., 2011. Dedicated Short-Range Communications (DSRC) Standards in the United States. *Proceedings of the IEEE*, 99(7), pp.1162–1182.

Kenney, J.B. et al., 2012. Panel Discussion. In *Proceedings of the ninth ACM international workshop on Vehicular inter-networking, systems, and applications*.

Klein Wolterink, W., Heijenk, G. & van den Berg, H., 2012. Analytically modelling the performance of piggybacking on beacons in VANETs. In *Proceedings of the ninth ACM international workshop on Vehicular inter-networking, systems, and applications - VANET '12*. New York, New York, USA: ACM Press, p. 43.

Laboratory for Communications and Applications, 2012. Traffic and Network Simulation Environment. Available at: http://lca.epfl.ch/projects/trans/ [Accessed December 11, 2015].

Lin, J.-C. et al., 2012. Wireless communication performance based on IEEE 802.11p R2V field trials. *IEEE Communications Magazine*, 50(5), pp.184–191.

Lozano, R. et al., 2012. Global and regional mortality from 235 causes of death for 20 age groups in 1990 and 2010: a systematic analysis for the Global Burden of Disease Study 2010. *Lancet*, 380(9859), pp.2095–128.

Maier, G., Paier, A. & Mecklenbrauker, C.F., 2011. Packet detection and frequency synchronization with antenna diversity for IEEE 802.11p based on real-world measurements. In *2011 International ITG Workshop on Smart Antennas*. IEEE, pp. 1–7.

Maier, G., Paier, A. & Mecklenbrauker, C.F., 2012. Performance evaluation of IEEE 802.11p infrastructure-to-vehicle real-world measurements with receive diversity. In *2012 8th International Wireless Communications and Mobile Computing Conference (IWCMC)*. IEEE, pp. 1113–1118.

Mangel, T. & Hartenstein, H., 2011. 5.9GHz IEEE 802.11p inter-vehicle communication: Non-Line-of-Sight reception under competition. In *2011 IEEE Vehicular Networking Conference (VNC)*. IEEE, pp. 155–162.

Mangel, T., Klemp, O. & Hartenstein, H., 2011. A validated 5.9 GHz Non-Line-of-Sight path-loss and fading model for inter-vehicle communication. In *2011 11th International Conference on ITS Telecommunications*. IEEE, pp. 75–80.

Masui, H., Kobayashi, T. & Akaike, M., 2002. Microwave path-loss modeling in urban line-of-sight environments. *IEEE Journal on Selected Areas in Communications*, 20(6), pp.1151–1155.

Mecklenbrauker, C.F. et al., 2011a. Vehicular Channel Characterization and Its Implications for Wireless System Design and Performance. *Proceedings of the IEEE*, 99(7), pp.1189–1212.

Mecklenbrauker, C.F. et al., 2011b. Vehicular Channel Characterization and Its Implications for Wireless System Design and Performance. *Proceedings of the IEEE*, 99(7), pp.1189–1212.

Miloslavov, A., Veeraraghavan, M. & Smith, B.L., 2011. Validation of vehicular network simulation models with field-test measurements. In *2011 7th International Wireless Communications and Mobile Computing Conference*. IEEE, pp. 853–859.

Molisch, A.F. et al., 2009a. A survey on vehicle-to-vehicle propagation channels. *IEEE Wireless Communications*, 16(6), pp.12–22.

Molisch, A.F. et al., 2009b. Propagation aspects of vehicle-to-vehicle communications - an overview. In *2009 IEEE Radio and Wireless Symposium*. IEEE, pp. 179–182.

Molisch, A.F., 2005. *Wireless Communications*, Wiley-IEEE Press.

Molisch, A.F. & Tufvesson, F., 2004. *Multipath propagation models for broadband wireless systems* M. Ibnkahla, ed., CRC Pres.

Murthy, C.S.R. & Manoj, B.S., 2004. *Ad Hoc Wireless Networks: Architectures and Protocols (Prentice Hall Communications Engineering and Emerging Techno)*, Prentice Hall.

NS-2, 2011. The Network Simulator - NS-2. Available at: http://www.isi.edu/nsnam/ns/ [Accessed December 11, 2015].

NS-3, 2011. The Network Simulator - NS-3. Available at: https://www.nsnam.org/ [Accessed December 11, 2015].

Oda, Y., Tsunekawa, K. & Hata, M., 2000. Advanced LOS path-loss model in microcellular mobile communications. *IEEE Transactions on Vehicular Technology*, 49(6), pp.2121–2125.

OMNet++ Authors, 2015. OMNeT++ Discrete Event Simulator - Home. Available at: https://omnetpp.org/ [Accessed December 11, 2015].

Paier, A. et al., 2010. Overview of Vehicle-to-Vehicle Radio Channel Measurements for Collision Avoidance Applications. In *2010 IEEE 71st Vehicular Technology Conference*. IEEE, pp. 1–5.

Parsons, J.D., 2000. *The Mobile Radio Propagation Channel*, Wiley.

Puñal, O., Aguiar, A. & Gross, J., 2012. In VANETs we trust?: characterizing RF jamming in vehicular networks. *VANET12 Proceedings of the 9th ACM International Workshop on VehiculAr InterNETworking Systems and Applications (2012)*, pp.83–92.

Riverbed Technology, 2015. OPNET. Available at: http://www.riverbed.com/products/steelcentral/opnet.html?redirect=opnet [Accessed December 11, 2015].

Robert, L., Leinmüller, T. & Strassberger, M., 2008. OPENWAVE ENGINE/WSU-A PLATFORM FOR C2C-CC. *15th World Congress on Intelligent Transport Systems, New York, USA*, pp.1–5.

Robinson, T., Chan, E. & Coelingh, E., 2010. Operating platoons on public motorways: an introduction to the SARTRE platooning programme. In *Proceedings of the 17th ITS World Congress*.

SAE, 2010. DSRC Implementation Guide A guide to users of SAE J2735 message sets over DSRC. *Communication*.

SAE International, SAE International. Available at: https://www.sae.org/ [Accessed November 6, 2015].

SAFESPOT, 2010. SAFESPOT. Available at: http://www.safespot-eu.org/ [Accessed November 24, 2015].

Sarkar, S.K., 2012. *Wireless Sensor and Ad Hoc Networks Under Diversified Network Scenarios*, Artech House.

SARTRE, 2012. The SARTRE project. Available at: http://www.sartre-project.eu/en/Sidor/default.aspx [Accessed December 29, 2012].

SCALEABLE Network Technologies, 2014. QualNet | SCALABLE Network Technologies. Available at: http://web.scalable-networks.com/content/qualnet [Accessed December 11, 2015].

Schulze, M., 2014. *DRIVE C2X - Project overview*, Available at http://www.drive-c2x.eu/publications.

Schwartz, R.S. et al., 2012. Exploiting beacons for scalable broadcast data dissemination in VANETs. *Proceedings of the ninth ACM international workshop on Vehicular inter-networking, systems, and applications - VANET '12*, p.53.

Seeberger, D., 2006. *D06 Standardization Overview*,

Sepulcre, M. & Gozalvez, J., 2012. Experimental evaluation of cooperative active safety applications based on V2V communications. *Proceedings of the ninth ACM international workshop on Vehicular inter-networking, systems, and applications - VANET '12*, p.13.

Sharafkandi, S. et al., 2012. A novel use of EDCA to improve vehicle safety communication. *Proceedings of the ninth ACM international workshop on Vehicular inter-networking, systems, and applications - VANET '12*, p.115.

Shivaldova, V. et al., 2012. On roadside unit antenna measurements for vehicle-to-infrastructure communications. In *2012 IEEE 23rd International Symposium on Personal, Indoor and Mobile Radio Communications - (PIMRC)*. IEEE, pp. 1295–1299.

Sommer, C. et al., 2011. A computationally inexpensive empirical model of IEEE 802.11p radio shadowing in urban environments. In *2011 Eighth International Conference on Wireless On-Demand Network Systems and Services*. IEEE, pp. 84–90.

Subramanian, A.P. et al., 2008. A measurement study of inter-vehicular communication using steerable beam directional antenna. *Proceedings of the fifth ACM international workshop on VehiculAr Inter-NETworking - VANET '08*, p.7.

Subramanian, S., Werner, M. & Liu, S., 2012. Congestion control for vehicular safety: synchronous and asynchronous MAC algorithms. *Proceedings of the 9th ACM international workshop on VehiculAr InterNETworking VANET (2012)*, pp.63–72.

Sukuvaara, T., Ylitalo, R. & Katz, M., 2013. IEEE 802.11p Based Vehicular Networking Operational Pilot Field Measurement. *IEEE Journal on Selected Areas in Communications*, 31(9), pp.409–417.

SUMO, 2015. SUMO. Available at: http://sumo.dlr.de/wiki/Main_Page [Accessed December 11, 2015].

Tan, I. et al., 2008. Measurement and Analysis of Wireless Channel Impairments in DSRC Vehicular Communications. In *2008 IEEE International Conference on Communications*. IEEE, pp. 4882–4888.

Tielert, T. et al., 2011. Design methodology and evaluation of rate adaptation based congestion control for Vehicle Safety Communications. In *2011 IEEE Vehicular Networking Conference (VNC)*. IEEE, pp. 116–123.

Timm-Giel, A. et al., 2007. Directional Antennas for Vehicular Communication - Experimental Results. In *2007 IEEE 65th Vehicular Technology Conference - VTC2007-Spring*. IEEE, pp. 357–361.

United States Government Accountability Office, 2015. *Intelligent Transportation Systems: Vehicle-to-Infrastructure Technologies Expected to Offer Benefits, but Deployment Challenges Exist*,

United States Government Accountability Office, 2013. *Intelligent Transportation Systems: Vehicle-to-Vehicle Technologies Expected to Offer Safety Benefits , but a Variety of Deployment Challenges Exist*,

University of Florence RCL, 2006. HIDENETS. Available at: http://rcl.dsi.unifi.it/projects/hidenets [Accessed November 24, 2015].

University of Michigan Transportation Research Institute, 2014. Safety Pilot Model Deployment. Available at: http://www.umtri.umich.edu/our-results/projects/safety-pilot-model-deployment [Accessed November 24, 2015].

US DoT Federal Highway Administration, 2008. Gearing Up for SafeTrip-21. *FHWA-HRT-08-006*. Available at: https://www.fhwa.dot.gov/publications/publicroads/08sep/02.cfm [Accessed November 23, 2015].

US DoT ITS JPO, 2015a. Intelligent Transportation Systems - CICAS. Available at: http://www.its.dot.gov/cicas/ [Accessed November 23, 2015].

US DoT ITS JPO, 2015b. Intelligent Transportation Systems - Connected Vehicle Research. Available at: http://www.its.dot.gov/connected_vehicle/connected_vehicle_research.htm [Accessed November 23, 2015].

US DoT ITS JPO, 2015c. Intelligent Transportation Systems - Vehicle-to-Vehicle (V2V) Communications for Safety. Available at: http://www.its.dot.gov/safety/v2v_comm_safety.htm [Accessed November 23, 2015].

US DoT ITS JPO, 2015d. RITA - Intelligent Transportation Systems - Connected

Vehicle. Available at: http://www.its.dot.gov/landing/cv.htm [Accessed December 29, 2012].

Vinel, A., 2012. 3GPP LTE Versus IEEE 802.11p/WAVE: Which Technology is Able to Support Cooperative Vehicular Safety Applications? *IEEE Wireless Communications Letters*, 1(2), pp.125–128.

VSC, 2006. *Vehicle Safety Communications Project Final Report DOT HS 810 591*,

VSC-A, 2011. *Vehicle Safety Communications–Applications (VSC-A) Final Report*,

Wang, L.-C., Huang, S.-Y. & Chen, A., 2004. On the throughput performance of CSMA-based wireless local area network with directional antennas and capture effect: a cross-layer analytical approach. In *2004 IEEE Wireless Communications and Networking Conference (IEEE Cat. No.04TH8733)*. IEEE, pp. 1879–1884.

Weinfield, A., Kenney, J. & Bansal, G., 2011. An Adaptive DSRC Message Transmission Rate Control Algorithm. In *18th World Congress on Intelligent Transport Systems*.

Weisstein, E.W., Reflection. Available at: http://mathworld.wolfram.com/Reflection.html [Accessed May 5, 2015].

Wiedersheim, B., Sall, M. & Reinhard, G., 2009. SeVeCom — Security and privacy in Car2Car ad hoc networks. In *2009 9th International Conference on Intelligent Transport Systems Telecommunications, (ITST)*. IEEE, pp. 658–661.

World Health Organisation, 2008. *Global burden of disease, 2008*, World Health Organization.

World Health Organisation, 2013. *Global Status Report on Road Safety 2013*, WHO.

Xian, Y. & Huang, C.-T., 2012. Traffic-aware geographic forwarding in vehicular ad hoc networks. *Proceedings of the ninth ACM international workshop on Vehicular inter-networking, systems, and applications - VANET '12*, p.107.

Xiang, W., Huang, Y. & Majhi, S., 2008. The Design of a Wireless Access for Vehicular Environment (WAVE) Prototype for Intelligent Transportation System (ITS) and Vehicular Infrastructure Integration (VII). In *2008 IEEE 68th Vehicular Technology Conference*. IEEE, pp. 1–2.

Xu, K., Garrison, B.T. & Wang, K.-C., 2010. Performance modeling for IEEE 802.11 vehicle-to-infrastructure networks with directional antennas. In *2010 IEEE Vehicular Networking Conference*. IEEE, pp. 215–222.

Zaggoulos, G. & Nix, A., 2008. WLAN/WDS Performance using Directive Antennas in Highly Mobile Scenarios: Experimental Results. In *2008 International Wireless Communications and Mobile Computing Conference*. IEEE, pp. 700–705.